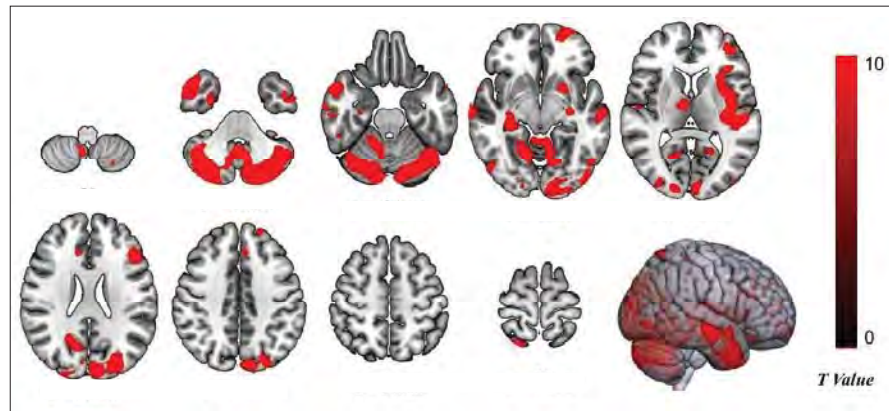


# Journal

of the

## National Science Foundation of Sri Lanka





## **JOURNAL OF THE NATIONAL SCIENCE FOUNDATION OF SRI LANKA**

### **Editorial Board**

Ajit Abeysekera (Editor in Chief)  
J.K.D.S. Jayanetti  
L.P. Jayatissa  
P. Prasad M. Jayaweera  
Jagath Manatunge  
S.S.N. Perera  
Rohini de A. Seneviratne  
Saman Seneweera  
S.A.H.A. Suraweera  
P. Wijekoon  
M.J.S. Wijeyaratne

### **Language Editor**

R.D. Guneratne

### **Editorial Office**

Nadeeja Wickramarachchi (Principal Scientific Officer)  
Uthpala T. Karunarathne (Senior Scientific Officer)  
Upuli Ratnayake (Scientific Officer)

### **International Editorial Advisory Board**

Chamil Abeykoon, UK  
Dilanthi Amaratunga, UK  
Dilantha Fernando, Canada  
Leslie Gunatilaka, USA  
Saman K. Halgamuge, Australia  
Kithsiri W. Jayasena, Australia  
Vassilios Kapaklis, Sweden  
Wah Yun Low, Malaysia  
Thomas Mathew, USA  
Shanthi Mendis, Switzerland  
Javier Francisco Ortega, USA  
Malik Peiris, Hong Kong  
Kamal Premaratne, USA  
Nalin Samarasinha, USA  
Ravi Silva, UK  
Christopher C. Steel, Australia

**Publication :** Published quarterly (March, June, September and December) by the National Science Foundation of Sri Lanka.

**Manuscripts:** Research Articles, Research Communications, Reviews and Correspondences in all fields of Science and Technology may be submitted for consideration for publication. A guide to the preparation of manuscripts is provided in each issue. The guidelines may also be obtained by visiting the NSF website.

**Disclaimer:** No responsibility is assumed by the National Science Foundation of Sri Lanka for statement and opinions expressed by contributors to this Journal.

Manuscripts and all correspondence relating to them should be e mailed to the Editorial Office, National Science Foundation, 47/5, Maitland Place, Colombo 07, Sri Lanka.

E-mail: [jnsf@nsf.gov.lk](mailto:jnsf@nsf.gov.lk)

Fax: 94-11- 2694754

JNSF home page: <http://www.nsf.gov.lk/index.php/nsfscience-magazine>

**Publication :** A publication fee of US\$ 250 will be levied for each manuscript except, when the corresponding author is affiliated to a Sri Lankan institution, in two stages.

- A processing fee of US\$ 20 will be levied for each manuscript at peer-review stage.
- Remaining US\$ 230 will be charged for accepted articles at the time of publication.

**Copyright :** © National Science Foundation of Sri Lanka

Articles in the Journal of the National Science Foundation of Sri Lanka are Open Access articles published under the Creative Commons CC-BY-ND License (<http://creativecommons.org/licenses/by/4.0/>). This license permits use, distribution and reproduction, commercial and non-commercial, provided that the original work is properly cited and is not changed anyway.

**Indexing :** The JNSF is indexed in Science Citation Index Expanded, Journal Citation Reports/ Science Edition, BIOSIS Previews, Zoological Record, Biological Abstracts, Chemical Abstracts, Scopus, DOAJ, TEEAL, Ulrich's, AGRICOLA and EBSCOhost, CAB Abstracts, SafetyLit, Journal TOCs, EBSCO Applied Science & Technology Source Ultimate

**JOURNAL OF THE  
NATIONAL SCIENCE FOUNDATION  
OF SRI LANKA**

Volume 52 Number 3 September 2024

---

**C O N T E N T S**

---

**EDITORIAL**

**281 Is there such a thing as self-plagiarism?**

*Ajit Abeysekera*

---

**RESEARCH ARTICLES**

**283 Construction of an effective telephone bandwidth specifically for speaker recognition**

*T Thiruvaran*

**299 Prevalence and abundance of plant-parasitic nematodes associated with corn (*Zea mays L.*) in Anuradhapura, Sri Lanka**

*N Thiruchelvan, S Casonato, G Mikunthan, LM Condron, R Moukarzel and M Kularathna*

**311 Computational analysis of diameter eccentricity based and hyper diameter eccentricity based indices for linear saturated monocarboxylic acids**

*D Sarkarai and K Desikan*

**321 Structural brain network topology in migraine vs. healthy subjects: A graph theory study**

*ADI Amarasinghe, DIH Wijewickrama, IS De Fonseka, MAD Lawanya, WNS Fernando, DAD Wishwanthi, G Senanayake, S Pushpakumara and WM Ediri Arachchi*

**331 An electrical double-layer supercapacitor based on a biomass-activated charcoal electrode and ionic liquid with excellent charge-discharge cycle stability**

*GRA Kumara, ADT Medagedara, HW Gadiarachchi, DGBC Karunarathne, K Tennakone, RMG Rajapakse and TMWJ Bandara*

**343 Influence of cultivar selection on blast and brown spot diseases in rice: Molecular screening of blast resistance genes**

*S Terensan, OVDSJ Weerasena, NS Kottearachchi, JN Silva and HNS Fernando*

**359 Predicting water content in engine oil using SPA-ISSA-BP methods**

*Chen Bin, Quan YuXuan, Liu Ge, Li JianZhong, Nie GaoXing, Zhang YongChang, Shan ChenZe, Chen JunSen, Chen Rui, Chen Xi and Zhang MengWei*

**371 Bioaccumulation and health risks of chromium and cadmium in *Basella alba* with emphasis on Urea, muriate of potash and triple super phosphate mixtures**

*MDMCK Amarasena and WMDN Wijeyaratne*

**385 Effective removal of Pb(II) ions using Fe<sub>3</sub>O<sub>4</sub>/MgO adsorbent: A comprehensive study**

*V Gurinathanan, KB Wijayaratne, BS Dassanayake, PG Mantilaka and CS Perera*

**401 An efficient and improved algorithm for generating an equivalent planar architecture of the data vortex switch**

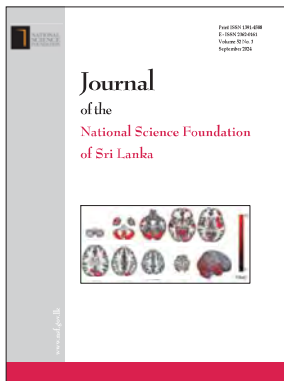
*A Soni and N Sharma*

**413 Cycle structures with more than three nontrivial cycles of automorphisms of Latin squares**

*MJL Mendis*

---

**Guidelines for Contributors**



**Cover:** Regional gross volume reductions in patients with migraine compared to healthy subjects detected by Voxel-based morphometry. All detected areas, indicated in black to red (corresponding to T values from 0 - 10).

See *J.Natn.Sci.Foundation Sri Lanka* 2024 **52**(3): 321 – 330

## EDITORIAL

### Is there such a thing as self-plagiarism?

The Oxford English Dictionary defines the word 'plagiarize' as "take the work or idea of someone else and pass it off as one's own". Taken in this sense, the term 'self-plagiarism' is an oxymoron. Nevertheless, the term is widely used and is defined in the Merriam Webster dictionary as "The re-use of one's own words, ideas or artistic expressions from preexisting material, especially without acknowledgement of their earlier use". We prefer the use of the ethically neutral term 'text recycling' to cover most situations where authors use previously published text in a new paper.

Text recycling can occur in many different contexts. Editors of research journals need to exercise good judgement in deciding when it is permissible and when it is not. It is not meaningful to merely consider similarity percentages generated by plagiarism detecting software and set cut off levels. In evaluating text recycling, the JNSF considers *intent* to be of paramount importance. Is

there an attempt to mislead by not providing references to previously published work? Related to intent is the issue of *novelty*. Does the paper contain sufficient new material worth disseminating to the scientific community? The answers to these two questions generally provide a reasonable basis to form a judgement on permissible and non-permissible text recycling.

One situation in which text recycling is permissible is in the description of experimental methods which have been published before, but need to be restated in the context of a new paper using the same method but with different substances and different values for parameters such as mass, volume, temperature and time. In such a situation, the attempt to reduce the similarity percentage of the paper by modifying the sentences and phrases used can result in an awkward text lacking the clarity and focus of the original. Ironically, it can even be conceived as an attempt to mislead!

**Ajit Abeysekera**



## RESEARCH ARTICLE

### Electronics

# Construction of an effective telephone bandwidth specifically for speaker recognition

T Thiruvaran

Department of Electrical and Electronic Engineering, Faculty of Engineering, University of Jaffna, Ariviyal Nagar, Killinochchi 44000, Sri Lanka.

Submitted: 22 May 2023; Revised: 20 March 2024; Accepted: 27 May 2024

**Abstract:** Although the telephone bandwidth is 0-4 kHz, the speaker specific information is not evenly distributed within this range but extends beyond 4 kHz. This is because the hypopharynx, especially the piriform fossa, affects the higher frequency region and contributes more to inter-speaker variation. By effectively shifting the higher bands to a lower frequency region, where speaker specific information is reduced, an effective 4 kHz bandwidth can be constructed to enhance speaker recognition performance. To achieve this a method was already proposed, which is extended in this paper to experimentally demonstrate and validate with more experiments. Furthermore, this paper defines the theoretically possible frequency space for which the frequency shifting method can be applied. To validate the method for different combinations of bands, possible bands were shifted in various directions in small steps. Speaker recognition experiments were conducted at each step to compare the performance against the baseband without any frequency shifting. Using the results of these extensive experiments, an approximate frequency space was defined where this frequency shifting performed better than the conventional baseband of 0-4 kHz signal. A simplified frequency shifting method was also investigated. Finally, the speech intelligibility of the frequency shifted narrow band speech signal was analyzed using objective speech quality measures. This showed that intelligibility was not significantly affected by the frequency shifting method.

**Keywords:** Frequency band shifting, speaker recognition, speaker specific information, speech intelligibility

## INTRODUCTION

Automatic speaker recognition can be used as a remote biometric authentication when speech is transmitted over a telephone channel. The bandwidth of the speech signal that can be used for the authentication system is limited to 4 kHz so as to match the telephone bandwidth. This could be one of the reasons why the regular National Institute of Standards and Technology (NIST) speaker recognition evaluation is conducted using speech signals sampled at 8 kHz (NIST, 2008). On the other hand, it has been shown through several psycho-acoustic experiments that this narrow telephone bandwidth of 0-4 kHz is not the only frequency range that contains the most speaker specific information, but higher frequency regions have more speaker specific information (Dang & Honda, 1997; Kitamura *et al.*, 2005; Lu & Dang, 2008; Hyon *et al.*, 2012).

Kitamura *et al.*, (2005) concluded that the hypopharynx behaves relatively stable during vowel sound production but varies more among different speakers. This conclusion was reached through a morphological analysis of inter-speaker and intra-speaker variation using MRI images. In terms of the frequency region, the spectra beyond 2.5 kHz are known to be

\* Corresponding author (thiruvaran@eng.jfn.ac.lk;  <https://orcid.org/0000-0003-0569-9669>)



This article is published under the Creative Commons CC-BY-ND License (<http://creativecommons.org/licenses/by-nd/4.0/>). This license permits use, distribution and reproduction, commercial and non-commercial, provided that the original work is properly cited and is not changed in anyway.

affected by variations of the speaker's hypopharynx. The hypopharynx consists of the laryngeal tube and bilateral cavities of the piriform fossa, which are located at the bottom of the vocal tract. In particular, the piriform fossa showed inter-speaker variation in shape, area and depth of those cavities (Kitamura *et al.*, 2005).

Furthermore, Takemoto *et al.*, (2006) studied the role of the laryngeal cavity in relation to vocal tract resonance. The laryngeal cavity was found to contribute significantly to the formation of the fourth formant. It specifically suggests that the fourth formant is defined almost only by the geometry of the laryngeal cavity. In addition, the cluster of 3<sup>rd</sup> and 4<sup>th</sup> formants were also shown to be controlled by the geometry of the laryngeal cavity. This is a significant finding for speaker recognition since the geometry of the laryngeal cavity is a speaker dependent property. This again supports the fact that the higher formant region, compared to the lower formant region, is significant for speaker recognition. A recent analysis on identical twins, having implications on forensic speaker recognition, revealed that higher frequency formants have a greater speaker discriminative ability compared to lower frequency formants (Cavalcanti *et al.*, 2021). In particular, the fourth formant was found to contain the highest speaker discriminative ability.

Further to the above findings of the lower vocal tract areas such as the piriform fossa that contribute to speaker specific information, Dang & Honda (1997) used MRI images of the piriform fossa to investigate their effect on the frequency spectra. The area function of the piriform fossa was shown to have more variation among different subjects but behaved relatively stable for vowel production. Further results revealed that the piriform fossa affected the frequency range from 4-5 kHz. This finding was again confirmed in an experiment using MRI based 3D printed vocal tract (Delvaux *et al.*, 2014). This further supports the findings that higher frequency regions are significant for speaker recognition.

In addition to the above morphological analysis, statistical based feature level analysis was done by Lu & Dang (2008) to quantify the distribution of speaker specific information in different frequency regions using the F-ratio, and mutual information on a 16 kHz database. It was concluded that three regions, specifically 100–300Hz, 4–5.5 kHz, and an area around 7.5 kHz contained more speaker specific information. Further, the study suggested that the area between 0.5 kHz and 3.5 kHz contained relatively less speaker relevant information. Their findings were validated by obtaining a better speaker recognition performance using a non-uniform filter bank that highlights the frequency regions with higher speaker specific information.

Another study analyzed the speaker specific information at the feature, model and classification level on NIST data (Thiruvaran *et al.*, 2009). At the feature level it used scatter matrix-based separation index measures. At the model level, it utilized a Kullback-Leibler distance-based measure. At the classification level, a series of speaker recognition experiments were conducted by leaving out one band to determine the contribution of that band on speaker recognition. The observations derived from these three levels of analysis for the telephone bandwidth data can be summarized as follows. The frequency range approximately between (1) 300-1000 Hz contributes to speaker recognition but not consistently in all three analyses; (2) 1000-2000 Hz contributes weakly to speaker recognition, consistent with Dang & Honda (1997); (3) 2000-3000 Hz contributes strongly to speaker recognition supporting the effect of the piriform fossa (Hyon *et al.*, 2012); and (4) 3000-3700 Hz is undetermined since it crosses the stop band region of the telephone bandwidth.

The study of a wide band signal with a bandwidth of 22.05 kHz reveals that the spectrum between 2000 - 5000 Hz contains significant speaker-specific information, as demonstrated in speaker recognition experiments (Thiruvaran *et al.*, 2009). Thus, all the above findings imply that the telephone bandwidth misses these speaker-specific information.

These observations provide motivation to develop a method that effectively utilizes the parts of speech bandwidth containing rich speaker-specific information. This method would enable the transmission over a telephone channel while retaining the advantage of remote authentication. The objective is to construct an effective 4 kHz band speech signal that includes speaker-specific information from both narrow and wide band signals. This signal will then be down sampled to an 8 kHz sampling frequency so that it can be transmitted over a telephone channel. To achieve this objective a frequency shifting method was proposed earlier (Thiruvaran *et al.*, 2015). This paper seeks to extend this method by providing experimental validation for a range of frequencies. This shall be done with extensive experiments, reformulating the conditions, defining a theoretically possible frequency space for this method to be applicable, and finally studying the speech intelligibility of the frequency shifted signals. Based on the experiments an approximate frequency range will be determined where this method outperforms the baseband signal of 0-4 kHz. Additionally, a simple frequency shifting method without the lower band, would be shown to be ineffective as an alternative for the proposed frequency shifting method. Thereby this method will comprehensively demonstrate



the effectiveness of the frequency shifting method for speaker recognition.

This frequency-shifting method can be implemented through a mobile app that needs to be installed by clients or customers of a service institute, such as a bank or any institute, that requires secure access. The mobile app will convert the bandwidth of the speech signal using the proposed frequency-shifting method and then transmit it over the telephone channel.

It is worth noting that recently, methods for bandwidth extension for the recognition of narrow band speakers has been widely discussed (Abel & Fingscheidt, 2018; Nidadavolu *et al.* 2018; Kaminishi *et al.* 2019; Kamnishi *et al.* 2020). However, the method proposed in this paper is conceptually different from those bandwidth extension methods. Bandwidth extension methods involve adding extra bandwidth beyond the narrow band together with the full narrow band, resulting in an effective bandwidth of more than the narrow bandwidth of 4 kHz. On the contrary, the method discussed in this paper replaces some spectral content from the narrow band with some spectral content taken from beyond the narrow band while the total bandwidth remains at 4 kHz.

There is another context to the spectral shifting discussed in the literature that is related to cochlear implants (CI) where only a limited number of electrodes are used to process the speech. There are significant differences between the neural pattern generated by CI and the central speech pattern that post-lingually deafened patients previously developed in their brain (Fu *et al.*, 2005). One reason suggested is the spectral shift or distortion due to the CI electrodes compared to the natural cochlear. This spectral shifting is actually a distortion in the CI and the effect and implication of this spectral shifting is further discussed in literature (Li and Fu, 2010, Chennupati *et al.*, 2018). However, the use of the term ‘spectral shifting’ in the above CI related literature is entirely different from the one addressed in this paper. It is important to note that the spectral shifting discussed in this paper is not the same as in the aforementioned context.

## MATERIALS AND METHODS

### Frequency shifting process and conditions on band edge frequencies

This section briefly describes the process of shifting a high frequency band to replace a relatively less speaker-

specific frequency band to form an effective telephone speech bandwidth, which was initially proposed in Thiruvaran *et al.*, (2015). Based on the above studies on the distribution of speaker-specific information, it can be broadly concluded that there are two distinct areas contributing significantly to speaker recognition compared to other areas of the spectrum. These areas are (i) in the very low frequency region, and (ii) extend beyond the narrow band telephone bandwidth region. These areas are symbolically represented in Figure 1 as band AB and band CD where the actual value of  $f_1$ ,  $f_2$  and  $f_3$  would vary under different analysis. Hereafter, for simplicity of explanation, the first band and the second band are referred to as ‘band AB’ and ‘band CD’, respectively, as illustrated in Figure 1. The first band is loosely connected with the vocal fold and lower formant area, while the second band is related to the hypopharynx area in the human speech production system.

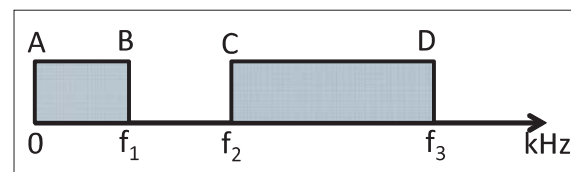


**Figure 1:** Frequency of bands contributing to speaker recognition (Thiruvaran *et al.*, 2015)

If the biometric authentication is to support remote authentication, then the signal should be transmitted over the telephone channel with a bandwidth of 4 kHz. It is observed from the discussion in the introduction that the second band CD in Figure 1 spans outside the telephone bandwidth of 4 kHz. To effectively use the two bands, shown in Figure 1, a method is illustrated as a schematic diagram in Figure 2, which was first proposed in Thiruvaran *et al.*, (2009). First, the lower band AB is extracted using a low pass filter. Then the second band CD is extracted by a band pass filter. Subsequently, this band pass signal must be moved to fill the gap between  $f_1$  and  $f_2$  as shown in Figure 1. This moving or shifting is performed by modulating the band pass signal by a frequency of  $(f_2 - f_1)$ . Then this modulated signal is added to the lower band signal that is extracted by the first low pass filter. This is followed by applying a low pass filter to remove the content beyond the telephone bandwidth of 4 kHz. This filtering also serves as an anti-aliasing filter for the final down sampling step. After the down sampling, the shifted 4 kHz signal can be used for telephone transmission.

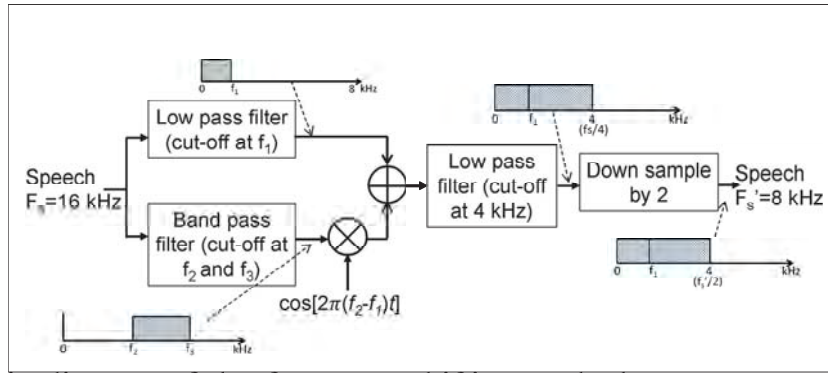


**Figure 2:** Schematic diagram of the frequency shifting method to construct an effective telephone bandwidth specific to speaker recognition. The frequency spectrums at different places in the schematic are also included (Thiruvaran *et al.*, 2015).

**Conditions on the band edge frequencies**

The conditions to be satisfied by this frequency shifting method, which was previously derived (Thiruvaran *et al.*, 2015), are outlined here with modifications. The inequalities now involve only two parameters namely,  $f_1$  and  $f_2$ . This adjustment aims to facilitate the subsequent experiments where these two parameters will be varied. In order to obtain a 4 kHz telephone bandwidth, the condition in (1) is introduced that ensures that band AB and band CD together form a 4 kHz bandwidth. The variables and values in all the equations and figures are in kHz.

$$f_3 - (f_2 - f_1) = 4 \quad \dots(1)$$

Since this first condition (1) is an equation, the number of free parameters reduces from 3 to 2. Thus, the rest of the conditions are defined with two parameters,  $f_1$  and  $f_2$ .

Further, it is necessary to avoid distortions due to modulation. There are two possibilities for distortions. The band after the bandpass filter before modulation is illustrated in Figure 3 (a). Let the magnitude spectrum after modulation be as illustrated in Figure 3 (b) where band C'D' and C''D'' are the modulated bands of the band pass signal of the band CD. The first possibility of distortion is when the frequency of point C'' becomes less than that of point D'; that is, in Figure 3 (b) if band C''D'' falls on band C'D'. To avoid this distortion, equation (2) must be satisfied. When this condition is combined with equation (1), it reduces to (3), which is the second condition.

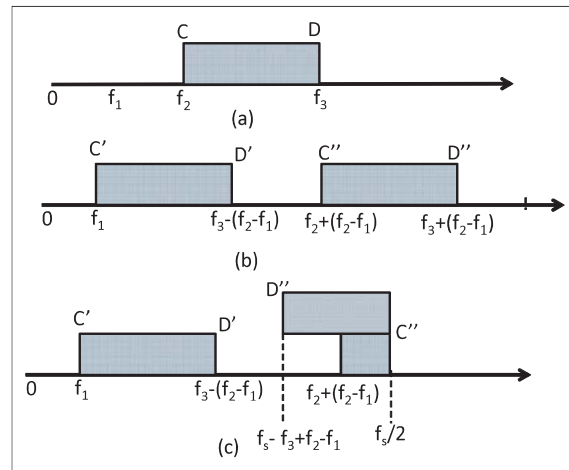


**Figure 3:** Positive side of the frequency spectrum after modulation. (a) spectrum of the band pass signal before modulation, (b) after modulation when there is no aliasing and (c) when there is aliasing; the aliased section is drawn with an opposite lines of hatching. (modified from Thiruvaran *et al.*, 2015)

$$f_3 - (f_2 - f_1) \leq f_2 + (f_2 - f_1) \quad \dots(2)$$

$$4 \leq 2f_2 - f_1 \quad \dots(3)$$

The second possibility of distortion is when the band edge D'' is beyond  $f_s/2$ , where  $f_s$  is the sampling frequency of the original signal before down sampling. In this case the possibility of distortion arises when the band C''D'' is aliased onto the band C'D'. In Figure 3(c)

the point D'' has aliased since in this case  $f_3 + f_2 - f_1$  is greater than  $f_s/2$ . The aliased point will fall back at  $f_s - (f_2 + f_3 - f_1)$  as illustrated in Figure 3 (c). To avoid this distortion the point D'' should not fall onto band C'D'. For this, the condition in (4) should be satisfied. This condition reduces to (5) when  $f_3$  is eliminated.

$$f_s - (f_2 + f_3 - f_1) \geq (f_3 - f_2 + f_1) \quad \dots(4)$$

$$f_2 - f_1 \leq 4 \quad \dots(5)$$

It should be noted that any aliasing of the band C''D'' on itself does not affect the final output since the subsequent low pass filter ultimately removes the band C''D''.

The motivation for this method is to include a higher band within the 4 kHz bandwidth. This means the first band AB should be less than 4 kHz, which is the fourth condition as in (6).

$$f_1 < 4 \quad \dots(6)$$

Thus, there are four constraints on  $f_1$ ,  $f_2$  and  $f_3$ , namely equations (1), (3), (5) and (6) that must be satisfied for this frequency shifting method to be applicable.

This paper hypothesizes that by carefully selecting the frequencies,  $f_1$ ,  $f_2$  and  $f_3$ , the performance of the speaker recognition system can be improved compared to taking the band of 0-4 kHz when performing remote authentication through a telephone channel.

**Theoretically possible frequency space for band edge frequencies**

The theoretically possible frequency space suitable for the proposed frequency shifting is defined here using the conditions derived in the previous section when the sampling frequency was 16 kHz. Though the sampling frequency of the wide band signal considered is 16 kHz, this technique is applicable for any wide band signal for a sampling frequency higher than 16 kHz. However, the distribution of speaker specific information beyond 8 kHz is not that significant (Thiruvaran *et al.*, 2009).

The theoretically possible frequency range for bands AB and CD (Figure 1) is the range of possible band edge frequencies  $f_1$ ,  $f_2$ , and  $f_3$  that satisfy the four conditions defined in (1), (3), (5) and (6). Since equation (1) resulted in two free variables,  $f_1$  and  $f_2$  are taken as the free variables to define the theoretically possible frequency space for the band edge frequencies. This theoretically

possible frequency space is shown in Figure 4 where the trapezoidal area defined by the lines QR, RS, ST, and TQ define the possible values of  $f_1$  and  $f_2$  that satisfy all the inequalities. Lines RS, QT, and ST represent the inequalities (3), (5) and (6), respectively.

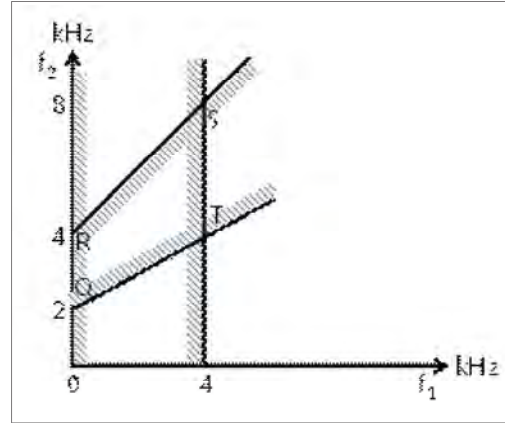


**Figure 4:** Theoretically possible frequency space for the frequency shifting method to be applicable in terms of the band edge frequencies of  $f_1$  and  $f_2$  for the bands AB and CD.

**Selection of a suitable bandwidth for frequency band shifting**

**Experiment to determine the initial band AB**

Initially, an empirical study was performed to check which frequency bands performed better after frequency shifting when compared to the conventional baseband signal of 0-4 kHz. That is, speaker recognition experiments were conducted with the signal obtained after performing this frequency shifting with different band edge frequencies. These results are compared with the conventional speaker recognition system that uses the 0-4 kHz bandwidth. Here the problem of selecting a suitable range of bandwidth for AB and CD (Figure 1) can be considered as selecting suitable values for the band edge frequencies  $f_1$ ,  $f_2$  and  $f_3$  subject to the four conditions defined in (1), (3), (5) and (6).

Initially, speaker recognition experiments were conducted to determine the frequency area in the spectrum that contributes more to speaker recognition, i.e., to determine the spectral area that contains the most speaker discriminative information. This is studied by taking a single bandwidth of 1 kHz at a time and extracting the features for the speaker recognition experiment.

### Experiments with varying bandwidth

The most suitable bands were found by gradually expanding or contracting bands AB and CD while ensuring that conditions defined by (1), (3), (5) and (6) were met. Since an empirical search spanning all possible scenarios would take a very long time, only a limited search was performed. For simplicity the starting point for the search for suitable bands was fixed by considering  $f_1$  as 1 kHz,  $f_2$  as 3 kHz and  $f_3$  as 6 kHz.

### Database and speaker recognition system

For this experiment a speech database of the IARPA Babel Tamil language collection sampled at 16 kHz was used (Chen *et al.*, 2015). Recordings of 247 male speakers in this database were used for this experiment with approximately 80 hours of recording. Each speaker had an average of about 300 recordings. Out of 247 speakers, 97 were used for the universal background model (UBM) and the rest 150 speakers used for evaluation. The evaluation list was prepared with 15,000 target and 89,400 non-target trials. The popular speaker recognition database of NIST, used for regular evaluations (NIST 2008), with a 8 kHz sampling frequency was not suitable for this experiment.

A Mel-frequency cepstral coefficient (MFCC)-based standard feature was used as the feature. An i-vector-probabilistic linear discriminant analysis (PLDA)-based backend was used (Ye *et al.*, 2016). The equal error rate (EER), which is the point where miss probability and

false alarm probability are the same, was used as the performance metric.

### Frequency shifting without the lower band – an alternative method

This section analyses a simpler modified method for frequency shifting by using a single band of 4 kHz bandwidth from a high frequency area beyond 2 kHz. The band EF in Figure 5 (a) is shifted according to the schematic diagram illustrated in Figure 5 (b). In this method, a single higher frequency band is obtained by a band-pass filter and then moved to the baseband by modulating it using an oscillator with a frequency of  $f_d$ . After modulation, the band that was shifted to the baseband is retained by the low-pass filter with a cut-off frequency of 4 kHz. This low pass filter will act as an anti-aliasing filter for the subsequent down sampling by a factor of 2, for this particular case, where the original sampling frequency was 16 kHz.

This system differs from that in Figure 2 by not having the low-pass filter parallel branch and the added module since there is no lower frequency band. This modification was motivated by the observation that the hypopharyngeal cavities are less affected by the phonetic content, which modify the spectrum beyond 2.5 kHz (Takemoto *et al.*, 2006).

Thereafter three-speaker recognition experiments were conducted by using a 4 kHz bandwidth of signal beginning after 2 kHz.

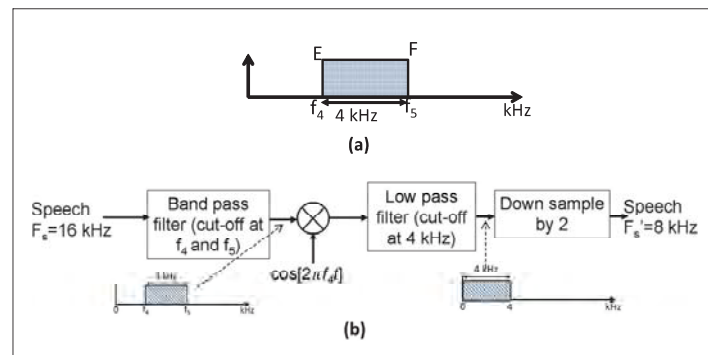


**Figure 5:** (a) The band EF of 4 kHz bandwidth in the higher speaker specific area as a single band, and (b) the schematic diagram of the frequency shifting to shift band EF to the baseband to form the narrow band 4 kHz signal.

### Effect of frequency shifting on intelligibility

When the signal is distorted by the proposed method, the quality, specifically intelligibility, is an important factor to be analyzed. Though the proposed method was developed with the primary focus on speaker authentication, speech intelligibility cannot be compromised adversely. That is, the strength of the speaker specific information must be improved to increase the accuracy of the recognition of the speaker, as long as intelligibility is reasonably sufficient and not necessarily at its best. If the content of the speech is slightly unclear then it can be repeated to clarify the content.

In this section, the quality of the reconstructed speech signal, after the proposed frequency band shifting process, is objectively analyzed using the metrics perceptual evaluation of speech quality (PESQ) (International Telecommunication Union (ITU), 2001) and the virtual speech quality objective listener (ViSQOL) (Hines *et al.*, 2015). ViSQOL gave comparable performance to perceptual objective listening quality analysis (POLQA), which is released by ITU as a licensed software (International Telecommunication Union, 2011). The purpose of this analysis is to determine if there is a significant drop in the intelligibility of the reconstructed signal.

One hundred recordings in the TIMIT database was used for this experiment. The original recordings of 16 kHz sampling frequency were converted to 8 kHz signals after performing the band shifting according to Figure 2. The recordings were then compared with the reference recordings obtained by directly down sampling (0-4 kHz baseband signal) without shifting the bands using PESQ and ViSQOL metrics. The reference recordings are the baseband signal used in speaker recognition experiments.

### Filter design

Non-linear elliptic filters with 0.5 dB pass band ripple, 60 dB stop band attenuation, and a 500 Hz transition band were utilized in the filter design. Minor variations in the ripple and attenuation did not produce any significant change in the results. The elliptic filter was selected for its narrow transition band.

Phase information could not be preserved when a band outside the 0-4 kHz range is shifted within the band, regardless of whether a linear filter or non-linear filter was used. Non-linear filters are used to take advantage

of lower computational complexity resulting from the use of lower order filters. Further, the phase distortion is tolerable in speaker recognition. The standard MFCC feature used in state-of-the-art speaker recognition systems does not preserve phase information but works well for that task. Though the phase is a concern in speech reconstruction, the purpose is not speech enhancement but to avoid complete loss of intelligibility. The quality of the reconstructed speech is always lower than the original since the process is optimized for speaker information and not for phonetic information. The band shifting is the primary reason for the drop in quality but the phase distortion due to non-linear filters may also cause a drop in the quality. The phase is distorted not only by non-linear filters but primarily by the band shifting process. Thus, even if a linear filter is used the phase distortion cannot be avoided. Further, as mentioned earlier, since the purpose is not speech enhancement the phase distortion is tolerable. Thus, non-linear filters were used.

## RESULTS AND DISCUSSION

### Results of speaker recognition experiments to find the initial band AB

For the experiments described to find initial band AB, the performance in terms of EER against the bandwidth is shown in Figure 6 where the x-axis shows the band used for each experiment. It can be assumed that a lower EER corresponds to a higher level of speaker specific information. The pattern of variation observed here is similar to the general pattern, discussed in the introduction, where the distribution of speaker specific information in the frequency space is discussed. It was observed that the 0-1 kHz band gave the lowest EER and thus can be considered as having the most speaker specific information. The 0-1 kHz band was chosen as the initial range for the band AB in the upcoming experiments in the next section. The objective was to test different band edge frequencies to determine the appropriate range of frequency for the above frequency shifting method. This observation partly justifies the selection of initial values of  $f_i$  mentioned at the end of the experiments with varying bandwidths.

Further, it could be observed that the variation of the EER was not monotonic against the bandwidth. That is, the EER increases from 0-1 kHz to the 1-2 kHz band, and then decreases to the 3-4 kHz band, and then again increases thereafter. This shows that the speaker specific information in the bandwidth from 2-4 kHz is higher than that of the 1-2 kHz bandwidth.

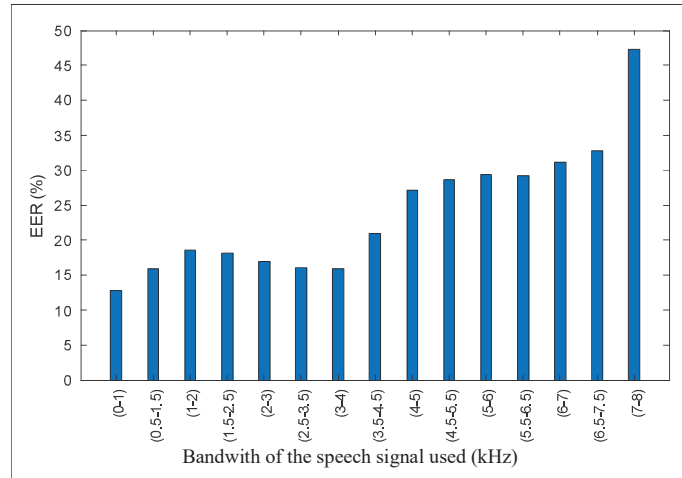


**Figure 6:** Speaker recognition performance of different areas of the frequency spectrum taking only 1 kHz of the speech spectrum in each experiment.

**Results of experiments with varying bandwidths**

The results of varying the frequencies of  $f_1$ ,  $f_2$  and  $f_3$  as the bands are systematically changed, are shown and discussed for the following five cases.

**Case I: Band AB is squeezed from point B and CD is expanded from point C**

From the initial position, the band AB is reduced by changing  $f_1$  from 1 to 0.2 kHz in steps of 0.1 kHz, while

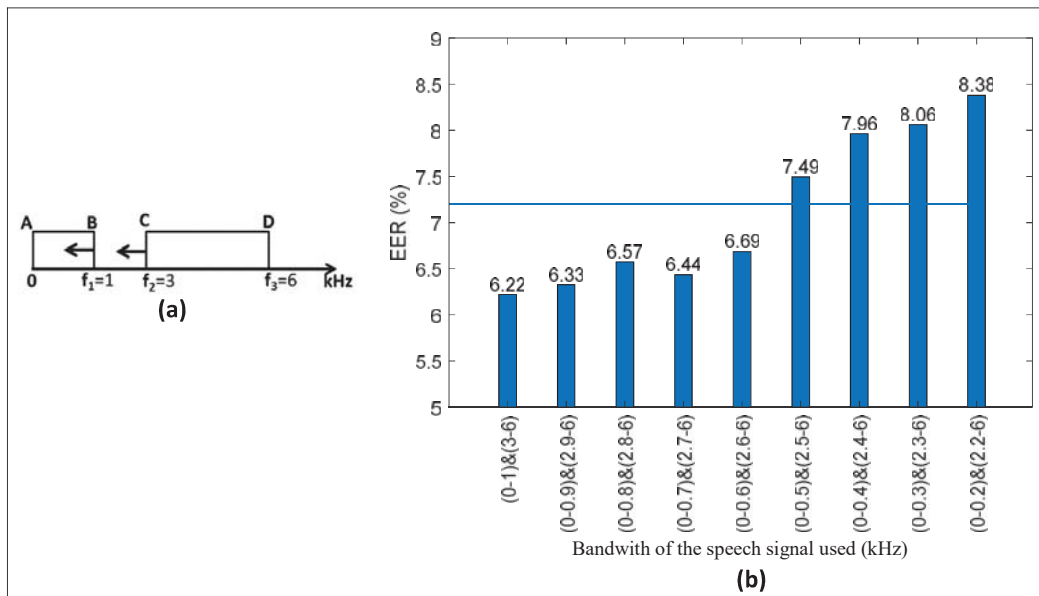


**Figure 7:** (a) The directions of bandwidth adjustments from the initial position in steps of 0.1 kHz, and (b) the speaker recognition performances. The performance when using the baseband of 0 to 4 kHz is superimposed as a line graph.

band CD is expanded by changing  $f_2$  from 3 to 2.2 kHz in steps of 0.1 kHz (Figure 7a). This ensures that the total bandwidth of bands AB and band CD together will remain at 4 kHz, satisfying the requirements of the telephone bandwidth. In each case the bands were shifted and down sampled according to the schematic shown in Figure 2. The band shifted signal was used to extract features and speaker recognition experiments were conducted. The corresponding speaker recognition experiments with the step-by-step-variation for the 8 steps are shown in Figure 7 (b). Here the performance with the baseband (0-4 kHz band) is superimposed as a

line. It can be observed that out of the nine cases experimented, five outperformed the results with the baseband of 1-4 kHz. When the band AB was reduced to 0.5 kHz or below, the performance dropped below the baseline system and thereby losing more speaker discriminative spectral contents. This supports the observation from Figure 6 where the 0-1 kHz band gave the lowest performance, which implied more useful information about the speaker was retained. The experiment with 0-1 kHz and 3-6 kHz will be replicated in all subsequent cases to ensure continuity.

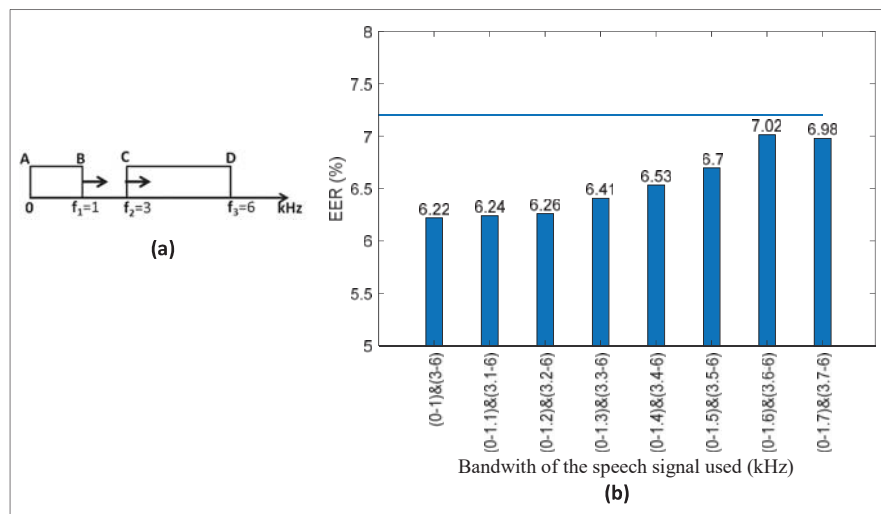


**Figure 8:** (a) The directions of bandwidth adjustments from the initial position in steps of 0.1 kHz at a time, and (b) the speaker recognition performances. The performance when using the baseband of 0 to 4 kHz is superimposed as a line graph.

**Case II: B and AB is expanded from point B, and CD is squeezed from point C**

Similarly, the band AB was expanded by changing  $f_1$  from 1 kHz to 1.7 kHz in steps of 0.1 kHz while the band CD was reduced by changing  $f_2$  from 3 kHz to 3.7 kHz in steps of 0.1 kHz (Figure 8a) and the corresponding speaker recognition results are shown in Figure 8b. The reason to stop at 1.7 kHz is to limit the number of experiments due to computational complexity. It can be observed that all the eight cases experimented have outperformed the results with a baseband of 1 to 4 kHz. The trend of increasing EER when the band AB is increased from 0-1 kHz to 0-1.7 kHz partly supports the observation in Figure 6 where the 1-2 kHz spectrum gave the lowest performance within the 4 kHz bandwidth, implying relatively lower speaker specific information.

**Case III: Band AB is squeezed from point B and band CD is expanded from point D**

In the same manner, the third possibility of varying the initial position of bands AB and CD is to change  $f_1$  from 1 kHz to 0.2 kHz in steps of 0.1 kHz while band CD is expanded by changing  $f_3$  from 6 kHz to 6.8 kHz in steps of 0.1 kHz (Figure 9a). The corresponding speaker recognition experiments are shown in Figure 9 (b) and the performance with the baseband (1 to 4 kHz) is superimposed as a line. Out of the nine experiments the results of five experiments outperformed the results with the baseband of 1-4 kHz. When the bandwidth of AB was reduced to 0.5 kHz or below, the performance did not improve more than the baseline system, similar to the observation in Figure 7.

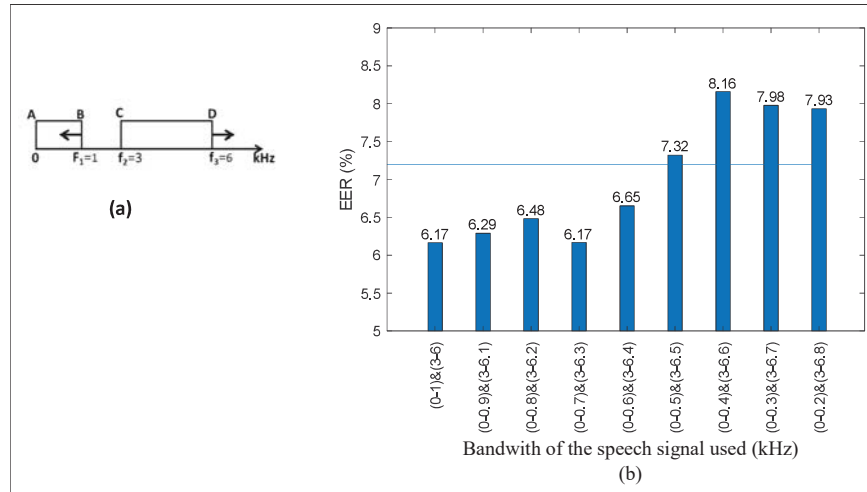


**Figure 9:** (a) The directions of bandwidth adjustments from the initial position in steps of 0.1 kHz, and (b) the speaker recognition performances. The performance when using the baseband of 0 to 4 kHz is superimposed as a line graph.

**Case IV: Band AB is expanded from point B and band CD is squeezed from point D**

As the fourth possibility for changing both bands, the band AB was expanded by changing  $f_1$  from 1 kHz to 1.9 kHz in steps of 0.1 kHz while the band CD

was reduced by changing  $f_3$  from 6 kHz to 5.1 kHz in steps of 0.1 kHz. This is shown in Figure 10a and the corresponding speaker recognition results are shown in Figure 10b. It can be observed that all the experiments have outperformed the results with a baseband of 1 to 4 kHz.

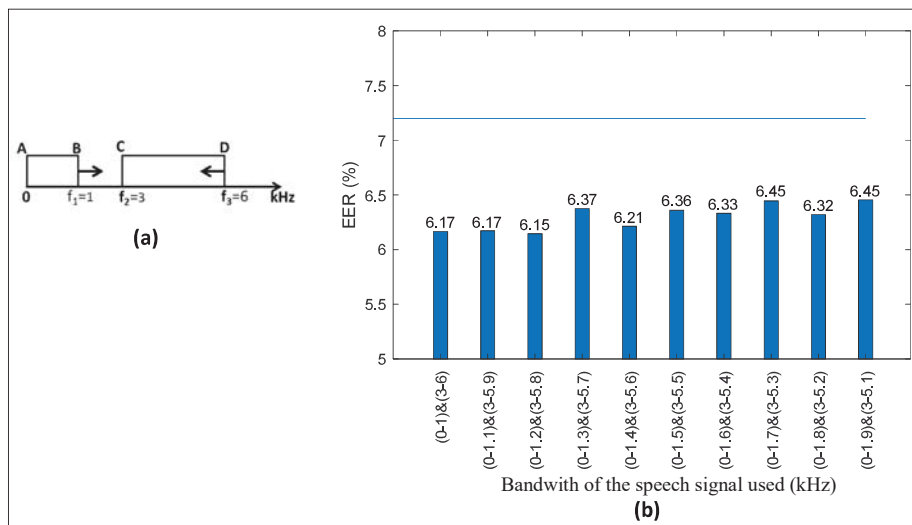


**Figure 10:** (a) The directions of bandwidth adjustments from the initial position in steps of 0.1 kHz, and (b) the speaker recognition performances. The performance when using the baseband of 0 to 4 kHz is superimposed as a line graph.



**Case V: Band AB is fixed and band CD is shifted**

As the final set of experiments, the band AB was fixed at 0 to 1 kHz but band CD was shifted. This is performed by changing  $f_2$  from 2.5 kHz to 4 kHz while changing  $f_3$  from 5.5 kHz to 7 kHz in steps of 0.5 kHz. Here the starting point of  $f_2$  at 2.5 kHz (while  $f_1$  still maintained at 1 kHz) touches one of the boundary lines QT as labelled in Figure 4; this implies  $f_2$  cannot be reduced below

2.5 kHz while having  $f_1$  at 1 kHz. Only four steps were tested including the previously tested band CD at 3 to 6 kHz; this is to streamline the number of experiments. This frequency change is illustrated in Figure 11a and the corresponding speaker recognition results are shown in Figure 11b. It can be observed that, out of the four experiments, three had outperformed the results with a baseband of 1 to 4 kHz.

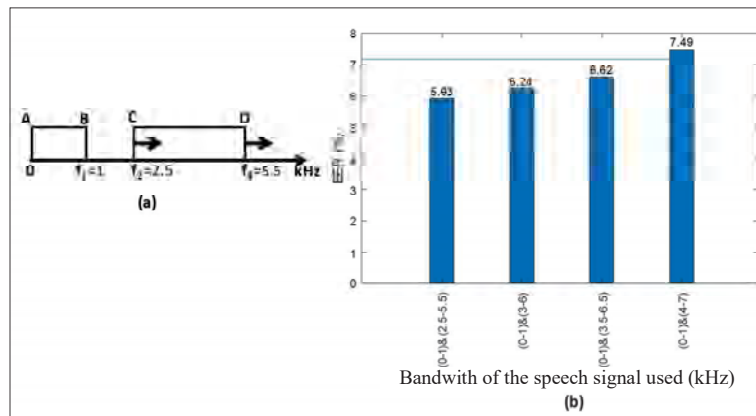


**Figure 11:** (a) The directions of bandwidth adjustments from the initial position in steps of 0.5 kHz, and (b) the speaker recognition performances. The performance when using the baseband of 0 to 4 kHz is superimposed as a line graph.

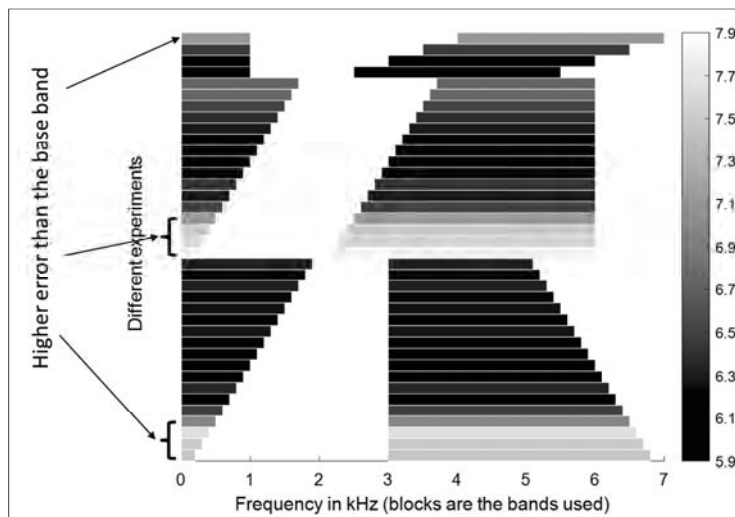


**Figure 12:** Summary of all the experiments performed under the 5 cases. The results of EER is coded gray and the corresponding bandwidths used are shown as blocks. The 9 experiments where the performance was not better than the baseband are also indicated.

The results of these five cases are summarised in Figure 12, with a gray colour code representing the corresponding EER, and the blocks represent the corresponding bandwidths. Considering all the five cases together it can be observed that out of 36 experiments with different bandwidths the proposed system performed better than the baseline system in 27 experiments. The nine cases where the performance was not better than the baseband are also indicated in Figure 12. Further a surface plot is shown in Figure 13 where the variation of EER is shown over the area spanned by  $f_1$  and  $f_2$ . A plane is superimposed representing the EER when the baseband 0-4 kHz is used.

Considering all the above analysis the following conclusions can be made in a broad sense. When a part of the band (1 kHz) is taken from between 4 to 6.5 kHz (approximately), and replaced within the range 1.5 to 2.5 kHz region, the performance improved compared to using the baseband of 0 to 4 kHz alone. When the spectrum between approximately 0.5 to 1 kHz is not utilized, performance drops. Furthermore, the bandwidth of 0-1 kHz for band AB, and 2.5-3.5 kHz for band CD can be considered a local optimum. Overall, the results demonstrate the validity of the proposed method in improving the speaker recognition system.

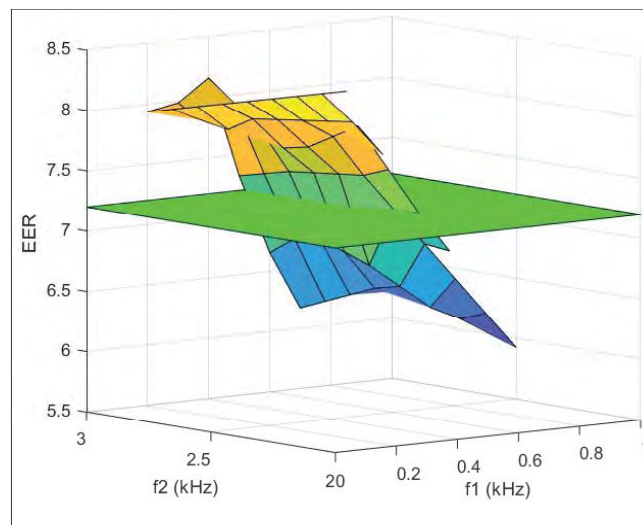


**Figure 13:** Surface plot showing the EER of all the experimented cases against  $f_1$  and  $f_2$ . A plane is superimposed representing the EER when the baseband (0-4 kHz) is used.

### Approximate suitable frequency space for band edge frequencies

This section superimposes the frequency points experimented in the previous sections under the five cases on the theoretically possible frequency space defined in Figure 4. The approximate suitable region is defined by connecting the end-points of the frequency points at which speaker recognition was better than that of the baseband signal. This approximate region is illustrated in

Figure 14. The starting point ( $f_1 = 1, f_2 = 3$  kHz) is named as point 'a', and the frequency points experimented in each case and the lines representing these experiments are as follows: case I – line ae, case II – line ab, case III – line af, case IV – line ac, case V – line ag and case VI – line ad. Since all the possible variations of  $f_1$ ,  $f_2$ , and  $f_3$  were not experimented, the suitable region found is an approximate area based on the limited experiments conducted.

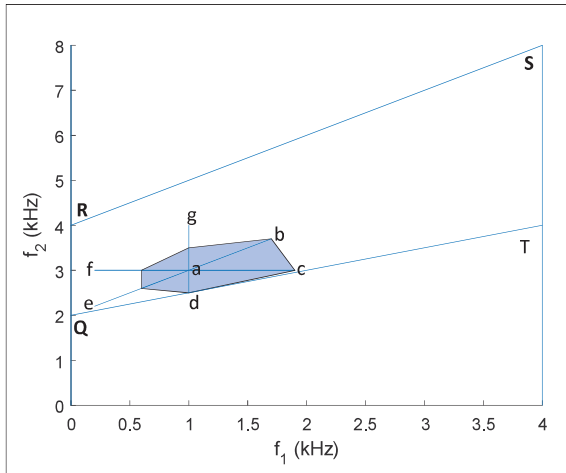


**Figure 14:** Approximate suitable frequency space for the bands AB and CD defined by the band edge frequencies of  $f_1$  and  $f_2$  superimposed on the possible frequency space.

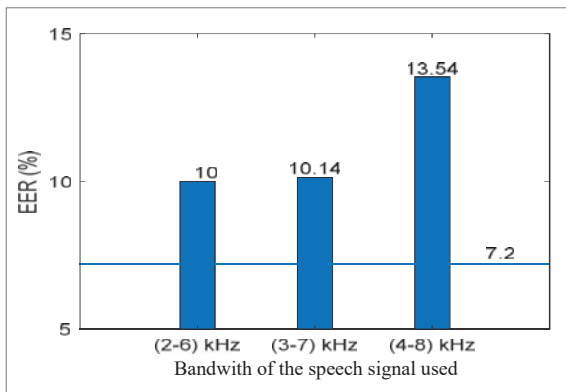


**Figure 15:** Speaker recognition results with shifted single band of 4 kHz bandwidth according to the schematic in Figure 15 (b), and the results of baseband (0 to 4 kHz) are superimposed as a line graph.

**Results of the alternative method**

The results for the three bandwidths chosen are shown in Figure 15 where the baseline results for the 0-4 kHz band is shown as a line graph. It can be observed that none of the experimented bands outperformed the baseline results i.e., shifting of a 4 kHz single band was not successful. Therefore, the band shifting method in Figure 2 was used. If this had performed better it would have facilitated a simpler system as illustrated in Figure 5 (b)

than what is proposed in Figure 2. One possible reason why this did not perform better is that it does not use the low frequency region, possibly due to losing glottal related information. This again justifies the need to keep the lower frequency band and therefore the necessity for the added module in Figure 2.

**Results of experiments on speech intelligibility**

The box plot of PESQ scores and ViSQOL scores for the speech intelligibility experiments, for all the five cases discussed previously are shown in Figures 16 and 17, respectively, where each case starts with the bands of 0-1 kHz and 3-6 kHz, similar to the speaker recognition results given for different cases. The box plot shows the 2<sup>nd</sup> and 3<sup>rd</sup> quartiles as a box, mean as a triangle, median as a horizontal line, minimum and maximum as the ends of the lines and any outliers as circles.

When a threshold line is drawn for PESQ at 2 in Figure 16 the entire 2<sup>nd</sup> and 3<sup>rd</sup> quartiles are below the threshold line for the last four experiments in case I, and the last three experiments in case III. Interestingly, the last four experiments in case I and case III in the speaker recognition experiments also did not perform better than the baseband experiment as can be seen from Figures 7 and 9. That is, for the experiments where the speaker recognition performed better than that of the baseband, the PESQ score was also better. Similarly, for ViSQOL when a threshold line at 2 is drawn in Figure 17 the mean is below the threshold for the three experiments in case III and for the last experiment in case V. Here again the corresponding speaker recognition experiments did not perform better than the baseband signal as can be seen from Figures 7 and 11. Thus, for the cases where the band shifting performed better than the base band (the region shown in Figure 14), PESQ and ViSQOL gave a reasonable performance.

Further, the PESQ score is almost correlated with the bandwidth of band AB (Figure 17). For example, for case I, the bandwidth of band AB is decreased from 0-1 kHz to 0-0.2 kHz in steps of 0.1 kHz, and the PESQ score is monotonically reduced along that bandwidth change. A similar pattern can be observed for case III. For these two cases the speaker recognition performance is better than the baseband signal for the first 5 experiments (Figures 7 and 9) and the corresponding average PESQ for these 5 experiments were approximately higher than 2. That is, the bands that gave a lower PESQ also gave a higher EER in the speaker recognition experiments. ViSQOL almost follows the same trend for these two cases.

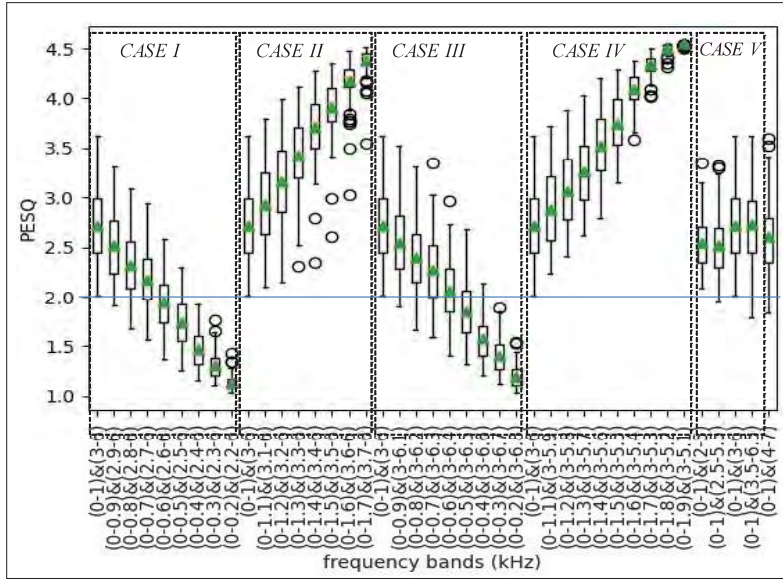


**Figure 16:** Box plots for PESQ score of the reconstructed signals using the proposed frequency band shifting method for 100 recordings from NTIMIT database against the frequency bands used. The cases are marked by a threshold line at drawn at PESQ 2.

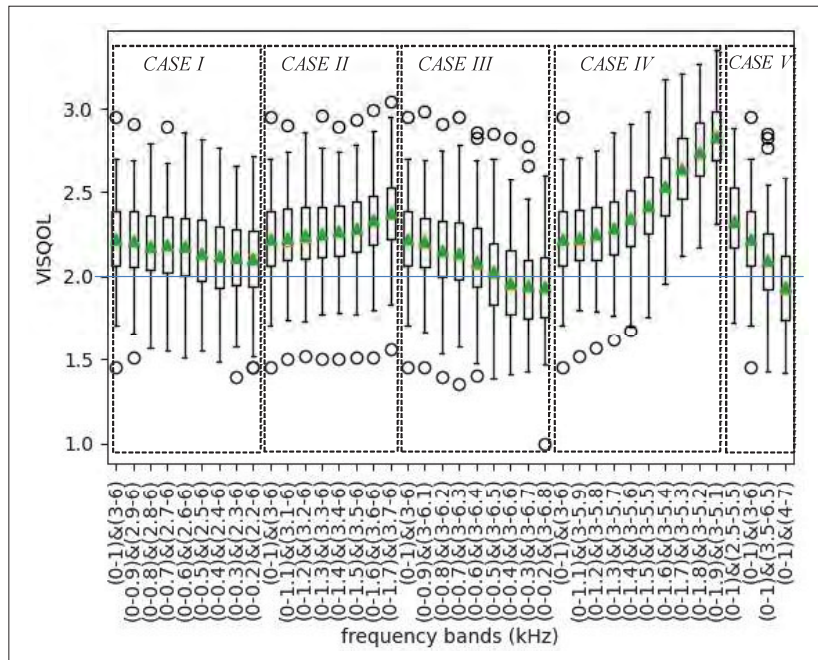


**Figure 17:** Box plot of ViSQOL score for the reconstructed signals using the frequency band shifting method for 100 recordings from the NTIMIT database against the frequency bands used. The experimental cases are marked by dash box and a super imposed threshold line at 2.

For case II and case IV, the bandwidth of band AB was gradually increased and the PESQ score also increased. A slight increasing trend was observed for the ViSQOL score as well. For these two cases the speaker recognition performance was better than the base band experiment for all the bandwidths experimented (Figures 8 and 10).

For case V where band AB was fixed at 0-1 kHz, the PESQ score shows a very small reduction when using the 2.5-5.5 kHz band compared to the 2-5 kHz band; it then slightly increases and then gradually declines, but overall remains unchanged. The corresponding speaker recognition performance showed a similar pattern but in the opposite direction, and the ViSQOL score declined gradually.

Overall, it can be concluded that the frequency shifting method when applied within the suitable region as depicted in Figure 14 does not significantly distort the signal. Additional informal listening tests have also shown that the quality of the reconstructed speech is sufficient to recognize the content of the speech.

#### Limited experiments on a dataset of a different language

A subset of the Voxceleb dataset was used to perform three experiments to determine whether the above findings are consistent when applied to a dataset of a different language. This subset had 200 speakers with 25,539 recordings in the English language. The selected three experiments were: (1) utilizing only the base band (0-4 kHz), (2) utilizing 0-1 kHz band and 2.5 – 5.5 kHz band, which yielded the optimal performance in the experiments outlined at the experiments with varying bandwidths, and (3) utilizing 0-1 kHz band and 3 – 6 kHz band. The EER obtained in these experiments were 8.2%, 7.05% and 7.5%, respectively. It is evident that both cases of band shifting (experiment 2 and 3) performed better than using only the baseband. Further, the band used in experiment 2 provided the best alignment with the findings from the experiments with varying bandwidths.

#### Limitations of the above experiments

The first limitation is the limited space beginning from point 'a' in Figure 14 for the experimental search due to the time-consuming nature of experiments. Even the variation from that point did not extend beyond a certain limit. This is because of the time-consuming nature of the speaker recognition experiments. The second limitation is that the experiments are not sufficient to find a global optimum. Since there are infinite different possible pairs

of  $f_1$  and  $f_2$ , it is difficult to experimentally find a global optimum. On the other hand, even if a global optimum is found this will have a bias based on the database used, back-end usage, and the parameters used. The third limitation is the use of an objective speech quality measure to study the intelligibility rather than a subjective speech quality measure since the purpose is only to verify if the intelligibility is retained and not to improve the listening quality. This is why an objective measure is preferred to the time-consuming subjective measure.

In addition to biometric authentication, speaker recognition is useful in areas such as in forensic applications and tracking communication by criminals for the law enforcing authority. For these and other applications it is necessary to use the 0-4 kHz bandwidth; the method proposed in this paper may not be applicable if the legal system challenges the use of a traditional bandwidth. However, for the application of remote biometric authentication, it could be possible to use an optimum bandwidth of 4 kHz that contains more speaker-specific information rather than only the 0-4 kHz band.

#### CONCLUSION

The frequency shifting method was empirically demonstrated for several different cases to perform better than only using the 0-4 kHz for narrow band speaker recognition. Further, for the four conditions required for the frequency shifting method, a theoretical possible frequency space is defined. Based on the experimental results, this space was further refined to find a suitable frequency space where the frequency shifting method performed better. A simple frequency shifting method without the lower band was demonstrated to be an inadequate method. Finally, the intelligibility of the frequency shifted signal was shown to be adequate to recognize the speech content. Based on the experiments the following conclusions can be made broadly. When a part of the band (1 kHz) is taken from approximately 4 to 6.5 kHz and replaced within the range of the 1.5 to 2.5 kHz region, the performance was improved compared to using only the baseband of 0 to 4 kHz band. When the spectrum approximately from 0.5 to 1 kHz is not used the performance declined. Furthermore, the bandwidth of 0-1 kHz for band AB, and 2.5-3.5 kHz for band CD can be considered as a local optimum. For future studies, the same frequency shifting method can be applied to other speech-related applications such as language recognition and emotion recognition by identifying the specific speech bandwidth containing the respective discriminative information.

## Acknowledgements

The author would like to acknowledge the useful feedback from E. Ambikairajah and V. Sethu from the University of New South Wales, Australia

## REFERENCES

- Abel J. & Fingscheidt, T. (2018). Artificial speech bandwidth extension using deep neural networks for wideband spectral envelope estimation. *IEEE/ACM Transactions on Audio, Speech, and Language Processing*, 26(1), 71-83. <https://doi.org/10.1109/TASLP.2017.2761236>
- Cavalcanti, J. C., Eriksson, A. & Barbosa, P. A. (2021). Acoustic analysis of vowel formant frequencies in genetically-related and non-genetically related speakers with implications for forensic speaker comparison. *PLoS One*, 16(2), Article e0246645. <https://doi.org/10.1371/journal.pone.0246645>
- Chen, N.F., Ni, C., & Chen, I. F. (2015, April 19-24). *Low-resource keyword search strategies for Tamil* (Conference abstract) IEEE International Conference on Acoustics, Speech and Signal Processing (ICASSP), South Brisbane, Australia. <https://doi.org/10.1109/ICASSP.2015.7178996>
- Chennupati, N., Kadiri, S. R., Yegnanarayana, B. (2018). Spectral and temporal manipulations of SFF envelopes for enhancement of speech intelligibility in noise. *Computer Speech and Language*, 54, 86-105. <https://doi.org/10.1016/j.csl.2018.09.002>
- Dang, J. & Honda, K. (1997). Acoustic characteristics of the piriform fossa in models and humans. *The Journal of the Acoustical Society of America*, 101(1), 456-465. <https://doi.org/10.1121/1.417990>
- Delvaux, B. & Howard, D. (2014). A new method to explore the spectral impact of the piriform fossae on the singing voice: Benchmarking Using MRI-Based 3D-Printed Vocal Tracts. *PLOS ONE*, 9(7), Article e102680. <https://doi.org/10.1371/journal.pone.0102680>
- Fu, Q. J., Nogaki, G., Galvin III, J. J. (2005). Auditory training with spectrally shifted speech: Implications for cochlear Implant patient auditory rehabilitation. *Journal of the Association for Research in Otolaryngology*, 6(2), 180-189. <https://doi.org/10.1007/s10162-005-5061-6>
- Hines, A., Skoglund, J., Kokaram, A. C. & Harte, N. (2015). ViSQOL: an objective speech quality model. *Journal on Audio, Speech, and Music Processing*, 2015, Article 13. <https://doi.org/10.1186/s13636-015-0054-9>
- Hyon, S., Wang, H., Wei, J. & Dang, J. (2012). *A method of speaker identification based on phoneme mean F-ratio contribution* (Conference proceeding abstract). Annual conference of INTERSPEECH, Portland, USA. <https://doi.org/10.21437/Interspeech.2012-349>
- International Telecommunication Union. (2001). *Perceptual evaluation of speech quality (PESQ), an objective method for end-to-end speech quality assessment of narrow-band telephone networks and speech codecs*. ITU-T Recommendation. <https://www.itu.int/rec/T-REC-P.862>
- International Telecommunication Union. (2011). *Perceptual objective listening quality prediction*. ITU-T Recommendation. <https://www.itu.int/rec/T-REC-P.863>
- Kaminishi, R., Miyamoto, H., Shiota, S. & Kiya, H. (2019). *Investigation on blind bandwidth extension with a non-linear function and its evaluation of x-vector-based speaker verification*. Twentieth annual conference of INTERSPEECH, Graz, Austria. <https://doi.org/10.21437/Interspeech.2019-1510>
- Kaminishi, R., Miyamoto, H., Shiota, S. & Kiya, H. (2020). Blind bandwidth extension with a non-linear function and its evaluation on automatic speaker verification. *IEICE Transactions on Information and Systems*, 103(D), 42-49. <https://doi.org/10.1587/transinf.2019MUP0008>
- Kitamura, T., Honda, K. & Takemoto, H. (2005). Individual variation of the hypopharyngeal cavities and its acoustic effects. *Acoustical Science and Technology*, 26(1), 16-26. <https://doi.org/10.1250/ast.26.16>
- Li, T., & Fu, Q. J. (2010). Effects of spectral shifting on speech perception in noise. *Hearing Research* 270(1-2), 81-88. <https://doi.org/10.1016/j.heares.2010.09.005>
- Lu, X., & Dang, J. (2008). An investigation of dependencies between frequency components and speaker characteristics for text-independent speaker identification. *Speech Communication*, 50(4), 312-322. <https://doi.org/10.1016/j.specom.2007.10.005>
- Nidadavolu, P. S., Lai, C. I., Villalba, J. & Dehak, N. (2018). *Investigation on bandwidth extension for speaker recognition*. Nineteenth annual conference. INTERSPEECH, Hyderabad, India. <https://doi.org/10.21437/Interspeech.2018-2394>
- NIST. 2008. *The NIST year 2008 speaker recognition evaluation plan*. <http://www.nist.gov/speech/tests/sre/2008/index.html>
- Takemoto, H., Adachi, S., Kitamura, T., Mokhtari, P. & Honda, K. (2006). Acoustic roles of the laryngeal cavity in vocal tract resonance, *The Journal of the Acoustical Society of America*, 120(4), 2228-2238. <https://doi.org/10.1121/1.2261270>
- Thiruvanan, T., Ambikairajah, E. & Epps, J. (2009). *Analysis of band structures for speaker-specific information in FM feature extraction*, Annual conference of INTERSPEECH, Brighton, UK. <https://doi.org/10.21437/Interspeech.2009-39>
- Thiruvanan, T., Sethu, V., Ambikairajah, E. & Li, H. (2015). Spectral shifting of speaker-specific information for narrow band telephonic speaker recognition. *IET Electronics Letters*, 51(25), 2149-2151. <https://doi.org/10.1049/el.2015.3117>
- Ye, J., Lee, K. A., Tang, Z. & et al. (2012). *PLDA modeling in I-vector and supervector space for speaker verification*. Thirteenth annual conference of INTERSPEECH, Portland, Oregon, USA. <https://doi.org/10.21437/Interspeech.2012-460>

## RESEARCH ARTICLE

# Nematology

## Prevalence and abundance of plant-parasitic nematodes associated with corn (*Zea mays* L.) in Anuradhapura, Sri Lanka

N Thiruchchelvan<sup>1,4\*</sup>, S Casonato<sup>2,4</sup>, G Mikunthan<sup>1</sup>, LM Condrón<sup>3</sup>, R Moukarzel<sup>4</sup> and M Kularathna<sup>4</sup>

<sup>1</sup> Department of Agricultural Biology, Faculty of Agriculture, University of Jaffna, Ariviyal Nagar, Kilinochchi 44000, Sri Lanka.

<sup>2</sup> Sugar Research Australia, 216 Dallachy Road, Tully, Queensland, 4854, Australia.

<sup>3</sup> Department of Soil and Physical Sciences, Faculty of Agriculture and Life Sciences, Lincoln University, Lincoln 7647, Canterbury, New Zealand.

<sup>4</sup> Department of Pest Management and Conservation, Faculty of Agriculture and Life Sciences, Lincoln University, Lincoln 7647, Canterbury, New Zealand

Submitted: 27 June 2023; Revised: 01 June 2024; Accepted: 24 June 2024

**Abstract:** The prevalence and abundance of plant-parasitic nematodes (PPNs) associated with corn (*Zea mays*; Poaceae) in the Anuradhapura district of Sri Lanka are poorly understood. This study investigated the occurrence and population densities of major PPN genera associated with corn. Over 92% of the corn fields were positive for PPNs in all the sampled fields. Major PPN genera identified were *Pratylenchus* spp. (71.4%), *Helicotylenchus* spp. (28.6%), *Meloidogyne* spp. (21.4%), *Criconebella* spp. (21.4%), and *Hoplolaimus* spp. (35.7%). The mean population density of *Pratylenchus* spp. was 2020 nematodes kg<sup>-1</sup> of soil, in the Anuradhapura corn fields. During the cropping season from November (2021) to February (2022), all PPN genera except *Meloidogyne* spp. were observed. *Pratylenchus* spp. were detected at levels below 1000 nematodes kg<sup>-1</sup> of soil at the seedling stage, except in Kelenikawewa where the initial population was 1865 nematodes kg<sup>-1</sup>. At the time of harvest, *Pratylenchus* spp. increased by 2 to 10 folds. These findings suggest a potential impact of *Pratylenchus* spp. on corn yield in Anuradhapura, highlighting the need for further research to assess damage levels and the overall effect of PPNs on corn production in Sri Lanka.


**Keywords:** Anuradhapura, nematode diversity, plant-parasitic nematodes, *Pratylenchus*, Sri Lanka, *Zea mays* (maize)

### INTRODUCTION

Corn (*Zea mays* L.) is a key cereal crop grown after rice (*Oryza sativa* L.) in Sri Lanka (Malaviarachchi *et al.*,

2007). Corn production in Sri Lanka has recently increased (DOA, 2020) due to the rising demand for poultry feed (Malaviarachchi *et al.*, 2007). Corn-based food items are popcorn, boiled corn cobs, and locally produced ready-mix cereals 'Thripasha' and 'Samapasha'. Consequently, the local production of corn has increased from 150 to 360 tons between 2000 and 2020 (Esham *et al.*, 2005; Esham, 2014; DOA, 2020). Corn is grown in almost 80,000 ha in Sri Lanka in climatically dry and intermediate zones with rainfed cultivation during the *Maha* season (DOA, 2020) and the Anuradhapura district alone contributes 30% of the country's extent (Hamangoda & Pushpakumari, 2019; Vidanapathirana *et al.*, 2022). However, this cropping system has lower productivity compared to irrigated or protected agriculture, primarily due to erratic weather, biotic stresses, and poor adoption of improved agronomic practices (Esham, 2014).

In Sri Lanka, open-pollinated corn varieties are in use for cultivation including *Bhadra*, *Ruwan*, *Aruna*, and *Muthu* (Vidanapathirana *et al.*, 2022). Despite this, hybrid varieties are more popular among farmers (Malaviarachchi *et al.*, 2007; Esham, 2014; Vidanapathirana *et al.*, 2022). The Department of Agriculture in Sri Lanka released the first local hybrid corn variety, *Sampath*, in 2004. Subsequently, some private companies introduced imported hybrid varieties, such as *Jet* and *Pacific* (Esham, 2014). In 2019, four

\* Corresponding author (thiruchchelvan@univ.jfn.ac.lk;  <https://orcid.org/0000-0003-3800-7104>)



This article is published under the Creative Commons CC-BY-ND License (<http://creativecommons.org/licenses/by-nd/4.0/>). This license permits use, distribution and reproduction, commercial and non-commercial, provided that the original work is properly cited and is not changed in anyway.

more hybrid varieties were introduced by the Department of Agriculture. However, the *Jet* and *Pacific* varieties remain the most cultivated hybrids in the Anuradhapura district due to their high yield potential (6 tons ha<sup>-1</sup>) and export demand (Vidanapathirana *et al.*, 2022). In 2020, average corn yields in Sri Lanka were 4 tons ha<sup>-1</sup>, which is below the maximum yield potential (Vidanapathirana *et al.*, 2022). This could be due to a variety of factors including biotic factors such as pests and diseases and abiotic stresses such as drought, and soil edaphic characters (Malaviarachchi *et al.*, 2007; Esham, 2014). Among biotic factors, the association of PPN with corn is highly influential on its yield (Sikandar *et al.*, 2021; Khanal & Land, 2023).

Plant-parasitic nematodes are known to infect almost all cultivated crops and are responsible for 14-20% of global annual yield losses (Jung & Wyss, 1999; Mesa-Valle *et al.*, 2020). These losses are estimated to be over 358 billion USD (Abd-Elgawad & Askary, 2015; Khanal & Land, 2023). A variety of nematodes are known to cause damage to corn, including genera such as *Anguina* spp., *Criconebella* spp., *Ditylenchus* spp., *Helicotylenchus* spp., *Hirschmanniella* spp., *Hoplolaimus* spp., *Meloidogyne* spp., *Pratylenchus* spp., *Radopholus* spp., *Rotylenchus* spp., *Trichodorus* spp., *Tylenchulus* spp., and *Xiphinema* spp. (Nicol *et al.*, 2011). Among these, *Meloidogyne* spp. and *Pratylenchus* spp. are known to cause the most damage and potential economic losses in corn (Sikora *et al.*, 2005).

In Sri Lanka, there is limited information available regarding the association of PPN with corn. A survey from 1991 to 1995 in 16 districts of Sri Lanka indicated PPN associations with different crop species (Ekanayake & Toida, 1997). Ekanayake & Toida (1997) identified six nematode species associated with corn: *Criconebella ornata*, *Helicotylenchus dihystra*, *Hoplolaimus seinhorsti*, *Pratylenchus zaeae*, *P. brachyurus*, and *Xiphinema elongatum*, although nematode population abundance and distribution were not investigated. In this context, the objective of this study was to identify the prevalence and abundance of PPNs associated with corn fields in the Anuradhapura district, Sri Lanka.

## MATERIALS AND METHODS

### Preliminary sampling

Preliminary sampling was undertaken in February 2021 across 14 corn fields located in five locations, Horowupotana, Kahatagasdigiliya, Kelenikawewa, Ranorawa, and Elayapaththuwa, situated within the

Anuradhapura district (8°3114" N, 80°4037" E), Sri Lanka. A complete cropping history of the sampled fields was recorded. The sampling sites were divided into 1 ha blocks. From selected blocks, 25 soil core samples were taken in a zigzag pattern across the field as described by Marais *et al.* (2017). Samples were taken in the corn rhizosphere to a depth of 30 cm using a 4 cm diameter soil corer (Eijkelkamp, Japan). To minimize cross-contamination, tools were cleaned between each sampling using a metal brush and tissue paper. About a kilogram of soil from subsamples (25 cores ha<sup>-1</sup>) was thoroughly mixed to make a composite sample before being transferred to labelled plastic bags. Subsequently, the bags were sealed, and stored in darkness in cooler boxes (Marina Cooler Box) and the soil samples were taken to the laboratory and placed in a refrigerator at 4 °C until they were processed.

### Intensive secondary sampling

From the 14 corn fields, four fields in Horowupotana (8°33'01.4"N, 80°45'44.0"E), Kahatagasdigiliya (8°28'13.3"N, 80°44'27.7"E), Kelenikawewa (8°20'29.8"N, 80°41'37.6"E), and Elayapaththuwa (8°23'20.6"N, 80°18'26.0"E) with high PPN abundance were selected for intensive sampling. Soil samples were collected when the seedlings were 2-3 wks old (2021 November) and at harvesting (14-15 wks after planting in 2022 February), during the *Maha* cropping season in 2021/2022. Each field was divided into four equal quadrants. A composite sample from a quadrant was collected in a zigzag pattern, giving a total of four composite samples per field. At each sampling point in a quadrant, 12 soil cores (500 g soil) were collected randomly using a soil sampler within a 4 m radius from the centre point of the sample. Apart from this modified sampling pattern, other procedures and techniques were identical to the methods mentioned previously.

### Nematode extraction: Sieving-centrifugal-sugar flotation method for soil sample

The sieving-centrifugal-sugar flotation method (Jenkins, 1964; Marais *et al.*, 2017) was used to extract nematodes from the soil samples to determine nematode density. Briefly, 100 g of soil from the composite sample was placed in a 5 L container and thoroughly mixed with 1 L tap water. After manually mixing and stirring, the mixture was allowed to settle for 30 s before transferring to nested aperture sieves 150-µm on top of 38-µm aperture sieves (W.S. Tyler, USA). This process was repeated three times for each sample to recover most nematodes in the soil. The deposit from the bottom sieve (38-µm aperture) was



transferred into 50 mL centrifuge tubes and centrifuged at 568 g rotational centrifugal force (RCF) for 5 min. The supernatant was removed carefully, and the pellet was thoroughly mixed with sucrose solution (624 g of sugar/L tap water) and spun again in the centrifuge (Tomy, Japan) for one min at 568 g RCF. After centrifugation, the supernatant was passed through a 38- $\mu$ m-aperture sieve and carefully washed using water dispensed from a wash bottle to collect the extracted nematodes into a 100 mL sterile specimen bottle with a lid. Samples were kept at 4 °C until they were morphologically identified (Kularathna *et al.*, 2019). Using an inverted compound light microscope (Nikon, Japan) at  $\times 40$  magnification, the nematodes were identified at the genus level based on morphological descriptions (Fortuner, 1988; Mai *et al.*, 1996).

### Statistical analysis

Nematode populations from the survey were characterized using standardized ecological nematology indices (Boag, 1993). Nematode prevalence was calculated using the equation 1.

$$\text{Prevalence (\%)} = (\text{nN/nS}) \times 100 \quad \dots(1)$$

where the nN is the number of samples containing nematodes taxon or genus, and nS is the total number of samples collected.

The proportion of the sample comprising PPNs was derived by equation 2.

$$\text{Percentage of PPN} = (\text{PPN/Nematodes}) \times 100 \quad \dots(2)$$

where PPN is the total number of PPNs recovered, and Nematodes is the total number of nematodes (PPN and all non-PPN) recovered.

Genus-specific prevalence data were recorded as the presence (1) or absence (0) of each genus at each survey site and the total number of genera was the number of different genera detected at a single survey site.

Simpson's diversity index (1-D), was calculated by equation 3:

$$\text{Simpson's diversity index (1-D)} = 1 - [\sum n(n-1)/N(N-1)] \quad \dots(3)$$

where n is the total number of nematodes of a specific genus, and N is the total number of nematodes across all genera in the sample.

Evenness (E) expresses how evenly individuals in a community are distributed over the different genera and was calculated by equation 4:

$$\text{Evenness (E)} = 1 - [\sum n(n-1)/N(N-1)]/s \quad \dots(4)$$

where s is the total number of different genera (Fleming *et al.*, 2016). Simpson's biodiversity index (1-D) and evenness (E) were calculated only for the PPN diversity. Higher values (ranging from 0-1) of the Simpson biodiversity index (1-D) indicate higher nematode diversity; if it was zero there was a single nematode genus in the population.

Nematode abundance data were analyzed using a one-way ANOVA and a post hoc Bonferroni test at 95% confidence intervals was performed (GenStat statistical software ver. 20). The data was checked for normality and then transformed using the square root method before statistical analysis.

## RESULTS AND DISCUSSION

### Prevalence of plant parasitic nematodes in the corn fields of Anuradhapura, Sri Lanka - Preliminary samples

The prevalence of PPN was 92.9% and was found in 13 out of 14 corn fields (Table 1). Among the recovered PPN, the root-lesion nematode (RLN) *Pratylenchus* spp., had a prevalence of 71.4% occurring in 10 out of 14 fields sampled. *Pratylenchus* spp. were the most prevalent PPN detected, compared to other PPN genera such as the spiral nematode (*Helicotylenchus* spp.) (28.6%), root-knot nematode (*Meloidogyne* spp.) (21.4%), ring nematode (*Criconemella* spp.) (21.4%) and lance nematode (*Hoplolaimus* spp.) (35.7%). All these genera, except *Meloidogyne* spp., were previously reported in corn fields in Sri Lanka (Ekanayake & Toida 1997). The mean population of *Pratylenchus* spp. was 2020 nematodes kg<sup>-1</sup> of soil recovered from the preliminary sampling. The mean population of *Helicotylenchus* spp. (spiral nematode) had a mean abundance of 963 nematodes kg<sup>-1</sup> of soil. The abundance of *Meloidogyne* spp. J2 (root-knot nematode) and *Criconemella* spp. (ring nematode) was observed to be 54 nematodes per kg of soil and 411 nematodes per kg of soil, respectively.

The prevalence percentages and diversity indices of PPN identified in 14 corn fields are presented in Table 2. The percentage of PPNs ranged from 0 to 81% of the total nematode population. Field 8 in Kelenikawewa had the highest PPN percentage of 81% followed by Field 6

(Kahatagasdigiliya) at 72%, Field 4 (Horowupotana) at 72%, Field 2 (Horowupotana) at 55% of PPN population of total nematodes. No PPN (0%) was detected in Field 10 in Ranorawa. Simpson's biodiversity index (1-D) ranged from 0 to 0.49 with Evenness from 0 to 0.25. Field 14

(Elayapaththuwa) was the richest in biodiversity among the 14 fields that were sampled as (1-D) was 0.49 with an Evenness of 0.25. Comparatively, the same field recorded an exceptionally low percentage of PPN (0.83%).

**Table 1:** Prevalence and abundance of plant-parasitic nematodes in the corn fields of Anuradhapura, Sri Lanka : preliminary sampling

Nematode (taxa/genus/ common name)	Prevalence <sup>a</sup>	Prevalence % <sup>b</sup>	Abundance kg <sup>-1</sup> of soil			
			Mean <sup>c</sup>	Median <sup>d</sup>	Maximum	Damage level*
PPN (All genera)	13	92.9	1862	1142	8500	-
PPN Genera						
<i>Pratylenchus</i> (lesion)	10	71.4	2020	1038	7517	1000
<i>Helicotylenchus</i> (spiral)	4	28.6	963	54	3708	4000
<i>Meloidogyne</i> J2 (root-knot)	3	21.4	54	50	100	200
<i>Criconemella</i> (ring)	3	21.4	411	200	900	6000
<i>Hoplolaimus</i> (lance)	5	35.7	113	33	400	1500

<sup>a</sup> Number of positive samples/total sample count

<sup>b</sup> The % of positive samples/total sample count

<sup>c</sup> Total number of nematodes/numbers of positive samples

<sup>d</sup> Median for nematode abundance in positive samples

\* Damage level as summarised (Olthof, 1987; Evans *et al.*, 1993; Thompson *et al.*, 2010; Niblack, 2014; Fleming *et al.*, 2016)

**Table 2:** Abundance and diversity indexes of plant-parasitic nematodes in the corn fields of Anuradhapura district, Sri Lanka : Preliminary sampling

Fields	Corn variety	PPN % <sup>a</sup>	Most abundant PPN	Simpson biodiversity (1-D)	E (Evenness)
1	Pacific 984	31.6	<i>Pratylenchus</i>	0.00	0.00
2	Pacific 984	54.8	<i>Pratylenchus</i>	0.04	0.02
3	Pacific 999	45.9	<i>Pratylenchus</i>	0.00	0.00
4	Pacific 984	71.7	<i>Pratylenchus</i>	0.15	0.05
5	Pacific 999	26.7	<i>Pratylenchus</i>	0.00	0.00
6	Pacific 999	72.1	<i>Pratylenchus</i>	0.10	0.03
7	Pacific 999	42.6	<i>Pratylenchus</i>	0.34	0.11
8	Pacific 999	81.3	<i>Pratylenchus</i>	0.21	0.05
9	Pacific 984	44.2	<i>Helicotylenchus</i>	0.03	0.02
10	Pacific 999	0		NA	NA
11	Pacific 999	40.9	<i>Pratylenchus</i>	0.00	0.00
12	Pacific 984	5.3	<i>Hoplolaimus</i>	0.00	0.00
13	Jet	14.7	<i>Pratylenchus</i>	0.08	0.04
14	Jet	0.8	<i>Hoplolaimus</i>	0.49	0.25

<sup>a</sup> Plant-parasitic nematodes (PPN) % = number of PPN/total nematodes in a field

### Abundance of plant-parasitic nematodes in the Anuradhapura corn fields, Sri Lanka - Preliminary sampling

The 14 sampled fields in five locations within the Anuradhapura district, Sri Lanka differed significantly

( $p < 0.001$ ) in total nematode number, PPN, RLN, and spiral nematode abundance (Table 3). The Kelenikawewa area was highly populated with PPN of 4804 nematodes kg<sup>-1</sup> and RLN 4213 nematodes kg<sup>-1</sup>. In the Kelenikawewa area, there was a low abundance of other PPN, which included *Meloidogyne*, *Criconemella*,

and *Hoplolaimus* nematodes, with a combined total of 592 nematodes kg<sup>-1</sup> and *Helicotylenchus* not detected. RLN abundance in Kahatagasdigiliya and Horowupotana was 1717 nematodes kg<sup>-1</sup> and 1350 nematodes kg<sup>-1</sup>, respectively. Of the five areas, Ranorawa (186 nematodes kg<sup>-1</sup>) was the only area with RLN abundance below 500 nematodes kg<sup>-1</sup> of soil. *Helicotylenchus* was the next abundant PPN with numbers varying depending

on the sampling area (Table 3). The abundance of *Helicotylenchus* differed significantly ( $p < 0.001$ ) between the areas, with relatively low levels detected in Horawupotana (27 nematodes kg<sup>-1</sup>) and Kahatagasdigiliya (17 nematodes kg<sup>-1</sup>) while comparatively, the Ranorawa area had nearly 45 times greater numbers with 1236 nematodes kg<sup>-1</sup>. *Helicotylenchus* spp. was not detected in the Kelenikawewa and Elyapaththuwa areas.

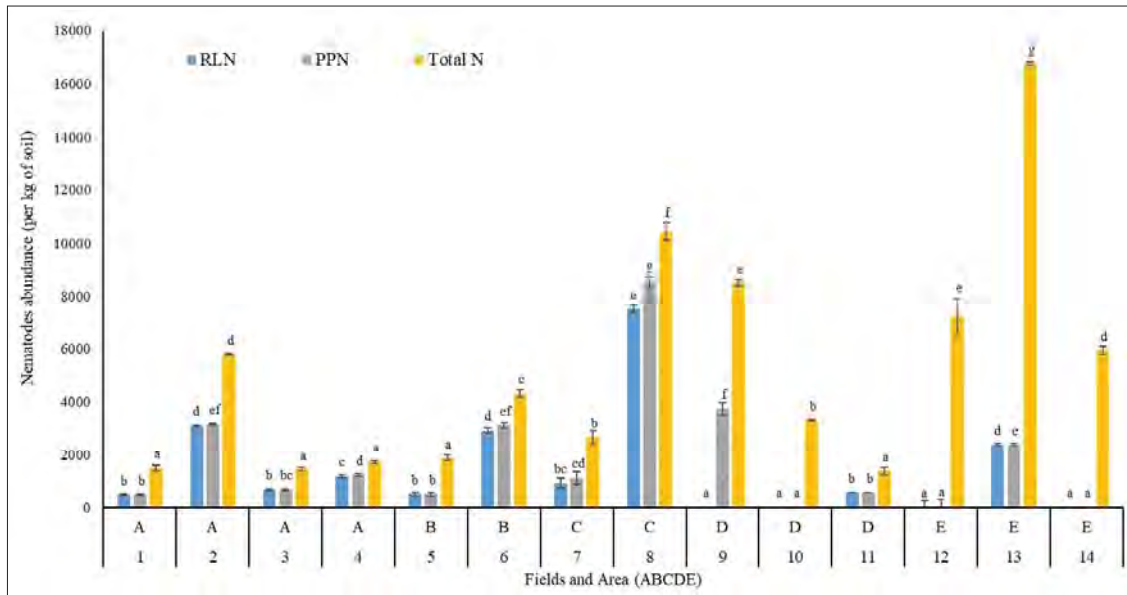


**Figure 1:** Abundance of plant-parasitic nematodes in the corn fields of Anuradhapura district, Sri Lanka-Preliminary sampling. The same letters on the coloured bars, representing RLN (blue), PPN (grey), and Total (yellow) nematodes in different areas and fields, are not significantly different according to the Bonferroni test at a 95% confidence level (Error bars with SEM). Area: A-Horowupotana, B- Kahatagasdigiliya, C- Kelenikawewa, D- Ranorawa and E- Elayapaththuwa, 1-14 sampled fields numbers. PPN plant-parasitic nematodes, RLN root-lesion nematodes, and Total N- total nematodes (PPN and non-PPN)

**Table 3:** Abundance of plant-parasitic nematodes recorded in the sampled area of Anuradhapura district, Sri Lanka- Preliminary sampling.

Area	Mean abundance of nematodes kg <sup>-1</sup> of soil (± SEM)				
	<i>Pratylenchus</i> spp.	<i>Helicotylenchus</i> spp.	PPN	Other PPN	Total
Horowupotana	1350 ± 219.1 <sup>b</sup>	27.1 ± 6.7 <sup>a</sup>	1377.1 ± 223.8 <sup>a</sup>	0 ± 0 <sup>a</sup>	2602.1 ± 384.9 <sup>a</sup>
Kahatagasdigiliya	1716.7 ± 372.3 <sup>bc</sup>	16.7 ± 9.4 <sup>a</sup>	1808.3 ± 398.8 <sup>ab</sup>	75 ± 24.2 <sup>b</sup>	3095.8 ± 377.1 <sup>ab</sup>
Kelenikawewa	4212.5 ± 1004 <sup>c</sup>	0 ± 0 <sup>a</sup>	4804.2 ± 1123.2 <sup>b</sup>	591.7 ± 122.9 <sup>c</sup>	6558.3 ± 1187.8 <sup>bc</sup>
Ranorawa	186.1 ± 66.2 <sup>a</sup>	1236.1 ± 429.8 <sup>b</sup>	1433.3 ± 407.3 <sup>a</sup>	11.1 ± 7.6 <sup>a</sup>	4391.7 ± 734.6 <sup>ab</sup>
Elyapaththuwa	794.4 ± 284.9 <sup>a</sup>	0 ± 0 <sup>a</sup>	801.1 ± 283.8 <sup>a</sup>	7.2 ± 2.2 <sup>ab</sup>	9973.9 ± 1192.3 <sup>c</sup>

Nematode abundance in 14 corn fields sampled in the Anuradhapura district, Sri Lanka is illustrated in Figure 1. Total nematode abundance between the fields was significantly different ( $p < 0.001$ ) with levels varying from 16,767 to 1,367 nematodes  $\text{kg}^{-1}$  of soil. There were five fields with lower levels of total nematode abundance per kg of soil compared to the other 9 corn fields. Nematode abundance did not differ significantly ( $p > 0.05$ ) between the following five fields with lower levels: Horowupotana Fields 1 (1475 nematodes  $\text{kg}^{-1}$ ), 3 (1433  $\text{kg}^{-1}$ ) and 4 (1717 nematodes  $\text{kg}^{-1}$ ), Field 5 in Kahatagasdigiliya (1875 nematodes  $\text{kg}^{-1}$ ), and Field 11 in Ranorawa (1367 nematodes  $\text{kg}^{-1}$ ). Higher total nematode abundance was recorded (from highest to lowest) in Field 13 from Elayapaththuwa (16,767 nematodes  $\text{kg}^{-1}$ ), Fields 8 and 9 in Kelenikawewa (10442 nematodes  $\text{kg}^{-1}$ ), (8500 nematodes  $\text{kg}^{-1}$ ), Field 12 in Elayapaththuwa (7220 nematodes  $\text{kg}^{-1}$ ), Field 2 Horowupotana (5783 nematodes  $\text{kg}^{-1}$ ), and Field 6 Kahatagasdigiliya (4317 nematodes  $\text{kg}^{-1}$ ). The PPN abundance differed significantly ( $p < 0.001$ ) between fields. In this survey, *Pratylenchus* spp. (RLN) was recorded as the predominating nematode in the sampled fields and its abundance differed significantly ( $p < 0.001$ ) with the highest (7517 RLN nematodes  $\text{kg}^{-1}$  of soil) in Field 8 from Kelenikawewa.

The diversity of PPN varied across the sampled fields, with different nematode genera exhibiting varying prevalence percentages. The abundance of PPNs varied among the sampled fields. Kelenikawewa exhibited the highest abundance of PPN, particularly *Pratylenchus* spp. (4213 nematodes  $\text{kg}^{-1}$  of soil) compared to other

areas, potentially indicating its severe infestation. This observation is consistent with findings from previous studies indicating high populations of *Pratylenchus* spp. recorded in various crops, including corn (Schmitt & Barker, 1981; Grabau & Chen, 2016; Simon *et al.*, 2018). Comparatively, the incidence and abundance of the genus *Pratylenchus* spp. in the Anuradhapura corn fields were considerably higher than those found in corn and cereal crops in other parts of the world (Thompson *et al.*, 2010; Tylka *et al.*, 2011; Fleming *et al.*, 2016; Simon *et al.*, 2018). This could be influenced by many factors such as host susceptibility (Batista da Silva, 2013; Fleming *et al.*, 2016), soil and ecological conditions in the respective area (Kable & Mai, 1968; Castillo *et al.*, 1996; Kandji *et al.*, 2003; Govaerts *et al.*, 2007; Fleming *et al.*, 2016; Karuri *et al.*, 2017), and crop rotation and management practices (Wang & McSorley, 2005; Thompson *et al.*, 2010; Simon *et al.*, 2018; Tylka *et al.*, 2019).

#### Prevalence of the plant-parasitic nematodes associated with selected corn fields in the Anuradhapura district, Sri Lanka - Intensive sampling.

The prevalence of PPNs and their abundance at the seedling (November 2021) and harvesting stages of corn (February 2022) varied between the two samples (Table 4). The total nematode population increased from sampling in November 2021 to February 2022, with higher numbers observed at the time of harvesting (8404 nematodes  $\text{kg}^{-1}$ ) compared to the seedling stage (1689 nematodes  $\text{kg}^{-1}$ ). The prevalence of *Pratylenchus* spp. at the seedling stage (SS) of corn was 81%, with 13

**Table 4:** Prevalence and abundance of plant-parasitic nematodes in selected corn fields in the Anuradhapura district, Sri Lanka- Intensive sampling.

Nematode (taxa/genus/ common name)	Prevalence <sup>a</sup>		Abundance $\text{kg}^{-1}$ of soil					
	SS	HS	Mean <sup>b</sup>		Median <sup>c</sup>		Maximum	
			SS	HS	SS	HS	SS	HS
PPN (All genera)	16 (100)	16 (100)	854.16	5545.30	825.01	4983.33	1433.34	8416.68
PPN Genera								
<i>Pratylenchus</i> (lesion)	13 (81)	16 (100)	727.08	4338.54	641.68	3893.75	1270.84	6675.00
<i>Helicotylenchus</i> (spiral)	5 (31)	15 (93.75)	81.95	873.95	50.00	754.18	116.66	2429.16
<i>Criconebella</i> (ring)	9 (56)	14 (87.5)	113.55	245.84	106.26	262.51	145.84	366.66
<i>Hoplolaimus</i> (lance)	6 (38)	14 (87.5)	100.00	187.33	104.16	98.95	104.16	504.18

SS- Sampling at the seedling stage of corn (November 2021)

HS- Sampling at the harvesting stage of corn (February 2022)

<sup>a</sup>No. of positive samples/total sample count and the values in parenthesis are in percentages

<sup>b</sup>Total no. of nematodes/no. of positive samples

<sup>c</sup>Median is for nematode abundance in positive samples

out of 16 composite samples from four fields showing its presence. However, at the harvesting stage (HS), the prevalence increased to 100%, as observed in all 16 composite samples collected from the same four fields sampled. *Helicotylenchus* spp. prevalence at SS and HS were 31% and 94%, respectively. *Criconemella* spp. was 56% and 87.5% and *Hoplolaimus* spp. 38% and 87.5% at the SS and HS, respectively. The mean abundance of the nematodes increased from the SS to the HS of corn irrespective of genera. *Pratylenchus* was the most abundant PPN genus in all the fields at both sampling times. However, sampling at HS yielded an abundance of *Helicotylenchus* (874 nematodes kg<sup>-1</sup>). *Criconemella* (113 and 246 nematodes kg<sup>-1</sup>) and *Hoplolaimus* (100 and 187 nematodes kg<sup>-1</sup>) were observed in all the fields sampled. The genus *Meloidogyne* spp. (J<sub>2</sub> stage) was not observed in any fields sampled.

#### **The abundance and reproduction factor of plant-parasitic nematodes associated with corn at the seedling and harvesting stage in the Anuradhapura district, Sri Lanka - Intensive sampling**

Nematode abundance in the four selected corn fields were sampled in November 2021, and February 2022; abundance was greater in HS compared to SS (Table 5). The mean abundance of the total nematodes was significantly different ( $p < 0.001$ ) among the fields at both times of sampling. The HS yielded a higher abundance compared to the SS. The mean of the total nematode population at the SS (pi) and HS (pf) were at Kelenikawewa (2996, 19075 nematodes kg<sup>-1</sup>), followed by Horowupotana (2258, 7321 nematodes kg<sup>-1</sup>), Elyapaththuwa (796, 3415 nematodes kg<sup>-1</sup>) and then Kahatagasdigiliya (450, 2890 nematodes kg<sup>-1</sup>), respectively. The abundance of the PPN and *Pratylenchus* was also significantly different ( $p < 0.001$ ) in the four fields sampled. Plant-parasitic nematodes abundance at the SS in all the fields were lower than 1000 nematodes kg<sup>-1</sup> of soil except in Kelenikawewa (2100 nematodes kg<sup>-1</sup>). However, at the HS, the PPN abundance of all the fields was recorded above 2000 PPN kg<sup>-1</sup>. The highest PPN abundance was recorded at Kelenikawewa (11017 nematodes kg<sup>-1</sup>), followed by Horowupotana (6017 nematodes kg<sup>-1</sup>), Elyapaththuwa (2535 nematodes kg<sup>-1</sup>), and Kahatagasdigiliya (2223 nematodes kg<sup>-1</sup>).

In all the fields, the *Pratylenchus* population was as high as the PPN abundance in the respective fields. The mean abundance of *Pratylenchus* at the SS Kelenikawewa field was 1863 nematodes kg<sup>-1</sup> and Horowupotana field 500 nematodes kg<sup>-1</sup> but in the fields of Kahatagasdigiliya (204.2 nematodes kg<sup>-1</sup>) and

Elyapaththuwa (88 nematodes kg<sup>-1</sup>) RLN abundance was below 500 kg<sup>-1</sup> of soil. At the HS, the *Pratylenchus* abundance in all four fields were above 1000 nematodes kg<sup>-1</sup>. The highest *Pratylenchus* abundance was recorded with a 5-fold increase compared to the SS at the Kelenikawewa field (9863 nematodes kg<sup>-1</sup>). Comparing the Kelenikawewa field with other fields the mean population of *Pratylenchus* was lower but above 1000 nematodes kg<sup>-1</sup> of soil as follows: Horowupotana 3925 nematodes kg<sup>-1</sup>, 7.9 fold increased), Elyapaththuwa 2000 nematodes kg<sup>-1</sup>, 22.9 fold increased, and Kahatagasdigiliya 1567 nematodes kg<sup>-1</sup>, 7.7 fold increased. These findings indicated that when corn matures the abundance of *Pratylenchus* also increases. All types of nematodes, except for spiral nematodes, were recorded in high abundance in the Kelenikawewa field, and the next most prevalent was Horowupotana. A high *Helicotylenchus* population was recorded in the Horowupotana field (1767 nematodes kg<sup>-1</sup>) at the HS compared to other fields.

Intensive sampling in subsequent seasons was carried out on fields with the highest *Pratylenchus* abundance, considering the potential severity of its infestation in these specific areas. Similarly, McDonald & Nicol (2005) and McDonald *et al.* (2017) reported that *Pratylenchus* spp. is sporadic when their numbers are substantially higher with high prevalence in corn fields. Analysis of PPN abundance at different stages of corn growth revealed an increase in population from the SS to the HS. The studies conducted by Simon *et al.* (2018); Chowdhury *et al.* (2020); Han *et al.* (2021), & Thapa *et al.* (2023) indicated that sampling at different corn growth stages could alter the nematode abundance. However, Thapa *et al.* (2023) observed higher PPN abundance in corn fields at the HS than in the SS, as we also discovered in this study. In contrast, Simon *et al.* (2018) stated that the SS would be better for recovering most of the PPNs in terms of diversity. However, this study indicates the diversity and abundance were higher at the HS than at SS in corn fields in Sri Lanka.

The reproductive factor (Rf) of *Pratylenchus* was calculated ( $Rf = pf/pi$ ) using the mean initial population (pi) at the SS and the mean final population (pf) at the HS of corn. The *Pratylenchus* multiplications were Kelenikawewa 5.3, Horowupotana 7.9, Kahatagasdigiliya 7.7, and Elyapaththuwa 22.9. However, the abundance of *Pratylenchus* in the Kelenikawewa field (9863 abundance kg<sup>-1</sup>) was 2.5 times higher than in the Horowupotana (3925 nematodes kg<sup>-1</sup>) and 5 times higher than the other two fields.

The population of PPN and *Pratylenchus* spp. at Elayapaththuwa and Kahatagasdigiliya locations had lower levels of nematodes in February (2022) compared to the previous year (February 2021). PPN populations in the Kelenikawewa and Horowupotana field had increased (Figure 2). The results indicated that there was a population increase of 31.2% (2021 February- 7517 nematodes kg<sup>-1</sup> and in 2022 February- 9863 nematodes kg<sup>-1</sup>) of *Pratylenchus* spp. at the Kelenikawewa field compared to the previous year. The mean population of *Pratylenchus* spp. in both seasons (February 2021 and February 2022) showed a 26.3% increase in Horowupotana (3108 and 3925 nematodes kg<sup>-1</sup>). However, the population of *Pratylenchus* spp. decreased

by 19.2% and 46.6% in Elayapaththuwa (2383 and 2000 nematodes kg<sup>-1</sup>) and Kahatagasdigiliya (2933 and 1567 nematodes kg<sup>-1</sup>) fields, respectively (Figure 2). These population changes could be influenced by soil characteristics such as texture, structure, pH, moisture content, and nutrient contents, which are known to be major contributors to the change in population density and dissemination of nematodes (Kandji *et al.*, 2003; Fleming *et al.*, 2016). Also, climatic factors such as rainfall, and temperature have impacts on the population densities of PPNs (Govaerts *et al.*, 2007; Karuri *et al.*, 2017). Thus, further studies need to be conducted to determine the relationship of soil and environmental characteristics on nematode populations.

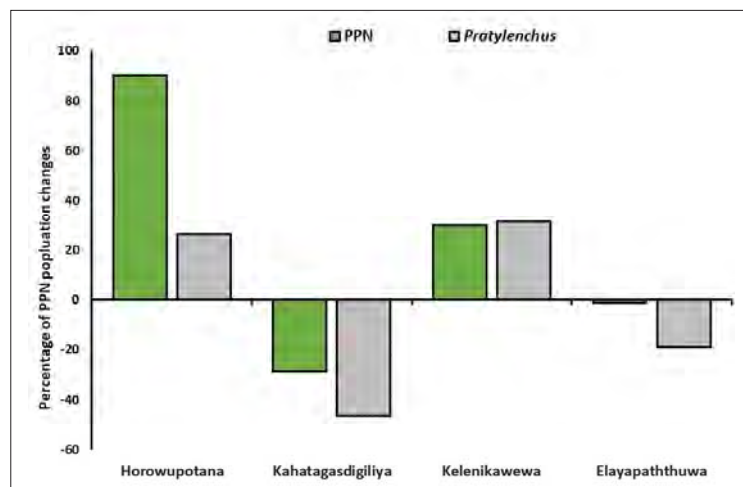


**Figure 2:** Changes in abundance (%) of plant-parasitic nematodes in 2022 February compared to 2021 February in four sampled fields in the Anuradhapura district. PPN-plant-parasitic nematodes, *Pratylenchus*- root-lesion nematodes

*Pratylenchus* spp. were the most abundant PPN genus throughout both sampling periods, indicating its persistence and potential threat to corn production in Sri Lanka. The Rf of *Pratylenchus* was substantially higher compared to other nematode genera in most fields, indicating its greater reproductive potential. In the Anuradhapura district, corn is cultivated as a rainfed crop where crops get zero irrigation and are completely reliant on rainfall. In the *Maha* season (September to March) the Anuradhapura district receives 49% (615 out of 1255 mm) of the average annual rainfall from October to December (Climate Data, 2023). There is limited information available in Sri Lanka regarding the susceptibility of corn varieties used against PPNs in the

sampled areas of Anuradhapura, Sri Lanka. Furthermore, there are limitations for soil testing facilities to assess soil physiochemical properties or to evaluate the relationship of these soil factors with PPN populations in Sri Lanka. Therefore, due to the lack of information and facilities, corn farmers in the Anuradhapura district continuously cultivated corn for more than a decade without implementing any crop rotation practices, driven only by market demand. Additionally, their practice includes growing the same corn varieties for multiple seasons. As reports indicate, this type of cropping practice could lead to a severe buildup of PPNs (Arjun *et al.*, 1983). Therefore, this could be the reason behind the high levels of PPNs, especially *Pratylenchus* nematodes.

This research could not compare the population levels of *Pratylenchus* nematodes, which causes economic losses to the Sri Lankan corn industry. Nevertheless, findings from Thompson *et al.* (2010), Tylka *et al.* (2011), Simon *et al.* (2018), Chowdhury *et al.* (2020), and Niblack (2014) have reported generalised threshold levels for *Pratylenchus*: up to 100 RLN kg<sup>-1</sup> of soil with no significant damage to the crops, above 100 to 250 RLN kg<sup>-1</sup> of soil with minor damage, and 250 to 500 RLN kg<sup>-1</sup> of soil with a moderate level of damage. Therefore, their findings demonstrate that severe damage to corn could arise from an RLN population between 500 to 1000 RLN kg<sup>-1</sup> of soil or any number above 1000 kg<sup>-1</sup> of soil. Further, it suggests that RLN levels were above the levels mentioned by previous authors and could lead to a severe economic threat to the Sri Lankan corn industry. Further investigations are necessary to assess the true extent of the damage. Additional studies should focus on developing a threshold level specific to the corn-growing regions of Sri Lanka and evaluating the pathogenicity and reproduction of RLN in corn varieties commonly used in Sri Lanka.

## CONCLUSION

This study highlights the widespread presence of PPNs in corn-producing areas of the Anuradhapura district, with *Pratylenchus* spp. emerging as the predominant genus. Variations in PPN abundance and diversity were observed, with some areas, such as Kelenikawewa, exhibiting higher infestation levels. *Pratylenchus* spp. had a higher reproductive potential than other PPN genera observed in this study. Temporal analysis revealed dynamic trends in nematode population, with some fields increasing while others declining. These fluctuating nematode dynamics emphasised the need for continuous monitoring and adaptive management strategies. Overall, the findings highlight the importance of nematode management strategies to mitigate the impact of PPNs on corn yields and ensure sustainable production in the region. Further research focusing on the primary factors driving PPN population dynamics would be essential for the development of targeted and sustainable management practices.

## Acknowledgments

The authors thank Prof K. Pakeerathan, Department of Agricultural Biology, University of Jaffna for providing laboratory access at the Research and Training Lab (JICA) and Mr V. Jeyaprasath and Mr Bandara Abesinghe for assisting the sample collection.

## Funding

This study was funded by the AHEAD Grant [Grant number AHEAD/Ph.D./R3/Agri/463] and Lincoln University, New Zealand Research Fund [Grant number 3601/AGLS/45401/1145841]

## REFERENCES

- Abd-Elgawad, M. M. M., & Askary, T. H. (2015). Impact of phytonematodes on agriculture economy. In *Biocontrol agents of phytonematodes*. CABI.  
<https://doi.org/doi:10.1079/9781780643755.0003>
- Arjun, L., Sanwal, K. C., & Mathur, V. K. (1983). Changes in the nematode population of undisturbed land with the introduction of land development practices and cropping sequences. *Indian Journal of Nematology*, 13(2), 133-140.
- Batista da Silva, M. (2013). Studies on extraction and control of plant-parasitic nematodes on corn. *MSC thesis*. Iowa State University, Iowa, USA.  
<https://doi.org/10.31274/etd-180810-3186>
- Boag, B. (1993). Standardization of ecological terms in nematology. *Fundamental and Applied Nematology*, 16(02), 190-191.
- Castillo, P., Gómez-Barcina, A., & Jiménez-Díaz, R. M. (1996). Plant parasitic nematodes associated with chickpea in southern Spain and effect of soil temperature on reproduction of *Pratylenchus thornei*. *Nematologica*, 42(2), 211-219.  
<https://doi.org/10.1163/004325996X00057>
- Chowdhury, I. A., Yan, G., & Friskop, A. (2020). Occurrence of vermiform plant-parasitic nematodes in North Dakota corn fields and impact of environmental and soil factors. *Canadian Journal of Plant Pathology*, 42(3), 429 - 444.  
<https://doi.org/10.1080/07060661.2019.1674384>
- Climate Data (2023). Anuradhapura climate Sri Lanka. <https://en.climate-data.org/asia/sri-lanka/north-central/anuradhapura-4862/>.
- DOA (2020). *Maize*. Department of Agriculture, Sri Lanka. <https://www.doa.gov.lk/FCRDI/index.php/en/crop/43-maize-e>.
- Ekanayake, H. M. R., & Toida, Y. (1997). Nematode parasites on agricultural crops and their distribution in Sri Lanka. *JIRCAS Journal*, 4, 29-39.
- Esham, M. (2014). Technical efficiency and determinants of maize production by smallholder farmers in the Moneragala district of Sri Lanka. *Mediterranean Journal of Social Sciences*, 5(27 P1), 416-422.  
<https://doi.org/10.5901/mjss.2014.v5n27p416>
- Esham, M., Usami, K., Kobayashi, H., & Matsumura, I. (2005). Determinants of farmers' participation in farmers-agribusiness linkage and its implication for income distribution in Sri Lanka a case study of hybrid maize production. *Journal of Rural Problems*, 41(01), 200-205.  
<https://doi.org/10.7310/arfe1965.41.200>
- Evans, K., Trudgill, D. L., & Webster, J. M. (1993). *Plant*

- parasitic nematodes in temperate agriculture*. CAB International, UK.
- Fleming, T. R., McGowan, N. E., Maule, A. G., & Fleming, C. C. (2016). Prevalence and diversity of plant parasitic nematodes in Northern Ireland grassland and cereals, and the influence of soils and rainfall. *Plant Pathology*, 65(09), 1539-1550.  
<https://doi.org/10.1111/ppa.12525>
- Fortuner, R. (1988). A new description of the process of identification of plant-parasitic nematode genera. In: *Nematode identification and expert system technology* (eds R. Fortuner). Springer, USA.  
[https://doi.org/10.1007/978-1-4684-9016-9\\_6](https://doi.org/10.1007/978-1-4684-9016-9_6)
- Govaerts, B., Fuentes, M., Mezzalama, M., Nicol, J. M., Deckers, J., Etchevers J. D., Figueroa-Sandoval, B., & Sayre, K. D. (2007). Infiltration, soil moisture, root rot, and nematode populations after 12 years of different tillage, residue, and crop rotation managements. *Soil and Tillage Research*, 94(01), 209-219.  
<https://doi.org/10.1016/j.still.2006.07.013>
- Grabau, Z. J., & Chen, S. (2016). Determining the role of plant-parasitic nematodes in the corn-soybean crop rotation yield effect using nematicide application: II. Soybean. *Agronomy Journal*, 108(03), 1168-1179.  
<https://doi.org/10.2134/agronj2015.0432>
- Hamangoda, I., & Pushpakumari, G. (2019). *Agstat* (eds J. Galabada & S. Mathangaweera, Vol. XVI). Socio-Economics and Planning Centre Department of Agriculture, Sri Lanka. <https://www.doa.gov.lk/SEPC/images/PDF/AgStat.pdf>.
- Jenkins, W. (1964). A rapid centrifugal-flotation technique for separating nematodes from soil. *Plant Disease Reporter*, 48(09), 692.
- Jung, C., & Wyss, U. (1999). New approaches to control plant parasitic nematodes. *Applied Microbiology and Biotechnology*, 51(04), 439-446.  
<https://doi.org/10.1007/s002530051414>
- Kable, P. F., & Mai, W. F. (1968). Influence of soil moisture on *Pratylenchus penetrans*. *Nematologica*, 14(01), 101-122.  
<https://doi.org/10.1163/187529268X00697>
- Kandji, S. T., Ogot, C. K. P. O., & Albrecht, A. (2003). Crop damage by nematodes in improved-fallow fields in western Kenya. *Agroforestry Systems*, 57(1), 51-57.  
<https://doi.org/10.1023/A:1022949431814>
- Karuri, H. W., Olago, D., Neilson, R., Njeri, E., Opere, A., & Ndegwa, P. (2017). Plant parasitic nematode assemblages associated with sweet potato in Kenya and their relationship with environmental variables. *Tropical Plant Pathology*, 42(01), 1-12.  
<https://doi.org/10.1007/s40858-016-0114-4>
- Khanal, C., & Land, J. (2023). Study on two nematode species suggests climate change will inflict greater crop damage. *Scientific Reports*, 13(1), 14185.  
<https://doi.org/10.1038/s41598-023-41466-x>
- Kularathna, M. T., Overstreet, C., McGawley, E. C., Stetina, S. R., Khanal, C., Godoy, F. M. C., & McInnes, B. K. (2019). Pathogenicity and reproduction of isolates of reniform nematode, *Rotylenchulus reniformis*, from Louisiana on soybean. *Nematropica* 49(01), 31-41.
- Mai, W. F., Mullin, P. G., Lyon, H. H., & Loeffler, K. (1996). *Plant-parasitic nematodes-A pictorial key to genera*, 5<sup>th</sup> edition, Cornell University Press, New York, USA.
- Malaviarachchi, M. A. P. W. K., Karunaratne, K. M., & Jayawardane, S. N. (2007). Influence of plant density on yield of hybrid maize (*Zea mays* L.) under supplementary irrigation. *The Journal of Agricultural Science-Sri Lanka*, 3(02), 58-66.  
<https://doi.org/10.4038/jas.v3i2.8100>
- Marais, M., Swart, A., Fourie, H., Berry, S. D., Knoetze, R., & Malan, A. P. (2017). Techniques and procedures. In *Nematology in South Africa: A view from the 21<sup>st</sup> century* (eds H. Fourie, V. W. Spaul, R. K. Jones, M. S. Daneel & D. De Waele), Springer, Cham, Switzerland.  
[https://doi.org/10.1007/978-3-319-44210-5\\_4](https://doi.org/10.1007/978-3-319-44210-5_4)
- McDonald, A., De Waele, D., & Fourie, H. (2017). Nematode pests of maize and other cereal crops. In: *Nematology in South Africa: A View from the 21st Century*. Springer, Cham, Switzerland.  
[https://doi.org/10.1007/978-3-319-44210-5\\_8](https://doi.org/10.1007/978-3-319-44210-5_8)
- McDonald, A. H., & Nicol, J. M. (2005). Nematode parasites of cereals. In *Plant Parasitic Nematodes in Subtropical and Tropical Agriculture*. CABI Books, CAB International, UK.  
<https://doi.org/10.1079/9780851997278.0131>
- Mesa-Valle, C. M., Garrido-Cardenas, J. A., Cebrian-Carmona, J., Talavera, M., & Manzano-Agugliaro, F. (2020). Global research on plant nematodes. *Agronomy*, 10(8): 1148.  
<https://doi.org/10.3390/agronomy10081148>
- Niblack, T. L. (2014). Nematodes. In: *Illinois Agronomy Handbook*, pp. 209-218. <http://extension.cropsciences.illinois.edu/handbook/pdfs/chapter15.pdf>.
- Nicol, J. M., Turner, S. J., Coyne, D. L., Nijs, L. D., Hockland, S., & Maafi, Z. T. (2011). Current nematode threats to world agriculture. In: *Genomics and molecular genetics of plant-nematode interactions* (eds J. Jones, G. Gheysen & C. Fenoll), Springer, Dordrecht, Netherlands.  
[https://doi.org/10.1007/978-94-007-0434-3\\_2](https://doi.org/10.1007/978-94-007-0434-3_2)
- Olthof, T. H. (1987). Effects of fumigants and systemic pesticides on *Pratylenchus penetrans* and potato yield. *Journal of Nematology*, 19(04), 424-430.
- Schmitt, D. P., & Barker, K. R. (1981). Damage and reproductive potentials of *Pratylenchus brachyurus* and *P. penetrans* on soybean. *Journal of Nematology*, 13(03), 327-332.
- Sikandar, A., Khanum, T. A., & Wang, Y. (2021). Biodiversity and community analysis of plant-parasitic and free-living nematodes associated with maize and other rotational crops from Punjab, Pakistan. *Life*, 11(12), 1426.  
<https://doi.org/10.3390/life11121426>
- Sikora, R., Bridge, J., & Starr, J. (2005). Management practices: an overview of integrated nematode management technologies. In M. Luc, R.A. Sikora & J. Bridge (Eds.), *Plant Parasitic Nematodes in Subtropical and Tropical Agriculture*, CABI Books, CAB International, UK, pp.



- 793-825.  
<https://doi.org/10.1079/9780851997278.0793>
- Simon, A. C. M., Lopez-Nicora, H. D., Niblack, T. L., Dayton, E. A., Tomashefski, D., & Paul, P. A. (2018). Cropping practices and soil properties associated with plant-parasitic nematodes in corn fields in Ohio. *Plant Disease*, 102(12), 2519-2530.  
<https://doi.org/10.1094/pdis-03-18-0471-re>
- Strange, R. N., & Scott, P. R. (2005). Plant disease: A threat to global food security. *Annual Review of Phytopathology*, 43(1), 83-116.  
<https://doi.org/10.1146/annurev.phyto.43.113004.133839>
- Thapa, S., Darling, E., Cole, E., Poley, K., & Quintanilla, M. (2023). Distribution of plant-parasitic nematodes in Michigan corn fields. *Journal of Nematology*, 55(1), 1-13.  
<https://doi.org/10.2478/jofnem-2022-0015>
- Thompson, J. P., Clewett, T. G., Sheedy, J. G., Reen, R. A., O'Reilly, M. M., & Bell, K. L. (2010). Occurrence of root-lesion nematodes (*Pratylenchus thornei* and *P. neglectus*) and stunt nematode (*Merlinius brevidens*) in the northern grain region of Australia. *Australasian Plant Pathology*, 39(3), 254-264.  
<https://doi.org/10.1071/AP09094>
- Tylka, G., Gebhart, G. D., Marett, C. C., & Mullaney, M. P. (2019). Evaluation of soybean varieties resistant to soybean cyst nematode in Iowa—2019. <https://www.plantpath.iastate.edu/tylkalab/iowa-state-university-scن-resistant-soybean-variety-trials>.
- Tylka, G., Sisson, A. J., Jesse, L. C., Kennicker, J., & Marett, C. C. (2011). Testing for plant-parasitic nematodes that feed on corn in Iowa 2000-2010. *Plant Health Progress*, 12(1)  
<https://doi.org/10.1094/PHP-2011-1205-01-RS>
- Vidanapathirana, R., Rambukwella, R., & Priyadarshana, D. (2022). *The maize value chain*. Hector Kobbekaduwa Agrarian Research and Training Institute, Colombo, Sri Lanka.



## RESEARCH ARTICLE

### Mathematical Chemistry

# Computational analysis of diameter eccentricity based and hyper diameter eccentricity based indices for linear saturated monocarboxylic acids

D Sarkarai and K Desikan\*

Department of Mathematics, School of Advanced Sciences, Vellore Institute of Technology, Chennai, India.

Submitted: 30 August 2023; Revised: 20 June 2024; Accepted: 21 July 2024


**Abstract:** Chemical graph theory deals with chemical graphs, which are used to represent chemical systems. Topological indices of molecular graphs are an important area of research in chemical graph theory. These indices are numerical values associated with compounds that aim to establish connections between chemical structures and physical attributes, chemical reactivity, and biological activity. Many graph polynomials have been proposed to compute various topological indices. Quantitative structure-property relationship (QSPR) analysis of chemical compounds involves several regression methods that rely on these topological indices. In this article, we utilize the newly introduced  $\mathcal{D}\varepsilon$ -polynomial to calculate the eccentricity-based indices such as the diameter eccentricity based and hyper diameter eccentricity based index values for nineteen linear saturated monocarboxylic acids. Quantitative structure-property relationship (QSPR) analysis is also performed for the seven thermodynamic properties of monocarboxylic acids. The relationship between thermodynamic properties and topological indices is explored using linear, quadratic and cubic regression models. The best fit curvilinear regression models were determined based on the  $R^2$  and RMSE values of the models. To further investigate the statistical significance of our models, we also conducted chi-square goodness-of-fit tests to identify the best fit models.

**Keywords:** Diameter, eccentricity, monocarboxylic acids, QSPR, radius.

## INTRODUCTION

Linear saturated carboxylic acids can be represented by the formula RCOOH, where R is a linear alkenyl group. One of the fundamental ideas in chemistry is that a molecule's qualities are inextricably linked to its structural characteristics. Chemical graph theory is a discipline in chemistry that deals with graphs. It involves working with chemical graphs, which are used to represent chemical systems (Kirmani *et al.*, 2021). One of the most important fields of research in chemical graph theory is topological indices of molecular graphs. These studies are beneficial for determining the relationship between the molecular structure of a drug and its physicochemical properties (Basavanagoud & Praveen, 2020). For the quantitative structure -property relationship (QSPR) and quantitative structure-activity relationship (QSAR) analysis of chemical compounds, several regression methods based on topological indices have been used (Kulli, 2018; Shafiei, 2016).

A topological graph index, also known as a molecular descriptor, is a mathematical formula that may be applied to any graph that represents a chemical structure. This index may be used to assess mathematical values and

\* Corresponding authors (kalyanidesikan@vit.ac.in;  <https://orcid.org/0000-0002-3074-5826>)



This article is published under the Creative Commons CC-BY-ND License (<http://creativecommons.org/licenses/by-nd/4.0/>). This license permits use, distribution and reproduction, commercial and non-commercial, provided that the original work is properly cited and is not changed in anyway.

further study a molecule's physical and other features. As a result, it is an effective means of eliminating costly and time-consuming laboratory studies (Baev, 2012). The topological index was first used by Harold Wiener (Wiener, 1947). He proposed the concept of the path number of a graph, which is the total of all the distances between pairs of carbon atoms in a molecule. The first generic Zagreb index was proposed by Gutman and Das (Gutman & Das, 2004). The Geometric-arithmetic (GA) index was established by Yuan *et al.* (Yuan *et al.*, 2009) and contrasted with the well-known Randic index. The atom-bond connectivity index, sometimes known as the ABC index, was proposed by Estrada *et al.* (Estrada *et al.*, 1988). Due to its relationship with the thermodynamic characteristics of alkanes, the ABC index is significant (Gutman *et al.*, 2012). Eccentricity-based topological indices have also piqued the curiosity of several researchers. The eccentric connectivity index (ECI) was developed by Madan *et al.* in 2005 as a distance-based topological indicator and Ghorbani in 2012 provided new descriptions for the Zagreb indices by defining them in terms of the eccentricity of a molecular graph. The reverse ECI for a series of nanocones and fullerene structures was recently explored by Qudair Baig *et al.* in 2015.

In this study, we have considered the molecular structures of 19 monocarboxylic acids ranging from C2 – C20. To predict the thermodynamic properties of these monocarboxylic acids we have obtained the most relevant topological indices and developed curvilinear regression models. Shafiei (2015) established the values for the indices of Randic, Balaban, Szeged, and Harary for monocarboxylic acids. Havare (2019) analyzed QSPR models, to predict the thermodynamic characteristics of monocarboxylic acids using the forgotten topological index, forgotten coindex, max-min Rodeg index, and inverse sum Rodeg index.

Many graph polynomials have been proposed to compute various topological indices. The Hosoya polynomial (Hosoya 1988) is the most well-known polynomial to calculate distance-based topological indices such as the Wiener index and hyper Wiener index. The M-polynomial (Deutsch & Klavzar, 2015) is one of several algebraic polynomials published in 2015 that can be used to calculate a variety of degree-based topological indices. Recently, Mondal *et al.* (2021) proposed the neighbourhood M- polynomial. Their attention was on the neighbourhood indices that were based on degrees. The Padmakar-Ivan polynomial (PI polynomial) was initially

introduced by Ashrafi *et al.* (2006) who also studied a few of its features. Our  $\mathcal{DE}$ -Polynomial can be used to compute diameter eccentricity based and hyper diameter eccentricity based topological indices (Deepalakshmi & Desikan, 2023).

The following describes the structure of the paper: In the diameter eccentricity based and hyper diameter eccentricity based indices section, we present some fundamental concepts related to the newly introduced polynomial and indices. The Methodology and Illustration section presents the edge partition methodology for computing the  $\mathcal{DE}$ -Polynomial for nineteen linear saturated monocarboxylic acids. An illustration for deriving the  $\mathcal{DE}$ -Polynomial and the proposed indices for propanoic acid is also presented in this section. The curvilinear regression analysis of the monocarboxylic acid section shows the regression analysis of the indices vis-à-vis their thermodynamic properties to identify the best fit models. We discover that the cubic regression models, validated thorough  $R^2$  and RMSE values, are the best fit models to predict the thermodynamic characteristics of monocarboxylic acids studied in this paper.

#### Diameter eccentricity based and hyper diameter eccentricity based indices

Let  $G$  be a simple, finite and connected graph with  $V(G)$  as the vertex set and  $E(G)$  as the edge set. Let  $d_p$  be the degree of a vertex  $p$  in  $G$  and  $\varepsilon_p$  the eccentricity of the vertex  $p$ . Let  $\Delta(G)$  and  $\delta(G)$  be the maximum and minimum degrees of the vertices of  $G$ , respectively.

**Definition 1.** (Deutsch & Klavzar, 2014). The eccentricity index for a graph  $G$  is defined as

$$\varepsilon(G) = \sum_{p,q \in E} [\varepsilon_p + \varepsilon_q] \quad \dots(1)$$

where  $\varepsilon_p$  denotes the eccentricity of the vertex  $p$ .

The Revan vertex degree of  $p$  in  $G$  is defined as  $r_p = \Delta(G) + \delta(G) - d_p$  (Kulli, 2017, 2018). Based on this definition, we introduce a new type of vertex degree known as diameter eccentricity based vertex degree of  $p$  in  $G$  as

$$d\varepsilon_p = D(G) + 1 - \varepsilon_p$$

where  $D(G)$  is the diameter of the graph  $G$ .

Example:

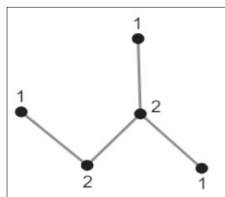


Figure 1:  $\mathcal{DE}$  –values for the molecular graph of propanoic acid  $\mathcal{P}$

The eccentricity of a vertex is a measure of its centrality. Diameter, on the other hand, may be considered as a measure of the spread of the graph. Our diameter eccentricity based vertex degree incorporates both these measures and specifies the relevance of a vertex in relation to the entire graph. Diameter eccentricity based and hyper diameter eccentricity based indices for each connected graph  $G$  are determined using the newly introduced polynomial named  $\mathcal{DE}$ -Polynomial, defined as follows,

$$\begin{aligned} \mathcal{DE}(G) &= \sum_{i \leq j} (\text{number of edges } pq \text{ such that} \\ &\quad d_{\mathcal{E}_p} = i, d_{\mathcal{E}_q} = j) \alpha^i \beta^j \\ &= \sum_{i \leq j} r\rho_{(i,j)} \alpha^i \beta^j f(\alpha, \beta) \end{aligned} \quad \dots(2)$$

where  $r\rho_{(i,j)}$  signifies the number of edges in the edge partitions determined by the diameter eccentricity based vertex degrees of the end vertices of the edges of the graph while  $\alpha$  and  $\beta$  are variables. Our  $\mathcal{DE}$ -Polynomial is a function of  $\alpha$  and  $\beta$ . In Table 1 we present our indices as functions of  $d_{\mathcal{E}_p}$  and  $d_{\mathcal{E}_q}$ .

Table 1: Description of proposed indices

Indices	$f(d_{\mathcal{E}_p}, d_{\mathcal{E}_q})$
First $\mathcal{DR}\mathcal{E}$ Index ( $\mathcal{DR}_1\mathcal{E}$ )	$d_{\mathcal{E}_p} + d_{\mathcal{E}_q}$
Second $\mathcal{DR}\mathcal{E}$ Index ( $\mathcal{DR}_2\mathcal{E}$ )	$d_{\mathcal{E}_p} * d_{\mathcal{E}_q}$
First Hyper $\mathcal{DR}\mathcal{E}$ Index ( $H\mathcal{DR}_1\mathcal{E}$ )	$(d_{\mathcal{E}_p} + d_{\mathcal{E}_q})^2$
Second Hyper $\mathcal{DR}\mathcal{E}$ Index ( $H\mathcal{DR}_2\mathcal{E}$ )	$(d_{\mathcal{E}_p} * d_{\mathcal{E}_q})^2$

Using our  $\mathcal{DE}$ -polynomial, we can compute our diameter eccentricity based indices,  $\mathcal{DR}_1\mathcal{E}$  and  $\mathcal{DR}_2\mathcal{E}$ , as well as our hyper diameter eccentricity based indices,  $H\mathcal{DR}_1\mathcal{E}$  and  $H\mathcal{DR}_2\mathcal{E}$ . Table 2 shows the methodology for deriving our indices from the  $\mathcal{DE}$ -polynomial.

Table 2: Derivation of proposed indices from  $\mathcal{DE}$ -polynomial

Indices	Derivation from $\mathcal{DE}(G)$
$\mathcal{DR}_1\mathcal{E}$	$(\partial_\alpha + \partial_\beta)(\mathcal{DE}(G)) _{\alpha=1, \beta=1}$
$\mathcal{DR}_2\mathcal{E}$	$(\partial_\alpha * \partial_\beta)(\mathcal{DE}(G)) _{\alpha=1, \beta=1}$
$H\mathcal{DR}_1\mathcal{E}$	$(\partial_\alpha + \partial_\beta)^2(\mathcal{DE}(G)) _{\alpha=1, \beta=1}$
$H\mathcal{DR}_2\mathcal{E}$	$(\partial_\alpha * \partial_\beta)^2(\mathcal{DE}(G)) _{\alpha=1, \beta=1}$

In Table 2,

$$\partial_\alpha \mathcal{DE}(G) = \partial_\alpha f(\alpha, \beta) = \alpha \frac{\partial(f(\alpha, \beta))}{\partial \alpha},$$

$$\partial_\beta \mathcal{DE}(G) = \partial_\beta f(\alpha, \beta) = \beta \frac{\partial(f(\alpha, \beta))}{\partial \beta}$$

### METHODOLOGY AND ILLUSTRATION

We use the method of edge partitions and employ the newly introduced  $\mathcal{DE}$ -Polynomial to compute our results for the molecular graphs of monocarboxylic acids. Let  $r\rho_{(p,q)}$  denote the number of edges in the edge partition  $(d_{\mathcal{E}_p}, d_{\mathcal{E}_q})$  in the graph  $G$ . We make use of the diameter eccentricity based vertex degrees of the end vertices of the edges. The edge partitions for the 19-monocarboxylic acids are presented in Tables 3-21.

Table 3:  $\mathcal{DE}$  –Edge partitions of ethanoic acid

$(d_{\mathcal{E}_p}, d_{\mathcal{E}_q})$	(1,2)
$r\rho_{(p,q)}$	3

From Table 3 we observe that the edges of ethanoic acid can be divided into 1 partition based on the distance eccentricity based vertex degrees of the end vertices of the edges in the molecular graph of ethanoic acid.

Table 4:  $\mathcal{DE}$  –Edge partitions of propanoic acid

$(d_{\mathcal{E}_p}, d_{\mathcal{E}_q})$	(1,2)	(2,2)
$r\rho_{(p,q)}$	3	1

From Table 4 we observe that the edges of propanoic acid can be divided into 2 partitions based on the distance eccentricity based vertex degrees of the end vertices of the edges in the molecular graph of propanoic acid.

**Table 5:**  $\mathcal{DE}$  –Edge partitions of butanoic acid

$(d\varepsilon_p, d\varepsilon_q)$	(1,2)	(2,3)
$r\rho_{(p,q)}$	3	2

From Table 5 we observe that the edges of butanoic acid can be divided into 2 partitions based on the distance eccentricity based vertex degrees of the end vertices of the edges in the molecular graph of butanoic acid.

**Table 6:**  $\mathcal{DE}$  –Edge partitions of pentanoic acid

$(d\varepsilon_p, d\varepsilon_q)$	(1,2)	(2,3)	(3,3)
$r\rho_{(p,q)}$	3	2	1

From Table 6 we observe that the edges of pentanoic acid can be divided into 3 partitions based on the distance eccentricity based vertex degrees of the end vertices of the edges in the molecular graph of pentanoic acid.

**Table 7:**  $\mathcal{DE}$  –Edge partitions of hexanoic acid

$(d\varepsilon_p, d\varepsilon_q)$	(1,2)	(2,3)	(3,4)
$r\rho_{(p,q)}$	3	2	2

From Table 7 we observe that the edges of hexanoic acid can be divided into 3 partitions based on the distance eccentricity based vertex degrees of the end vertices of the edges in the molecular graph of hexanoic acid.

**Table 8:**  $\mathcal{DE}$  –Edge partitions of heptanoic acid

$(d\varepsilon_p, d\varepsilon_q)$	(1,2)	(2,3)	(3,4)	(4,4)
$r\rho_{(p,q)}$	3	2	2	1

From Table 8 we observe that the edges of heptanoic acid can be divided into 4 partitions based on the distance eccentricity based vertex degrees of the end vertices of the edges in the molecular graph of heptanoic acid.

**Table 9:**  $\mathcal{DE}$  –Edge partitions of octanoic acid

$(d\varepsilon_p, d\varepsilon_q)$	(1,2)	(2,3)	(3,4)	(4,5)
$r\rho_{(p,q)}$	3	2	2	2

From Table 9 we observe that the edges of octanoic acid can be divided into 4 partitions based on the distance eccentricity based vertex degrees of the end vertices of the edges in the molecular graph of octanoic acid.

**Table 10:**  $\mathcal{DE}$  –Edge partitions of nonanoic acid

$(d\varepsilon_p, d\varepsilon_q)$	(1,2)	(2,3)	(3,4)	(4,5)	(5,5)
$r\rho_{(p,q)}$	3	2	2	2	1

From Table 10 we observe that the edges of nonanoic acid can be divided into 5 partitions based on the distance eccentricity based vertex degrees of the end vertices of the edges in the molecular graph of nonanoic acid.

**Table 11:**  $\mathcal{DE}$  –Edge partitions of decanoic acid

$(d\varepsilon_p, d\varepsilon_q)$	(1,2)	(2,3)	(3,4)	(4,5)	(5,6)
$r\rho_{(p,q)}$	3	2	2	2	2

From Table 11 we observe that the edges of decanoic acid can be divided into 5 partitions based on the distance eccentricity based vertex degrees of the end vertices of the edges in the molecular graph of decanoic acid.

**Table 12:**  $\mathcal{DE}$  –Edge partitions of undecanoic acid

$(d\varepsilon_p, d\varepsilon_q)$	(1,2)	(2,3)	(3,4)	(4,5)	(5,6)	(6,6)
$r\rho_{(p,q)}$	3	2	2	2	2	1

From Table 12 we observe that the edges of Undecanoic acid can be divided into 6 partitions based on the distance eccentricity based vertex degrees of the end vertices of the edges in the molecular graph of undecanoic acid.

**Table 13:**  $\mathcal{DE}$  –Edge partitions of dodecanoic acid

$(d\varepsilon_p, d\varepsilon_q)$	(1,2)	(2,3)	(3,4)	(4,5)	(5,6)	(6,7)
$r\rho_{(p,q)}$	3	2	2	2	2	2

From Table 13 we observe that the edges of dodecanoic acid can be divided into 6 partitions based on the distance eccentricity based vertex degrees of the end vertices of the edges in the molecular graph of dodecanoic acid.

**Table 14:**  $\mathcal{DE}$  –Edge partitions of tridecanoic acid

$(d\varepsilon_p, d\varepsilon_q)$	(1,2)	(2,3)	(3,4)	(4,5)	(5,6)	(6,7)	(7,7)
$r\rho_{(p,q)}$	3	2	2	2	2	2	1

From Table 14 we observe that the edges of tridecanoic acid can be divided into 7 partitions based on the distance eccentricity based vertex degrees of the end vertices of the edges in the molecular graph of tridecanoic acid.

**Table 15:**  $\mathcal{DE}$  –Edge partitions of tetradecanoic acid

$(d\varepsilon_p, d\varepsilon_q)$	(1,2)	(2,3)	(3,4)	(4,5)	(5,6)	(6,7)	(7,8)
$r\rho_{(p,q)}$	3	2	2	2	2	2	2

From Table 15 we observe that the edges of tetradecanoic acid can be divided into 7 partitions based on the distance eccentricity based vertex degrees of the end vertices of the edges in the molecular graph of tetradecanoic acid.

**Table 16:**  $\mathcal{DE}$  –Edge partitions of pentadecanoic acid

$(d\varepsilon_p, d\varepsilon_q)$	(1,2)	(2,3)	(3,4)	(4,5)	(5,6)	(6,7)	(7,8)	(8,8)
$r\rho_{(p,q)}$	3	2	2	2	2	2	2	1

From Table 16 we observe that the edges of pentadecanoic acid can be divided into 8 partitions based on the distance eccentricity based vertex degrees of the end vertices of the edges in the molecular graph of pentadecanoic acid.

**Table 17:**  $\mathcal{DE}$  –Edge partitions of hexadecanoic acid

$(d\varepsilon_p, d\varepsilon_q)$	(1,2)	(2,3)	(3,4)	(4,5)	(5,6)	(6,7)	(7,8)	(8,9)
$r\rho_{(p,q)}$	3	2	2	2	2	2	2	2

From Table 17 we observe that the edges of hexadecanoic acid can be divided into 8 partitions based on the distance eccentricity based vertex degrees of the end vertices of the edges in the molecular graph of hexadecanoic acid.

**Table 18:**  $\mathcal{DE}$  –Edge partitions of heptadecanoic acid

$(d\varepsilon_p, d\varepsilon_q)$	(1,2)	(2,3)	(3,4)	(4,5)	(5,6)	(6,7)	(7,8)	(8,9)	(9,9)
$r\rho_{(p,q)}$	3	2	2	2	2	2	2	2	1

From Table 18 we observe that the edges of heptadecanoic acid can be divided into 9 partitions based on the distance eccentricity based vertex degrees of the end vertices of the edges in the molecular graph of heptadecanoic acid.

**Table 19:**  $\mathcal{DE}$  –Edge partitions of octadecanoic acid

$(d\varepsilon_p, d\varepsilon_q)$	(1,2)	(2,3)	(3,4)	(4,5)	(5,6)	(6,7)	(7,8)	(8,9)	(9,10)
$r\rho_{(p,q)}$	3	2	2	2	2	2	2	2	2

From Table 19 we observe that the edges of octadecanoic acid can be divided into 9 partitions based on the distance eccentricity based vertex degrees of the end vertices of the edges in the molecular graph of octadecanoic acid.

**Table 20:**  $\mathcal{DE}$  –Edge partitions of nonadecanoic acid

$(d\varepsilon_p, d\varepsilon_q)$	(1,2)	(2,3)	(3,4)	(4,5)	(5,6)	(6,7)	(7,8)	(8,9)	(9,10)	(10,10)
$r\rho_{(p,q)}$	3	2	2	2	2	2	2	2	2	1

From Table 20 we observe that the edges of nonadecanoic acid can be divided into 10 partitions based on the distance eccentricity based vertex degrees of the end vertices of the edges in the molecular graph of nonadecanoic acid.

**Table 21:**  $\mathcal{DE}$  –Edge partitions of eicosanoic acid

$(d\varepsilon_p, d\varepsilon_q)$	(1,2)	(2,3)	(3,4)	(4,5)	(5,6)	(6,7)	(7,8)	(8,9)	(9,10)	(10,11)
$r\rho_{(p,q)}$	3	2	2	2	2	2	2	2	2	2

From Table 21 we observe that the edges of eicosanoic acid can be divided into 10 partitions based on the distance eccentricity based vertex degrees of the end vertices of the edges in the molecular graph of eicosanoic acid.

**Illustration of  $\mathcal{DE}$ - polynomial and  $\mathcal{DE}$  indices for propanoic acid**

Let  $P$  denote the molecular graph of propanoic acid considered in Figure 1. It has 5 vertices and 4 edges.

Consider

$$\begin{aligned} \mathcal{DE}(P) &= \sum_{i \leq j} (r\rho_{(i,j)}) \alpha^i \beta^j \\ &= r\rho_{(1,2)} \alpha^1 \beta^2 + r\rho_{(2,2)} \alpha^2 \beta^2. \end{aligned}$$

Using the edge partitions given in Table 4, it is clear that  $r\rho_{(1,2)} = 3, r\rho_{(2,2)} = 1$ .

Applying the values in  $\mathcal{DE}(P)$  we derive the  $\mathcal{DE}$ -polynomial for propanoic acid as follows:

$$\mathcal{DE}(P) = 3\alpha^1 \beta^2 + 1\alpha^2 \beta^2$$

We now compute the diameter eccentricity based and hyper diameter eccentricity based indices of the molecular graph of propanoic acid  $P$  using  $\mathcal{DE}$ -Polynomial as follows:

$$\begin{aligned}
DR_1\varepsilon(P) &= (\partial_\alpha + \partial_\beta)(D\varepsilon(P))|_{\alpha=\beta=1} \\
&= (\partial_\alpha D\varepsilon(P) + \partial_\beta D\varepsilon(P))|_{\alpha=\beta=1} \\
&= (\partial_\alpha(f(\alpha, \beta)) + \partial_\beta(f(\alpha, \beta)))|_{\alpha=\beta=1} \\
&= ((\alpha \frac{\partial(3\alpha^1\beta^2+1\alpha^2\beta^2)}{\partial\alpha}) + (\beta \frac{\partial(3\alpha^1\beta^2+1\alpha^2\beta^2)}{\partial\beta}))|_{\alpha=\beta=1} \\
&= (9\alpha^1\beta^2 + 4\alpha^2\beta^2)|_{\alpha=\beta=1} = 13.
\end{aligned}$$

Similarly, the other three indices can be obtained as follows:

$$\begin{aligned}
DR_2\varepsilon(P) &= (\partial_\alpha * \partial_\beta)(D\varepsilon(P))|_{\alpha=\beta=1} \\
&= (\partial_\alpha * \partial_\beta)(f(\alpha, \beta))|_{\alpha=\beta=1} \\
&= (6\alpha^1\beta^2 + 4\alpha^2\beta^2)|_{\alpha=\beta=1} = 10.
\end{aligned}$$

$$\begin{aligned}
HDR_1\varepsilon(p) &= (\partial_\alpha + \partial_\beta)^2(D\varepsilon(P))|_{\alpha=\beta=1} \\
&= (\partial_\alpha + \partial_\beta)^2(f(\alpha, \beta))|_{\alpha=\beta=1} \\
&= (27\alpha^1\beta^2 + 16\alpha^2\beta^2)|_{\alpha=\beta=1} = 43.
\end{aligned}$$

$$\begin{aligned}
HDR_2\varepsilon(p) &= (\partial_\alpha * \partial_\beta)^2(D\varepsilon(P))|_{\alpha=\beta=1} \\
&= (\partial_\alpha * \partial_\beta)^2(f(\alpha, \beta))|_{\alpha=\beta=1} \\
&= (12\alpha^1\beta^2 + 16\alpha^2\beta^2)|_{\alpha=\beta=1} = 28.
\end{aligned}$$

Similarly, we can obtain the proposed index values for the other monocarboxylic acid.

### Curvilinear regression analysis of monocarboxylic acids

In this section, we will conduct a quantitative structure property relationship (QSPR) analysis on the topological

indices listed in Table 1 for the seven thermodynamic properties of monocarboxylic acids (Shafiei, 2015; Shafiei, 2016; Havare, 2019): Thermal energy (TE kcal/mol), constant heat capacity of gas (CV cal/mol K), entropy of gas (EGS cal/mol K), enthalpy of formation of liquid (EFL kJ/mol), enthalpy of combustion of liquid (ECL kJ/mol), enthalpy of sublimation (ES kJ/mol) and Enthalpy of vaporization (EV kJ/mol).

We perform curvilinear regression analysis to identify the best fit models for predicting the seven thermodynamic properties of monocarboxylic acids using our proposed topological descriptors. We have performed linear, quadratic and cubic regression analysis given by the following equations:

$$P = \tilde{\alpha}_1(TI) + \tilde{\gamma} \quad \dots(3)$$

$$P = \tilde{\alpha}_1(TI)^2 + \tilde{\alpha}_2(TI) + \tilde{\gamma} \quad \dots(4)$$

$$P = \tilde{\alpha}_1(TI)^3 + \tilde{\alpha}_2(TI)^2 + \tilde{\alpha}_3(TI) + \tilde{\gamma} \quad \dots(5)$$

where  $P$  is the thermodynamic property (dependent variable),  $\tilde{\gamma}$  is the regression model constant, and  $\tilde{\alpha}_i$ 's are the regression coefficients for the topological descriptors (TI), respectively.

We have derived and compared the linear, quadratic and cubic regression models based on  $R^2$  and RMSE values. We have taken into consideration models with  $R^2 \geq 0.8$  (as per International Academy of Mathematical Chemistry Guidelines).

We also performed  $\chi^2$ -goodness of fit test to validate our models. The hypotheses which we considered for checking the goodness of fit of the regression models are:

$H_0$  : Proposed regression model is a good fit.

$H_1$  : Proposed regression model is not a good fit.

We have computed the values of the proposed indices for the 19-monocarboxylic acids. Tables 22 and 23 show the computed values for the proposed indices and the thermodynamic properties of monocarboxylic acids, respectively.



**Table 22:** Topological descriptor values of monocarboxylic acids

Name	$DR_{1\varepsilon}$	$DR_{2\varepsilon}$	$HDR_{1\varepsilon}$	$HDR_{2\varepsilon}$
Ethanoic acid	9	6	27	12
Propanoic acid	13	10	43	28
Butanoic acid	19	18	77	84
Pentanoic acid	25	27	113	165
Hexanoic acid	33	42	175	372
Heptanoic acid	41	58	239	628
Octanoic acid	51	82	337	1172
Nonanoic acid	61	107	437	1797
Decanoic acid	73	142	579	2972
Undecanoic acid	85	178	723	4268
Dodecanoic acid	99	226	917	6500
Tridecanoic acid	113	275	1113	8901
Tetradecanoic acid	129	338	1367	12772
Pentadecanoic acid	145	402	1623	16868
Hexadecanoic acid	163	482	1945	23140
Heptadecanoic acid	181	563	2269	29701
Octadecanoic acid	201	662	2667	39340
Nonadecanoic acid	221	762	3067	49340
Eicosanoic acid	243	882	3549	63540

**Table 23:** Thermodynamic property values of monocarboxylic acids

Acids name	CV	ECL	EFL	EGS	ES	EV	TE
Ethanoic acid	13.442	875.16	483.5	67.558	46.3	49.7	44.38
Propanoic acid	17.767	1527.3	510.8	74.612	50	56.1	64.578
Butanoic acid	22.163	2183.5	533.9	81.713	54.9	62.9	84.565
Pentanoic acid	26.538	2837.8	558.9	87.271	58.2	69	104.607
Hexanoic acid	30.927	3494.3	581.8	94.058	63	75	124.667
Heptanoic acid	35.421	4146.9	608.5	101.646	64.8	81.7	144.655
Octanoic acid	39.911	4799.9	634.8	109.25	69.4	86.9	164.637
Nonanoic acid	44.399	5456.1	658	116.353	72.3	93.6	184.621
Decanoic acid	48.889	6079.3	713.7	123.676	76.3	100.8	204.604
Undecanoic acid	53.378	6736.5	736.2	130.987	78.9	106.7	224.587
Dodecanoic acid	57.867	7377	775.1	138.293	82.2	115.9	244.57
Tridecanoic acid	62.255	8024.2	807.2	145.633	84.9	121.2	264.554
Tetradecanoic acid	66.844	8676.7	834.1	152.932	87.7	130.2	284.537
Pentadecanoic acid	71.627	9327.7	862.4	162.308	91.4	136.5	304.405
Hexadecanoic acid	75.73	9977.2	892.2	167.564	94.5	144.3	324.571
Heptadecanoic acid	80.216	10624.4	924.4	174.86	100.7	159.6	344.556
Octadecanoic acid	84.704	11280.1	947.4	182.181	102.8	164.7	364.539
Nonadecanoic acid	89.192	11923.4	984.1	189.486	105	172.9	384.522
Eicosanoic acid	93.681	12574.2	1012.6	196.113	109.9	179.2	404.506

CV: constant heat capacity; ECL: enthalpy of combustion of liquid; EFL: enthalpy of formation of liquid; EGS: enthalpy of gas; ES: enthalpy of sublimation; EV: enthalpy of vaporization; TE: thermal energy

## RESULTS AND DISCUSSION

We observed that the cubic regression models were the best fit models with low RMSE values. From the cubic regression models, we concluded that the best index is  $DR_1\varepsilon$ .

### Best fit regression models

In this section we present the best fit cubic regression models based on  $DR_1\varepsilon$  for the seven thermodynamic properties of monocarboxylic acids.

$$CV = 5\varepsilon - 06 (DR_1\varepsilon)^3 - 0.0028(DR_1\varepsilon)^2 + 0.726(DR_1\varepsilon) + 9.004 \quad \dots(6)$$

$$ECL = 0.0008(DR_1\varepsilon)^3 - 0.4202(DR_1\varepsilon)^2 + 107.3 (DR_1\varepsilon) + 243.2 \quad \dots(7)$$

$$EFL = 2\varepsilon - 05 (DR_1\varepsilon)^3 - 0.0129(DR_1\varepsilon)^2 + 4.305 (DR_1\varepsilon) + 452.8 \quad \dots(8)$$

$$EGS = 7\varepsilon - 06 (DR_1\varepsilon)^3 - 0.0039(DR_1\varepsilon)^2 + 1.12 (DR_1\varepsilon) + 60.65 \quad \dots(9)$$

$$ES = 6\varepsilon - 06 (DR_1\varepsilon)^3 - 0.0028(DR_1\varepsilon)^2 + 0.6204(DR_1\varepsilon) + 43.3 \quad \dots(10)$$

$$EV = 4\varepsilon - 06 (DR_1\varepsilon)^3 - 0.0025(DR_1\varepsilon)^2 + 0.9176(DR_1\varepsilon) + 45.54 \quad \dots(11)$$

$$TE = 2\varepsilon - 05 (DR_1\varepsilon)^3 - 0.0128(DR_1\varepsilon)^2 + 3.29 (DR_1\varepsilon) + 24.98 \quad \dots(12)$$

Table 24: Statistical parameters for best fit model

Property	Curve equation	Best predictor	$R^2$	RMSE	$\chi^2$
CV	(6)	$DR_1\varepsilon$	0.9991	0.8063	0.622021
ECL	(7)	$DR_1\varepsilon$	0.9989	131.8854	152.6476
EFL	(8)	$DR_1\varepsilon$	0.9990	5.7997	1.117039
EGS	(9)	$DR_1\varepsilon$	0.9993	1.2122	0.682761
ES	(10)	$DR_1\varepsilon$	0.9957	1.3837	0.725426
EV	(11)	$DR_1\varepsilon$	0.9972	2.3514	0.978772
TE	(12)	$DR_1\varepsilon$	0.9990	3.9413	19.14061

The table value for  $\chi^2$  with degrees of freedom 18 at the 5% and 1% levels of significance are 28.869 and 34.809, respectively. From Table 24, we see that the calculated  $\chi^2$  values of the seven thermodynamic properties, except one property (enthalpy of combustion of liquid), were less than the table value at both levels of significance. Thus, we accept all the models except the model for ECL.

Figures 2 to 5 depict the regression plots for the properties versus the best predictor index.

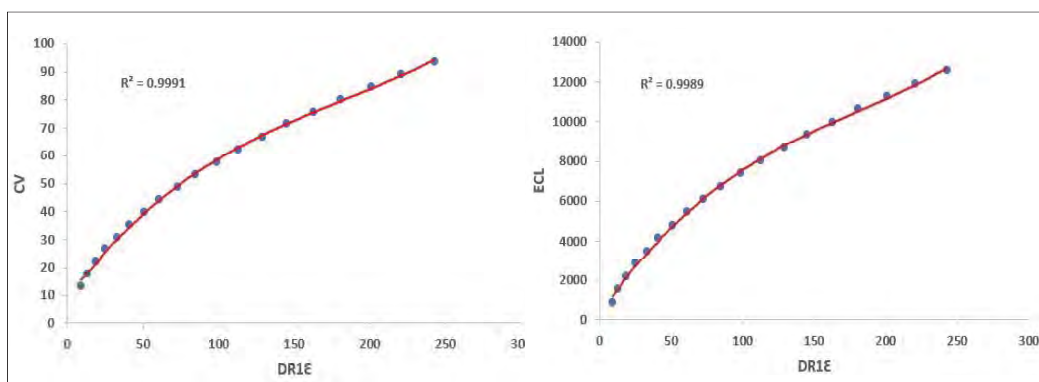


Figure 2: Cubic regression curve for  $CV$  and  $ECL$  against  $DR_1\varepsilon$

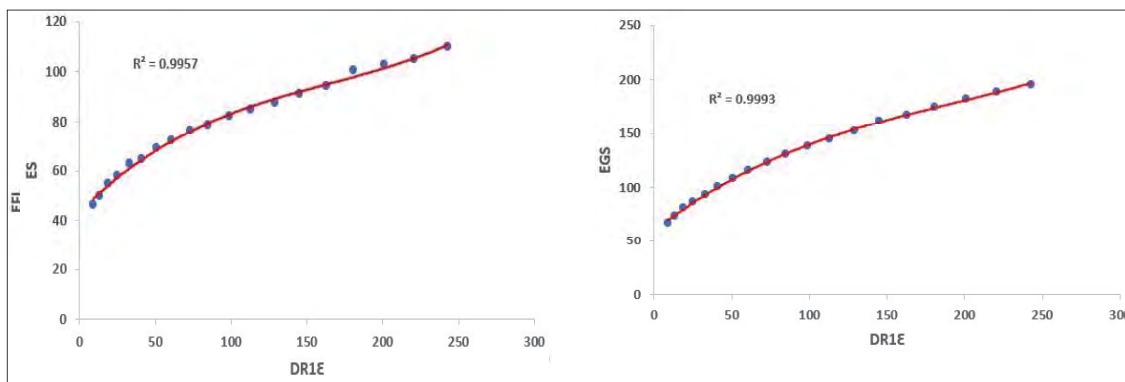


Figure 3: Cubic regression curve for  $FFI$  and  $EGS$  against  $DR_1\epsilon$

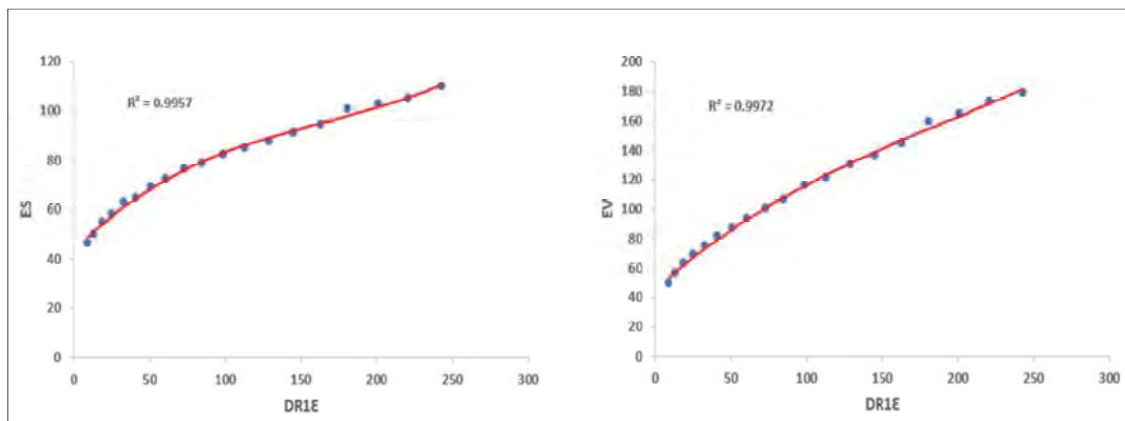


Figure 4: Cubic regression curve for  $ES$  and  $EV$  against  $DR_1\epsilon$

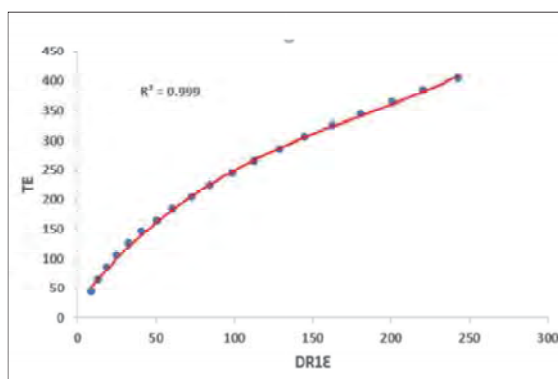


Figure 5: Cubic regression curve for  $TE$  against  $DR_1\epsilon$

## CONCLUSION

In this paper, we have utilized the newly introduced  $\mathcal{D}\epsilon$ -Polynomial to derive the diameter eccentricity based and hyper diameter eccentricity based topological descriptors for nineteen linear saturated monocarboxylic acids. We conducted a QSPR analysis on seven thermodynamic properties of monocarboxylic acids using our proposed indices. We conclude that the cubic regression models based on our index  $\mathcal{D}\mathcal{R}_1\epsilon$  provide the best fits for the thermodynamic properties in terms of  $R^2$  and RMSE values. We also conducted chi-square goodness-of-fit tests to determine the statistical significance of our proposed models. The tests showed that the cubic regression models were a good fit for six of the thermodynamic properties, with the exception of enthalpy of combustion of liquid (ECL).

## REFERENCES

- Ashrafi, A. R., Manoochehrian, B., & Yousefi-Azari, H. (2006). On the PI polynomial of a graph. *Utilitas Mathematica*, 71, 97-108.
- Badea, G. I., & Radu, G. L. (Eds.). (2018). *Carboxylic acid: key role in life sciences*. Intech. <http://doi.org/10.5772/intechopen.688350>
- Baev, A. K. (2012). *Specific intermolecular interactions of organic compounds*. Springer Science & Business Media. <http://doi.org/10.1007/978-3-642-21622-0>
- Baig, A. Q., Imran, M., & Ali, H. (2015). On topological indices of poly oxide, poly silicate, DOX, and DSL networks. *Canadian Journal of Chemistry*, 93(7), 730-739. <https://dx.doi.org/10.1139/cjc-2014-0490>
- Bajaj, S., Sambhi, S. S., & Madan, A. K. (2005). Topological models for prediction of anti-HIV activity of acylthiocarbamates. *Bioorganic and Medicinal Chemistry*, 13(9), 3263-3268. <https://doi.org/10.1016/j.bmc.2005.02.033>
- Basavanagoud, B., & Jakkannavar, P. (2020). M-polynomial and degree-based topological indices of graphs. *Electronic Journal of Mathematical Analysis and Applications*, 8(1). <https://doi.org/10.21608/ejmaa.2020.312808>
- Das, K. C. (2010). Atom-bond connectivity index of graphs. *Discrete Applied Mathematics*, 158(11), 1181-1188. <https://doi.org/10.1016/j.dam.2010.03.006>
- Deutsch, E., & Klavžar, S. (2014). M-polynomial and degree-based topological indices. arXiv preprint. <https://arxiv.org/10.48550/arXiv.1407.1592>
- Ghorbani, M., & Hosseinzadeh, M. A. (2012). A new version of Zagreb indices. *Filomat*, 26(1), 93-100. <https://doi.org/10.2298/FIL1201093G>
- Gutman, I., Tošović, J., Radenković, S., & Marković, S. (2012). On atom-bond connectivity index and its chemical applicability. *Indian Journal of Chemistry*, 51(5), 690-694.
- Gutman, I., & Das, K. C. (2004). The first Zagreb index 30 years after. *MATCH Communication in Mathematical and in Computer Chemistry*, 50(1), 83-92.
- Havare, Ö. Ç. (2019a). Determination of some thermodynamic properties of monocarboxylic acids using multiple linear regression. *Bitlis Eren Üniversitesi Fen Bilimleri Dergisi*, 8(2), 466-471. <https://doi.org/10.17798/bitlisfen.500500>
- Havare, O. C. (2019b). QSPR analysis with curvilinear regression modeling and topological indices. *Iranian Journal of Mathematical Chemistry*, 10(4), 331-341. <https://doi.org/10.22052/IJMC.2019.191865.1448>
- Hosoya, H. (1988). On some counting polynomials in chemistry. *Discrete Applied Mathematics*, 19(1-3), 239-257. [https://doi.org/10.1016/0166-218X\(88\)90017-0](https://doi.org/10.1016/0166-218X(88)90017-0)
- Kirman, S. A. K., Ali, P., & Azam, F. (2021). Topological indices and QSPR/QSAR analysis of some antiviral drugs being investigated for the treatment of COVID-19 patients. *International Journal of Quantum Chemistry*, 121(9), e26594. <https://doi.org/10.1002/qua.26594>
- Kulli, V. R. (2018). Hyper-Revan indices and their polynomials of silicate networks. *International Journal of Current Research in Science and Technology*, 4(3), 17-21.
- Kulli, V. R. (2017). Revan indices of oxide and honeycomb networks. *International Journal of Mathematics and its Applications*, 55, 7.
- Mondal, S., De, N., Siddiqui, M. K., & Pal, A. (2020). Topological properties of para-line graph of some convex polytopes using neighborhood M-polynomial. *Biointerface Research In Applied Chemistry*, 11(3), 9915-9927. <https://doi.org/10.33263/BRIAC113.99159927>
- Sarkarai, D., & Desikan, K. (2023). QSPR/QSAR analysis of some eccentricity based topological descriptors of antiviral drugs used in COVID-19 treatment via  $\mathcal{D}\epsilon$ -polynomials. *Mathematical Biosciences and Engineering*, 20(9), 17. <https://doi.org/10.3934/mbe.2023769>
- Shafiei, F. (2015). Relationship between topological indices and thermodynamic properties and of the monocarboxylic acids applications in QSPR. *Iranian Journal of Mathematical Chemistry*, 6(1), 15-28. <https://doi.org/10.22052/IJMC.2015.8944>
- Shafiei, F. (2016). Quantitative structure-property relationship to predict quantum properties of monocarboxylic acids by using topological indices. *Journal of Physical and Theoretical Chemistry*, 13(3), 227-235.
- Wiener, H. (1947). Correlation of heats of isomerization, and differences in heats of vaporization of isomers, among the paraffin hydrocarbons. *Journal of the American Chemical Society*, 69(11), 2636-2638. <https://doi.org/10.1021/ja01203a022>
- Yuan, Y., Zhou, B., & Trinajstić, N. (2010). On geometric-arithmetic index. *Journal of Mathematical Chemistry*, 47, 833-841. <https://doi.org/10.1007/s10910-009-9603-8>

## RESEARCH ARTICLE

### Graph Theory

# Structural brain network topology in migraine vs. healthy subjects: A graph theory study

ADI Amarasinghe<sup>1</sup>, DIH Wijewickrama<sup>1</sup>, IS De Fonseka<sup>1</sup>, MAD Lawanya<sup>1</sup>, WNS Fernando<sup>1</sup>, DAD Wishwanthi<sup>1</sup>, G Senanayake<sup>2</sup>, S Pushpakumara<sup>3</sup> and WM Ediri Arachchi<sup>1\*</sup>

<sup>1</sup> Department of Radiography and Radiotherapy, Faculty of Allied Health Sciences, General Sir John Kotelawala Defence University, Ratmalana, Sri Lanka.

<sup>2</sup> Department of Radiology, University Hospital, General Sir John Kotelawala Defence University, Ratmalana, Sri Lanka.

<sup>3</sup> Department of Neurology and Neurosurgery, University Hospital, General Sir John Kotelawala Defence University, Ratmalana, Sri Lanka.

Submitted: 12 November 2023; Revised: 11 July 2024; Accepted: 28 July 2024


**Abstract:** There is compelling evidence that migraine is associated with a decline in grey matter in the brain. We postulate that these changes might affect the architecture of the structural brain networks and normal wiring leading to altered functioning of the brain. Therefore, our goal was to compare the global brain network topology of patients with migraines and healthy subjects using grey matter structural networks. The study involved 45 patients with migraine and 46 healthy subjects. 3D, T1-weighted brain images were obtained using a 3 Tesla MRI scanner. Images were preprocessed, and grey matter volume images were generated. Group-level structural connectivity matrices were created using Pearson correlation, and the matrices were binarized by applying a series of sparsity thresholds to compute global network topologies. According to the between-group results, patients with migraines showed increases in small-worldness and global efficiency while local efficiency and synchronization did not differ significantly between patients and healthy subjects ( $p < 0.05$ ). Assortativity values were widely dispersed across different levels of sparsity and were significantly higher in the healthy network compared to the migraine network at sparsities of 0.4 and 0.5 ( $p < 0.05$ ). Furthermore, as network sparsity increased, there was a noticeable trend towards a hierarchy property among patients. According to our findings, patients with migraines exhibit better integration and poorer segregation of information processing in the human brain. Graph theory-based approach provides valuable information on network topological metrics in migraine.

**Keywords:** Graph theory, grey matter, migraine, neuroimaging, structural networks.

## INTRODUCTION

Migraine is defined as a common, disabling, primary brain disorder characterized by recurrent pulsating and throbbing pain in the head accompanied by symptoms such as nausea, sensitivity to light, sound, or scent and vomiting (Simon, 2018). Some believe that it is a neurological disorder affecting gastrointestinal and autonomic functionalities (Planchuelo-Gómez *et al.*, 2020) while others believe that it is a neurovascular disorder that is related to dilation and constriction of blood vessels in the head (Kim *et al.*, 2019). Approximately 15% of the global population suffers from migraine and statistically around 19% of females and 11% of males are affected (Vos *et al.*, 2012).

Structural neuroimaging has brought novel insights in evaluating brain changes in migraine. The findings from this approach have been used to enhance the understanding of the pathophysiology of migraine and to illustrate the potential consequences and risks linked to migraine. Several studies on magnetic resonance imaging (MRI) based neuroanatomy, conducted using voxel-based morphometry (VBM) and surface-based morphometry (SBM) techniques, reveal that repetitive migraine attacks could alter the structural volume and thickness of the brain, particularly in the grey matter (GM) regions (Jia & Yu, 2017; Zhang *et al.*, 2017).

\* Corresponding authors ([wasmadushanka@kdu.ac.lk](mailto:wasmadushanka@kdu.ac.lk);  <https://orcid.org/0000-0003-3750-8070>)



This article is published under the Creative Commons CC-BY-ND License (<http://creativecommons.org/licenses/by-nd/4.0/>). This license permits use, distribution and reproduction, commercial and non-commercial, provided that the original work is properly cited and is not changed in anyway.

It is believed that abnormalities in the networks of the brain may underlie cognitive and behavioral deficits in migraine. Therefore, it is crucial to investigate how the structural network arrangement in the brains of migraine sufferers are affected by structural brain changes. Additionally, studying how the topological characteristics of the brain networks could correspond to the pathophysiology of migraine is important (Lerch *et al.*, 2006; Power *et al.*, 2010).

Graph theory can visually represent the brain network architecture and provides a valuable method for assessing the architecture of large-scale brain networks. This is done by calculating a summary of connectivity matrices that describe the network's properties (Wang *et al.*, 2020). The above technique sheds new light on the mechanisms of neurological disorders and helps in the discovery of new imaging biomarkers for neurological disease diagnosis.

We hypothesize that migraine could affect the amount of grey matter in the brain. This in turn may alter the structural network connection between different areas of the brain leading to changes in network topological properties in the brains of migraine sufferers. Therefore, analyzing structural brain MRI images using graph theory to identify key differences of network attributes of those with migraine could significantly benefit its diagnosis. However, these studies are largely absent.

## MATERIALS AND METHODS

### Subjects

This study was conducted on 45 chronic migraine patients (35 females;  $39.69 \pm 11.1$  years) and 46 healthy controls (28 females;  $37.57 \pm 12.12$  years). The most appropriate research design was a case - control study. The study was approved by the Ethics Review Committee of the Faculty of Medicine, General Sir John Kotelawala Defence University (KDU), Sri Lanka and in accordance with the current version of the Declaration of Helsinki (World Medical Association, 2001). The patients were chosen from the neurology and neurosurgery unit of the University Hospital, KDU, and confirmed as migraine subjects (interictal phase) by skilled consultant neurologists using the International Classification of headache disorders criteria (ICHD-3) and a neurological examination. The imaging data were obtained from the MR imaging database of the Department of Radiology, University Hospital, KDU. The control group with healthy brains were selected by an experienced radiologist from

the same database who underwent MRI scans of brains and confirmed them as healthy. All subjects were above 18 years of age.

### Magnetic resonance image acquisition

Brain MRI scans were performed by a 3 Tesla scanner (Ingenia, Philips Healthcare, The Netherlands), using an 8-channel head coil. The following parameters were used in a turbo field echo (TFE) sequence to obtain three-dimensional (3D), T1-weighted images: repetition time (TR) = 8.2 ms; echo time (TE) = 3.8 ms; TFE factor = 150; flip angle (FA) = 8°; the field of view (FOV) = 240 mm × 240 mm; matrix = 240 × 222; slice thickness = 1 mm; gap = 0 mm; Multi-shot mode sagittal slices and acquisition time = 329 s.

### Image preprocessing

All images were examined for consistent orientation and pre-processed using the CAT12 and SPM 12 toolboxes. A Spatial Adaptive Non-Local Means filter was used to adjust bias fields, normalize intensity, and eliminate image noise. Skull stripping was done using the adaptive probability region growing (APRG) approach. The preprocessed images were then subjected to VBM analysis using CAT12.

### Computing grey matter volumes using voxel-based morphometry (VBM)

Preprocessed images were spatially normalized to the same stereotactic space (Montreal Neurological Institute (MNI) space) and each brain was separated into GM, WM, and CSF tissue classes. Spatial smoothing was applied to the modulated GM volume images of each subject utilizing an isotropic Gaussian kernel with an 8-mm full-width at half-maximum width (FWHM).

### Grey matter network construction

Smoothed grey matter volumes were concatenated to develop 4D volumes for each group. The GREYNA toolkit was used to develop brain structural networks and global network topology metrics. The entire brain was parcellated into 90 cortical and subcortical anatomical regions using an automated anatomical labeling (AAL) atlas excluding the cerebellum. Then the time courses were extracted from each anatomical region and averaged. Group level association matrices were then developed using Pearson correlation with a size of 90 × 90. In these matrices, nodes represent brain regions and edges represent brain connectivity.

### Network metrics computation

Binary adjacency matrices were developed (undirected graph), where an edge is drawn between two regional nodes if the Pearson correlation coefficient between them exceeds the threshold. We then systematically explored the properties of the graphs over a range of thresholds based on network sparsity resulting in fully connected small world graphs. This thresholding procedure was repeated for a series of thresholds ranging from 0.05 to 0.5 with an increment step of 0.05, resulting in 10 sparsity thresholds. We used the GREYNA toolkit to compute global network topological metrics such as small-worldness, global efficiency, local efficiency, assortativity, synchronization and hierarchy. Above metrics were compared with those of random networks to determine their level non-randomness.

### Statistical analysis

The gender ratio was compared using the Pearson chi-square test while the differences in age were analyzed using the two-sample t-test.

The two-sample t-test between groups was performed to detect the differences in grey matter volumes. Next, the statistical significance of between-group differences in the global network measures was determined using a non-parametric permutation test with 1000 iterations. For each randomly assigned group, an association matrix was created. The correlation matrices were then thresholded at different network sparsities to create the binary adjacency matrices. The network metrics were computed for each network at every density. A permutation distribution of differences was created under the null hypothesis. The actual between-group difference in network metrics was then placed in the corresponding permutation distribution and its percentile position was used to compute a two-tailed p value. Multiple comparisons were automatically taken into consideration by the nonparametric permutation test ( $P < 0.05$ ) (Bruno, Hosseini, & Kesler, 2012).

Image processing steps are shown in Figure 1.

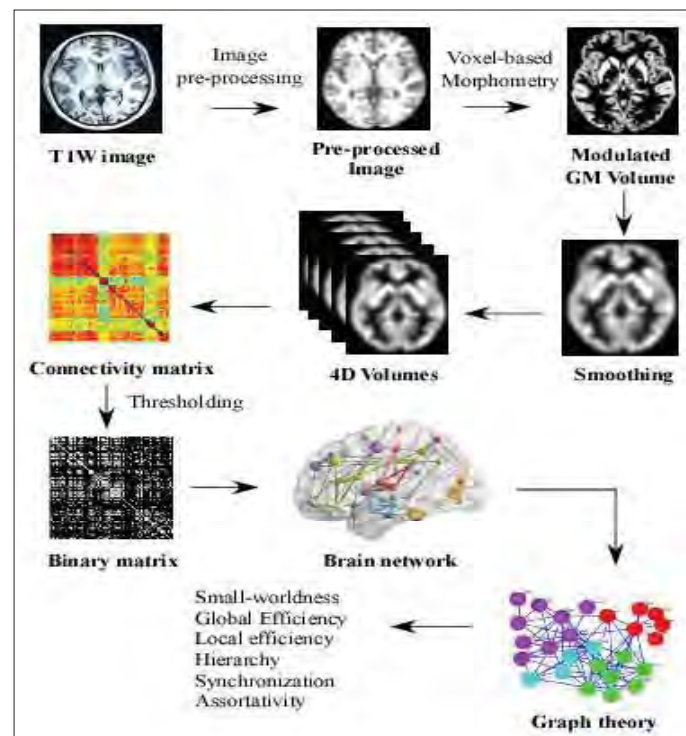


**Figure 1:** Schematic diagram of image pre-processing, brain network construction, and graph theoretical analysis using structural MRI data.

## RESULTS AND DISCUSSION

### Demographic data

No significant differences were detected in age (two sample t test,  $p=0.51$ ) or gender (Chi-square test,  $p=0.07$ ) between patients with migraines and healthy subjects.

### Grey matter volume changes detected between patients with migraine and healthy subjects

Widespread reductions in grey matter volume were found in migraine patients compared to healthy subjects covering both hemispheres. The results are shown in Figure 2 and summarized in supplemental Table 1.

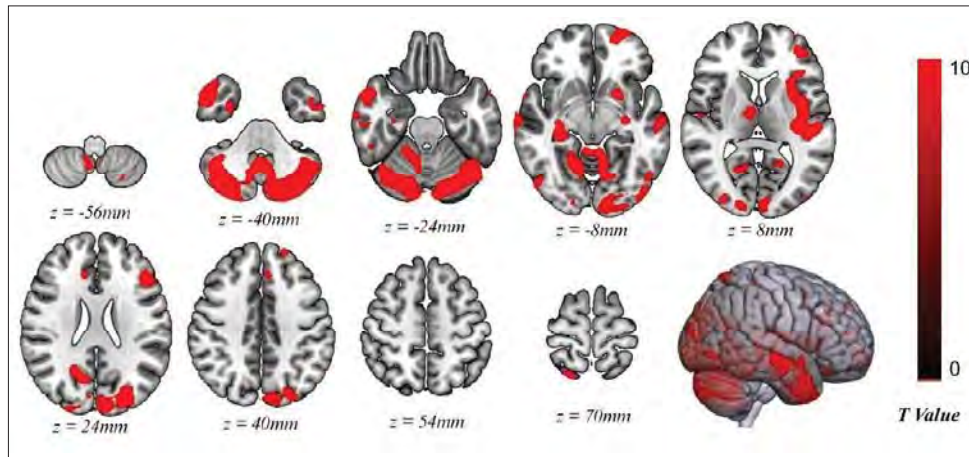


**Figure 2:** Regional gross volume reductions in patients with migraine compared to healthy subjects detected by Voxel-based morphometry. All detected areas, indicated in black to red (corresponding to T values obtained from two-sample t tests) had reduced volumes in patients with migraine compared with healthy subjects ( $p < 0.05$ , FWE corrected).

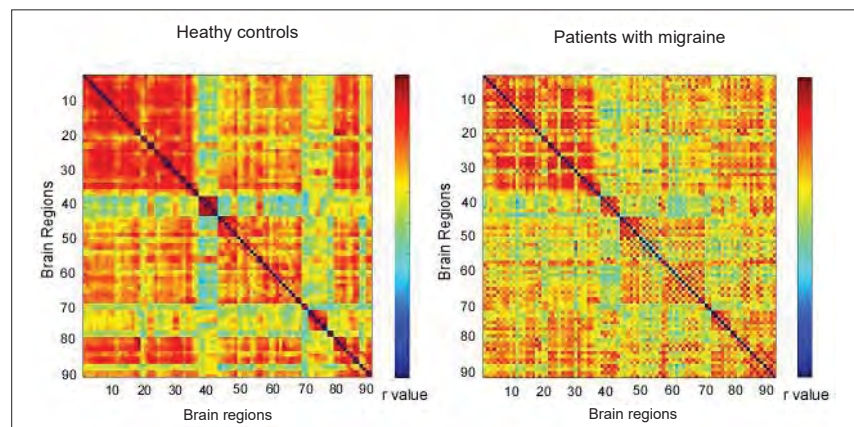


**Figure 3:** Pearson correlation-based association matrices of patients with migraine and healthy subjects. Each association matrix is composed of 90 x 90 edges. The grey matter (GM) regions of interest (ROIs) that were used in the research are denoted by the numbers 1 to 90 on the x- and y-axes. Correlation represents the strength of the structural connectivity (correlation coefficient,  $r$ ) for each edge connection.



Bilateral reductions in grey matter volume were found in the cerebellum, middle occipital gyrus, middle temporal gyrus, superior occipital gyrus, cuneus and parahippocampus. In addition, unilateral GM reductions were found in the right fusiform, left insula, right hippocampus, and left superior frontal regions.

### Comparison of structural connectivity matrices between healthy subjects and migraine patients

The association matrices within each group, without applying the threshold, are shown in Figure 3. In comparison to the correlation coefficient matrix of healthy subjects, the matrix belonging to migraineurs shows a more diverse distribution and has fewer condensed areas likely due to a lower number of edges.

### Global network measures (within-group)

Figure 4 shows the analysis results of global network measures across various network sparsities. Across a wide range of sparsities, the networks of both groups were organized in a small-worldness pattern ( $\sigma > 1$ ,  $\lambda \sim 1$ ,  $\gamma > 1$ ). Compared with patients, healthy subjects exhibited less small-worldness ( $\sigma$ ) (Figure 4a) and a less normalized clustering coefficient ( $\gamma$ ) (Figure 4c). However, migraine patients had a decreased normalized characteristic path length ( $\lambda$ ) (Figure 4b).

Both global efficiency (Eglob) (Figure 4d) and local efficiency (Eloc) (Figure 4e) showed a positive relationship with network sparsity threshold values. Local efficiencies of patients with migraine and healthy subjects were similar in all sparsities than global efficiencies. The assortativity values (Figure 4f) of the healthy were higher than the migraine patients from 0.25 to 0.5 network sparsity thresholds. Therefore, at high sparsities, the linking rate of nodes with similar number of edges was lower in migraine patients. Due to the indecisive data points, it was difficult to determine a relationship or clear separation between migraine patients and healthy subjects for synchronization (Figure 4g). Hierarchical organizations of migraine patients (Figure 4h) were found to be greater than those of healthy subjects at higher network sparsities and showed a positive correlation

with network sparsities.

### Global network measures (between-groups)

The grey matter networks of migraine brains had significantly more normalized clustering ( $\gamma$ ) at sparsities ranging from 0.2 to 0.5 ( $p < 0.05$ ; Figure 5c) when compared to the healthy subjects. The healthy network exhibited an overall tendency towards longer normalized path lengths ( $\lambda$ ) with significant differences from 0.05 to 0.5, with the exception of 0.1 across the whole range of sparsities ( $p < 0.05$ ; Figure 5b). Except 0.15 and 0.05, this pattern resulted in a substantially higher small-worldness ( $\sigma$ ) in the migraineurs than the healthy network sparsities from 0.1 to 0.5. (Figure 5a).

Patients with migraine exhibited significantly higher global efficiency (Eglob) in their network compared to healthy controls across sparsities ranging from 0.05 to 0.5, except for 0.4. ( $p < 0.05$ ; Figure 5d). Across the entire range of sparsities, we did not detect significant differences in migraine for local efficiency (Eloc), ( $p < 0.05$ ; Figure 5e) and the reported differences were distributed for both reduced and increased local efficiencies.

Assortativity values were largely dispersed among their sparsities and were considerably higher in the healthy network than in the migraine network at sparsities of 0.4 and 0.5 ( $p > 0.05$ ; Figure 5f).

There was no clear comparison in the synchronization of patients with migraine and healthy networks as the values were distributed within the confidence intervals at all levels of sparsities (Figure 5g). With increasing sparsity, the 95% CI boundaries showed a near-random behavior. This made it difficult for a reliable prediction for the identification of migraine patients based on synchronization properties.

There was a significant hierarchical network organization in migraine grey matter networks with network sparsity values ranging from 0.4 to 0.5 ( $p < 0.05$ ; Figure 5h). Therefore, as sparsity increases, there is a strong tendency to surpass the confidence interval for the hierarchical property.

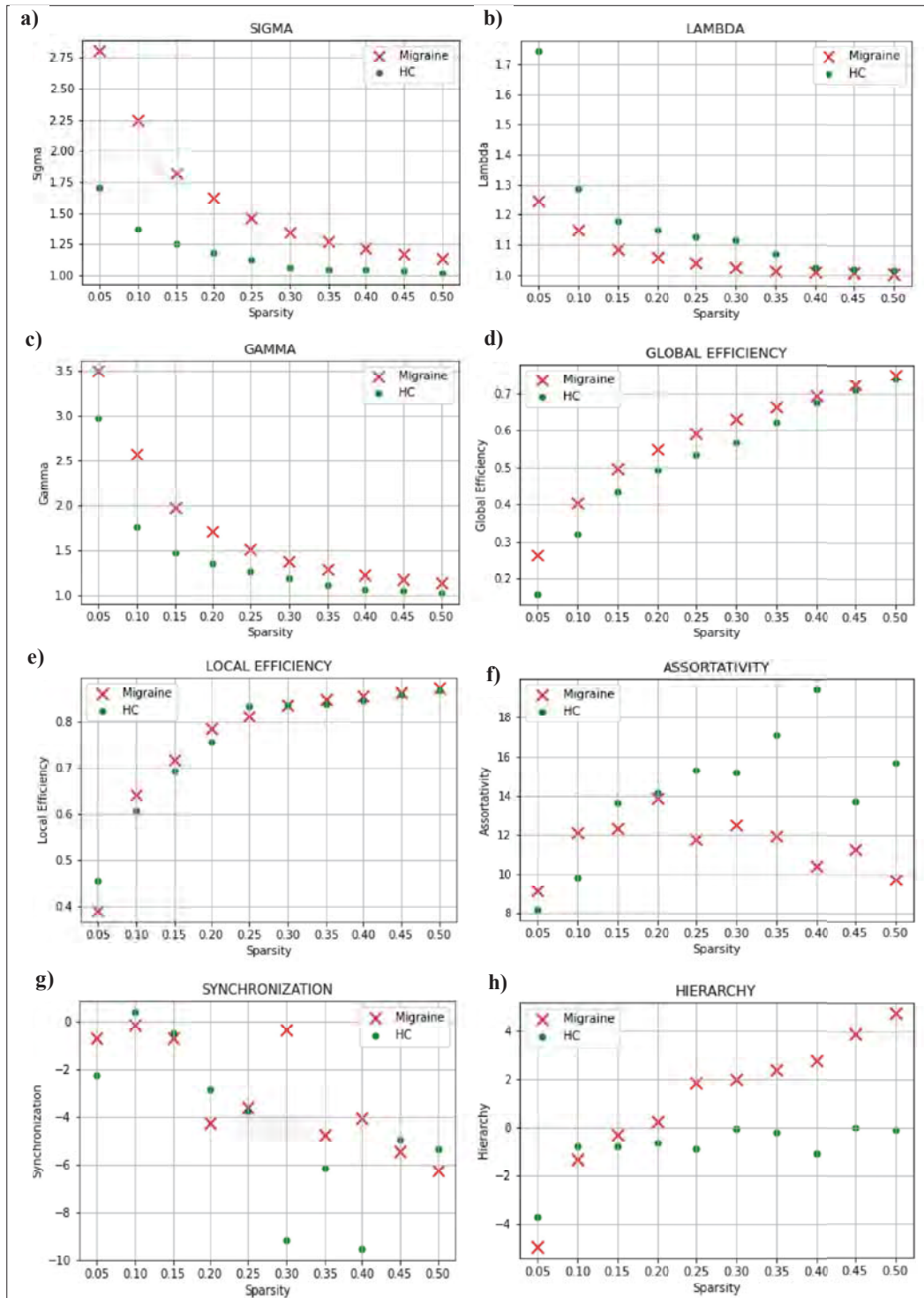


**Figure 4:** Changes in global network metrics of the patients with migraine and healthy subjects as a function of network density (0.05 – 0.5). (a) Small-worldness; (b) normalized path length; (c) normalized clustering coefficient; (d) global efficiency; (e) local efficiency; (f) assortativity; (g) synchronization and (h) hierarchy.

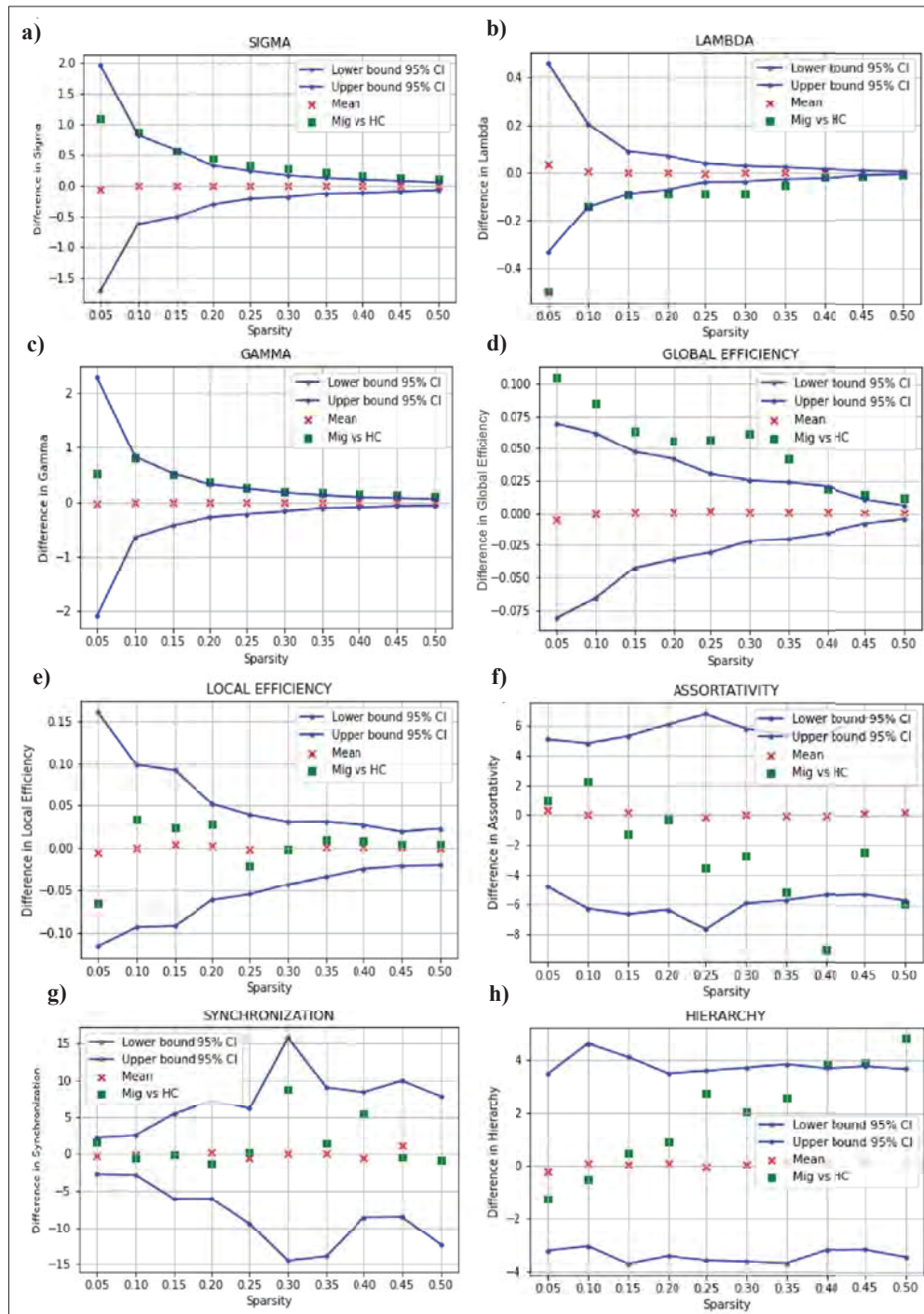


**Figure 5:** Differences in global network metrics between patients with migraine and healthy subjects as a function of network density (0.05 – 0.5). Between group differences are given in green squares and values that fall outside the confidence interval (blue lines, 95% confidence intervals) denote the densities at which the difference between the groups is significant. Positive numbers denote densities where patients’ values are higher than healthy subjects’ values, while negative values denote the reverse.

A comparison of grey matter between patients and healthy subjects revealed widespread reductions in grey matter volume. Grey matter volume reductions which were detected in our study include cerebellum, middle occipital, middle temporal, superior occipital, cuneus, and parahippocampus. These reductions have been reported in previous studies to varying extents (Valfrè *et al.*, 2007, Coppola *et al.*, 2017). However, compared to most of the literature our study reported several reductions in regional grey matter volume reductions unilaterally. These reductions were observed in the right fusiform, left insula, right hippocampus, right thalamus and left superior frontal regions (Cao *et al.*, 2022).

To our knowledge this would be the first study to compare the highest number of brain network metrics in the same study. The small-world property provides a structural substrate for both functional segregation and functional integration, which is the ratio of normalized clustering coefficient ( $\gamma$ ) to normalized characteristic path length ( $\lambda$ ) (Watts & Strogatz, 1998). If a network has a higher clustering tendency, it indicates a strong connection or exchange of information between a node and its neighbours. If a network has a long path length it means that information processing is delayed.

A study has been conducted to determine hierarchical changes of brain structural and functional networks using female migraine patients (Liu *et al.*, 2012). It was found that the global topology of the patients' structural and functional networks was aberrant compared to that of healthy subjects. There were greater mean clustering coefficients but no appreciable change in the shortest absolute path length. The small-world properties of grey matter volume correlation networks showed a numerically higher small-worldness in patients in, similar to our findings. In some studies migraine patients scored higher on cognitive tests than non-migraine patients (Wen *et al.*, 2016).

Local efficiency, also known as segregation, measures the efficiency of information exchange between adjacent nodes. It is calculated as the average nodal efficiency of all nodes in the graph considering only the neighboring node point and always excluding the node of interest (Cohen & D'Esposito, 2016). Global efficiency, or integration, measures the brain network's ability to transfer information among all nodes (parallel information transmission). It has been found that patients with chronic migraine had altered global network properties characterized by lower global and local efficiency (DeSouza *et al.*, 2020). In contrast to these findings, the global efficiency was found to be improved in migraineurs in the current study (Wen *et al.*, 2016).

It has specifically considered the existence of assortative type networks, which may have a significant effect on the function of networked systems. They are internally dense and externally sparse, maintaining the segregation of information processing (Newman, 2002; Bazinet *et al.*, 2023). To our knowledge, no evidence has been found to date regarding assortativity in relation to migraineurs. However, in this study, assortativity values were found to be significantly higher in the healthy network compared to the migraine network at sparsities of 0.4 and 0.5 with p-values less than 0.05. This proves that migraine disrupts the connections of nodes of similar quality in the brain network at those levels of sparsities.

Synchronization measures the likelihood of all nodes fluctuating in the same wave pattern (Xiang *et al.*, 2020). It is believed that small world routes and scale-free networks can achieve synchronizability more efficiently than standard graphs, random graphs and ideal constructive schemes (Barahona & Pecora, 2002; Nishikawa *et al.*, 2003). Other evidence shows that activity synchronizations between brain regions can play a critical role in cognitive integration and brain function (Varela *et al.*, 2001; Vuksanović & Hövel, 2014). However, we did not find changes in synchronization in our study.

Network hierarchy is one of the fundamental characteristics of the brain that demonstrates the hierarchical network structure of the brain. The main feature of a network hierarchy is the high connectivity within a hub's network but with less clustering. This type of network arrangement helps to report relationships among nodes and reduce wiring costs (Ravasz, 2002). Our results show that the hierarchical properties of migraine patients are increased with sparsity, and the values are significant when it reaches higher sparsity values.

Many studies have reported that migraineurs are reported to have the worst cognitive performance. However, it is not surprising that other studies have reported conflicting results, particularly in the interictal phase (Vuralli *et al.*, 2018). Therefore, more studies are warranted in the future to conclude on the pathophysiology of migraine at the network level.

There are three limitations to our study. First, the structural covariance network analysis was performed by correlating the grey matter volume across subjects without creating individual matrices for each subject. Second, we were unable to detect any associations between network measures and clinical parameters because we developed metrics at the group level network. Third, the study was retrospective and therefore we were unable to provide clinical data of patients.

## CONCLUSION

In summary, when compared to healthy subjects, the migraine group showed an altered network topology in the brain. This was characterized by an increase in small-worldness and global efficiency (integration) as well as a decreasing assortativity (segregation). These changes may alter functional demands in the brain of migraineurs' leading to distinct profiles of cooperative and competitive connections that underlie various different aspects of sensory, cognitive, and affective comorbidities.

## REFERENCES

- Barahona, M., & Pecora, L. M. (2002). Synchronization in small-world systems. *Physical Review Letters*, *89*(5). <https://doi.org/10.1103/physrevlett.89.054101>
- Bazinet, V., Hansen, J. Y., Vos de Wael, R., Bernhardt, B. C., van den Heuvel, M. P., & Misisic, B. (2023). Assortative mixing in micro-architecturally annotated brain connectomes. *Nature Communications*, *14*(1), 2850. <https://doi.org/10.1038/s41467-023-38585-4>
- Bruno, J., Hosseini, S. M. H., & Kesler, S. (2012). Altered resting state functional brain network topology in chemotherapy-treated breast cancer survivors. *Neurobiology of Disease*, *48*(3), 329–338. <https://doi.org/10.1016/j.nbd.2012.07.009>
- Cao, Z., Yu, W., Zhang, Z., Xu, M., Lin, J., Zhang, L., & Song, W. (2022). Decreased gray matter volume in the frontal cortex of migraine patients with associated functional connectivity alterations: A VBM and rs-FC study. *Pain Research and Management*, *2022*, 1–7. <https://doi.org/10.1155/2022/2115956>
- Cohen, J. R., & D'Esposito, M. (2016). The segregation and integration of distinct brain networks and their relationship to cognition. *Journal of Neuroscience*, *36*(48), 12083–12094. <https://doi.org/10.1523/jneurosci.2965-15.2016>
- Coppola, G., Petolicchio, B., Di Renzo, A., Tinelli, E., Di Lorenzo, C., Parisi, V., Serrao, M., Calistri, V., Tardioli, S., Cartocci, G., Ambrosini, A., Caramia, F., Di Piero, V., & Pierelli, F. (2017). Cerebral gray matter volume in patients with chronic migraine: correlations with clinical features. *The Journal of Headache and Pain*, *18*(1). <https://doi.org/10.1186/s10194-017-0825-z>
- DeSouza, D. D., Woldeamanuel, Y. W., Sanjanwala, B. M., Bissell, D. A., Bishop, J. H., Peretz, A., & Cowan, R. P. (2020). Altered structural brain network topology in chronic migraine. *Brain Structure & Function*, *225*(1), 161–172. <https://doi.org/10.1007/s00429-019-01994-7>
- Jia, Z., & Yu, S. (2017). Grey matter alterations in migraine: A systematic review and meta-analysis. *NeuroImage: Clinical*, *14*, 130–140. <https://doi.org/10.1016/j.nicl.2017.01.019>
- Kim, Y. S., Kim, M., Choi, S. H., You, S.-H., Yoo, R.-E., Kang, K. M., Yun, T. J., Lee, S.-T., Moon, J., & Shin, Y.-W. (2019). Altered vascular permeability in migraine-associated brain regions: Evaluation with dynamic contrast-enhanced MRI. *Radiology*, *292*(3), 713–720. <https://doi.org/10.1148/radiol.2019182566>
- Lerch, J. P., Worsley, K., Shaw, W. P., Greenstein, D. K., Lenroot, R. K., Giedd, J., & Evans, A. C. (2006). Mapping anatomical correlations across cerebral cortex (MACACC) using cortical thickness from MRI. *NeuroImage*, *31*(3), 993–1003. <https://doi.org/10.1016/j.neuroimage.2006.01.042>
- Liu, J., Zhao, L., Li, G., Xiong, S., Nan, J., Li, J., Yuan, K., von Deneen, K. M., Liang, F., Qin, W., & Tian, J. (2012). Hierarchical alteration of brain structural and functional networks in female migraine sufferers. *PLoS ONE*, *7*(12), e51250. <https://doi.org/10.1371/journal.pone.0051250>
- Newman, M. E. J. (2002). Assortative mixing in networks. *Physical Review Letters*, *89*(20). <https://doi.org/10.1103/physrevlett.89.208701>
- Nishikawa, T., Motter, A. E., Lai, Y.-C., & Hoppensteadt, F. C. (2003). Heterogeneity in oscillator networks: Are smaller worlds easier to synchronize? *Physical Review Letters*, *91*(1). <https://doi.org/10.1103/physrevlett.91.014101>
- Planchuelo-Gómez, Á., García-Azorín, D., Guerrero, Á. L., Rodríguez, M., Aja-Fernández, S., & de Luis-García, R. (2020). Gray matter structural alterations in chronic and episodic migraine: A morphometric magnetic resonance imaging study. *Pain Medicine*, *21*(11), 2997–3011. <https://doi.org/10.1093/pm/pnaa271>
- Power, J. D., Fair, D. A., Schlaggar, B. L., & Petersen, S. E. (2010). The development of human functional brain networks. *Neuron*, *67*(5), 735–748. <https://doi.org/10.1016/j.neuron.2010.08.017>
- Ravasz, E. (2002). Hierarchical organization of modularity in metabolic networks. *Science*, *297*(5586), 1551–1555. <https://doi.org/10.1126/science.1073374>
- Simon, R. P., Greenberg, D., & Aminoff, M. J. (2009). *Clinical Neurology*. McGraw Hill Professional.
- Valfrè, W., Rainero, I., Bergui, M., & Pinessi, L. (2007). Voxel-based morphometry reveals gray matter abnormalities in migraine. *Headache: The Journal of Head and Face Pain*, *48*(1), 109–117. <https://doi.org/10.1111/j.1526-4610.2007.00723.x>
- Varela, F., Lachaux, J.-P., Rodriguez, E., & Martinerie, J. (2001). The brainweb: Phase synchronization and large-scale integration. *Nature Reviews Neuroscience*, *2*(4), 229–239. <https://doi.org/10.1038/35067550>
- Vos, T., Flaxman, A. D., Naghavi, M., Lozano, R., Michaud, C., Ezzati, M., Shibuya, K., Salomon, J. A., Abdalla, S., Aboyans, V., Abraham, J., Ackerman, I., Aggarwal, R., Ahn, S. Y., Ali, M. K., AlMazroa, M. A., Alvarado, M., Anderson, H. R., Anderson, L. M., & Andrews, K. G. (2012). Years lived with disability (YLDs) for 1160 sequelae of 289 diseases and injuries 1990–2010: a systematic analysis

- for the Global Burden of Disease Study 2010. *The Lancet*, 380(9859), 2163–2196.  
[https://doi.org/10.1016/s0140-6736\(12\)61729-2](https://doi.org/10.1016/s0140-6736(12)61729-2)
- Vuksanović, V., & Hövel, P. (2014). Functional connectivity of distant cortical regions: Role of remote synchronization and symmetry in interactions. *NeuroImage*, 97, 1–8.  
<https://doi.org/10.1016/j.neuroimage.2014.04.039>
- Vuralli, D., Ayata, C., & Bolay, H. (2018). Cognitive dysfunction and migraine. *The Journal of Headache and Pain*, 19(1).  
<https://doi.org/10.1186/s10194-018-0933-4>
- Wang, L., Zou, L., Chen, Q., Su, L., Xu, J., Zhao, R., Shan, Y., Zhang, Q., Zhai, Z., Gong, X., Zhao, H., Tao, F., & Zheng, S. (2020). Gray matter structural network disruptions in survivors of acute lymphoblastic leukemia with chemotherapy treatment. *Academic Radiology*, 27(3), e27–e34.  
<https://doi.org/10.1016/j.acra.2019.04.010>
- Watts, D. J., & Strogatz, S. H. (1998). Collective dynamics of “small-world” networks. *Nature*, 393(6684), 440–442.
- Wen, K., Nguyen, N. T., Hofman, A., Ikram, M. A., & Franco, O. H. (2016). Migraine is associated with better cognition in the middle-aged and elderly: the Rotterdam Study. *European Journal of Neurology*, 23(10), 1510–1516.  
<https://doi.org/10.1111/ene.13066>
- World Medical Association (2001). World Medical Association Declaration of Helsinki. Ethical principles for medical research involving human subjects. *Bulletin of the World Health Organization*, 79(4), 373–374.  
<https://iris.who.int/handle/10665/268312>
- Xiang, J., Xue, J., Guo, H., Li, D., Cui, X., Niu, Y., Yan, T., Cao, R., Ma, Y., Yang, Y., & Wang, B. (2019). Graph-based network analysis of resting-state fMRI: test-retest reliability of binarized and weighted networks. *Brain Imaging and Behavior*, 14(5), 1361–1372.  
<https://doi.org/10.1007/s11682-019-00042-6>
- Zhang, J., Wu, Y.-L., Su, J., Yao, Q., Wang, M., Li, G.-F., Zhao, R., Shi, Y.-H., Zhao, Y., Zhang, Q., Lu, H., Xu, S., Qin, Z., Cui, G.-H., Li, J., Liu, J.-R., & Du, X. (2017). Assessment of gray and white matter structural alterations in migraineurs without aura. *The Journal of Headache and Pain*, 18(1).  
<https://doi.org/10.1186/s10194-017-0783-5>

## RESEARCH ARTICLE

### Electronics

# An electrical double-layer supercapacitor based on a biomass-activated charcoal electrode and ionic liquid with excellent charge-discharge cycle stability

GRA Kumara<sup>1\*</sup>, ADT Medagedara<sup>1</sup>, HW Gadiarachchi<sup>1</sup>, DGBC Karunarathne<sup>1</sup>, K Tennakone<sup>1</sup>, RMG Rajapakse<sup>2</sup> and TMWJ Bandara<sup>3</sup>

<sup>1</sup> National Institute of Fundamental Studies, Hantana Road, Kandy, Sri Lanka.

<sup>2</sup> Department of Chemistry, Faculty of Science, University of Peradeniya, Peradeniya, Sri Lanka.

<sup>3</sup> Department of Physics, Faculty of Science, University of Peradeniya, Peradeniya, Sri Lanka.

Submitted: 27 November 2023; Revised: 03 May 2024; Accepted: 04 July 2024


**Abstract:** Supercapacitors that exhibit high power density and safety are emerging as alternative energy storage devices. The construction and performance of a supercapacitor using the ionic liquid, triethylammonium thiocyanate, as the electrolyte and biomass-activated charcoal films as the electrode are described. Enhancements in both energy and power density were observed even for 10,000 charge-discharge cycles. The fabricated supercapacitor with ionic liquid and activated charcoal-based electrodes showed an impressive specific capacitance retention of 142% even after 10,000 cycles at a scan rate of 500 mV s<sup>-1</sup>, which is attributed to the clearing of ion conducting pathways and enhanced charge transport with increasing temperature. Impedance analysis confirmed the reduction of resistive losses with increasing cycle numbers. The initial energy and power densities of the Electrical double-layer capacitance (EDLC) were 0.926 W h kg<sup>-1</sup> and 5681 W kg<sup>-1</sup>, and they showed 42.2 % and 60.6 % increments after supercapacitors cycles. The study reveals low-cost biomass-based activated carbon electrodes and trimethylamine thiocyanate can be used to prepare supercapacitors with remarkable cycling performances.

**Keywords:** Activated carbon, supercapacitor, triethylammonium thiocyanate

## INTRODUCTION

The rapid increase in energy consumption is a major reason for many researchers to focus on finding sustainable energy sources and developing energy

conversion and storage techniques. Renewable energy sources such as wind, solar, hydropower and geothermal are promising resources to conserve degradable energy sources (Fridleifsson, 2001; Panwar *et al.*, 2011; Kumar *et al.*, 2016). However, the main issue with the utilization of most renewable energy sources is the intermittency of the energy supply. This can be overcome by using reliable energy storage technologies. The most common energy storage methods are batteries, supercapacitors, and H<sub>2</sub> storage (Scrosati & Garche, 2010; Lucia, 2014; Poonam *et al.*, 2019). When it comes to energy storage methods, energy density, power density, durability and long cycle life are some of the key factors that determine the quality of the device. Lithium-ion batteries (LIBs) are one of the most versatile devices to store energy. LIBs have a high energy density, but it has numerous drawbacks, including short cycle life, harmful compounds used in manufacturing, the inclusion of highly flammable substances and long charging time. Supercapacitors have certain characteristics, including quick charging, long cycle life, and high power density, which make them suitable for use in practical applications (Portet *et al.*, 2005; Brousse *et al.*, 2007). Hence, they appear to be one of the most promising replacements for batteries for certain applications. To enhance the practical viability of supercapacitors, improving energy density, durability, and cycle stability are the main areas of focus in ongoing supercapacitor research.

\* Corresponding author (kumara.as@nifs.ac.lk;  <https://orcid.org/0000-0001-9804-2652>)



This article is published under the Creative Commons CC-BY-ND License (<http://creativecommons.org/licenses/by-nd/4.0/>). This license permits use, distribution and reproduction, commercial and non-commercial, provided that the original work is properly cited and is not changed in anyway.

In supercapacitors the two main charge storage mechanisms are electrical double-layer capacitance and pseudo capacitance (Karthikeyan *et al.*, 2021). Electrical double-layer capacitance (EDLC) is based on charge accumulation at the electrode-electrolyte interface due to electrostatic forces, forming a double layer of charges. Carbon-based materials including carbon nanotubes, porous carbon, templated carbon, and activated carbon are commonly used as electrode materials for EDLC-type supercapacitors (Gambay *et al.*, 2001; Fuertes *et al.*, 2005; Pan *et al.*, 2010; Yin *et al.*, 2020). In pseudocapacitors, charge is stored through Faradaic reactions (Karthikeyan *et al.*, 2021). Conducting polymers and metal oxides are well-known electrode materials for pseudocapacitors (Chen *et al.*, 2014; Bryan *et al.*, 2016). In these materials, capacitive processes occur due to fast surface redox reactions, giving them capacitive properties; however, they show poor cyclability (Abruña *et al.*, 2008).

Two main functional components in a supercapacitor are the electrode and the electrolyte. Activated carbon-based electrodes offer higher cycle life in addition to their low cost. However, most of the activated carbons commercially available are produced from precursors derived from fossil fuels (Abioye & Ani, 2015). Attempting to use green carbon materials, which are agro-industrial waste in device applications gives several direct and indirect advantages. The utilization of biomass-derived activated carbon electrodes for supercapacitor fabrication reduces their production cost. The electrode material utilized in this work was fabricated using activated carbon powder made from coconut shells.

In general, ionic liquids offer many advantages over conventional aqueous electrolytes or volatile organic solvent-based electrolytes for the devices, though their conductivity is lower than that of liquid electrolytes. To fabricate EDLC with longer cycle life and stability, such ionic liquids are an ideal candidate. Trimethylamine thiocyanate (TAT) is primarily used as a crystal growth inhibitor of CuI crystal to improve the performance in solid-state dye-sensitized solar cells (Kumara *et al.*, 2002). However, novel TAT-based electrolytes have not been widely studied as an electrolyte for supercapacitors. One of the main issues in batteries and supercapacitors is performance degradation with charge-discharge cycling. In a previous study, it was demonstrated that there is a possibility of utilizing TAT ionic liquid as an electrolyte for the activated carbon-based supercapacitor (Medagedara *et al.*, 2022). In this study, our primary objective is to investigate the performance degradation issue associated with charge-discharge cycling in supercapacitors. Specifically, we investigate the potential

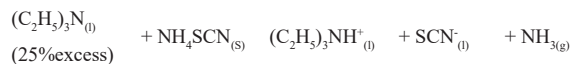
of utilizing trimethylamine thiocyanate (TAT) ionic liquid as an electrolyte to enhance the electrochemical performance and cycle stability of activated carbon-based supercapacitors. Through a series of electrochemical tests including cyclic voltammetry (CV), galvanostatic charge-discharge (GCD), and electrochemical impedance spectroscopy (EIS), we aim to demonstrate the effectiveness of TAT-based electrolytes in improving both energy and power density, even over an extended cycling period of 10,000 charge-discharge cycles. The study reveals a 142 % capacity improvement after 10,000 cycles, which is a good value for a biomass-derived carbon electrode-based supercapacitor that shows an extremely high power density of 9124 W kg<sup>-1</sup> (Abioye & Ani, 2015; Dos Reis *et al.*, 2020; Patel *et al.*, 2021).

## MATERIALS AND METHODS

Titanium plates with dimensions of 2cm×1cm×0.45mm were used as current collector plates. Ammonium thiocyanate (NH<sub>4</sub>SCN, 98.0% (m/m) assay) and dichloromethane (CH<sub>2</sub>Cl<sub>2</sub>, 99.5% (m/m) assay) were purchased from Fujifilm Wako Pure Chemical Corporation, Osaka, Japan. Triethylamine (C<sub>6</sub>H<sub>15</sub>N, 99.0% purity) was purchased from Daejung Chemicals, Siheung-si, South Korea. Hexane (C<sub>6</sub>H<sub>14</sub>, 99.0% purity) was procured from Sigma-Aldrich, St. Louis, Missouri, United States. Polyvinylpyrrolidone (PVP) was obtained from Research-Lab Fine Chem Industries, Mumbai, India. Medium retention filter papers (model-F1001, retention range 10-13µm) were obtained from Chmlab, Barcelona, Spain.

### Ionic liquid electrolyte triethylammonium-thiocyanate

To begin with, the moisture in ammonium thiocyanate was removed by placing it on top of a hot plate for 30 min at 90 °C. Anhydrous ammonium thiocyanate was then combined with triethylamine, (triethylamine in 25% excess of the stoichiometric quantity). Thereafter, the mixture was heated for 3 min at 120 °C. It is necessary to keep heating the mixture until all of the NH<sub>3</sub> has been expelled from the mixture. Triethylammonium-thiocyanate is formed during this reaction, as shown in the equation below.



(C<sub>2</sub>H<sub>5</sub>)<sub>3</sub>NH<sup>+</sup><sub>(l)</sub> and SCN<sup>-</sup><sub>(l)</sub> ions separate from the reaction mixture as these ions are insoluble in triethylamine. The



ionic component settles at the bottom of the vessel due to its high molecular mass. The ionic components including unreacted  $\text{NH}_4\text{SCN}$  and  $(\text{C}_2\text{H}_5)_3\text{N}$  were then extracted from the mixture.

The solution was washed with hexane three times to ensure that there was no unreacted  $(\text{C}_2\text{H}_5)_3\text{N}$  present; excess dichloromethane was then added to the resultant product. If there was any unreacted  $\text{NH}_4\text{SCN}$  present in the solution a white-colored precipitate would be formed. The supernatant was obtained by centrifugation and the excess dichloromethane was removed by evaporation to obtain colorless triethylammonium-thiocyanate. Finally, the colorless ionic liquid was dried under vacuum for 1 h at  $70^\circ\text{C}$ , followed by  $30^\circ\text{C}$  for 5 d (Konno *et al.*, 2004; Medagedara *et al.*, 2022).

### Activated carbon electrodes

Initially, coconut shells were thoroughly cleaned by removing fibrous debris from the surface followed

by burning in a box furnace under minimum-oxygen conditions. The burnt coconut shells were heated at  $900^\circ\text{C}$  for 20 min in a box furnace. The charcoal was then dumped into a distilled water bath to quench, dried, and finally disc-milled into a fine powder (Keppetipola *et al.*, 2021). This activated carbon sample was characterized using an X-ray ( $\lambda=1.5406 \text{ \AA}$ ) diffractometer (XRD; RigakuUltimaIV X-ray powder diffractometer) and Raman Spectroscopy.

The following steps were taken to create activated carbon-coated current collector plates: an activated carbon layer was formed on the surface of the current collector plate using the spray pyrolysis method. To accomplish this, a suspension of activated carbon and PVP was prepared consisting of 1 g of activated carbon powder, 0.05 g of PVP, and 10 ml of isopropanol. The suspension was then sonicated for 10 min. As shown in Figure 1, the resulting solution was sprayed onto titanium current collector plates. The solution-coated current collector plates were then sintered at  $200^\circ\text{C}$  for 20 min.

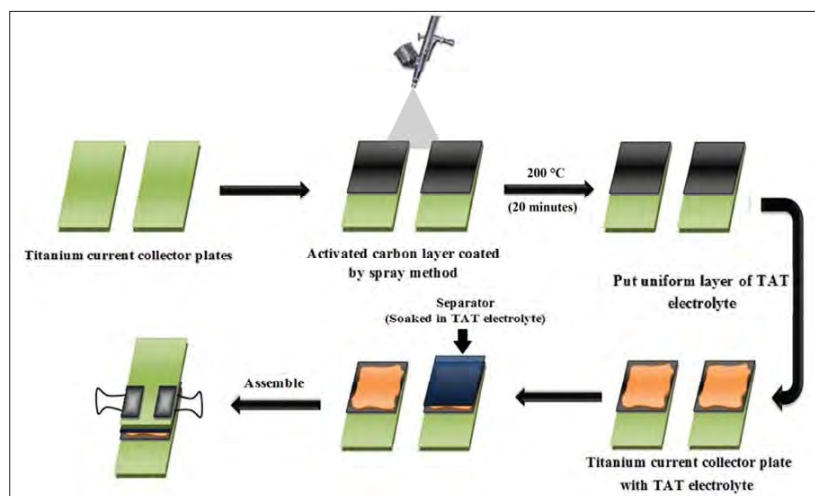


Figure 1: Schematic diagram for the process of making a supercapacitor with TAT electrolyte.

### Fabrication of supercapacitors and characterization

Initially, fabricated electrodes were wetted with TAT electrolyte and sandwiched with a membrane that can serve as a separator between the electrodes. This membrane is permeable to the ions present in the electrolyte. The characterization of the supercapacitor was done using a Metrohm Autolab Potentiostat/Galvanostat. Current collector plates were connected to the Metrohm Autolab

Potentiostat/Galvanostat and the cyclic voltammograms (CV) readings were taken. To investigate the stability of the cell, 10,000 CV cycles were performed at a scan rate  $500 \text{ mV s}^{-1}$  potential and retention of capacitance was checked. The following equation was used to calculate the specific capacitance of the cell:

$$C = \frac{1}{2m} \frac{\int IdV}{\Delta V \frac{dV}{dt}} \quad \dots(1)$$

Where  $m$  is the mass of the activated carbon layer on the electrode surface,  $I$  is the current,  $\Delta V$  is the potential range used, and  $dV/dt$  is the potential scan rate used for the CV experiment.

The following equations were used to calculate the energy density and the power density of the supercapacitor:

$$E = \frac{1}{2} CV^2 \quad \dots(2)$$

$$P = \frac{V^2}{4R} \quad \dots(3)$$

Where  $C$  is the specific capacitance of the supercapacitor,  $R$  is the equivalent series resistance for the two electrode system, and  $V$  is the potential window.

## RESULTS AND DISCUSSION

### Characterization of activated carbon

XRD peaks indicate the amorphous form of activated carbon. Based on the positions of the broad peaks at  $2\theta = 23.5^\circ$  and  $43.7^\circ$ , they are consistent with diffractions from the (002) and (100) planes of the activated carbon standard XRD pattern. These peaks correspond to d-spacing of 3.8 and 2.1 Å (JCPDS 75-1621).

As seen in Figure 2b, two primary bands are visible in the Raman spectra of activated carbon powder. The bands

at  $1350\text{ cm}^{-1}$  and  $1600\text{ cm}^{-1}$  correspond to the D and G bands, respectively. The two 1<sup>st</sup> order Raman shifts in the  $1000\text{--}1700\text{ cm}^{-1}$  range are related to  $sp^2$  hybridized carbon in the material. The graphite band (G band) is concerned with perfect graphitic vibration modes, whereas the defect band (D band) is concerned with disordered graphite (Islam *et al.*, 2019; Thapliyal *et al.*, 2022). The presence of disordered  $sp^2$ -hybridized carbons is evident from the broader D band in Figure 2b. By comparing the intensity values of the bands  $I_D/I_G$  where  $I_D$  and  $I_G$  are the intensities of the D and G bands, respectively, we can measure the level of structural defects, the degree of graphitization or decreased crystallinity of the activated transition from  $sp^2$  hybridization to  $sp^3$  carbon sample (Cuesta *et al.*, 1994). The sample's  $I_D/I_G$  ratio is 0.84, which indicates there are fewer structural deficiencies in this substance.

### Characterization of supercapacitor

The cyclic voltammograms, taken at 5, 10, 20, 50, 100, 250 and  $500\text{ mV s}^{-1}$  are shown in Figure 3. The nearly rectangular behavior of the CVs shown, particularly for slow scan rates, indicates the EDLC-type charge storage mechanism in the SCs. It can be observed that the rectangular shape of the CV curve is lost when the scan rate increases, which can be due to the relaxation effects of deep penetrating charge carriers. In other words, slow scan rates give sufficient time for deep penetrating charge carriers to diffuse into pores thereby enhancing the effective area of the double layer, which finally contributes to improve the capacitance. Therefore, specific capacitance decreases with an increasing scan rate due to polarization relaxation as shown in Table 1.

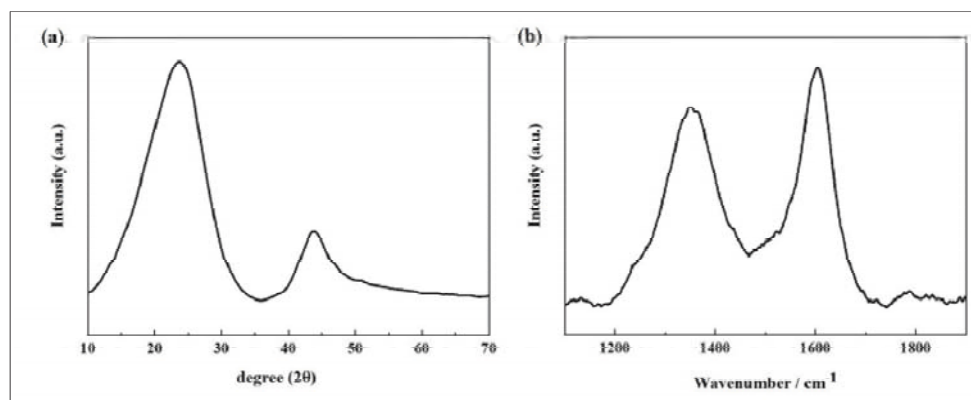


**Figure 2:** X-ray diffraction spectra of the activated carbon powder derived from coconut shell charcoal, and (b) Raman spectrum of the activated carbon powder derived from coconut shell charcoal.

Additionally, it can be observed that the cycling current increases with the increasing CV scan rate without reaching a plateau as seen for the lower rates. This may be a result of a rapid increase in potential difference.

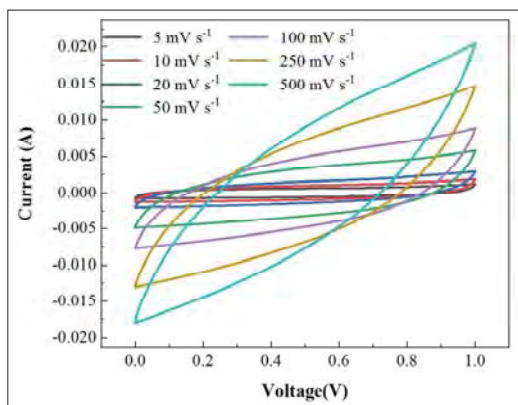


Figure 3: The cyclic voltammograms taken at different scan rates.

Table 01: The specific capacitance values of the prepared SC at different scan rates

Scan rate (mV s <sup>-1</sup> )	Area under the CV curve (mV A)	Specific capacitance (F g <sup>-1</sup> )
5	1.47	36.8
10	2.67	33.5
20	4.72	29.5
50	8.74	21.9
100	10.9	13.5
250	20.2	10.1
500	26.7	6.68

The study of the cycle life of supercapacitors is important to investigate the stability of devices. Figure 4a shows CV curves of initial and 10,000<sup>th</sup> scan cycles measured at 500 mV s<sup>-1</sup> scan rate, which was used to investigate the cycle stability of the fabricated supercapacitors. In this study, a rather high scan rate of 500 mV s<sup>-1</sup> is used to check the device functionality under rapid charging and discharging. A previous study demonstrated that a high capacity retention of approximately 94.4% can be achieved when using a scan rate of 100 mV s<sup>-1</sup> for 1000 cycles (Medagedara *et al.*, 2022). In the present study, cells were tested with a large number of scan cycles but at higher scan rates. Figure 4b shows selected CVs for the 1<sup>st</sup>, 1000<sup>th</sup>, 2000<sup>th</sup>, 3000<sup>th</sup>, 4000<sup>th</sup>, 5000<sup>th</sup>, 6000<sup>th</sup>, 7000<sup>th</sup>, 8000<sup>th</sup>, 9000<sup>th</sup> and 10,000<sup>th</sup> cycle for the supercapacitor with TAT electrolyte at a scan rate of 500 mV s<sup>-1</sup>. The enclosed area of the CV curve gradually increases with the number of CV scan cycles indicating the specific capacitance increment as given in Table 2.

The CV curve in Figure 4b shows an increase in the current flows through the device during charging and discharging with increasing number of cycles. The electrodes and the electrolyte, can heat up due to increased current, resulting in improved charge transport dynamics in the electrolyte and electrode as the number of cycles increases. Further, this can also be attributed to a reduction in internal resistance due to the large number of consecutive cycle repetitions conducted with a relatively high rate, which clears ion moving paths on the electrode surface. In addition, the initial CV cycles can clean or pretreat the electrode (McCarthy *et al.*, 2014). This effect can finally improve the polarization of charge carriers resulting in an enhancement of the specific capacitance. Such variations, that take place during the

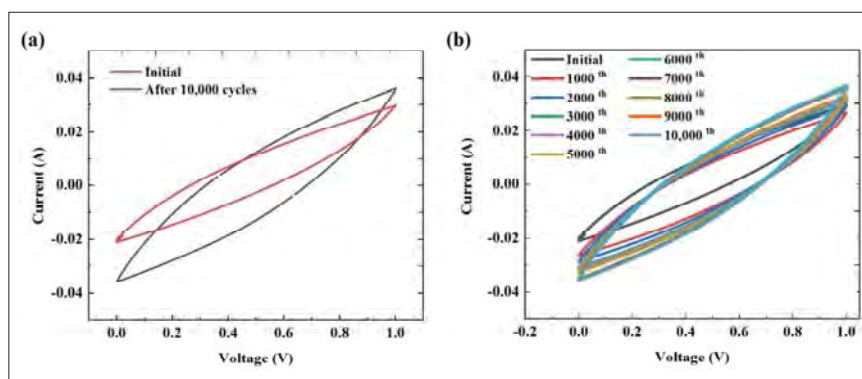


Figure 4: (a) Comparison of the initial and final cyclic volumetric changes of the cell after 10,000 cycles. (b) Selected cyclic voltammograms of 1000 steps 500 mV s<sup>-1</sup>.

cycling process, are further analyzed by taking EIS and GCD measurements before and after taking CVs.

**Table 2:** Variation of specific capacitance value and the enclosed area of the cyclic voltammograms (CV) with the number of cycles.

Cycle number	Area under the CV curve (mV A)	Specific capacitance (F g <sup>-1</sup> )
1 <sup>st</sup>	26.7	6.67
1000 <sup>th</sup>	27.4	6.85
2000 <sup>th</sup>	29.8	7.46
3000 <sup>th</sup>	32.2	8.06
4000 <sup>th</sup>	33.1	8.29
5000 <sup>th</sup>	34.4	8.60
6000 <sup>th</sup>	37.6	9.39
7000 <sup>th</sup>	37.2	9.30
8000 <sup>th</sup>	37.4	9.35
9000 <sup>th</sup>	37.5	9.38
10,000 <sup>th</sup>	37.9	9.48

Figure 5 illustrates the GCD curves of the TAT supercapacitor at various current densities. Figure 6 shows the GCD curve taken at 1 A g<sup>-1</sup> current density for 4 cycles before and after taking 10,000 CV cycles. During the discharge state, a small initial ohmic drop is caused by the cell's series resistance. The key factor causing this loss is the initial resistive loss at the electrode-electrolyte interface (Qu *et al.*, 2016). In addition, a significant decrease in the ohmic drop is observed, which can be attributed to decreased resistance. The triangular symmetric shape of GCD depicts (apart from the initial IR drop) the EDLC behavior of the supercapacitor (Vaquero *et al.*, 2013). After the cycling process (Figure 6b), the supercapacitor's charging and discharging time is longer compared to that of fresh cells (Figure 6a); this can be attributed to the improved charge storage capacity of the cells with continued CVs. Since the current density is constant, it takes a longer time to charge and discharge more charges. Figure 6 and the data given in Table 3 serve as evidence of the excellent stability of the EDLC fabricated in this study even after 10,000 CV cycles.

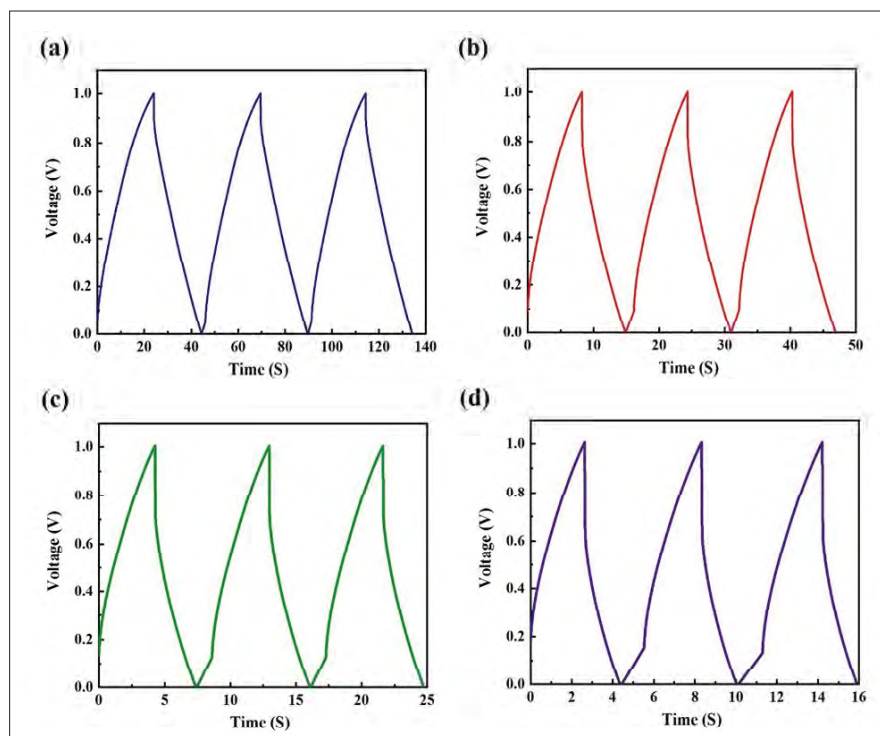


**Figure 5:** The GCD curves of the TAT supercapacitor at different current densities (a) 0.5, (b) 1.0, (c) 1.5, and (d) 2.0 A g<sup>-1</sup>.

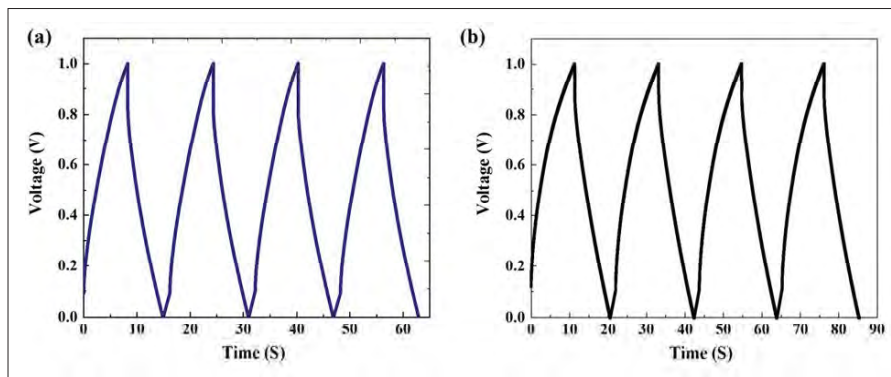


**Figure 6:** The GCD curves at 1 A g<sup>-1</sup> current density, (a) before taking 10,000 cycles, and (b) after taking 10,000 cycles.

**Table 3:** Specific capacitance, energy density and power density values of the supercapacitor before and after 10,000 cycles.

Number of cycles	Area under the CV curve (mV A)	Specific capacitance (F g <sup>-1</sup> )	Energy density (W h kg <sup>-1</sup> )	Power density (W kg <sup>-1</sup> )
Initial	26.7	6.670	0.926	5681
After 10000	37.9	9.481	0.951	9124

Equations (2) and (3) were used to calculate the energy and power densities of the supercapacitor. Table 3 shows the area under the CV curve, specific capacitance, energy density and power density of the supercapacitor before and after taking CVs for 10,000 cycles. More importantly, all of these parameters had higher values after 10,000 CV cycles compared to their initial values. The results reveal the excellent stability of the supercapacitors prepared, which can be mainly attributed to the selection of appropriate electrolyte and electrode materials.

Figure 7 depicts the variation of specific capacitance and the energy density of the EDLC with the number of cycles. As shown in Figure 7, there is a significant increase in specific capacitance from 6.67 F g<sup>-1</sup> to 9.48 F g<sup>-1</sup> in the first 6000 cycles. However, after 6000 cycles, the specific capacitance has become stable at around 9.40 F g<sup>-1</sup>. From the initial state to the final state, the specific capacitance of the supercapacitor increases with the number of cycles, from 6.67 F g<sup>-1</sup> to 9.48 F g<sup>-1</sup>, indicating a 142% enhancement compared to its initial value. The initial energy and power densities of the EDLC are 0.926 W h kg<sup>-1</sup> and 5681 W kg<sup>-1</sup>, and they increased to

1.317 W h kg<sup>-1</sup> and 9124 W kg<sup>-1</sup>, respectively, after 10,000 cycles. These were 42.2 % and 60.6 % increments of energy and power densities of the EDLC, respectively.

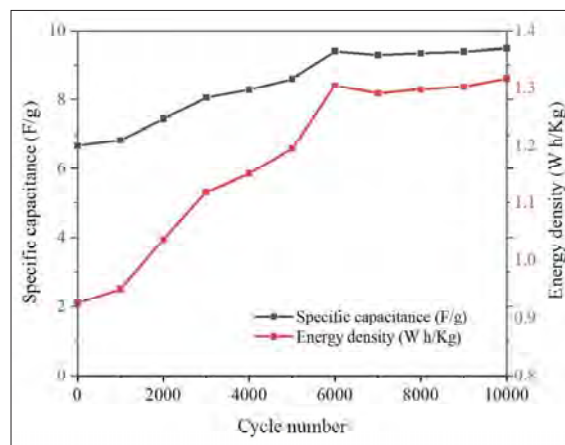


**Figure 7:** Variation of specific capacitance and the energy density values with the number of cycles.

Figure 8a shows the graph of the imaginary part ( $Z''$ ) of the impedance against the real part ( $Z'$ ) of the cell after 0, 2000, 4000 and 10,000 cycles. The shift of the curves towards lower  $Z'$  values as the number of cycles increases is evidence of a decrease in transport resistance. The real axis intercept of the curve indicates the equivalent series resistance (ESR) of the supercapacitor, which decreases with the number of cycles from 11  $\Omega$  to 6.8  $\Omega$  in this study. The EIS data proves the reduction of resistance with the increasing number of cycles. This reduction in internal resistance is due to the large number of cycle repetitions conducted with a relatively high rate, which causes the clearing of ion moving paths on the electrode surface or

enhanced ion penetration. In addition, the reduction of resistance can happen due to an increase in temperature resulting from the heat dissipated from the sequential and faster cycling process. The first 2000 cycles reduce the internal resistance by 2.4  $\Omega$ . In the beginning, electrodes show some resistance to ion movements, but after 2000 cycles it seems to be depleted. Therefore, the observed increase of super-capacitive parameters, with the increasing number of CV cycles given in Table 3, can be attributed to the reduction of resistive losses. The coulombic efficiency begins at 73% and stabilizes at 99% after 1000 cycles, as shown in Figure 8b.

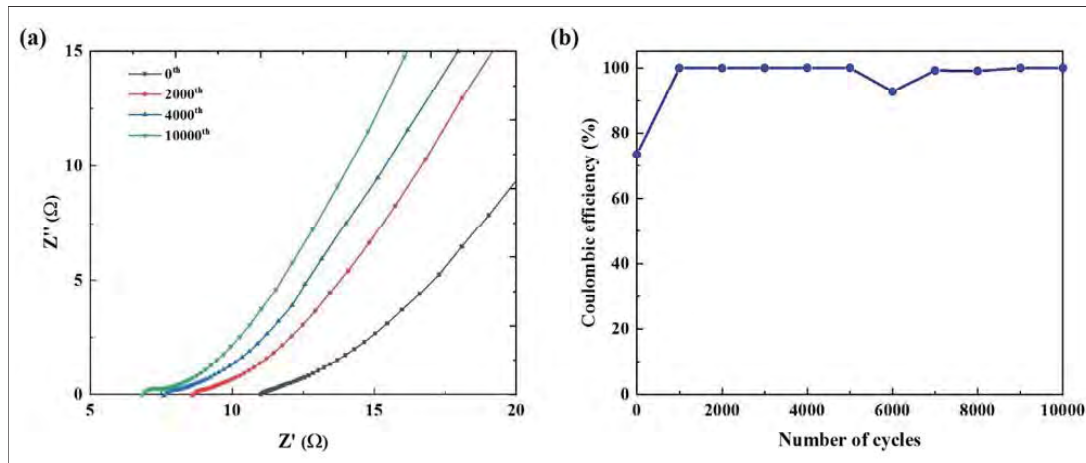


**Figure 8:** (a) Nyquist plot of TAT supercapacitor after 0, 2000, 4000 and 10,000 cycles, (b) coulombic efficiency variation with number of cycles

Electrochemical impedance spectroscopy was used to determine the frequency-dependent complex capacitance of the EDLC. The following equations (4 and 5) are used to calculate the frequency-dependent real ( $C'$ ) and imaginary ( $C''$ ) parts of the net capacitance:

$$C' = \frac{-Z''}{\omega(Z'^2 + Z''^2)} \quad \dots(4)$$

$$C'' = \frac{Z'}{\omega(Z'^2 + Z''^2)} \quad \dots(5)$$

The calculated real and imaginary specific capacitances

are given in Figures 9a and 9b, respectively, as a function of angular frequency. Figures 9c and 9d show  $\log C'$  and  $\log C''$  against  $\log \omega$ . Here  $C'$  and imaginary  $C''$  represent the resultant bulk and double-layer capacitances. In these curves, the high-frequency capacitances are related to the bulk capacitance of the cell while the low-frequency values correspond to the double-layer capacitance. In order to calculate frequency independent double layer capacitance (static capacitance), we need to determine  $C'_{(\omega=0)}$ . The respective logarithmic curves in Figure 9 shows a linear relationship. Therefore, the data were fitted with the equations  $\log(C') = m \log(\omega) + K$  and  $\log(C'') = m' \log(\omega) + K'$  to understand the behavior. Calculated  $m$  and  $K$  parameters are given in Table 4.

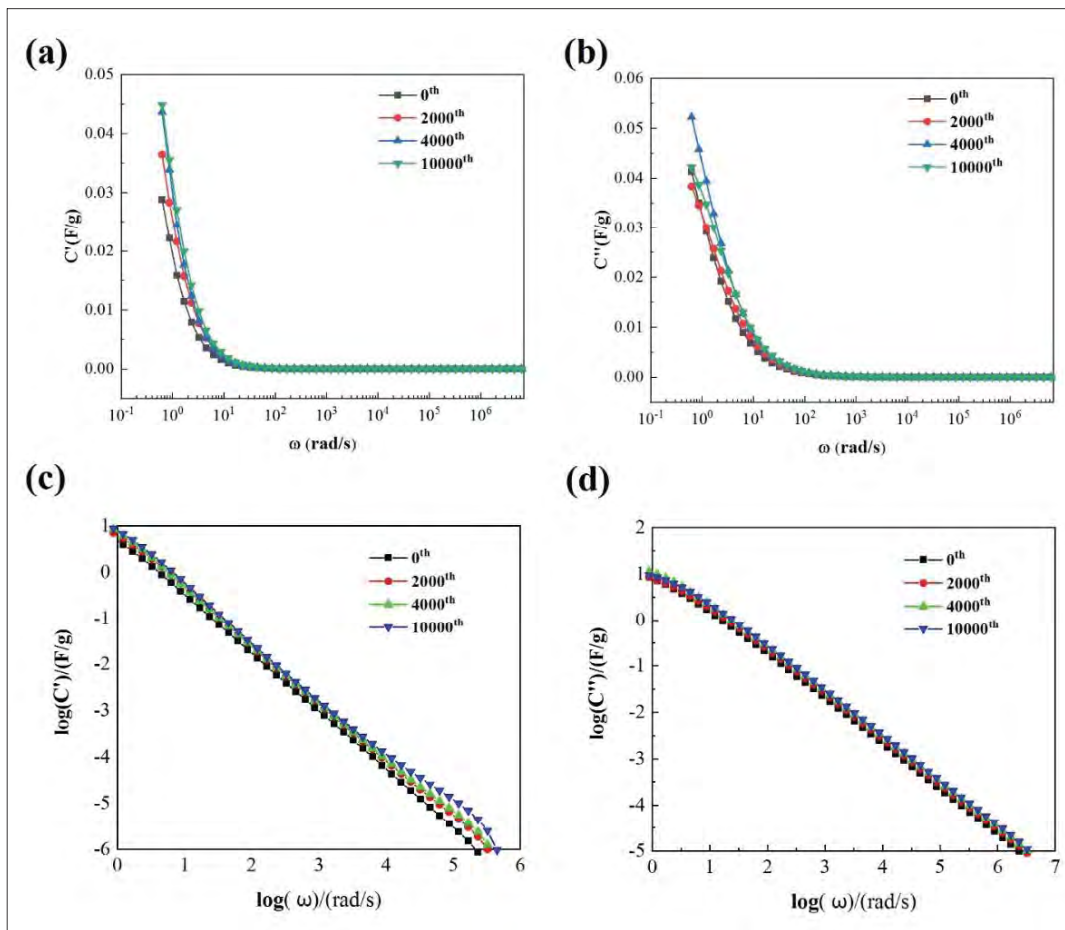


**Figure 9:** The frequency dependence of the real part (a) and the imaginary part (b) of the specific capacitance after 0, 2000, 4000 and 10,000 cycles. The logarithmic frequency dependence of the real part (c) and the imaginary part (d) of the specific capacitance after 0, 2000, 4000 and 10,000 cycles.

**Table 04:** The slope, intercept, and constant (*k*) values derived from the graph  $\log(C)$  vs.  $\log(\omega)$ .

	Cycle Number	Gradient ( <i>m</i> )	$\log(C)$ (F g <sup>-1</sup> )	Static <i>C</i> (F g <sup>-1</sup> )
Real ( <i>C'</i> )	0	-1.28	0.79	6.14
Imaginary ( <i>C''</i> )		-0.95	1.09	12.41
Real ( <i>C'</i> )	2000	-1.24	0.87	7.50
Imaginary ( <i>C''</i> )		-0.94	1.15	14.19
Real ( <i>C'</i> )	4000	-1.23	0.88	7.63
Imaginary ( <i>C''</i> )		-0.95	1.24	17.25
Real ( <i>C'</i> )	10,000	-1.19	0.89	7.76
Imaginary ( <i>C''</i> )		-0.94	1.22	16.78

## CONCLUSION

The results of this study demonstrate that TAT is a promising electrolyte for creating supercapacitors with high durability, stability and cycle life. The supercapacitor made with TAT and AC-based electrodes exhibited an impressive specific capacitance retention of 142% after 10,000 cycles at a scan rate of 500 mV s<sup>-1</sup>. The increase in specific capacitance from 6.67 to 9.48 F g<sup>-1</sup> may be attributed to the clearance of ion conducting pathways and improved charge transport with the rise in temperature. The use of prominent and stable AC electrodes and ionic liquid electrolytes is a major contributor to the impressive stability. The initial energy and power densities of the EDLC were 0.926 Wh kg<sup>-1</sup> and 5681 W kg<sup>-1</sup>, respectively, and they showed increments of 42.2 % and 60.6 % after 10,000 cycles. EIS data analysis reveals that the ESR value of the cell has decreased from 11 Ω to 7 Ω, after 10,000 cycles. The increase in EDLC performance with voltametric cycling is a result of the reduction of resistive losses. The study reveals that low-cost biomass-based activated carbon electrodes combined with an ionic liquid can be used to prepare EDLC with excellent cycling performance. This study introduces a method to determine frequency-independent or scan rate-independent ways to determine the specific capacitance (static capacitance) of EDLCs using complex impedance analysis.

## REFERENCES

- Abioye, A. M., & Ani, F. N. (2015). Recent development in the production of activated carbon electrodes from agricultural waste biomass for supercapacitors: A review. *Renewable and Sustainable Energy Reviews*, 52, 1282–1293. <https://doi.org/10.1016/J.RSER.2015.07.129>
- Abruña, H. D., Kiya, Y., & Henderson, J. C. (2008). Batteries and electrochemical capacitors Present and future applications of electrical energy storage devices are stimulating research into innovative new materials and novel architectures. *Physics Today*, 61, 43–47. <https://doi.org/10.1063/1.3047681>
- Brousse, T., Taberna, P. L., Crosnier, O., Dugas, R., Guillemet, P., Scudeller, Y., Zhou, Y., Favier, F., Bélanger, D., & Simon, P. (2007). Long-term cycling behavior of asymmetric activated carbon/MnO<sub>2</sub> aqueous electrochemical supercapacitor. *Journal of Power Sources*, 173(1), 633–641. <https://doi.org/10.1016/J.JPOWSOUR.2007.04.074>
- Bryan, A. M., Santino, L. M., Lu, Y., Acharya, S., & D'Arcy, J. M. (2016). Conducting polymers for pseudocapacitive energy storage. *Chemistry of Materials*, 28(17), 5989–5998. <https://doi.org/10.1021/acs.chemmater.6b01762>
- Chen, L. Y., Hou, Y., Kang, J. L., Hirata, A., & Chen, M. W. (2014). Asymmetric metal oxide pseudocapacitors advanced by three-dimensional nanoporous metal electrodes. *Journal of Materials Chemistry A*, 2(22), 8448–8455. <https://doi.org/10.1039/C4TA00965G>
- Cuesta, A., Dharmelincourt, P., Laureyns, J., Martínez-Alonso, A., & Tascón, J. M. D. (1994). Raman microprobe studies on carbon materials. *Carbon*, 32(8), 1523–1532. [https://doi.org/10.1016/0008-6223\(94\)90148-1](https://doi.org/10.1016/0008-6223(94)90148-1)
- Dos Reis, G. S., Larsson, S. H., de Oliveira, H. P., Thyrel, M., & Lima, E. C. (2020). Sustainable biomass activated carbons as electrodes for battery and supercapacitors—A mini-review. *Nanomaterials* 10(7), 1398. <https://doi.org/10.3390/NANO10071398>
- Fridleifsson, I. B. (2001). Geothermal energy for the benefit of the people. *Renewable and Sustainable Energy Reviews*, 5(3), 299–312. [https://doi.org/10.1016/S1364-0321\(01\)00002-8](https://doi.org/10.1016/S1364-0321(01)00002-8)
- Fuertes, A. B., Lota, G., Centeno, T. A., & Frackowiak, E. (2005). Templated mesoporous carbons for supercapacitor application. *Electrochimica Acta*, 50(14), 2799–2805. <https://doi.org/10.1016/J.ELECTACTA.2004.11.027>
- Gamby, J., Taberna, P. L., Simon, P., Fauvarque, J. F., & Chesneau, M. (2001). Studies and characterisations of various activated carbons used for carbon/carbon supercapacitors. *Journal of Power Sources*, 101(1), 109–116. [https://doi.org/10.1016/S0378-7753\(01\)00707-8](https://doi.org/10.1016/S0378-7753(01)00707-8)
- Islam, M. S., Anindya, K. N., Bhuiyan, A. G., & Hashimoto, A. (2019). Deconvolution of Raman spectra of disordered monolayer graphene: an approach to probe the phonon modes. *Bulletin of Materials Science*, 42(4), 1–5. <https://doi.org/10.1007/s12034-019-1856-7>
- Karthikeyan, S., Narenthiran, B., Sivanantham, A., Bhatlu, L. D., & Maridurai, T. (2021). Supercapacitor. evolution and review. *Materials Today*, 46, 3984–3988. <https://doi.org/10.1016/J.MATPR.2021.02.526>
- Keppetipola, N. M., Dissanayake, M., Dissanayake, P., Karunaratne, B., Dourges, M. A., Talaga, D., Servant, L., Olivier, C., Toupance, T., Uchida, S., Tennakone, K., Kumara, G. R. A., & Cojocaru, L. (2021). Graphite-type activated carbon from coconut shell: a natural source for eco-friendly non-volatile storage devices. *RSC Advances*, 11(5), 2854–2865. <https://doi.org/10.1039/D0RA09182K>
- Konno, A., Kitagawa, T., Sugiura, D., Kumara, G. R. A., & Tennakone, K. (2004). The effect of room temperature molten thiocyanate salts in CuI on the performance of solid-state dye-sensitized photovoltaic cells using CuI as a hole collector. *Proceedings - Electrochemical Society*, 10, 213–216.
- Kumar, Y., Ringenberg, J., Depuru, S. S., Devabhaktuni, V. K., Lee, J. W., Nikolaidis, E., Andersen, B., & Afjeh, A. (2016). Wind energy: Trends and enabling technologies. *Renewable and Sustainable Energy Reviews*, 53, 209–224. <https://doi.org/10.1016/J.RSER.2015.07.200>
- Kumara, G. R. A., Kaneko, S., Okuya, M., & Tennakone, K. (2002). Fabrication of dye-sensitized solar cells using triethylamine hydrothiocyanate as a CuI crystal growth inhibitor. *Langmuir*, 18(26), 10493–10495. <https://doi.org/10.1021/la020421p>



- Lucia, U. (2014). Overview on fuel cells. *Renewable and Sustainable Energy Reviews*, 30, 164–169. <https://doi.org/10.1016/J.RSER.2013.09.025>
- McCarthy, B. D., Martin, D. J., Rountree, E. S., Ullman, A. C., & Dempsey, J. L. (2014). Electrochemical reduction of brønsted acids by glassy carbon in acetonitrile-implications for electrocatalytic hydrogen evolution. *Inorganic Chemistry*, 53(16), 8350–8361. <https://doi.org/10.1021/ic500770k>
- Medagedara, A. D. T., Waduge, N. M., Bandara, T. M. W. J., Wimalasena, I. G. K. J., Dissanayake, M., Tennakone, K., Rajapakse, R. M. G., Rupasinghe, C. P., & Kumara, G. R. A. (2022). Triethylammonium thiocyanate ionic liquid electrolyte-based supercapacitor fabricated using coconut shell-derived electronically conducting activated charcoal electrode material. *Journal of Energy Storage*, 55, Article 105628. <https://doi.org/10.1016/j.est.2022.105628>
- Pan, H., Li, J., & Feng, Y. P. (2010). Carbon nanotubes for supercapacitor. *Nanoscale Research Letters*, 5(3), 654–668. <https://doi.org/10.1007/s11671-009-9508-2>
- Panwar, N. L., Kaushik, S. C., & Kothari, S. (2011). Role of renewable energy sources in environmental protection: A review. *Renewable and Sustainable Energy Reviews*, 15(3), 1513–1524. <https://doi.org/10.1016/j.rser.2010.11.037>
- Patel, K. K., Singhal, T., Pandey, V., Sumangala, T. P., & Sreekanth, M. S. (2021). Evolution and recent developments of high performance electrode material for supercapacitors: A review. *Journal of Energy Storage*, 44, Article 103366. <https://doi.org/10.1016/J.EST.2021.103366>
- Poonam, Sharma, K., Arora, A., & Tripathi, S. K. (2019). Review of supercapacitors: Materials and devices. *Journal of Energy Storage*, 21, 801–825. <https://doi.org/10.1016/J.EST.2019.01.010>
- Portet, C., Taberna, P. L., Simon, P., Flahaut, E., & Laberty-Robert, C. (2005). High power density electrodes for Carbon supercapacitor applications. *Electrochimica Acta*, 50(20), 4174–4181. <https://doi.org/10.1016/J.ELECTACTA.2005.01.038>
- Qu, G., Cheng, J., Li, X., Yuan, D., Chen, P., Chen, X., Wang, B., & Peng, H. (2016). A fiber supercapacitor with high energy density based on hollow graphene/conducting polymer fiber electrode. *Advanced Materials*, 28(19), 3646–3652. <https://doi.org/10.1002/ADMA.201600689>
- Scrosati, B., & Garche, J. (2010). Lithium batteries: Status, prospects and future. *Journal of Power Sources*, 195(9), 2419–2430. <https://doi.org/10.1016/J.JPOWSOUR.2009.11.048>
- Thapliyal, V., Alabdulkarim, M. E., Whelan, D. R., Mainali, B., & Maxwell, J. L. (2022). A concise review of the Raman spectra of carbon allotropes. *Diamond and Related Materials*, 127, Article 109180. <https://doi.org/10.1016/J.DIAMOND.2022.109180>
- Vaquero, S., Palma, J., Anderson, M., & Marcilla, R. (2013). Mass-balancing of electrodes as a strategy to widen the operating voltage window of carbon/carbon supercapacitors in neutral aqueous electrolytes. *International Journal of Electrochemical Science*, 8, 10293–10307. [https://doi.org/10.1016/S1452-3981\(23\)13111-7](https://doi.org/10.1016/S1452-3981(23)13111-7)
- Yin, J., Zhang, W., Alhebshi, N. A., Salah, N., & Alshareef, H. N. (2020). Synthesis strategies of porous carbon for supercapacitor applications. *Small Methods*, 4(3), Article 1900853. <https://doi.org/10.1002/SMTD.201900853>



## RESEARCH ARTICLE

### Plant Pathology

# Influence of cultivar selection on blast and brown spot diseases in rice: Molecular screening of blast resistance genes

S Terensan<sup>1,2\*</sup>, OVDSJ Weerasena<sup>2</sup>, NS Kottarachchi<sup>3</sup>, JN Silva<sup>3</sup> and HNS Fernando<sup>4</sup>

<sup>1</sup> Department of Agricultural Biology, Faculty of Agriculture, University of Jaffna, Kilinochchi, Sri Lanka.

<sup>2</sup> Institute of Biochemistry Molecular Biology and Biotechnology, University of Colombo, Colombo 3, Sri Lanka.

<sup>3</sup> Department of Biotechnology, Faculty of Agriculture and Plantation Management, Wayamba University of Sri Lanka, Makadura, Sri Lanka.

<sup>4</sup> Regional Rice Research and Development Centre, Bombuwala, Sri Lanka.

Submitted: 11 November 2023; Revised: 21 May 2024; Accepted: 02 July 2024

**Abstract:** The prevalence of blast and brown spot diseases in rice is a substantial threat to national food security. This study investigated the distribution patterns of blast and brown spot, comparing their occurrence and distribution with respect to cultivar selection and conducting molecular screening for the identification of blast resistance genes. The research was conducted over five cultivating seasons from Yala 2017 to Yala 2019 in the Northern Province of Sri Lanka. Incidence percentages of the two diseases were calculated in 114 randomly selected fields across the five districts; Jaffna, Mullaitheevu, Kilinochchi, Mannar, and Vavuniya. Molecular markers were used to screen for nine major blast-resistant genes in 25 commonly cultivated rice cultivars. The results showed a significant shift in the disease over the period of study. While blast disease incidence declined after Maha 2017, brown spot incidence increased steadily from Yala 2017, peaking in Yala 2019. Interestingly, farmers' cultivar preferences, often diverging from the Department of Agriculture recommendations, exhibited a strong correlation with disease occurrence. The cultivar *Attakkari* was identified as a highly susceptible cultivar, which had only three R genes and a major contributor to the progression of blast before Maha 2017. Despite higher brown spot incidence percentages observed in cultivars At362, Bw367, and Bg450, compared to Bg360, intensive post-Maha 2017 cultivation of Bg360 increased the average brown spot incidence to 43%. Cultivars grown after Maha 2017, with over five R genes, showed lower blast disease incidence, suggesting a genetic link to susceptibility. This lower incidence of blast was also observed in the disease evaluation test, where we used the same cultivars. Hence, this

study highlights rice cultivar selection as a decisive factor influencing disease occurrence. Given Sri Lanka's robust germplasm for blast-resistant genes, strategic cultivar selection has the potential for effective disease management.

**Keywords:** Blast disease, brown spot disease, cluster analysis, cultivar selection, molecular screening, rice cultivars.

## INTRODUCTION

Rice blast is a devastating disease, caused by *Magnaporthe oryzae* (Ascomycota; Pezizomycotina; Dothideomycetes; Pleosporomycetidae; Pleosporales; Pleosporineae; Pleosporaceae) in almost all rice growing areas around the world (Ou, 1985; Rossman *et al.*, 1990; Jagadeesh *et al.*, 2020). The disease is responsible for 30% of the annual yield loss globally (Nalley *et al.*, 2016). Next to blast, brown spot is considered as an important disease in rice fields, which reduces the quantity and quality of rice grains. Brown spot is mainly caused by *Bipolaris oryzae* (Ascomycota; Pezizomycotina; Sordariomycetes; Sordariomycetidae; Magnaporthales; Pyriculariaceae) (Dallagnol *et al.*, 2014). The average yield loss owing to brown spot ranges from 4% to 52% (Dhaliwal *et al.*, 2018). Both of these diseases together cause severe economic losses in rice. The incidence and severity of the two diseases vary depending on the geographical location and environmental conditions (Hossain *et*

\* Corresponding author (suvanthingit@univ.jfn.ac.lk; <https://orcid.org/0000-0002-9880-3199>)



This article is published under the Creative Commons CC-BY-ND License (<http://creativecommons.org/licenses/by-nd/4.0/>). This license permits use, distribution and reproduction, commercial and non-commercial, provided that the original work is properly cited and is not changed in anyway.

al., 2017). Blast is a common disease in both *Yala* and *Maha* cultivation seasons which can be controlled by a combination of cultural practices, fungicide application and selection of resistant cultivars. Selection of cultivars based on assessing the genotype for resistance is a promising strategy, which is preferred in highly blast-prone ecosystems since it is environmentally friendly and economically practical.

The resistance of rice plants to blast is controlled by blast resistance genes (R genes). R genes are located within all the 12 chromosomes of rice except chromosome 3 (Liu *et al.*, 2010). Rice and *M. oryzae* have been studied as a classical model for gene for gene interaction (Valent, 1997). During a blast infection, elicitor molecules from the pathogen activate the R genes present in rice to create a hypersensitive response, and resistance is acquired through resistance proteins coded by the R genes (Gururani *et al.*, 2012). Major blast resistant genes fall under the class of central nucleotide-binding site (NBS) and carboxy-terminal leucine-rich repeats (LRR). These NBS-LRR proteins are classified into two major classes, the N-terminal domain that shares homology with the mammalian Toll-interleukin-1-receptor (TIR) domain, while the other class encodes an amino-terminal coiled-coil motif (CC-NBS-LRR) (Chandrakanth *et al.*, 2020).

In the context of blast resistance genes, a noteworthy advancement has been the identification of over 86 dominant R genes out of approximately 350 Quantitative trait loci (QTLs) associated with blast resistance. Among them, 23 were molecularly characterized such as *pb1*, *Pi-a*, *Pi-b*, *Pi-d2*, *Pi-d3*, *Pi-k*, *Pik-h/Pi-54*, *Pik-m*, *Pik-p*, *Pish*, *Pi-t*, *Pi-ta*, *Piz-t*, *Pi-1*, *Pi-2/Piz-5*, *Pi5*, *Pi-9*, *pi-21*, *Pi-25*, *Pi-36*, *Pi-37*, *Pi-35*, and *Pi-64* to date (Fukuoka *et al.*, 2014; Ma *et al.*, 2015). But resistance can be conferred by major blast resistant genes (Zeigler *et al.*, 1994), and several studies have reported that rice plants containing the major blast resistance genes showed a uniform resistant response in nursery experiments (Imam *et al.*, 2014; Yan *et al.*, 2017). Also, several studies suggested that resistance is substantially associated with the number of R genes, which implies a positive correlation between number of R genes and resistance against *M. oryzae* (Ning *et al.*, 2020). On the other hand, regardless of the number, the pattern of R gene combination is a critical factor in determining the level of resistance against *M. oryzae* (Wu *et al.*, 2015). It is essential to screen and discover the combination pattern of R genes that exhibit a broad-spectrum and lasting resistance to maximize the practical use of blast resistance breeding in a particular country.

Hence, the present study was conducted to determine the distribution pattern of blast and brown spot diseases among the rice cultivars grown in the Northern Province of Sri Lanka over five consecutive rice growing seasons from *Yala* -2017 to *Yala* - 2019, to estimate the level of blast resistance based on the presence of R genes.

## MATERIALS AND METHODS

### Study site

The study was conducted in the five districts (Jaffna, Mullaitheevu, Kilinochchi, Mannar, and Vavuniya) in the Northern Province of Sri Lanka in randomly selected fields (n = 114). In the study sites, rice is grown in the two monsoonal seasons of *Maha* (September to March) and *Yala* (May to August). The *Maha* season cultivation is mostly dependent on North-East monsoonal rain, whereas the *Yala* season cultivation is dependent on irrigation from tanks and/or ground water. The province had temperatures ranging from 27 °C to 36 °C with an average annual rainfall of 1250 mm during the study period.

### Disease assessment

The prevalence of rice blast and brown spot diseases was determined during *Yala* - 2017, *Maha* - 2017, *Yala* - 2018, *Maha* - 2018 and *Yala* - 2019. Incidence of blast and brown spot diseases were studied with the assistance of the Rice Research Station, Paranthan, Sri Lanka, and the Pathology division of the Regional Rice Research and Development Centre, Bombuwala, Sri Lanka. The presence of rice blast and brown spot was examined in selected rice fields, where the diseases were recorded historically, by taking 10 points along a diagonal transect in each field by throwing a 1 m × 1 m quadrat. The latitude and longitude of the locations were also recorded. Information on the cultivar grown in a particular location was recorded. Incidence percentage was calculated using the following formula (Nutter, 1997):

$$\text{Incidence\% (IP)} = \frac{\text{Number of samples showing foliar spots}}{\text{Total number of samples}}$$

Average incidence percentage (AIP) was calculated for each cultivar in the studied locations. In addition, severity of the two diseases was assessed based on the 0-9 visual rating scale of the standard disease evaluation system for rice by International Rice Research Institute (IRRI, 2013).

### Molecular screening of rice blast resistant genes

This study was designed to check the presence of blast resistant genes in 25 selected cultivars (Bg 94-1, Bg 360, Bg 352, Suwandal, At 308, Moddaikaruppan, Bg 366, Pachchaperumal, Bg 300, At 362, Bw 351, Bg 250, At 402, Bg 251, Karuthaheenati, At 353, Bw 367, Bg 358, Ld 365, Bg 450, Attakari, Bw 372, Bg 369, Bg 406, and Co 10) grown during the study period. Genomic DNA was isolated from leaves using PhytoSpin D™ Plant Genomic DNA extraction kit. Eight PCR markers were used to detect nine different blast resistant genes; Pita/Pita2, Pik, Pikip, Piz, Pikh, Pizt, Pi9, and Pib; details of the markers are listed in Table 1. The PCR reaction mixture was prepared as follows: 1X PCR buffer, 2.5 mM MgCl<sub>2</sub>, 0.4 mM dNTP, 0.4 μM of each primer 1.5 U of GoTaq DNA polymerase (Promega, USA). The PCR amplification was performed with the following thermal profile: an initial denaturation of 94 °C for 5 min, 35 cycles at 94 °C for 30 s, primer annealing at different temperatures for 45 s (Table 1), 72 °C for 2 min, and a final extension at 72 °C for 8 min. The PCR products were separated by gel electrophoresis on 1% agarose gel in 1X TAE buffer at 60 V for 2 hours. A 100 bp DNA ladder was used as a molecular weight size marker.

### Disease evaluation

The disease assessment was conducted at the Regional Rice Research Station, Bombuwala, Sri Lanka. Seeds of the 25 cultivars were collected from the Rice Research Station, Paranthan, Sri Lanka. Seeds were surface sterilized with 70% ethanol and germinated in plastic pots containing sterile soil under greenhouse conditions. Each pot contained 25 seeds per cultivar. Urea (0.2 g/pot) was applied to increase vegetative growth and plants were watered daily. The concentration of conidial suspension of *M. oryzae* was adjusted to 1 × 10<sup>5</sup> per ml, and 10 ml of the suspension was inoculated into each pot using an atomizer when the plants were at the 4<sup>th</sup> or 5<sup>th</sup> leaf stage. After inoculation, pots were kept in a moist chamber for 48 h and then transferred to the green house. Disease scoring was carried out based on the Standard Evaluation System (SES) of the International Rice Research Institute (IRRI, 2013) after 7, 14, and 21 d. Scores of 0-3 were considered as resistant (R), 4-5 as moderately resistant (MR), and 6-9 as susceptible (S) as reported by Imam *et al.* (2014).

**Table 1:** List of PCR markers used to detect blast resistant genes

Gene	Primer name	Forward primer sequence 5' - 3'	Primer name	Reverse primer sequence 5' - 3'	AT (°C)	AL (bp)	References
Pita/Pita2	Pita3 F	AGTCGTGCGATGCGAGGACAGAAAAC	Pita3 R	GCATTCCTCCAAACCCTTTTGGCATGCAT	59	861	Hayashi <i>et al.</i> , 2006
Piz	Z56592 F	GGACCCCGGTTTTCCACGTGTAA	Z56592 R	AGGAATCTATTGCTAAGCATGAC	60	292	Hayashi <i>et al.</i> , 2004
Piz-t	Zi56591 F	TTGCTGAGCCATTGTTAAACA	Zi56591 R	ATCTCTTCAATATATGAAAGGCCAC	60	257	Hayashi <i>et al.</i> , 2006
Pik	RGA4_F3	GGAAAAGCTGATATGTTGTGCG	RGA4_R3	ACTCGGAGTCGGAGAGTCAAG	55	1200	Ariya-anandech <i>et al.</i> , 2018
Pikip	K.3957 F	ATAGTTGAATGATGGAATGGAAT	K3957 R	CTGCGCCCAAGCAATAAAGTC	60	148	Hayashi <i>et al.</i> , 2006
Pikh	Candidate GM F	CATGAGTTCCATTACTAATTCCTC	Candidate GMR	ACATTTGGTAGTAGTGCAATGTCA	55	1500	Sharma <i>et al.</i> , 2005
Pib	Pi28 F	GACTCGGTGACCAATTCGCC	Pi28 R	ATCAGGCCAGCCAGATTGTG	60	388	Hayashi <i>et al.</i> , 2006
Pi9	195R-1 F	ATGGTCCTTAATCTTAATG	195R-1 R	TTGCTCCAATCTCTCTGT	56	2000	Qu <i>et al.</i> , 2006

AT: Annealing temperature; AL: Amplicon length

### Cluster analysis

Cluster analysis was performed individually utilizing disease reaction scores obtained at 7, 14, and 21 d, and the number of blast resistant genes present in cultivars. For the analysis, the following programs were used in the following order in the Phylip V3.698 : Clique, Neighbor, and Draw tree. Finally, the result file was viewed in Mega X Software Version 10.1.8. The generated dendrograms were compared to identify similar clustering patterns.

## RESULTS AND DISCUSSION

### Distribution pattern of blast and brown spot diseases

Rice blast and brown spot have been reported as major rice diseases and are prevalent in all the rice growing seasons and districts in Sri Lanka, causing varying degrees of damage (Seneviratne & Jeyanandarajah, 2004). Both diseases infect an economically essential component, the seed, which decreases yield, degrades

seed quality, and renders food unsafe for human consumption (Figure 1). In terms of disease intensity at the study sites, the IP of blast ranged from 10% - 81%. The highest incidence of 81% was observed in the Paranthan area of the Kilinochchi district, which was severely affected by blast (Supplementary Table S1) during the *Yala* - 2017 and *Maha* - 2017.

After *Maha* - 2017, the blast incidence was not observed in any of the studied fields. However, the incidence of brown spot increased steadily from *Yala* - 2017 to *Yala* - 2019 and the IP ranged from 0% - 88% in the studied fields. *Yala* - 2019 cultivation had the highest brown spot disease (range of IP = 15.24% - 88.75%) and farmers experienced severe losses due to this (Supplementary Table S1). Since both are fungal diseases and present in the same host, epidemiology of one disease can influence the other disease as reported in previous studies (Bahous *et al.*, 2003; Terensan *et al.*, 2022). Also, *M. oryzae* is reported as a weak competitor in fields (Jia, 2009).

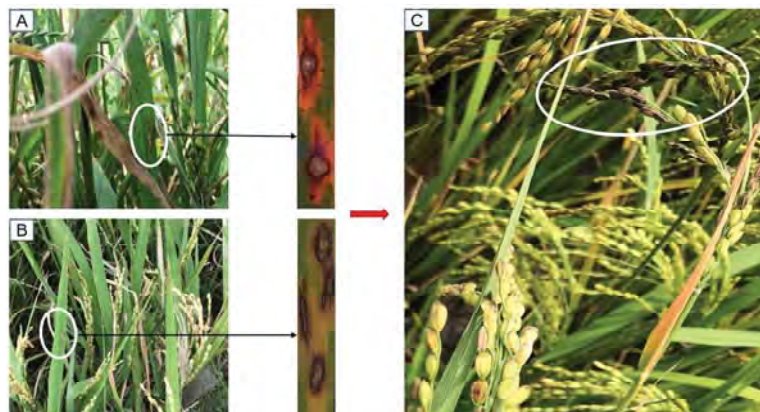


**Figure 1:** Symptoms of blast and brown spot diseases. A) Lesions of rice blast disease. B) Lesions of brown spot disease. C) Panicle infected with both diseases and turned black in colour.

The distribution of blast disease was observed to be higher in *Maha* - 2017 (AIP = 32.31) than *Yala* - 2017 (AIP = 28.22). Generally, the *Maha* season cultivation progress by a heavy rainfall leading to higher humidity that is conducive to blast fungus growth (Rice Research and Development Institute, Bathalagoda). Although a severe blast incidence was expected, as recorded in previous years (Food and Agriculture Organization/

World Food Programme, 2017; Northern Provincial Council of Sri Lanka 2019), it was not observed in *Maha* or *Yala*, 2017 except in few areas in the Kilinochchi (Kandavalai, Tharmapuram, Paranthan) and Mullaitheevu (Udayarkaddu) districts where Attakkari was the predominant cultivar (Supplementary Table S1), which was identified as a blast susceptible cultivar.

In contrast, the incidence of brown spots was low at the beginning of the study, but then increased to a level where farmers abandoned the fields without harvesting. There may be multiple factors contributing to this change in disease occurrence patterns. A few factors, such as the selection of cultivars by farmers and the presence of blast resistance genes in the cultivars grown in the region were analysed to check their influence on disease occurrence patterns. The *in vitro* disease evaluation by analysing the presence of R genes in the major cultivars was also carried out to validate field observations on the distribution and severity of blast disease.

### Cultivar selection and the occurrence of diseases

The study focussed on the selection of cultivars and their correlation with the distribution patterns with blast and brown spot diseases. It was assumed that this correlation

was one of the determining factors for the occurrence pattern of the diseases. Blast infection was observed in 17 different cultivars while the distribution of brown spots was observed in 27 cultivars (Figure 2). It was found that the selection of the cultivar Attakkari during *Maha* – 2017 and *Yala* – 2017 was the significant determining factor for blast occurrence during these two seasons. The earlier field trial conducted by the rice research stations failed due to the severe incidence of blast disease. It was identified as a highly blast - susceptible cultivar and this led to a higher incidence percentage (IP) in locations where it was cultivated, particularly in the districts of Kilinochchi, and Mullaitheevu where farmers have actively grown this cultivar. Similarly, several pockets in the Mannar district were severely infected by blast due to the selection of the same cultivar (Supplementary Table S1).

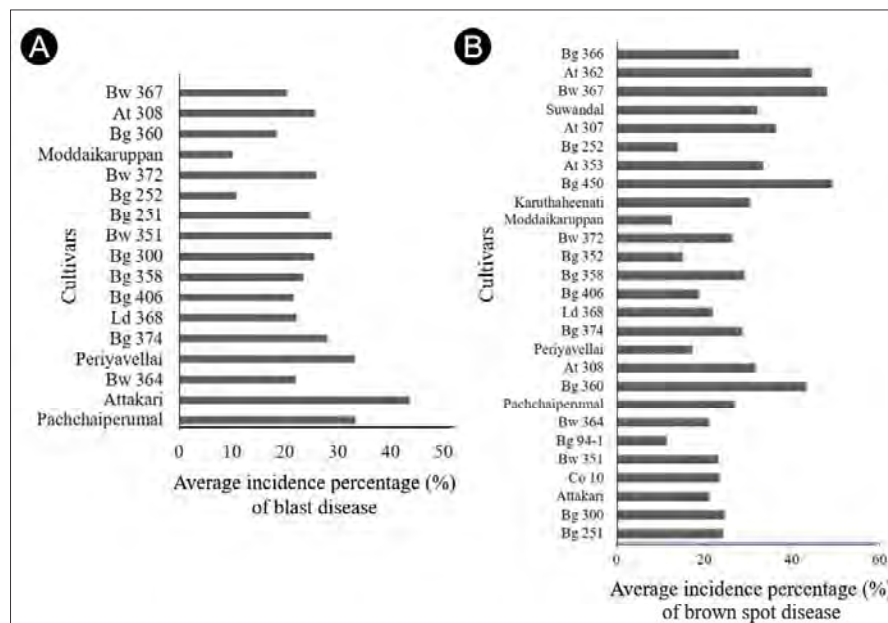


**Figure 2:** Distribution of A) blast and B) brown spot diseases among different rice cultivars grown in the study area with respect to average incidence percentage (AIP).

Despite the fact that the Department of Agriculture has advised farmers to avoid planting the cultivar Attakkari due to its blast susceptibility, based on their field trials,

farmers have cultivated this cultivar extensively until *Maha* – 2017 because it produces a high yield, round bold type of seeds, and has a strong market demand.

On the other side, significantly low blast IP (10.18%) was noticed in the Jaffna district during *Maha* – 2017, and infections were not observed in *Yala* – 2017 where farmers cultivated the red rice cultivar Moddaikaruppan to a higher extent, which is comparably resistant to blast. Therefore, selection of cultivars could be a reason for the absence of blast disease after *Maha* – 2017 to *Yala* – 2019 in the study sites. In addition to this cultivar Attakkari, Pachchaiperumal also had a higher blast IP, but the cultivation extent of this particular cultivar was limited to a few locations in Kilinochchi and Jaffna districts. Notably, Moddaikaruppan and Bg 252 were identified as significantly resistant cultivars to blast and recorded with symptoms below the severity scale of 2.

Based on the field survey and interviews conducted with the farmers and the Department of Agriculture, after *Maha* – 2017, farmers have grown a wide range of cultivars based on the availability of seed material, consumer preference and seeds stored from the previous cultivation. Briefly, higher brown spot infection was noticed in Bg 450, Bw 367, At 362, and Bg 360 while Bg 94-1, Periyavellai, Bg 352, Moddaikaruppan and Bw 364 showed lower infection. Farmers have cultivated Bg 360 in 50% of the studied locations during *Yala* – 2019 (Supplementary Table S1). Interestingly, Bg 360 was grown in the locations where severe brown spot infections were recorded. The highest average incidence percentage (AIP) was noticed in Shiruneelaceni (88.75%) and second highest was in Andankulam (85.4%) from the Mannar district. A similar yield reduction was observed in Vallipunam area from the Mullaitheevu district, where the same cultivar was grown and recorded with an AIP of 58.6%. Cultivar Bg 360 was chosen for intensive cultivation because of the market demand after *Yala* – 2018. Five cultivars, namely Periyavellai (2.6%), At 353 (1.8%), Bg 366 (1.8%), Bw 364 (2.6%), and Moddaikaruppan (2.6%) showed significant resistance to brown spot. However, they were grown only in a few locations.

According to observations, brown spot disease became the major rice disease following the introduction of Bg 360 (*'Keeri samba'*), not only in the Northern Province but also in other regions of Sri Lanka (Nalaka *et al.*, 2021; Senuka, 2023). Bg 360 is a white *'samba'* type cultivar with a higher market price. Most farmers save seeds from previous harvest to cultivate in the next planting season, without realizing that infected seeds can be a significant source of the pathogen's inoculum. This practice can result in the disease persisting continuously, especially when weather conditions are favorable. This may have promoted the existence of brown spot throughout the

study period. Moreover, a study by Chakrabarti (2001) reported that brown spot is generally severe in soils with low pH, low availability of potassium ( $K_2O$ ), and deficient in essential and trace elements. The dominant group of soil in the Northern Province is Reddish Brown Earth (RBE). The association of Low HumicGley (LHG) with RBE soil (92%) enhances paddy cultivation. However, RBE has low organic matter content and the nitrogen and phosphorus status are usually poor, while the potassium status varies from medium to low (Northern Provincial Council of Sri Lanka, 2014). Improper soil amendments has led to subsequent degradation in soil quality because farmers have failed to implement significant improvements in their agronomic practices. This could possibly be one of the reasons for the emergence of brown spot as a major rice disease.

### Detection of blast resistant genes by PCR and pathogenicity assay to assess resistance

This study was conducted to investigate the influence of R genes on blast disease in cultivars grown at the study sites. Twenty-five cultivars were genotyped for the presence of nine blast resistant genes (R genes) in this study. Table 2 summarizes the presence of R genes in the cultivars, which ranged from 3 to 9 based on the results obtained from gel electrophoresis (Supplementary Figures S1–S8). The cultivar Attakari, which was identified as susceptible to blast in the field, contained the fewest R genes ( $n=3$ ). Cultivars Bg 360, Bg 352, Bg 250, At 353, Bg 369, Bg 300 and At 362 were found to contain more than five genes out of the nine tested R genes, with less impact from blast. These cultivars were grown to a larger extent after *Maha* – 2017.

Furthermore, the results revealed that cultivars grown after *Maha* – 2017 possessed more than four blast resistant genes. As the number of R genes increased, resistance also switched from moderately resistant (MR) to resistant (R) response in the disease severity assessment. In fact, during the disease assessment, MR to R responses were recorded for all the 24 cultivars with the exception of cv. Attakari. This finding clearly indicates that several cultivars possess resistance towards the blast disease.

Based on disease severity assessment, cultivars were categorized into three groups, where 17 cultivars were highly resistant (score 0-3), seven were moderately resistant (score 4-5), and one (cv. Attakari) showed susceptible reaction (score 6-9). Data on the presence of R genes and the response to disease screening of all the cultivars were consistent.



**Table 2:** Status of blast resistant genes in cultivars grown in the study sites and the response to susceptibility/resistance levels

Code	Cultivar	Gene									Total number of R genes	DR Score	DR Status
		Pita	Pita2	Pikh	Piz	Pizt	Pik	Pikp	Pib	Pi9			
N1	Bg 94-1	1	1	0	1	0	1	1	1	0	6	3	R
N2	Bg 360	1	1	1	0	0	1	1	1	0	6	1	R
N3	Bg 352	1	1	1	1	0	1	1	1	0	7	2	R
N4	Suwandal	0	0	1	1	0	0	1	1	1	5	1	R
N5	At 308	1	1	0	0	0	1	1	1	0	5	2	R
N6	Moddaikaruppan	0	0	1	1	1	1	1	1	0	6	0	R
N7	Bg 366	0	0	1	1	0	0	1	1	0	4	3	R
N8	Pachchaperumal	1	1	1	1	1	1	1	1	1	9	0	R
N9	Bg 300	1	1	1	1	0	1	1	1	0	7	4	MR
N10	At 362	1	1	1	1	1	1	1	1	0	8	0	R
N11	Bw 351	1	1	1	0	0	0	1	1	0	5	5	MR
N12	Bg 250	1	1	1	1	0	1	1	1	1	8	4	MR
N13	At 402	0	0	0	1	0	0	1	1	0	3	3	R
N14	Bg 251	1	1	1	1	0	0	1	1	0	6	4	MR
N15	Karuthaheenati	0	0	1	1	0	1	1	1	0	5	1	R
N16	At 353	1	1	1	1	1	1	1	1	0	8	1	R
N17	Bg 450	0	0	1	0	1	1	1	1	0	5	0	R
N18	Bw 367	1	1	1	0	1	0	1	1	0	6	1	R
N19	Bg 358	1	1	1	1	0	0	1	1	0	6	1	R
N20	Ld 365	1	1	1	1	0	1	1	1	0	7	1	R
N21	Attakari	0	0	1	0	0	0	1	1	0	3	6	S
N22	Bw 372	0	0	1	0	0	1	1	1	0	4	5	MR
N23	Bg 369	1	1	1	1	0	1	1	1	0	7	0	R
N24	Bg 406	1	1	1	1	0	0	1	1	0	6	5	MR
N25	Co 10	1	1	1	1	0	1	1	1	0	7	4	MR

'1' represents presence of amplicon and '0' represents absence of amplicon. DR: disease resistance, R: resistant, MR: moderately resistant, S: susceptible.

The cluster analysis revealed that various cultivars correspond to similar groupings in the dendrograms (Figure 3) constructed using disease screening results and PCR assay findings. In both dendrograms, cv. Attakari and cv. At 402 (clusters C and D) were grouped separately, whereas certain cultivars were shown to be in similar groups (clusters A and B). Cultivars Co10, Bg 300, Bg 250 for example, were grouped together (Cluster A). Bg 450 and Moddaikkaruppan were also grouped together (Cluster B). However, a definite correlation was not observed in cultivars that were in the moderately resistant category, which were grouped in different clusters.

This is further illustrated as a scatter plot derived using the data generated (Figure 4). The plot clearly separates the susceptible cv. Attakari from the rest, and the resistant varieties are grouped together as illustrated by the cluster diagram.

The findings highlight a significant influence of cultivar selection on the severity of these two diseases. Furthermore, other factors such as agronomic practices and climate change may have also significantly contributed to the dynamics of disease incidence.

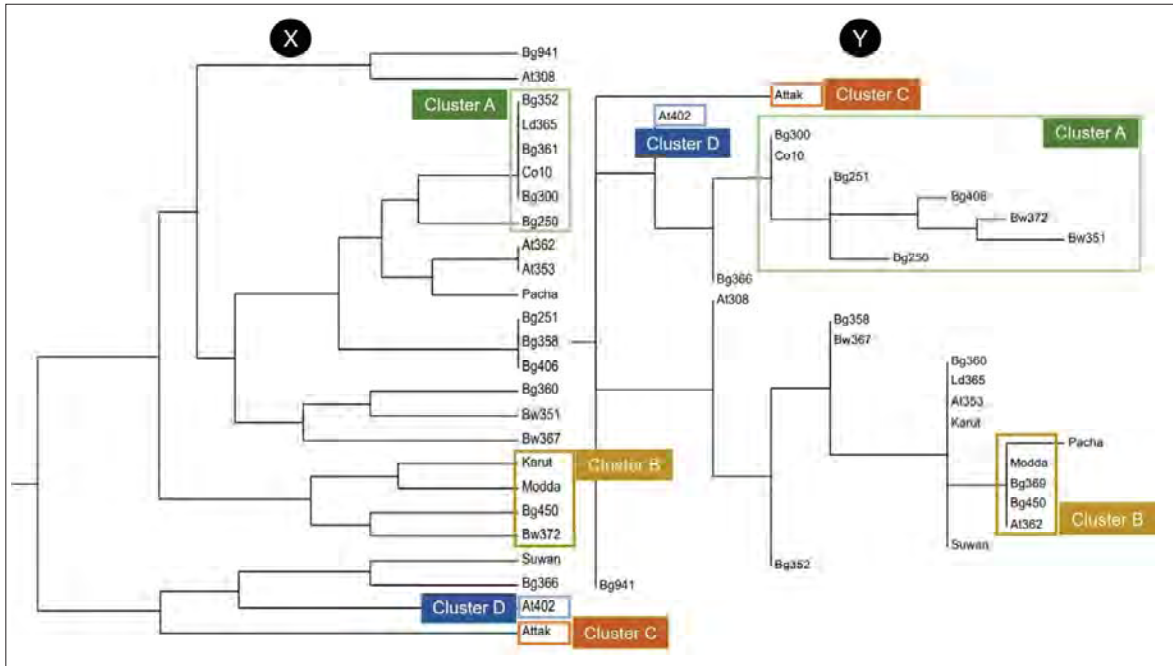


**Figure 3:** Dendrograms constructed based on the cluster analysis to compare the results of disease screening assay and the presence of resistance genes in 25 cultivars grown in the Northern Province. X: Dendrogram produced based on the number of blast resistant genes present in 25 cultivars. Y: Dendrogram based on resistance/susceptible levels in the blast disease screening. The similar clustering patterns of the cultivars are indicated by the use of the same color boxes.

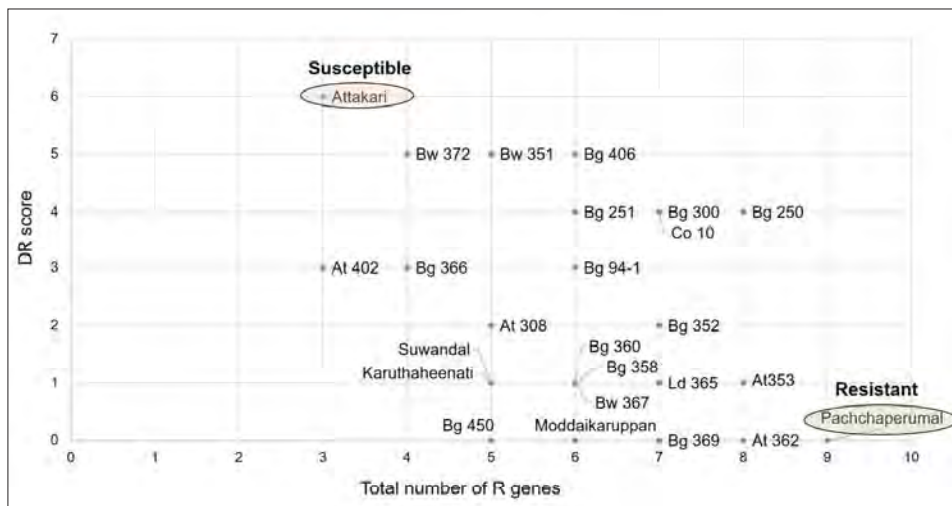


**Figure 4:** Scatter plot drawn for the total number of blast R genes against disease resistance score (DR score)

## CONCLUSION

The study reveals that choosing the susceptible cultivar Attakkari before *Maha* - 2017 has led to a severe incidence of blast. This is further supported by *in-vitro* disease evaluation where the number of R genes present in the cultivars was assessed. Therefore, the absence of blast disease after the *Maha* - 2017 may be attributed to a change in cultivar selection by the farmers. They are now growing cultivars with more blast-resistant genes than before *Maha*-2017. Similarly, the brown spot incidence was higher in locations where cultivar Bg 360 was cultivated. Additionally, when farmers grew disease-resistant cultivars of both diseases, the IP of both diseases decreased. Furthermore, it was observed that the accumulation of blast resistance genes enhances blast resistance in the tested cultivars. Therefore the selection of cultivars has a significant impact on the occurrence of the disease.

## Acknowledgement

This work was funded by the University Grants Commissions, Sri Lanka. (UGC/DRIC/PG2018 (I)/JFN02). We would like to appreciate the assistance provided by Regional Rice Research and Development Centre, Bombuwala to conduct disease evaluation trial in their fields. We would like to thank Mr. S. Sivaneson from the Rice Research Station, Paranthan for his assistance in the field study.

## REFERENCES

- Ariya-anandech, K., Chaipanya, C., Teerasan, W., Kate-Ngam, S., & Jantasuriyarat, C. (2018). Detection and allele identification of rice blast resistance gene, Pik, in Thai rice germplasm. *Agriculture and Natural Resources*, 52(6), 525-535.  
<https://doi.org/10.1016/j.anres.2018.11.009>
- Bahous, M., Touhami, A. O., & Douira, A. (2003). Interaction between *Pyricularia oryzae*, four *Helminthosporium* species and *Curvularia lunata* in rice leaves. *Phytopathologia Mediterranea*, 42(2), 113-122.  
<https://doi.org/10.1079/pwkb.20167800085>
- Chakrabarti, N. K. (2001). Epidemiology and disease management of brown spot of rice in India. In *Major Fungal Diseases of Rice* (pp.293-306). Springer, Dordrecht.  
[https://doi.org/10.1007/978-94-017-2157-8\\_21](https://doi.org/10.1007/978-94-017-2157-8_21)
- Chandrakanth, R., Sunil, L., Sadashivaiah, L., & Devaki, N.S. (2020). *In silico* modelling and characterization of eight blast resistance proteins in resistant and susceptible rice cultivars. *Journal of Genetic Engineering and Biotechnology*, 18(1),1-15.  
<https://doi.org/10.1186/s43141-020-00076-0>
- Dallagnol, L. J., Rodrigues, F. A., Mielli, M. V., & Ma, J. F. (2014). Rice grain resistance to brown spot and yield are increased by silicon. *Tropical Plant Pathology*, 39(1), 56-63.  
<https://doi.org/10.1590/s1982-56762014005000003>
- Dhaliwal, L. K., Sandhu, S. K., Kaur, S., & Singh, S. (2018). Effect of meteorological parameters on incidence of brown leaf spot in rice crop under different planting methods. *Journal of Agrometeorology*, 20 (1), 53-56.  
<https://doi.org/10.54386/jam.v20i1.505>
- Food and Agriculture Organization of the United Nations World Food Programme Rome. (2017).  
<http://www.fao.org/3/i7450e/i7450e.pdf>
- Fukuoka, S., Yamamoto, S. I., Mizobuchi, R., Yamanouchi, U., Ono, K., Kitazawa, N., Yasuda, N., Fujita, Y., Thi Thanh Nguyen, T., Koizumi, S., & Sugimoto, K. (2014). Multiple functional polymorphisms in a single disease resistance gene in rice enhance durable resistance to blast. *Scientific Reports*, 4, 4550.  
<https://doi.org/10.1038/srep04550>
- Gururani, M. A., Venkatesh, J., Upadhyaya, C. P., Nookaraj, A., Pandey, S. K., & Park, S. W. (2012). Plant disease resistance genes: current status and future directions. *Physiological Molecular Plant Pathology*, 78, 51-65.  
<https://doi.org/10.1016/j.pmpp.2012.01.002>
- Hayashi, K., Hashimoto, N., Daigen, M., & Ashikawa, I. (2004). Development of PCR-based SNP markers for rice blast resistance genes at the Pi-z locus. *Theoretical and Applied Genetics*, 108(7), 1212-1220.  
<https://doi.org/10.1007/s00122-003-1553-0>
- Hayashi, K., Yoshida, H., & Ashikawa, I. (2006). Development of PCR-based allele specific and InDel marker sets for nine rice blast resistance genes. *Theoretical and Applied Genetics*, 113(2), 251-260.  
<https://doi.org/10.1007/s00122-006-0290-6>
- Hossain, M., Ali, M. A., & Hossain, M. D. (2017). Occurrence of blast disease in rice in Bangladesh. *American Journal of Agricultural Science*, 4(4),74- 80.  
<https://doi.org/10.3329/brj.v22i1.41841>
- Imam, J., Alam, S., Mandal, N. P., Variar, M., & Shukla, P. (2014). Molecular screening for identification of blast resistance genes in North East and Eastern Indian rice germplasm (*Oryza sativa* L.) with PCR based makers. *Euphytica*, 196(2),199-211.  
<https://doi.org/10.1007/s10681-013-1024-x>
- IRRI Rice Knowledge Bank: Blast (node and neck). (2013).  
<http://www.knowledgebank.irri.org/training/fact-sheets/pestmanagement/diseases/item/blast-node-neck>
- Jagadeesh, D. Kumar, M. K. P., Amruthavalli, C., & Devaki, N. S. (2020). Genetic diversity of *Magnaporthe oryzae*, the blast pathogen of rice in different districts of Karnataka, India determined by simple sequence repeat (SSR) markers.

- Indian Phytopathology*, 73, 713-723.  
<https://doi.org/10.1007/s42360-020-00257-4>
- Jia, Y. (2009). A user-friendly method to isolate and single spore the fungi *Magnaporthe oryzae* and *Magnaporthe grisea* obtained from diseased field samples. *Plant Health Progress*, 10(1), 37.  
<https://doi.org/10.1094/php-2009-1215-01-br>
- Liu, J., Wang, X., Mitchell, T., Hu, Y., Liu, X., Dai, L., & Wang, G. L. (2010). Recent progress and understanding of the molecular mechanisms of the rice - *Magnaporthe oryzae* interaction. *Molecular Plant Pathology*, 11, 419-427.  
<https://doi.org/10.1111/J.1364-3703.2009.00607.X>
- Ma, J., Lei, C., Xu, X., Hao, K., Wang, J., Cheng, Z., Ma, X., Ma, J., Zhou, K., Zhang, X., & Guo, X. (2015). Pi-64, encoding a novel CC-NBS-LRR protein, confers resistance to leaf and neck blast in rice. *Molecular Plant-Microbe Interactions*, 28(5), 558-568.  
<https://doi.org/10.1094/mpmi-11-14-0367-r>
- Nalaka, W., Virajith, K., & Duminda, P. (2021). *Rice Value Chain in Polonnaruwa, Sri Lanka* (Report No. 248). Hector Kobbekaduwa Agrarian Research and Training Institute. [http://harti.gov.lk/images/download/research\\_report/new/Report\\_248\\_eng\\_Fin.pdf](http://harti.gov.lk/images/download/research_report/new/Report_248_eng_Fin.pdf)
- Nalley, L., Tsiboe, F., Durand-Morat, A., Shew, A., & Thoma, G. (2016). Economic and Environmental Impact of Rice Blast Pathogen (*Magnaporthe oryzae*) Alleviation in the United States. *PLoS ONE*, 11(12), e0167295.  
<https://doi.org/10.1371/journal.pone.0167295>
- Ning, X., Yunyu, W., & Aihong, L. (2020). Strategy for use of rice blast resistance genes in rice molecular breeding. *Rice Science*, 27(4), 263-277.  
<https://doi.org/10.1016/j.rsci.2020.05.003>
- Northern Provincial Council: Statistical information about the Northern province. (2014). <https://www.np.gov.lk/pdf/CSCluster/Statistical%20Information%20-%202014.pdf>
- Northern Provincial Council Sri Lanka, Management of Blast Disease in Paddy Cultivation (Tamil). (2019). <https://np.gov.lk/diseasemanagement-of-paddy/>
- Nutter Jr, F. W. (1997). Quantifying the temporal dynamics of plant virus epidemics: a review. *Crop Protection*, 16(7), 603-618.  
[https://doi.org/10.1016/s0261-2194\(97\)00055-0](https://doi.org/10.1016/s0261-2194(97)00055-0)
- Ou, S. H. (1985). *Rice disease* (2<sup>nd</sup> ed.). Commonwealth Agricultural Bureau International Mycological Institute, Farham House, United Kingdom.  
<https://doi.org/10.1017/s0014479700017245>
- Qu, S. H., Liu, G. F., Zhou, B., Bellizzi, M., Zeng, L. R., Dai, L. Y., Han, B., & Wang, G. L. (2006). The broad-spectrum blast resistance gene Pi-9 encodes a nucleotide-binding site-leucine-rich repeat protein and is a member of a multigene family in rice. *Genetics*, 172, 1901-1914.  
<https://doi.org/10.1534/genetics.105.044891>
- Rice Research and Development Institute, Bathalagoda.  
[https://doa.gov.lk/rrdi\\_ricediseases\\_riceblast/](https://doa.gov.lk/rrdi_ricediseases_riceblast/)
- Rossmann, A. Y., Howard, R. J., & Valent, B. (1990). *Pyricularia grisea* the correct name for the rice blast disease fungus. *Mycologia*, 82, 509- 512.  
<https://doi.org/10.1080/00275514.1990.12025916>
- Senuka, J. (2023, March 31). Farmers fume over import plan to plug keeri samba shortfall. *The Sunday Times*. <https://www.sundaytimes.lk/231231/news/>
- Sharma, T. R., Madhav, M. S., Singh, B. K., Shanker, P., Jana, T. K., Dalal, V., Pandit, A., Singh, A., Gaikwad, K., Upreti, H. C., & Singh, N. K. (2005). High-resolution mapping, cloning and molecular characterization of the Pi-k h gene of rice, which confers resistance to *Magnaporthe grisea*. *Molecular Genetics and Genomics*, 274, 569-578.  
<https://doi.org/10.1007/s00438-005-0035-2>
- Seneviratne, S. D. S., & Jeyanandarajah, P. (2004). Rice diseases-problems and progress. *Tropical Agricultural Research and Extension*, 7, 29-48.  
<https://doi.org/10.4038/tare.v7i0.5416>
- Terensan, S., Fernando, H. N. S., Silva, J. N., Perera, S. C. N., Kottearachchi, N. S., & Weerasena, O. J. (2022). Morphological and molecular analysis of fungal species associated with blast and brown spot diseases of *Oryza sativa*. *Plant Disease*, 106(6), 1617-1625.  
<https://doi.org/10.1094/pdis-04-21-0864-re>
- Valent, B. (1997). The rice blast fungus, *Magnaporthe grisea*. In *Plant relationships part B: Part B* (pp. 37-54). Springer Berlin Heidelberg.  
[https://doi.org/10.1007/978-3-642-60647-2\\_3](https://doi.org/10.1007/978-3-642-60647-2_3)
- Wu, Y., Xiao, N., Yu, L., Pan, C., Li, Y., Zhang, X., Liu, G., Dai, Z., Pan, X., & Li, A. (2015). Combination patterns of major R genes determine the level of resistance to the *M. oryzae* in rice (*Oryza sativa* L.). *PLoS One*, 10(6), p.e0126130.  
<https://doi.org/10.1371/journal.pone.0126130>
- Yan, L., Bai-Yuan, Y., Yun-Liang, P., Zhi-Juan, J., Yu-Xiang, Z., Han-Lin, W., & Chang-Deng, Y. (2017). Molecular Screening of Blast Resistance Genes in Rice Germplasm Resistant to *Magnaporthe oryzae*. *Rice Science*, 24(1), 41-47.  
<https://doi.org/10.1016/j.rsci.2016.07.004>
- Zeigler, R. S., Leong, S. A., & Teng, P. S. (1994). *Rice blast disease*. International Rice Research Institution. CAB International, UK.  
<https://doi.org/10.1046/j.1365-3059.1996.d01-159.x>

## Supplementary data

Detection of blast resistant genes in 25 cultivars grown in study sites.



**Figure S1a:** Gel image showing the presence of *Pi-ta/Pi-ta2* gene using the marker of Pita3-F/Pita3-R (861 bp). L: 100 bp ladder, Lane 1: Negative control, Lane 2: *Bg 94-1*, Lane 3: *Bg 360*, Lane 4: *Bg 352*, Lane 5: *At 308*, Lane 6: *Suwandal*, Lane 7: *Moddaikaruppan*, Lane 8: *Bw 372*, Lane 9: *Bg 406*, Lane 10: *Pachchaiperumal*, Lane 11: *Bg 358*, Lane 12: *Bg 300*, Lane 13: *Ld 365*, Lane 14: *Karuthaheenati*, Lane 15: *At 362*, Lane 16: *Bg 366*, Lane 17: *Bg 251*, Lane 18: *At 402*, Lane 19: *Bg 450*



**Figure S1b:** Gel image showing the presence of *Pi-ta/Pi-ta2* gene using the marker of Pita3-F/Pita3-R (861 bp). L: 100 bp ladder Lane 1: *Co10*, Lane 2: *Bg 369*, Lane 3: *Bw 351*, Lane 4: *Attakkari*, Lane 5: *Bg 250*, Lane 6: *Bw 367*, Lane 7: *At 353*



**Figure S2a:** Gel image showing the presence of *Piz* gene using the marker of Z56592 – F/ Z56592 – R (292 bp). L: 100 bp ladder, Lane 1: Negative control, Lane 2: *Bg 360*, Lane 3: *Bg 94-1*, Lane 4: *Bg 352*, Lane 5: *Suwandal*, Lane 6: *At 308*, Lane 7: *Moddaikaruppan*, Lane 8: *At 402*, Lane 9: *Bg 406*, Lane 10: *Pachchaiperumal*, Lane 11: *Bg 358*, Lane 12: *Bw 367*, Lane 13: *Ld 365*, Lane 14: *Karuthaheenati*, Lane 15: *At 362*, Lane 16: *Bg 366*, Lane 17: *Bg 251*, Lane 18: *Bw 372*, Lane 19: *Bg 450*



**Figure S2b:** Gel image showing the presence of *Piz* gene using the marker of Z56592 – F/ Z56592 – R (292 bp). L: 100 bp ladder, Lane 1: *Co10*, Lane 2: *Bg 369*, Lane 3: *Bw 351*, Lane 4: *Attakkari*, Lane 5: *Bg 250*, Lane 6: *Bg 300*, Lane 7: *At 353*



**Figure S3a:** Gel image showing the presence of *Pizt* gene using the marker of Z56591 – F/ Z56591 – R (257 bp). L: 100 bp ladder, Lane 1: Negative control, Lane 2: *Bg 94-I*, Lane 3: *Bg 360*, Lane 4: *Bg 352*, Lane 5: *Bw 367*, Lane 6: *At 308*, Lane 7: *Moddaikaruppan*, Lane 8: *Bg 366*, Lane 9: *Bg 450*, Lane 10: *At 402*, Lane 11: *Bg 358*, Lane 12: *Suwandal*, Lane 13: *Ld 365*, Lane 14: *Karuthaheenati*, Lane 15: *Pachchaiperumal*, Lane 16: *At 362*, Lane 17: *At 353*, Lane 18: *Bw 372*, Lane 19: *Bg 406*

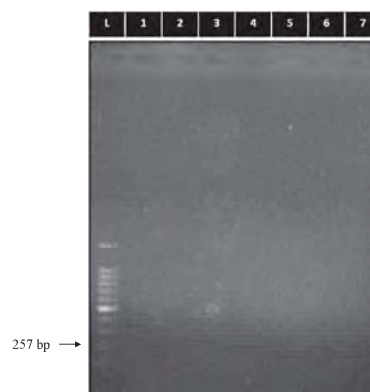


**Figure S3b:** Gel image showing the presence of *Pizt* gene using the marker of Z56591 – F/ Z56591 – R (257 bp). L: 100 bp ladder, Lane 1: *Co10*, Lane 2: *Bg 369*, Lane 3: *Bw 351*, Lane 4: *Attakkari*, Lane 5: *Bg 250*, Lane 6: *Bg 300*, Lane 7: *Bg 251*

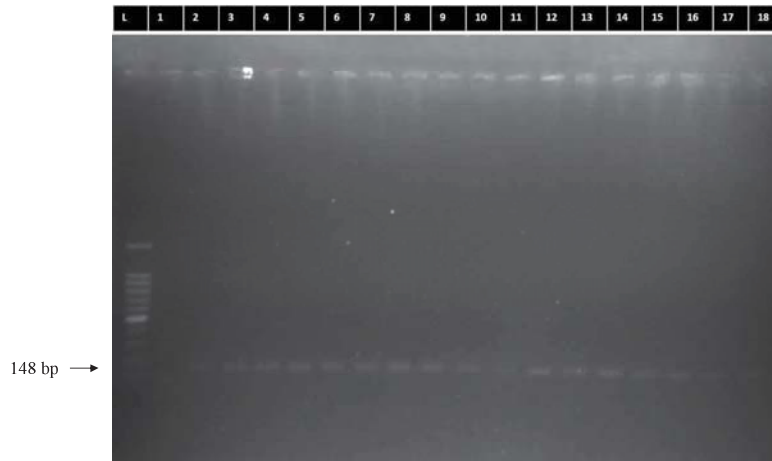


**Figure S4a:** Gel image showing the presence of *Pikp* gene using the marker of K3957 - F / K3957- R (148 bp). L: 100 bp ladder, Lane 1: Negative control, Lane 2: Bg 94-1, Lane 3: Bg 360, Lane 4: Bg 352, Lane 5: Bw 367, Lane 6: Co 10, Lane 7: *Moddaikaruppan*, Lane 8: Bg 251, Lane 9: Bg 450, Lane 10: Bg 300 Lane 11: At 308, Lane 12: *Suwandal*, Lane 13: Ld 365, Lane 14: Bg 366, Lane 15: *Pachchaiperumal*, Lane 16: *Attakkari*, Lane 17: At 353, Lane 18: Bw 372

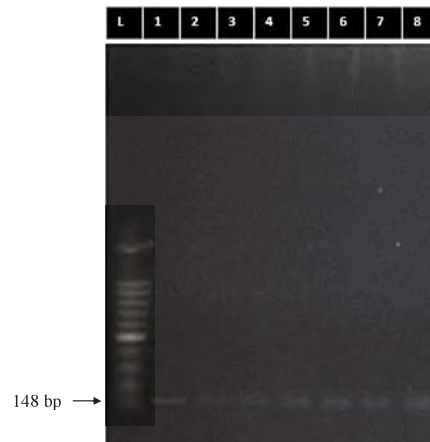


**Figure S4b:** Gel image showing the presence of *Pikp* gene using the marker of K3957 - F / K3957- R (148 bp). L: 100 bp ladder, Lane 1: *Bg 406*, Lane 2: *Bg 358*, Lane 3: *Bg 369*, Lane 4: *Bw 351*, Lane 5: *At 362*, Lane 6: *Bg 250*, Lane 7: *At 402*, Lane 8: *Karuthaheenati*

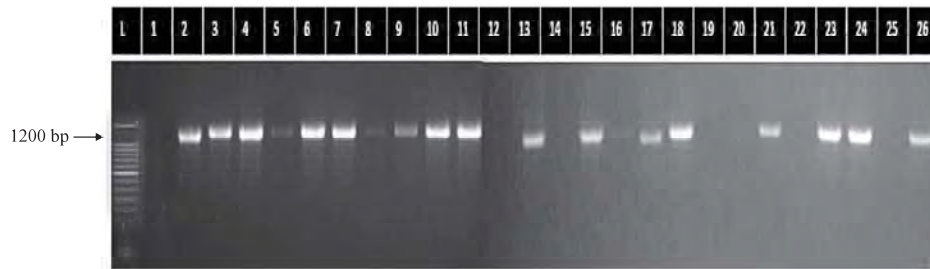


**Figure S5:** Gel image showing the presence of *Pik* gene using the marker of RGA4\_F3/ Z56591 RGA4\_R3 (1200 bp). L: 100 bp ladder, Lane 1: Negative control, Lane 2: *Bg 94-I*, Lane 3: *Bg 360*, Lane 4: *Bg 352*, Lane 5: *Bw 367*, Lane 6: *Co 10*, Lane 7: *Moddaikaruppan*, Lane 8: *Bg 251*, Lane 9: *Bg 450*, Lane 10: *Bg 300*, Lane 11: *At 308*, Lane 12: *Suwandal*, Lane 13: *Ld 365*, Lane 14: *Bg 366*, Lane 15: *Pachchaiperumal*, Lane 16: *Attakkari*, Lane 17: *At 353*, Lane 18: *Bw 372*, Lane 19: *Bg 406*, Lane 20: *Bg 358*, Lane 21: *Bg 369*, Lane 22: *Bw 351*, Lane 23: *At 362*, Lane 24: *Bg 250*, Lane 25: *At 402*, Lane 26: *Karuthaheenati*

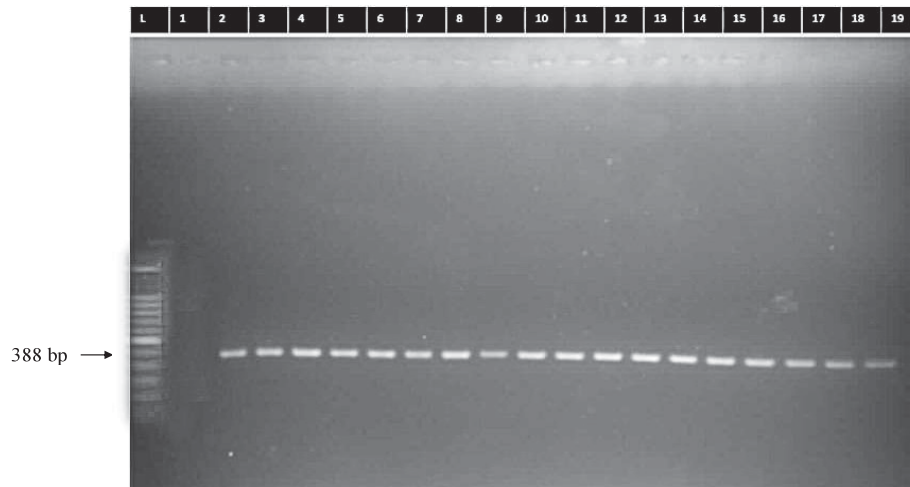


**Figure S6a:** Gel image showing the presence of *Pib* gene using the marker of Candidate Pi28 - F/ Pi28- R (388 bp). L: 100 bp ladder, Lane 1: Negative control, Lane 2: *Bg 94-I*, Lane 3: *Bg 360*, Lane 4: *Bg 352*, Lane 5: *Bw 367*, Lane 6: *At 402*, Lane 7: *Moddaikaruppan*, Lane 8: *Bg 251*, Lane 9: *Bg 450*, Lane 10: *Bg 300*, Lane 11: *Ld 365*, Lane 12: *Suwandal*, Lane 13: *At 308*, Lane 14: *Bg 366*, Lane 15: *Pachchaiperumal*, Lane 16: *Attakkari*, Lane 17: *At 353*, Lane 18: *Bw 372*, Lane 19: *Bg 406*, Lane 20: *Bg 358*, Lane 21: *Bg 369*, Lane 22: *Bw 351*, Lane 23: *At 362*, Lane 24: *Bg 250*, Lane 25: *Co 10*, Lane 26: *Karuthaheenati*



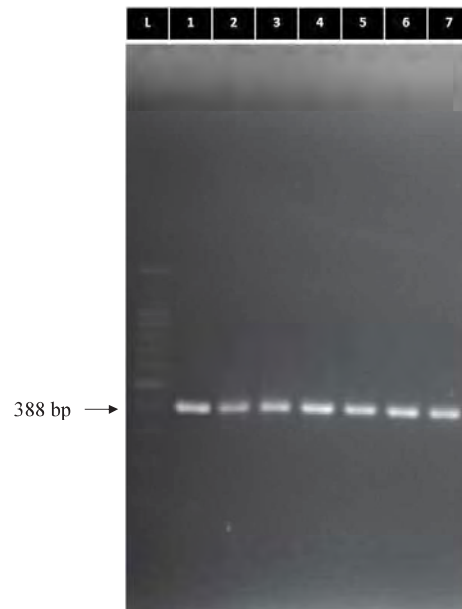


**Figure S6b:** Gel image showing the presence of *Pib* gene using the marker of Candidate Pi28 - F/ Pi28- R (388 bp). L: 100 bp ladder, Lane 1: *Bg* 358, Lane 2: *Bg* 369, Lane 3: *Bw* 351, Lane 4: *At* 362, Lane 5: *Bg* 250, Lane 6: *Co* 10, Lane 7: *Karuthaheenati*

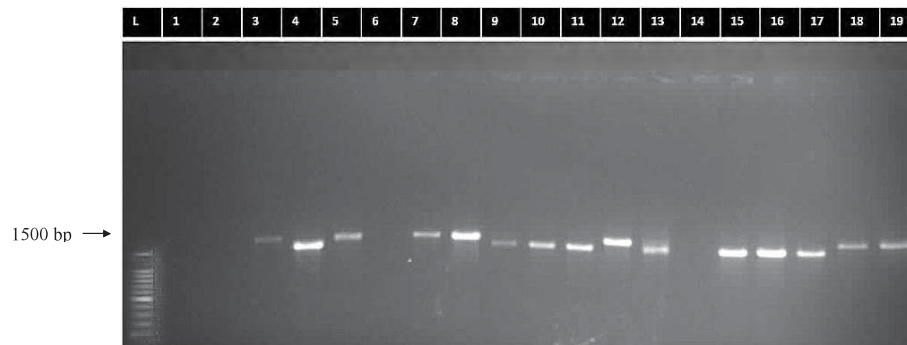


**Figure S7a:** Gel image showing the presence of *Pikh* gene using the marker of Candidate GM - F/ Candidate GM - R (1500 bp). L: 100 bp ladder, Lane 1: Negative control, Lane 2: *Bg* 94-I, Lane 3: *Bg* 360, Lane 4: *Bg* 352, Lane 5: *Bw* 367, Lane 6: *At* 402, Lane 7: *Moddaikaruppan*, Lane 8: *Bg* 251, Lane 9: *Bg* 450, Lane 10: *Bg* 300, Lane 11: *Ld* 365, Lane 12: *Suwandal*, Lane 13: *At* 308, Lane 14: *Bg* 366, Lane 15: *Pachchaiperumal*, Lane 16: *Attakkari*, Lane 17: *At* 353, Lane 18: *Bw* 372, Lane 19: *Bg* 406

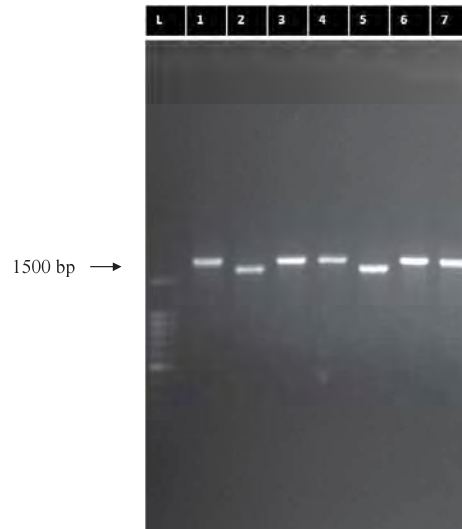


Figure S7b: Gel image showing the presence of *Pikh* gene using the marker of Candidate GM - F/ Candidate GM - R (1500 bp). L: 100 bp ladder, Lane 1: *Bg 358*, Lane 2: *Bg 369*, Lane 3: *Bw 351*, Lane 4: *At 362*, Lane 5: *Bg 250*, Lane 6: *Co 10*, Lane 7: *Karuthaheenati*



Figure S8: Gel image showing the presence of *Pi9* gene using the marker of Candidate 195R-1 F/ 195R-1 R (2000 bp). L: 100 bp ladder, Lane 1: Negative control, Lane 2: *Bg 94-1*, Lane 3: *Bg 360*, Lane 4: *Bg 352*, Lane 5: *Bw 367*, Lane 6: *At 402*, Lane 7: *Moddaikaruppan*, Lane 8: *Bg 251*, Lane 9: *Bg 450*, Lane 10: *Bg 300*, Lane 11: *Ld 365*, Lane 12: *Suwandal*, Lane 13: *At 308*, Lane 14: *Bg 366*, Lane 15: *Pachchaiperumal*, Lane 16: *Attakkari*, Lane 17: *At 353*, Lane 18: *Bw 372*, Lane 19: *Bg 406*, Lane 20: *Bg 358*, Lane 21: *Bg 369*, Lane 22: *Bw 351*, Lane 23: *At 362*, Lane 24: *Bg 250*, Lane 25: *Co 10*, Lane 26: *Karuthaheenati*

## RESEARCH ARTICLE

### Equipment Failure Analysis

# Predicting water content in engine oil using SPA-ISSA-BP methods

Chen Bin<sup>1</sup>, Quan YuXuan<sup>1</sup>, Liu Ge<sup>2\*</sup>, Li JianZhong<sup>3</sup>, Nie GaoXing<sup>4</sup>, Zhang YongChang<sup>1</sup>, Shan ChenZe<sup>1</sup>, Chen JunSen<sup>2</sup>, Chen Rui<sup>1</sup>, Chen Xi<sup>1</sup> and Zhang MengWei<sup>2</sup>

<sup>1</sup> School of Mechanical & Electrical, Hebei Key Laboratory of Safety Monitoring of Mining Equipment, North China Institute of Science and Technology, Hebei, 065201, China.

<sup>2</sup> School of Environmental Engineering, North China Institute of Science and Technology, Hebei, 065201, China.

<sup>3</sup> Laboratory of Environmental Biotechnology, CAS, Beijing, 100085, China.

<sup>4</sup> Faculty of Engineering, HKU, Hong Kong, 999077, China.

Submitted: 13 December 2023; Revised: 16 July 2024; Accepted: 24 July 2024

**Abstract:** Contamination of engine oil with water can accelerate oil oxidation and decomposition, resulting in oil degradation. Therefore, the detection and prediction of water content in engine oil is crucial to ensure the long-term safe operation of engines. In this study, near-infrared spectroscopy was used to analyse engine oils with varying water contents. Spectral data were obtained, and various methods, including Savitzky-Golay (SG) smoothing, orthogonal signal correction (OSC), and successive projection algorithm (SPA) were employed to compare the performance differences of principal component regression models. An Improved Sparrow Searches Algorithm (ISSA) was then applied to optimise the Back-Propagation Neural Network (BPNN) for predicting water content in SAE 10W-30 engine oil. The results showed that the performance of the principal component regression model constructed from spectral data after SG smoothing, OSC, and the SPA feature wavelength selection had improved. The BPNN optimised by the improved Sparrow Search Algorithm accelerated the convergence speed of the model and effectively improved the prediction accuracy of the BPNN. The obtained coefficient of determination ( $R^2$ ) was 0.99103, the root mean square error (RMSE) was  $2.2136 \times 10^{-4}$ , and the mean absolute error (MAE) was  $1.8889 \times 10^{-4}$ . These results provide an effective method for detecting and predicting the water content in engine oil.

**Keywords:** Engine oil, near-infrared spectroscopy, neural network, sparrow search algorithm, water content.

## INTRODUCTION

During the long-term operation of an engine, water contamination is inevitable due to factors such as

environmental moisture, seal failure, and thermal decomposition products. Some moisture enters the engine through components such as piston rings and cylinder walls, and then travels into the crankcase where it mixes with the engine oil (Khamidullaevnaz 2022). Water is present in engine oil in three different states: free, emulsified, and dissolved (Abdel-Aziz *et al.*, 2016; Hensel *et al.*, 2017). These water contaminants alter the physico-chemical properties of the engine oil, accelerating the depletion of engine additives. This leads to oil degradation, and the formation of corrosive acids and water (Alimova *et al.*, 2021; Zhou & Yang, 2021). This exacerbates oil deterioration, resulting in reduced lubricity, corrosion of engine components, and accelerated formation of sludge and carbon deposits. These problems have a significant impact on the safe and stable operation of the engine. Therefore, the ability to detect and predict water content in engine oil is of paramount importance.

Extensive research has been conducted both nationally and internationally on detecting water content in engine oil, leading to the development of various methods for this purpose. Currently, the most commonly used method for detecting water content in oil is the Karl Fischer titration method (Zhen *et al.*, 2020). However, the presence of additives in engine oil can lead to falsely elevated water content results, when using this method. The dielectric constant method is also prone to errors due to insufficient mixing of the environment and samples, leading to inaccuracies in the test results (Chen & Liu,

\* Corresponding author (lgncist@hotmail.com; <https://orcid.org/0009-0007-7733-9036>)



This article is published under the Creative Commons CC-BY-ND License (<http://creativecommons.org/licenses/by-nd/4.0/>). This license permits use, distribution and reproduction, commercial and non-commercial, provided that the original work is properly cited and is not changed in anyway.

2020). Gas chromatography, offers high precision and speed, but it requires expensive instrumentation, involves complex procedures, and requires extensive sample pre-processing. These factors contribute to increased test time (Xie *et al.*, 2018).

Near-infrared (NIR) spectroscopy refers to a specific region of the electromagnetic spectrum with wavelengths typically ranging between 780 and 2500 nm. Within this range, the vibrational modes of various chemical bonds and molecules produce distinct absorption features. One of the most prominent is the O-H bond vibrations in water molecules, which have a significant impact on the absorption spectrum in the near-infrared region. Although the spectral signals from O-H bonds can overlap with signals from other functional groups, the use of chemometric signal processing techniques allows for the signals to be separated and resolved. This approach provides accurate water content results and can effectively replace traditional methods of determining water content.

Spectroscopic analysis has been widely used in the detection of water content in oils. Fardin-Kia *et al.* (2019) found significant differences in oils with varying water contents in the near infrared region at  $5260\text{ cm}^{-1}$ . Based on this discovery, they proposed a quick, univariate Fourier transform near infrared (FT-NIR) method for detecting water content in oils.

Liu *et al.* (2020) developed a portable system for detecting water content in lubricating oil based on visible near infrared (VIS-NIR) reflectance. This system utilized reflectance spectroscopy data input into a neural network model for prediction, achieving a prediction coefficient of determination ( $R^2$ ) of 0.98. In a related study Liu *et al.* (2023) analysed the characteristic peaks in the NIR spectra of engine oil and identified strong absorption peaks at 931 nm, 1195-1212 nm, and 1391-1430 nm. After applying orthogonal signal correction (OSC) to the spectroscopic data, they established a partial least squares regression (PLSR) model. This model enabled accurate prediction of the water content in the oil.

Due to the large number of spectral wavenumbers obtained through spectroscopic analysis, which contain a significant amount of redundant data, building models directly with the original spectra can lead to problems such as reduced model generalisation ability and low prediction efficiency. Therefore, it is necessary to perform feature selection on the acquired spectral data. For example, Liu *et al.* (2023) conducted feature wavelength selection based on the regression coefficient matrix of

the partial least squares regression (PLSR) model. They utilized the selected wavelengths to rebuild the PLSR model leading to a significant enhancement of the prediction accuracy of the model. In their study, Zhang *et al.* (2021) applied swarm intelligence algorithms, such as slime mould algorithm and bat algorithm, to select feature wavelengths in near-infrared spectroscopic data of water-containing soil. This approach significantly enhanced the predictive performance of the model. Currently, most researchers utilize PLSR to establish predictive models. This is a linear regression model that effectively deals with multicollinearity problems. However, its capability to fit nonlinear relationships is relatively weak (Chiappini *et al.*, 2020).

In comparison, nonlinear regression models such as support vector regression (SVR), Gaussian Process Regression (GPR), and back-propagation neural network (BPNN) have robust nonlinear fitting capabilities and can fit complex nonlinear relationships. For instance, Liu *et al.* (2021) combined SVR with PLS to achieve precise prediction of water content in crude oil. Additionally, Zhao *et al.* (2010) used GPR to develop a prediction model for water content in lubricating oil based on NIR data giving superior results compared to the SVR model.

At present, SVR is facing challenges in selecting the appropriate kernel function for nonlinear problems. Additionally SVM are quite sensitive to noise in the data, which can lead to unstable model performance. On the other hand, GPR has high computational costs, with long training times, and its predictive performance decreases in high-dimensional spaces, making it unsuitable for spectral data modelling.

BPNN, however, is less affected by noise compared to SVM, has better capabilities in handling high-dimensional data than GPR, and its strong nonlinear fitting ability makes it excel in handling complex data. Specifically, BPNN can effectively learn and model complex nonlinear relationships through its multi-layer structure and nonlinear activation functions. Additionally, BPNN has adaptive learning capabilities, allowing it to automatically adjust network parameters using training data, thereby improving model prediction accuracy. However, the initial weights and biases of BPNN consist of pseudo-random numbers, which significantly affect the network's convergence speed and outcomes. Many researchers use optimisation algorithms such as genetic algorithms and particle swarm optimisation algorithms to optimise BPNN. For example, Wang *et al.* (2023) applied a genetic algorithm to optimise BPNN, achieving rapid detection of tea moisture content. Peng *et al.* (2023)

designed a BPNN with a double hidden layer optimised by a particle swarm algorithm. They developed a model that correlated multispectral data with crop moisture content, ultimately achieving accurate predictions of crop moisture content.

Currently, the presence of test noise and baseline drift during spectral acquisition adversely affects the accuracy of water content detection. Existing studies primarily use linear regression models, which are relatively ineffective in handling nonlinear relationships. Therefore, this study proposes a nonlinear modelling method that integrates various preprocessing techniques and optimisation algorithms to enhance the accuracy of water content detection in engine oil. Specifically, we will use Savitzky-Golay (S-G) convolution smoothing and orthogonal signal correction (OSC) to eliminate noise and apply the successive projection algorithm (SPA) for selecting wavelength of spectral features. Next, we will optimise the back-propagation neural network (BPNN) using the improved sparrow search algorithm (ISSA) to enhance the model's nonlinear fitting capability. Finally, we will evaluate the model's performance using  $R^2$ , root mean square error (RMSE), and mean absolute error (MAE) as metrics, and conduct a comparative analysis. This research aims to provide technical support for the long-term stability and safe operation of engines.

## MATERIAL AND METHODS

### Preparation of oil samples

SAE 10W-30 engine oil was chosen as the subject of the experiment. First, 10 ml of the original oil sample, free of water content, was placed in glass test tubes. Next, 10  $\mu$ l of oil was removed using a pipette, and 10  $\mu$ l of distilled water was added to create oil samples with a water content of 0.1%. By adjusting the volumes of oil removed and distilled water added, a total of 32 oil samples with varying water contents ranging from 0% to 0.9% were prepared. After preparation, the test tubes were placed in an ultrasonicator for 10 min to ensure thorough mixing of the oil and water. The Karl Fischer moisture meter was then used to accurately measure the water content of the oil samples, providing the final water content values of the oil samples. After the measurements, the test tubes were sealed and placed in a light-free environment to prevent photodegradation. The final water content values for the 32 oil samples are shown in Table 1.

**Table 1:** Water content of oil Samples

Sample number	Water content	Sample number	Water content
1	0	17	0.0045
2	0.0010	18	0.0047
3	0.0015	19	0.0048
4	0.0017	20	0.0049
5	0.0020	21	0.0050
6	0.0025	22	0.0052
7	0.0026	23	0.0057
8	0.0027	24	0.0060
9	0.0030	25	0.0063
10	0.0032	26	0.0067
11	0.0035	27	0.0070
12	0.0037	28	0.0072
13	0.0038	29	0.0073
14	0.0039	30	0.0078
15	0.0040	31	0.0080
16	0.0041	32	0.0090

### Experimental apparatus and spectroscopic testing method

The experiment used the ocean optics NIR\_Quest near infrared spectrometer, model number 512-1.9. This spectrometer employs the Beer-Lambert's law to obtain spectral information from oil samples. The wavelength of the spectrometer ranged from 900 nm to 1700 nm, with an optical resolution of 3.1 nm, a wavelength repeatability of 0.1 nm, an InGaAs detector, and a 50W quartz halogen lamp as the light source.

The spectrometer was connected to the computer through a USB interface, and spectral data were collected using the OCEANVIEW software. Reflectance fiber optic probes were used to acquire spectra of oil samples within the 900-1700 nm range. A total of 512 spectral bands were collected, with 20 scans per sample. Each oil sample underwent three replicate experiments, and the final result was determined by averaging the values.

### Successive projections algorithm

The SPA is a commonly used feature selection method that has the advantage of not relying on data distribution assumptions and performs well in feature selection in high-dimensional data. It selects the most informative features by calculating the projection vector sizes between feature bands, eliminating collinearity among variables, and improving modelling accuracy while reducing model complexity (Jia *et al.*, 2023; Liu *et al.*, 2023).

In each iteration, SPA selects the feature with the maximum projection with the remaining unselected features, gradually constructing a subset of features, reducing collinearity among wavelengths, and improving the accuracy and efficiency of problem modelling.

### Sparrow search algorithm and its improved algorithm

#### Sparrow search algorithm

The Sparrow Search Algorithm (SSA) is a heuristic optimisation algorithm inspired by the collective behaviour of sparrow populations in the natural world, utilized to solve various optimisation problems (Gharehchopogh *et al.*, 2023; Xue & Shen, 2020). The algorithm is inspired by the foraging behaviour of sparrow populations, where sparrows find food and avoid danger by cooperating and sharing information. In the algorithm, sparrows are divided into three groups: explorers, followers, and sentinels. Explorers, similar to the mutation operation in genetic algorithms, are responsible for exploring unknown regions in the solution space. Followers move towards the optimal solution based on the explorers' results, accelerating the global search process. Sentinels are randomly selected from the entire population and act as early warnings of danger; the entire population responds with anti-predatory behaviour when danger is detected.

#### Improved sparrow search algorithm

Due to problems such as uneven initial population distribution and low diversity in the later iterations, improvements are necessary for the SSA. The improvement strategies are as follows:

- (1) Initialization of population using tent chaotic and inverse mapping  
To ensure a uniformly distributed initial population, the Tent chaotic mapping (Li *et al.*, 2020) was used to generate N initial populations. This was followed by an inverse mapping process to generate N inverse

populations. The best N of these is then retained as the initial population.

- (2) Fusion of reverse learning and Cauchy mutation strategy

To expedite the convergence speed and assist the algorithm to find the optimal solution more quickly, reverse learning and Cauchy mutation have been integrated into the SSA algorithm (Ali & Pant, 2011; Xu *et al.*, 2023). The strategy to be used is selected based on the probability (rp), as shown in Equation (1).

$$r_p = -\exp\left(1 - \frac{gen}{gen_{max}}\right)^{20} + 2 \quad (01)$$

- (3) Greedy Rule

Finally, a greedy rule is introduced, where after updating the position of the optimal solution, its fitness is compared with the fitness of the old position to determine if the position should be updated.

### ISSA-BP Neural Network

Combining the improved sparrow search algorithm (ISSA) with the BPNN results in the ISSA-optimised BPNN. The specific procedure is outlined as follows:

- (1) Initialize the BPNN by determining the number of nodes in the input and output layers, and the number of hidden layers and nodes.
- (2) Set the parameters for the ISSA and the BPNN. Use Tent chaotic mapping and inverse mapping to generate the initial population, where the D-dimensional position vector of each individual represents the initial weights and biases of the BPNN.
- (3) Calculate individual fitness values and rank them.
- (4) Select high-fitness individuals as explorers, the remaining individuals as followers, and update their positions. Randomly select some individuals from the whole population as sentinels and update their positions.
- (5) Calculate the population fitness and rank them.
- (6) Based on the selection probability (rp), update the position of the optimal solution using the selected strategy. Calculate its fitness, and then decide whether to update the position according to the greedy rule.
- (7) Check if the termination condition is satisfied. If it is, output the results and exit the program. If not, repeat steps (3) through (6).

The flow chart is shown in Figure 1.

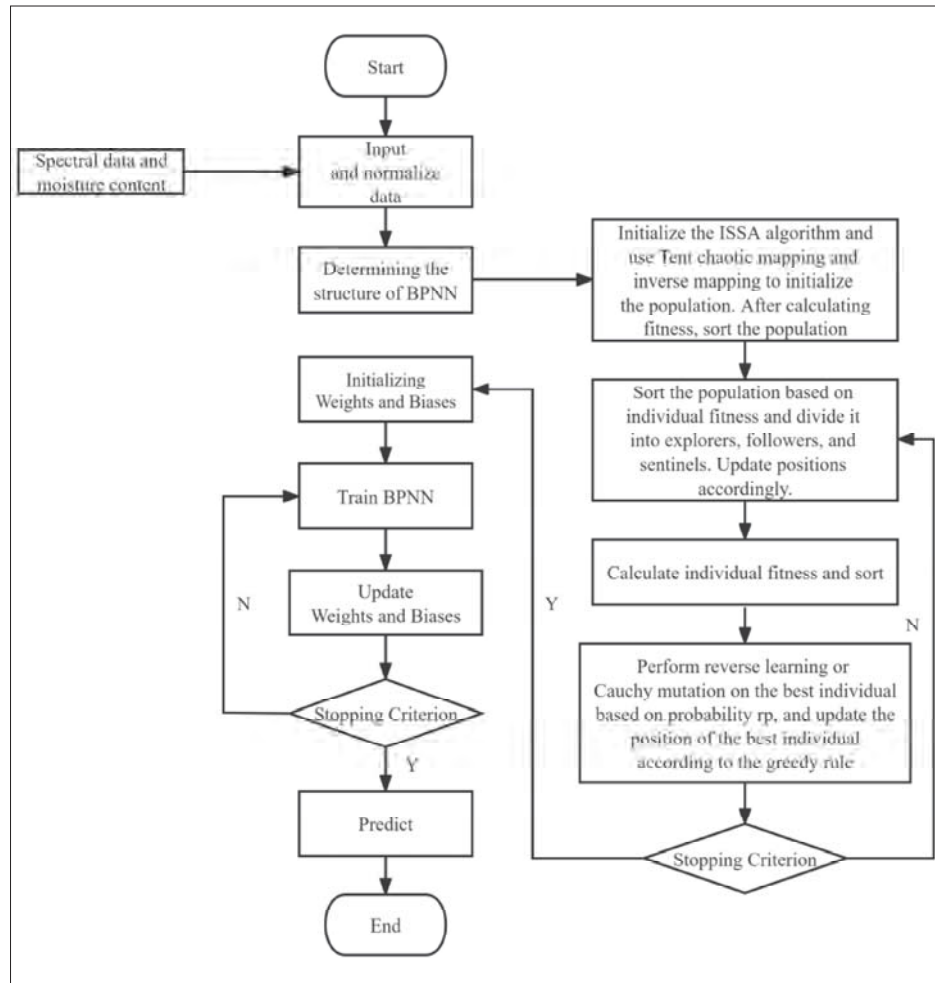


Figure 1: ISSA-BPNN Flowchart

**Modelling with SPA-ISSA-BPNN**

**Preprocessing of spectral data**

During the near-infrared inspection process, factors such as light leakage, fluctuations in light intensity, and sample contamination can cause interference, resulting in anomalies in the spectral data. These anomalies can significantly affect the predictive performance of the established ISSA-BPNN model. Therefore, it is necessary to remove outliers from the spectral data prior to modelling. First, principal component analysis (PCA) is applied to the spectral data. The score plot of the first two principal components is shown in Figure 2. Subsequently,

Hotelling’s T2 statistic ellipse with a confidence level of 95% is used to detect outliers. Sample number 32, with a moisture content of 0.9%, was found to be outside the ellipse, indicating that it is an outlier that needs to be removed.

Comparison of SVR model performance with and without removing outliers from spectral data. The performance metrics of the support vector regression (SVR) models constructed using spectral data before and after removing outliers are compared in Table 2. The validation performance of the model is significantly improved after outlier removal.

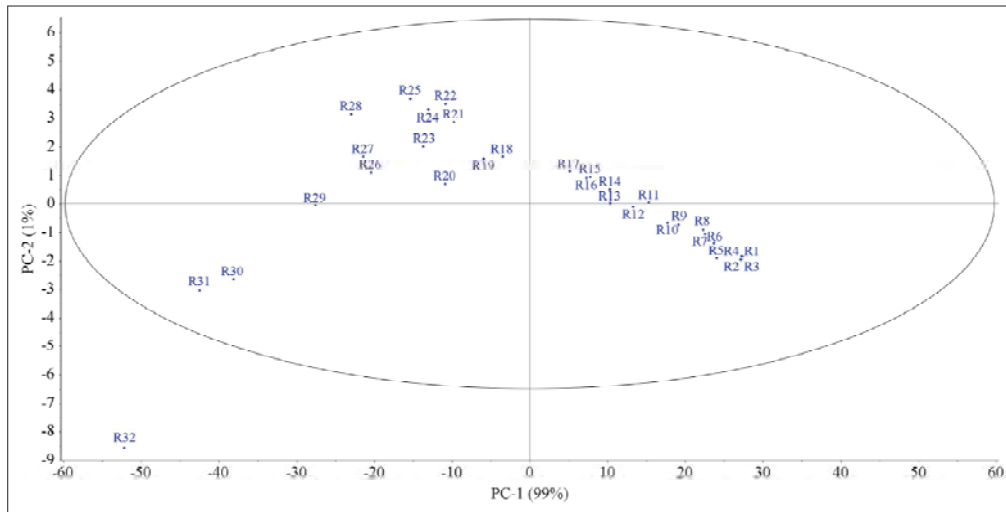


Figure 2: Score plot of PCA analysis

Table 2: Comparison of SVR Model performance metrics using spectral data before and after outlier removal

Model	$R^2_C$	$R_{MSE}^C$	$R^2_V$	$R_{MSE}^V$
Before remove outliers	0.9468	$5.081 \times 10^{-4}$	0.9283	$5.974 \times 10^{-4}$
After remove outliers	0.9454	$4.958 \times 10^{-4}$	0.9380	$5.314 \times 10^{-4}$

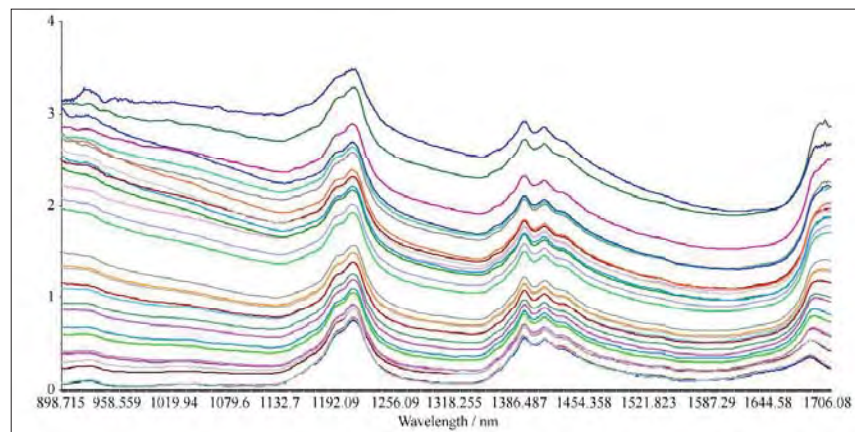


Figure 3: Raw spectra after outlier removal

Figure 3 shows the raw spectra of oil samples with various moisture contents after removing outliers. It is evident that the spectra of the oil samples with varying moisture

contents follow a similar trend to that of the moisture-free oil, with variations only in the intensity values. However, characteristic peaks are not visible in the original spectra,



and the spectra contain considerable noise making it difficult to build the ISSA-BPNN model. To address this issue, the original spectra were subjected to polynomial smoothing using a S-G convolution with a polynomial

order of 2 and a window width of 7. Subsequently, OSC was applied for further spectral processing. The processed spectral data are shown in Figure 4.

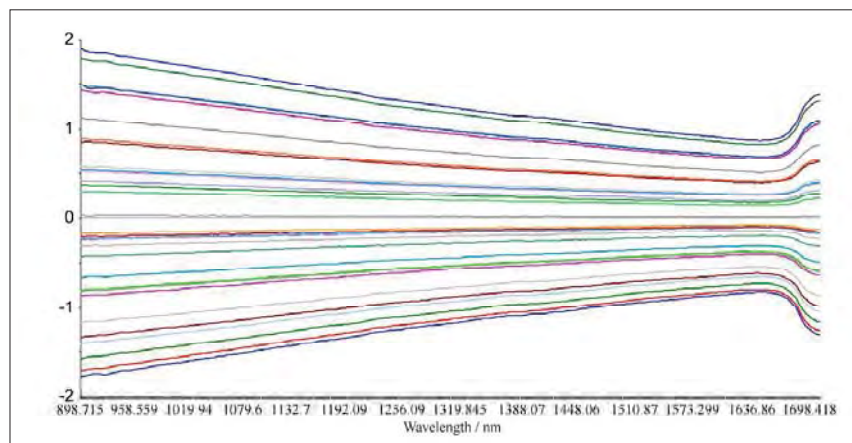


**Figure 4:** Spectral data after S-G filtering and OSC processing

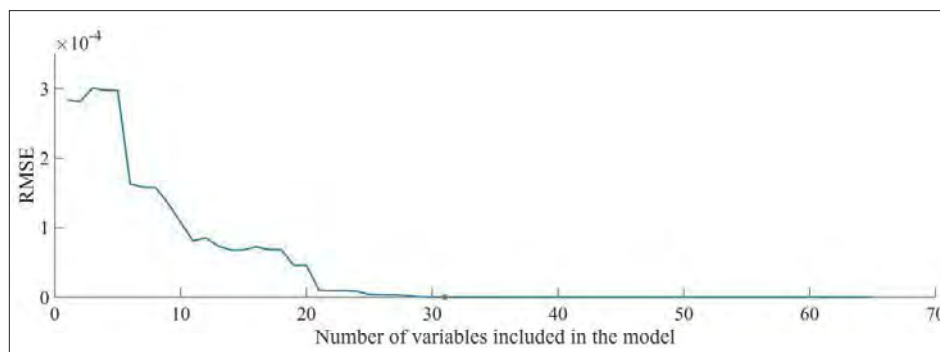


**Figure 5:** RMSE variation curve with different numbers of feature wavelengths

Due to the high volume of raw spectral data from the oil samples, which included many irrelevant spectral regions, the time for model building was prolonged, and the accuracy of predictions was compromised. Therefore, it was necessary to perform feature wavelength selection on the spectra. In this study, Spectral Projection Analysis (SPA) was utilized for selecting the spectral feature wavelengths. The wavelength extraction range was set from 25 to 50. The wavelengths selected by SPA were used to construct multiple linear regression (MLR) models. The RMSE values of the test sets for different

numbers of selected feature wavelengths are shown in Figure 5. It can be observed that the RMSE value of the test set decreases to a minimum when the number of selected wavelengths is 31 and remains stable thereafter. The specific selected wavelengths are listed in Table 3. The wavelengths selected by SPA are mostly clustered around 950 nm, 1220 nm, 1420 nm, 1500-1600 nm, and 1700 nm. Among them, 950 nm corresponds to the second harmonic absorption band of the O-H bond stretching vibration, 1220 nm corresponds to the combined frequency absorption band of O-H in water, and 1420 nm

corresponds to the first harmonic absorption band of O-H stretching vibration. The range of 1500-1600 nm may correspond to the vibration absorption peak of

C-H. Finally, 1700 nm corresponds to the first harmonic absorption band of O-H groups in water.

**Table 3:** Wavelengths selected by SPA algorithm

Algorithm	Number of selected wavelengths	Wavelength				
SPA	31	898.715	913.277	927.836	950.476	
		953.709	961.792	971.489	973.105	976.337
		986.031	987.646	1000.567	1002.182	1224.119
		1359.553	1381.738	1411.786	1441.76	1455.931
		1518.695	1524.951	1534.327	1562.403	1579.52
		1591.949	1655.376	1670.775	1689.214	1690.749
		1695.351	1707.611			

Principal component regression (PCR) models were constructed using the data after removing outliers. Data processed by S-G convolution smoothing and OSC, and data processed by S-G convolution smoothing and OSC after SPA feature selection, are shown in Table 4. It can be observed that the models constructed using preprocessed spectral data have better parameters compared to the models constructed using original spectral data. Both

R<sup>2</sup>C and R<sup>2</sup>V have improved by approximately 0.06, and RMSEC and RMSEV have decreased by approximately 50%. Moreover, the data after SPA feature selection shows a slight improvement in performance compared to the full spectrum processed with SG smoothing and OSC. This indicates that the feature wavelength selection has eliminated a significant amount of irrelevant information, further enhancing the performance of the model.

**Table 4:** PCR results of spectral data before and after preprocessing

Preprocessing method	R <sup>2</sup> <sub>C</sub>	R <sub>MSE</sub> <sup>C</sup>	R <sup>2</sup> <sub>V</sub>	R <sub>MSE</sub> <sup>V</sup>
Original	0.9371	5.128×10 <sup>-4</sup>	0.9368	6.843×10 <sup>-4</sup>
SG (7,2) + OSC	0.9855	2.270×10 <sup>-4</sup>	0.9818	2.435×10 <sup>-4</sup>
SPA+SG (7,2) + OSC	0.9868	2.234×10 <sup>-4</sup>	0.9880	2.441×10 <sup>-4</sup>

### Neural network modelling

To establish a model capable of predicting water content in oil and to assess its accuracy, the remaining 31 samples, after preprocessing, were randomly divided into a training set and a test set. The training set contained 24 samples,

while the test set contained 7 samples. The models were constructed using the selected SPA spectra dataset from the training set and the corresponding input standard BPNN and incremental sparse spectrum analysis with ISSA-BPNN. The parameters for the BPNN and ISSA algorithms are shown in Table 5.

**Table 5:** Parameters of BPNN and ISSA algorithm

Algorithm	Parameter name	Parameter value
BPNN	Training function	trainbr
	Maximum epochs	400
	Goal	$1 \times 10^{-4}$
	Ratio of training set and validation set	4:1
	Pop size	30
	Maximum iterations	80
	Explore ratio	0.4
	Follower ratio	0.6
	Sentinel ratio	0.4
	Upper bound	5
ISSA	Lower bound	-5
	Warning value	0.8
	Fitness function	MAE

## RESULTS AND DISCUSSION

The fitness evolution curve during the neural network iterations is shown in Figure 6. It can be observed that the fitness value reaches its minimum after 17

iterations, ranging between 0.010 and 0.011. This result demonstrates the strong global optimisation capability of the SSA algorithm, which effectively enhances the prediction accuracy of the BPNN.

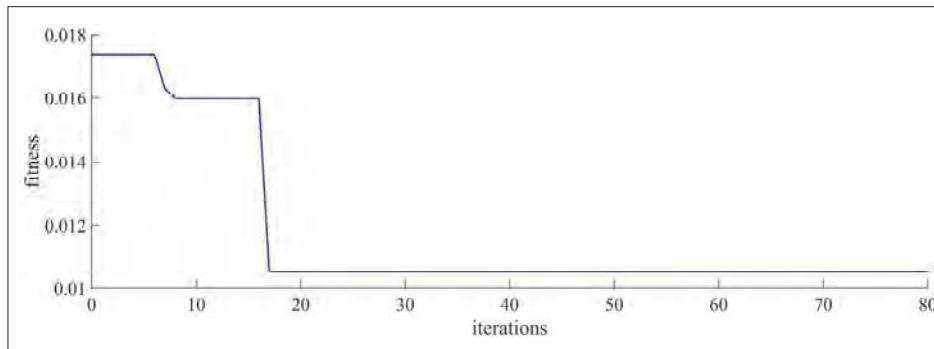


**Figure 6:** Fitness evolution curve during iterations

To visually demonstrate the significant improvement brought about by the ISSA-optimised BPNN, predictions were made on the test set using SPA-ISSA-BPNN, SPA-BPNN, and PCR models with identical training parameters. The results were then compared with the

actual values, as shown in Figure 7. It is evident from the comparison that the predictive performance of the model constructed by SPA-ISSA-BPNN is significantly superior to those constructed by BPNN and PCR.

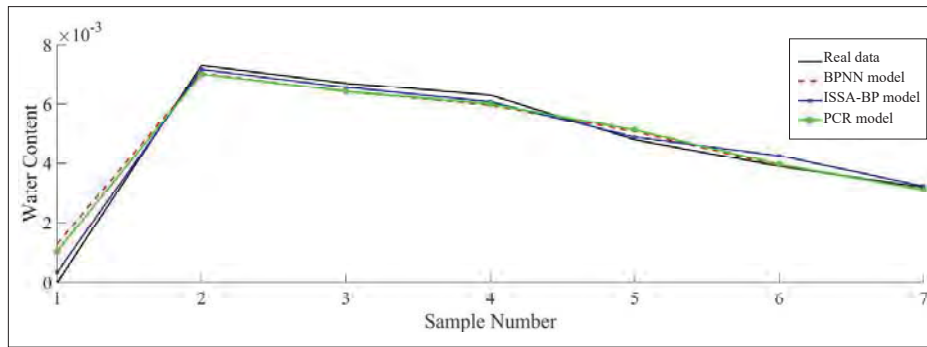


Figure 7: Comparison between Predicted Values and Actual Values

The residual comparison between the predicted values from the SPA-ISSA-BPNN, SPA-BPNN, and SPA-PCR models on the test set and the actual values is shown in Figure 8. It is evident that the residuals of the predicted

values from the SPA-ISSA-BPNN model are significantly lower than those of the SPA-BPNN and SPA-PCR model predictions when compared to the actual values.

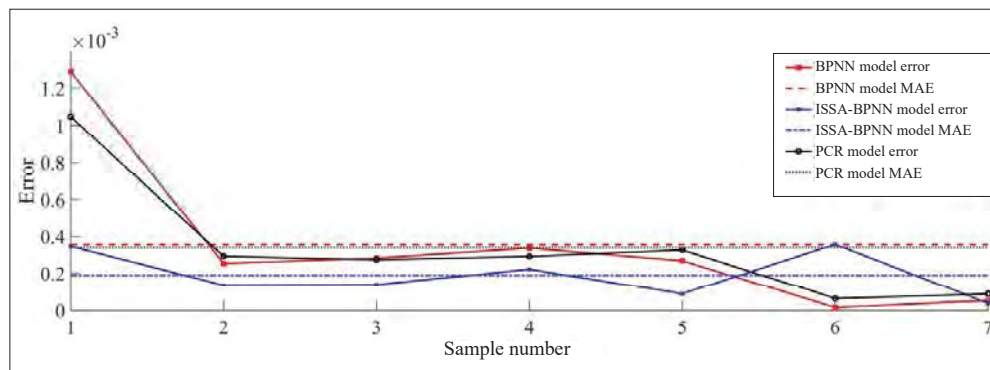


Figure 8: Comparison of residuals and mean absolute errors of predicted values

Table 6: Comparison of model performance metrics

Model	R <sup>2</sup>	R <sub>MSE</sub>	MAE
SPA-ISSA-BP	0.9910	2.2136×10 <sup>-4</sup>	1.8889×10 <sup>-4</sup>
SPA-BP	0.9479	5.3335×10 <sup>-4</sup>	3.5635×10 <sup>-4</sup>
SPA-PCR	0.9619	4.5656×10 <sup>-4</sup>	3.4009×10 <sup>-4</sup>

Using the coefficient of determination (R<sup>2</sup>), root mean square error (RMSE), and mean absolute error (MAE) as evaluation metrics, the comparison of the prediction

performance metrics for the SPA-ISSA-BPNN, SPA-BPNN, and SPA-PCR models is presented in Table 6. It can be observed that the SPA-ISSA-BP model reduced the R<sub>MSE</sub> and MAE by 2.272×10<sup>-5</sup> and 1.6746×10<sup>-4</sup>, respectively, compared to the SPA-BP model, with an increase in R<sup>2</sup> of 0.0431. The SPA-ISSA-BP model decreased the RMSE and MAE by 2.3520×10<sup>-5</sup> and 1.5120×10<sup>-4</sup>, respectively, compared to the SPA-PCR model, with an increase in R<sup>2</sup> by 0.0291. In conclusion, the initial weights and biases of the BPNN are random, which often causes the network to get stuck in local minima during training, resulting in high residual errors and low prediction accuracy. However, the ISSA-

optimised BPNN can effectively explore the solution space, and avoid getting stuck in local minima, and thus increasing the likelihood of the network converging to the global optimum. PCR, being a linear regression model, may not fully capture the nonlinear relationship between the spectral data and the component to be measured. Therefore, the residual errors of the ISSA-optimised BPNN model are smaller than those of the non-optimised BPNN model and the PCR model, indicating the higher prediction accuracy. This meets the practical accuracy requirements for the detection of water content in engine oil.

## CONCLUSION

In this study, near-infrared spectroscopy was used for the quantitative analysis of 31 samples with water contents ranging from 0% to 0.9%. The acquired spectral data were subjected to outlier removal, followed by S-G convolution and OSC processing. Subsequently, the SPA algorithm was used to select the feature wavelengths. The processed data were divided into training and test sets. A SPA-ISSA-BPNN model based on the selected feature wavelengths was established using the training set, and its predictive performance was compared with that of a regular BPNN model. The results showed that the performance metrics of the PCR models constructed using spectral data processed with SG, OSC, and SG, OSC, SPA were superior to those of the PCR model constructed using raw spectral data. Among these, the model built using spectral data processed with SG, OSC, and SPA showed better predictive performance than the model built using data processed with SG, OSC, thus reducing the complexity of the model. SPA-BP and SPA-ISSA-BPNN network models were developed using data processed with SG, OSC, and SPA. The performance metrics of the SPA-ISSA-BP model were superior, with an  $R^2$  of 0.99103, RMSE of  $2.2136 \times 10^{-4}$ , and MAE of  $1.8889 \times 10^{-4}$ .

In conclusion, the developed SPA-ISSA-BP engine oil water content prediction model utilizes SPA for feature wavelength selection, reducing the number of wavelengths required for modelling and simplifying model complexity. Additionally, the ISSA algorithm optimises the weights and biases of the BPNN network, further improving the model's accuracy and robustness. The constructed SPA-ISSA-BP engine oil water content prediction model ultimately achieves rapid detection of the water content in SAE 10W-30 engine oil. Although this study specifically focuses on SAE 10W-30 engine oil, the proposed method has broad applicability and potential. It provides a reference for monitoring the water

content in other types of engine oil, which is crucial for ensuring the long-term stability and safe operation of engines.

## Acknowledgments

The authors are grateful to National Natural Science Foundation of China (Grant number:51375516) and Open Project of Key Laboratory of Environmental Biotechnology (Grant number:kf2021004) for financial support.

## REFERENCES

- Abdel-Aziz, M. H., El-Ashtouky, E. S. Z., Zoromba, M. S., & Bassyouni, M. (2016). Oil-in-water emulsion breaking by electrocoagulation in a modified electrochemical cell. *International journal of electrochemical science*, *11*(11), 9634-9643.  
<https://doi.org/10.20964/2016.11.53>
- Ali, M., & Pant, M. (2011). Improving the performance of differential evolution algorithm using Cauchy mutation. *Soft Computing*, *15*(5), 991-1007.  
<https://doi.org/10.1007/s00500-010-0655-2>
- Alimova, Z., Akhmatjanov, R., Kholikova, N., & Karimova, K. (2021). Ways to improve the anticorrosive properties of motor oils used in vehicles. *E3S Web of Conferences*, *264*, Article 05004.  
<https://doi.org/10.1051/e3sconf/202126405004>
- Chen, B., & Liu, G. (2020). Research progress in on-line monitoring methods of micro-water content in transformer oil. *High Voltage Engineering*, *46*(4), 1405-1416.  
<https://doi.org/10.13336/j.1003-6520.hve.20200430034>
- Chiappini, F. A., Teglia, C. M., Forno, A. G., Goicoechea, & H. C. (2020). Modelling of bioprocess non-linear fluorescence data for at-line prediction of etanercept based on artificial neural networks optimised by response surface methodology. *Talanta*, *210*, Article 120664.  
<https://doi.org/10.1016/j.talanta.2019.120664>
- Fardin-Kia, A. R., Karunathilaka, S. R., Yakes, B. J., Lee, K., Ellsworth, Z., Brückner, L., & Mossoba, M. M. (2019). A rapid, univariate ft-nir procedure to determine moisture concentration in olive oil. *Journal of Oleo Science*, *68*(11), 1105-1112.  
<https://doi.org/10.5650/jos.ess19118>
- Gharehchopogh, F. S., Namazi, M., Ebrahimi, L., & Abdollahzadeh, B. (2023). Advances in sparrow search algorithm: a comprehensive survey. *Archives of Computational Methods in Engineering*, *30*(1), 427-455.  
<https://doi.org/10.1007/s11831-022-09804-w>
- Hensel, J. K., Carpenter, A. P., Ciszewski, R. K., Schabes, B. K., Kittredge, C. T., Moore, F. G., & Richmond, G. L. (2017). Molecular characterization of water and surfactant aot at nanoemulsion surfaces. *Proceedings of the National Academy of Sciences*, *114*(51), 13351-13356.  
<https://doi.org/10.1073/pnas.1700099114>

- Jia, Z., Wang, Z., Li, X., Qiu, H., Hou, G., & Fan, P. (2023). Marine sediment particle size classification based on the fusion of principal component analysis and continuous projection algorithm. *Spectroscopy and Spectral Analysis*, 43(10), 3075-3080.  
[https://doi.org/10.3964/j.issn.1000-0593\(2023\)10-3075-06](https://doi.org/10.3964/j.issn.1000-0593(2023)10-3075-06)
- Khamidullaevna, A. Z., & Bahtiyor H T. (2022). Studies of anticorrosive properties motor oils and ways to improve. *European International Journal of Multidisciplinary Research and Management Studies*, 2(06), 6-12.  
<https://doi.org/10.55640/eijmrms-02-06-02>
- Li, Y., Han, M., & Guo, Q. (2020). Modified whale optimization algorithm based on tent chaotic mapping and its application in structural optimization. *KSCE Journal of Civil Engineering*, 24(12), 3703-3713.  
<https://doi.org/10.1007/s12205-020-0504-5>
- Liu, C., Tang, X., Yu, T., Wang, T., Lu, Z., & Yu, W. (2020). Measurement of moisture content in lubricating oils of high-speed rail gearbox by vis-nir spectroscopy. *Optik*, 224, Article 165694.  
<https://doi.org/10.1016/j.ijleo.2020.165694>
- Liu, G., Chen, B., Shang, Z. X., & Quan, Y. X. (2023). Near infrared spectroscopy analysis of moisture in engine oil. *Spectroscopy and Spectral Analysis*, 43(2), 449-454.  
[https://doi.org/10.3964/j.issn.1000-0593\(2023\)02-0449-06](https://doi.org/10.3964/j.issn.1000-0593(2023)02-0449-06)
- Liu, H. M., Liu, Y. J., Zhong, Z. C., Song, Y., Li, Z., & Xu, Y. (2021). Detection and analysis of water content of crude oil by near infrared spectroscopy. *Spectroscopy and Spectral Analysis*, 41(2), 505-510.  
[https://doi.org/10.3964/j.issn.1000-0593\(2021\)02-0505-06](https://doi.org/10.3964/j.issn.1000-0593(2021)02-0505-06)
- Liu, K., Gao, G., Wang, F., Wu, D., Wu, Z., & Gong, Y. (2023). Research on oil-water two-phase water content detection model based on near-infrared spectroscopy, *Third International Symposium on Computer Engineering and Intelligent Communications*, 12462, Article 124620L.  
<https://doi.org/10.1117/12.2660957>
- Peng, Y., He, M., Zheng, Z., & He, Y. (2023). Enhanced neural network for rapid identification of crop water and nitrogen content using multispectral imaging. *Agronomy*, 13(10), Article 2464.  
<https://doi.org/10.3390/agronomy13102464>
- Wang, F., Xie, B., Lü, E., Zeng, Z., Mei, S., Ma, C., & Guo, J. (2023). Design of a moisture content detection system for yinghong no. 9 tea leaves based on machine vision. *Applied Sciences*, 13(3), Article 1806.  
<https://doi.org/10.3390/app13031806>
- Xie, W., Gong, Y., & Yu, K. (2018). Efficient quantification of water content in edible oils by headspace gas chromatography with vapour phase calibration. *Journal of the Science of Food and Agriculture*, 98(8), 3208-3212.  
<https://doi.org/10.1002/jsfa.8795>
- Xu, Z., Su, Y., Yang, F., & Zhang, M. (2023). A whale optimization algorithm with distributed collaboration and reverse learning ability. *Computers, Materials and Continua*, 75(3), 5965-5986.  
<https://doi.org/10.32604/cmc.2023.037611>
- Xue, J., & Shen, B. (2020). A novel swarm intelligence optimization approach: sparrow search algorithm. *Systems Science and Control Engineering*, 8(1), 22-34.  
<https://doi.org/10.1080/21642583.2019.1708830>
- Zhang, D., Liu, J., Yang, L., Cui, T., He, X., Yu, T., & N. O. Kheiry, A. (2021). Application of swarm intelligence algorithms to the characteristic wavelength selection of soil moisture content. *International Journal of Agricultural and Biological Engineering*, 14(6), 153-161.  
<https://doi.org/10.25165/j.ijabe.20211406.6629>
- Zhao, Y., Xu, X., Jiang, L. L., Zhang, Y., Tan, L. H., & He, Y. (2010). Determination of water content in automobile lubricant using near-infrared spectroscopy improved by machine learning analysis. *International Conference on Information Science and Applications*, 2010, 1-8.  
<https://doi.org/10.1109/ICISA.2010.5480392>
- Zhen, Z., Wang, H., Yue, Y., Li, D., & Li, J. (2020). Determination of water content of crude oil by azeotropic distillation karl fischer coulometric titration. *Analytical and Bioanalytical Chemistry*, 412(12).  
<https://doi.org/10.1007/s00216-020-02714-5>
- Zhou, F., & Yang, K. (2021). The influence of water content on the acid number of diesel engine lubricant in electrochemical measurement. *IOP Conference Series. Materials Science and Engineering*, 1043(5), 52054.  
<https://doi.org/10.1088/1757-899X/1043/5/052054>

## RESEARCH ARTICLE

### Environmental Science

# Bioaccumulation and health risks of chromium and cadmium in *Basella alba* with emphasis on Urea, muriate of potash and triple super phosphate mixtures

MDMCK Amarasena and WMDN Wijeyaratne\*

Department of Zoology and Environmental Management, Faculty of Science, University of Kelaniya, Dalugama, Kelaniya, Sri Lanka.

Submitted: 21 October 2023; Revised: 19 June 2024; Accepted: 09 August 2024

**Abstract:** *Basella alba* is a commonly consumed green leafy vegetable in South Asian countries and it is considered as an economical source of essential vitamins and dietary fibers. Urea, muriate of potash (MOP) and triple super phosphate (TSP) mixture is the most commonly used inexpensive fertilizer mixture in the commercial cultivation of *B. alba*. This study was conducted to assess the effect of using a mixture of Urea-MOP-TSP on the bioaccumulation potential of cadmium (Cd) and chromium (Cr) by the leaves of *B. alba*. Pots treated with the Urea-MOP-TSP mixture and compost were maintained in a greenhouse with controlled light and temperature settings. The concentrations of Cd and Cr in the root zone soil, roots and leaves of *B. alba* were analyzed using an Atomic Absorption Spectrophotometer after acid digestion. The health risk of consuming *B. alba* was evaluated using the daily intake of metals, health risk index and cancer risk index. The results showed that Cd and Cr can bioaccumulate in the leaves of *B. alba*. The bioaccumulation potential of Cr was higher than that of Cd. Although the daily intake of Cd and Cr from *B. alba* were below the maximum values stipulated by the WHO, the cancer risk index indicated potential cancer risks based on Cd intake due to consumption of *B. alba* cultivated using the Urea-MOP-TSP mixture. Furthermore, the health risks associated with the hyper-accumulation of Cd and Cr in the edible parts of *B. alba* cultivated using compost were significantly less compared to that of the plants treated with the Urea-MOP-TSP mixture. Therefore, if *B. alba* is cultivated using chemical fertilizer, it is recommended to regularly monitor the concentrations of Cd and Cr in the cultivation soil, chemical fertilizer and in the edible parts of *B. alba* to prevent the excessive buildup of Cd and Cr along the food chain. In addition, it is recommended to identify the potential microbial assemblages that can be inoculated to the cultivation soil to reduce the bioavailability of Cd and Cr.

**Keywords:** Bioconcentration, cadmium, cancer, chromium, daily intake of metals, hyperaccumulation.

## INTRODUCTION

Green leafy vegetables are nutritional foods that contain high concentrations of dietary fibers, vitamins and minerals. The phyto-chemicals found in the edible parts of green leafy vegetables have antioxidative and anti-inflammatory properties that provide health benefits to consumers (Brouwer-Brolsma *et al.* 2020). The nutritional and health benefits of green leafy vegetables have led to an increase in the consumer demand resulting in their cultivation on a commercial basis. Commercial cultivations mainly focus on increasing yield by applying chemical fertilizers in the cultivation plots (Upekshani *et al.* 2018).

Essential plant nutrients are added to the soil in commercial cultivations by applying chemical fertilizer mixtures, which contain nitrate, phosphate, and potassium. However, the fertilizer formulations contain organic and inorganic contaminants such as heavy metals, which have the potential to cause adverse impacts in the receiving environment (AlKhader 2015). Compared to organic fertilizers and soil modifiers, inorganic fertilizers breakdown easily when added to the soil. However, the quick breakdown of inorganic fertilizers can lead to contamination of the soil in agricultural fields. The main nitrogenous and phosphatic fertilizers can modify

\* Corresponding author ([dimuthu.wijeyaratne@kln.ac.lk](mailto:dimuthu.wijeyaratne@kln.ac.lk); <https://orcid.org/0000-0002-3502-0410>)



This article is published under the Creative Commons CC-BY-ND License (<http://creativecommons.org/licenses/by-nd/4.0/>). This license permits use, distribution and reproduction, commercial and non-commercial, provided that the original work is properly cited and is not changed in anyway.

the physical soil properties such as bulk density, hydraulic conductivity and can also alter the soil structure (Rashmi *et al.* 2020, Alengebawu *et al.*, 2021)

The root system of green leafy vegetables can absorb heavy metals, which can then accumulate in the edible and non-edible parts of the plant. This uptake of heavy metals can lead to a decrease in the nutritional quality of the vegetables and disrupt metabolic functions. As a result, essential nutrients may not be absorbed properly, chlorophyll synthesis may be inhibited, and enzymatic responses to oxidative stress can be induced (Edelstein *et al.*, 2018, Chaturvedi *et al.* 2019, Pavlíková *et al.*, 2023). Consumers may experience significant health impairments from consuming green leafy vegetables with accumulated metals, leading to chronic and acute toxic responses with prolonged consumption (Amin *et al.* 2013; Shakya & Khwaounjoo 2013; Wijeyaratne & Kumari 2021).

*Basella alba*, also known as Malabar spinach, is a very popular green leafy vegetable in South Asian countries due to their high fiber and mineral content (Deshmukh & Gaikwad, 2014). *B. alba* is a creeping vine commonly grown as a pot herb in home gardens in India, Sri Lanka and Indonesia. It can be easily cultivated in a variety of soils and is adaptable to extreme climatic conditions (Gayathree *et al.* 2020). However, several studies have shown that *B. alba* has the capacity to accumulate high concentrations of cadmium (Cd) and chromium (Cr) compared to other commonly consumed green leafy vegetables available in the market.

Furthermore, it has been noted that there are significantly high hazard quotients and health risk index values for Cd and Cr in comparison to As, Ni, Pb, Cu and Zn (Kananke *et al.* 2014; Sultana *et al.* 2019). However, these studies were conducted using samples from local markets in South Asian cities. Therefore there is no information available on the cultivation methods or irrigation water used for cultivation. Some studies conducted on *B. alba* cultivations were irrigated using textile wastewater, which recorded high concentrations of Cd and Cr in the edible parts of the plant and have been identified as potential health risks associated with long-term consumption (Alam *et al.* 2003; Shammi *et al.* 2016). These studies indicate a high risk associated with the accumulation of Cd and Cr in *B. alba*.

The consumer demand for *B. alba* in South Asian countries has increased in the past decade as it is a good source of nutrients at an affordable cost. Commercial cultivations of *B. alba* commonly use a fertilizer mixture of urea, muriate of potash (MOP) and triple super

phosphate (TSP). This fertilizer mixture provides the essential nutrients required for the growth of the plant and is very effective in producing a greener and higher quality *B. alba* desired by consumers to the market (Rosliza *et al.* 2009). However, the application of Urea, MOP and TSP can affect the mobility of Cd and Cr in the soil solution and can increase the uptake of these heavy metals by plants (Bandara *et al.* 2008; Jayasumana *et al.* 2015). Therefore, the present study focused on assessing the concentrations of Cd and Cr in the edible parts of *B. alba* cultivated using the above fertilizer mixture. Furthermore, the health risks associated with the consumption of leaves of *B. alba* cultivated using a mixture of Urea, MOP and TSP was also assessed. This was done in terms of the bioconcentration factor (BCF), soil to root translocation factor (TF (soil – root)), root to leaf translocation factors (TF (root – leaf)), target hazard quotient (THQ), hazard index (HI) and cancer risk index (CI) for Cd and Cr.

## MATERIALS AND METHODS

Soil samples were collected at a depth of 0-25 cm from the Landscape Management Unit of the University of Kelaniya, Sri Lanka. The study was conducted in a greenhouse at the University of Kelaniya, Sri Lanka.

### Preparation of the experimental units

Air dried soil samples were sieved through a 4 mm sieve, and used in the seed germination trays (44 x 214 x 52 mm) and in the experimental pots (pot volume: 2 L; pot height: 13 cm; pot diameter - top: 17 cm: pot diameter - bottom: 13 cm). *B. alba* seeds were purchased from the local market and germinated in the seed germination trays. After two weeks, healthy seedlings (6 seedlings per pot) were transplanted into individual prewashed plastic pots which contained 2.5 kg of sieved, air-dried soil.

Two sets of experiments namely Set 1: (chemical fertilizer urea, MOP and TSP mixture applied pots), and Set 2: (organic fertilizer with compost applied pots) were arranged in a randomized block design. Each set consisted of twenty replicate pots. The plants were watered regularly with well water and grown under natural light conditions.

### Physical and chemical properties of soil, compost and water

The physical and chemical properties of the soil samples, compost samples and water used for watering the plants were assessed using standard laboratory methods. The pH, and conductivity were measured using a calibrated digital



multiparameter water quality meter (YSI Environmental Model-556 MPS). The moisture content of the soil and compost samples was determined by the gravimetric method. The total organic matter content (TOM) and the  $\text{CaCO}_3$  content were determined by the mass loss on ignition method ( $550^\circ\text{C}$ , until a constant weight is attained) using a muffle furnace. The bulk density of the soil was determined using the core method and the bulk density of compost was determined by the method described by Ahn *et al.*, (2004). A 10 liter graduated cylinder was filled with compost and slightly compacted to eliminate large void spaces. The bulk density was then calculated by dividing the weight of the compost by the volume of compost in the graduated cylinder (Ahn *et al.* 2004). The percentage of gravel, clay, silt and sand content in the soil was determined using the pipette method as described by Bowman and Hutka (2002).

The soil and compost samples were acid-digested and the water samples acidified by adding concentrated  $\text{HNO}_3$  until the pH reached 6.0-6.5. The concentrations of Cd and Cr in the acid digested samples were analyzed using an atomic absorption spectrophotometer (Analytic Jena Model novAA 400p).

#### Application of fertilizer

Two weeks after transplanting, 25 g of a mixture containing urea, muriate of potash (MOP), and triple super phosphate (TSP) in a ratio of 2:1:1 was added to each experimental pot in Set 1, and 25 g of a commercial compost mixture was added to each experimental pot in Set 2 as recommended by the Department of Agriculture, Sri Lanka (2007).

#### Sampling of plants and soil

Sampling was conducted on three occasions at 4 wks, 8 wks and 12 wks (at the end of culture cycle) after fertilizer application. At each sampling event, two *B. alba* plants with their root zone soil were sampled from each pot. The roots and leaves of the plant samples were separated, thoroughly washed with distilled water and air-dried. The air-dried root and leaf samples were then oven-dried at  $105^\circ\text{C}$  until they reached a constant weight. The dried samples were then ground into a powder by using a clean electric grinder. The powdered samples were sieved through a 0.4 mm sieve and kept in a desiccator until they were acid digested.

The air-dried root-zone soil samples were oven-dried at  $105^\circ\text{C}$  until they reached a constant weight. These samples were ground into fine particles using a pre-acid

washed commercial mortar and pestle. The ground soil was sieved through a 2 mm sieve and samples were stored in a desiccator until they were ready for acid digestion.

#### Acid digestion of plant and soil samples

Acid digestion and metal analysis of the samples were done by following the procedure described in Wijeyaratne and Kumari (2021).

Powdered and homogenized leaf, root and soil samples (0.5 g) were acid digested in the Gerhardt Kjeldatherm digestion system at  $270^\circ\text{C}$  for 2 h using concentrated  $\text{HNO}_3$  and concentrated  $\text{HClO}_4$  in a 1:1 (v/v) ratio as the digestion medium. The digested solutions were allowed to cool and 5 mL of deionized water was added. The dissolved solution was swirled and filtered into a 50 mL volumetric flask through Whatman filter paper number 42. The clear solution was then diluted up to 50 mL with deionized water and analyzed for Cd and Cr by atomic absorption spectrophotometer (Analytic Jena Model novAA 400p) in the graphite furnace mode following the procedure described by the American Public Health Association (APHA, 1999).

The minimum detection limits for Cd and Cr were 0.02 mg/L and 0.001 mg/L, respectively. Sandy loam certified reference material CRM 023 (Sigma-Aldrich, USA) was used as the standard reference material for soil analysis, and white cabbage certified reference material BCR 485 (Sigma-Aldrich, USA) was used as the standard reference material for plant analysis. Continuing control verification was done after every 10 samples to ensure that variability was within 10%.

The accuracy of the analytical procedure was determined by calculating the percentage recovery of Cd and Cr in the spiked sample as described by Addis and Abebaw (2017). Soil and plant samples were spiked in triplicates at a known calibration concentration of Cd and Cr. The same digestion and analysis procedure was followed for both the original samples (non-spiked) and the spiked samples. The percentage recoveries of Cd and Cr were then calculated to evaluate the accuracy of the analytical procedure by the formula described by Addis and Abebaw (2017).

Percentage recovery of the metal (%R) =  $\frac{S_n - U_n}{A_n} \times 100$   
Where,

$S_n$  – Concentration of metal in the spiked sample  
 $U_n$  – Concentration of metal in the non-spiked sample  
 $A_n$  – Spiked concentration

### Bioconcentration factor and translocation factors

The heavy metal concentrations were used to calculate the bioconcentration factor, soil-to-root translocation factor, and root-to-leaf translocation factor of Cd and Cr in *B. alba* as described by Sulaiman *et al.* (2016) and Wijeyaratne and Kumari (2021).

The bio-concentration factor (BCF) of *B. alba* at the end of the culture cycle was calculated by the following formula:

$$BCF = \frac{C_{Plant}}{C_{Soil}}$$

Where,  $C_{plant}$  is the metal concentration in the plant part (leaves) and  $C_{soil}$  is the metal concentration in the soil (Wijeyaratne & Kumari 2021).

The soil to root translocation factor ( $TF_{s-R}$ ) at the end of the culture cycle was calculated by the following formula (Wijeyaratne & Kumari 2021):

$$TF_{s-R} = \frac{C_R}{C_S}$$

Where,  $C_R$  is the metal concentration in roots and  $C_S$  is the metal concentration in soil.

Root to leaf translocation factor ( $TF_{R-L}$ ) at the end of the culture cycle was calculated by the following formula (Wijeyaratne & Kumari 2021).

$$TF_{R-L} = \frac{C_L}{C_R}$$

Where  $C_L$  is the metal concentration in leaves and  $C_R$  is the metal concentration in roots.

### Assessing the health risks associated with consumption of *B. alba*

The health risks associated with the consumption of *B. alba* were calculated based on the daily intake of metals for Cd ( $DIM_{Cd}$ ) and Cr ( $DIM_{Cr}$ ), health risk index for Cd ( $HRI_{Cd}$ ) and Cr ( $HRI_{Cr}$ ), and cancer risk for Cd ( $CR_{Cd}$ ) and Cr ( $CR_{Cr}$ ).

The daily intake of Cd and Cr from *B. alba* was calculated using the following formula described by Gebreyohannes and Gebrekidan (2018):

$$DIM = \frac{C_{Metal} \times C_{Factor} \times D_F}{w}$$

Where,

$DIM$ : Daily Intake for Metal;

$C_{Metal}$ : Concentration of the metal (mg/kg);

$C_{Factor}$ : Conversion factor to convert fresh vegetable weight to dry weight (0.085 for green leafy vegetables (Benson *et al.* 2002));

$D_F$ : Daily average intake of green leafy vegetables (USEPA 2007a, USEPA 2007b, WHO/FAO 2007);

$w$ : Average body weight of a person (70 kg for adults and 30 kg for children (Walpole *et al.* 2012)).

The health risk index of *B. alba* for Cd and Cr was calculated using the following formula described by Gebreyohannes and Gebrekidan (2018):

$$HRI = \frac{DIM}{RoD}$$

Where,

$HRI$ : Health Risk Index for metal;

$DIM$ : Daily Intake for Metal;

$RoD$ : Reference oral Dose for metal (Cd: 0.001; Cr: 1.5 (Benson *et al.* 2002)).

An  $HRI < 1$  is considered safe for the exposed human populations (Gebreyohannes and Gebrekidan 2018; Khan *et al.*, 2020; Wijeyaratne and Kumari 2021).

The cancer risk index (CI) of *B. alba* for Cd and Cr was calculated using the following formula described by Gebeyehu and Bayissa (2020):

$$CI = DIM \times CPS_0$$

Where,

$CI$ : Cancer risk for metal;

$DIM$ : Daily intake for metal;

$CPS_0$ : the oral cancer

slope factor in (mg/kg/day)<sup>-1</sup>.  $CPS_0$  for Cd: 0.38 and  $CPS_0$  for Cr: 0.5 (Zeng *et al.* 2015; Yang *et al.* 2018).

### Statistical analysis

The Anderson Darling test was used to test for the normality of data and the non-normalized data were log-transformed.

The Student's t-test was used to compare the concentrations of Cd and Cr in the roots, leaves and root zone soil of *B. alba* across treatments where compost, Urea, MOP and TSP were applied at each sampling event. One-way analysis of variance followed by Tukey's

pairwise comparison was used to analyze the variation of Cd and Cr concentrations in the roots, leaves and root zone soil of *B. alba* in pots treated with compost and a mixture of urea, MOP and (TSP) over a culture cycle. Additionally, the variation of health risk assessment indices for Cd and Cr in the different treatments were analysed. Data analysis was conducted using R statistical software.

## RESULTS AND DISCUSSION

The physical and chemical properties of the soil, compost and water used in the experiment are given in Table 1. The soil used as the experimental medium had a sandy loam texture with a mean pH of 7.4. The physical and chemical properties of the soil medium and the compost were within favorable ranges for plant growth (Table 1).

**Table 1:** Physical and chemical properties of the soil, compost and water used in the experiment pots

Physical/Chemical Property	Soil	Compost	Water
pH	7.4 ± 0.2	7.6 ± 0.2	7.2 ± 0.1
Conductivity (µS/cm)	610.2 ± 31.2	410.5 ± 24.3	385.2 ± 25.2
Total organic matter content (%)	2.8 ± 0.6	35.6 ± 1.2	Not Applicable
Bulk density (g/cm <sup>3</sup> )	1.55 ± 0.4	0.64 ± 0.2	Not Applicable
Moisture content (%)	22.8 ± 1.3	23.1 ± 1.5	Not Applicable
CaCO <sub>3</sub> concentration (%)	4.5 ± 0.3	2.2 ± 0.3	Not Applicable
Percentage clay (%)	6.3 ± 1.3	Not Applicable	Not Applicable
Percentage silt (%)	41.0 ± 3.5	Not Applicable	Not Applicable
Percentage sand (%)	42.5 ± 2.6	Not Applicable	Not Applicable
Gravel content (%)	10.2 ± 1.8	Not Applicable	Not Applicable
Cd Concentration	1.39 ± 0.17	0.76 ± 0.23	Not detected
Cr Concentration	15.62 ± 0.5	15.6 ± 0.64	Not Detected

### Cadmium and chromium concentrations in the root zone soil of *B. alba* at the sampling events

Mean concentrations of Cd and Cr in the root zone soil of *B. alba* at different sampling events are given in Table 2.

Results are presented as Mean ± SD. In each row at a particular sampling event, the mean values with different superscript letters are significantly different from each other. (Student t- test,  $p < 0.05$ ;  $n = 40$ ). MOP: muriate of potash; TSP: triple super phosphate.

The mean concentration of Cd in the root zone of the soil ranged from 0.54 to 1.86 mg/kg and the mean concentration of Cr ranged from 15.59 to 19.67 mg/kg. The highest mean Cd and Cr concentrations were recorded in the root zone of the soil collected from the Urea-MOP-TSP mixture applied samples at the third sampling event (Table 2).

The mean concentrations of Cr were higher than the mean concentrations of Cd in both treatments at all sampling events. The concentrations of Cd and Cr in the root zone of the soil of *B. alba* collected from pots where Urea-MOP-TSP mixture was applied were significantly higher than those in pots where compost was applied at the second and third sampling events (Student's t-test,  $p < 0.05$ ; see Table 2). However, there was no significant difference in the concentrations of Cd and Cr between the pots that were applied with a Urea-MOP-TSP mixture and those with compost in the first sampling event (Student's t-test,  $p > 0.05$ ; see Table 2). The concentrations of Cd and Cr in the soil increased significantly after 8 and 12 weeks following the application of chemical fertilizer. The soil Cd concentration increased due to the application of phosphate fertilizer, which contain Cd based additives. If the amount of Cd added by the fertilizer exceeds the removal of Cd through leaching, bioturbation or erosion, prolonged application of phosphate fertilizer can significantly increase the Cd concentrations in agricultural soil (Grant & Sheppard 2008; AlKhader 2015).

**Table 2:** Mean concentrations of Cd and Cr in the root zone soil of *B. alba* collected from pots applied with urea, muriate of potash (MOP) and triple super phosphate (TSP) mixture and compost.

Metal	Concentration (mg/kg)	
	Urea, MOP and TSP mixture	Compost
Sampling Event 1: Four weeks after fertilizer application		
Cd	1.393 ± 0.17 <sup>a</sup>	0.758 ± 0.23 <sup>a</sup>
Cr	15.62 ± 0.53 <sup>a</sup>	15.59 ± 0.64 <sup>a</sup>
Sampling Event 2: Eight weeks after fertilizer application		
Cd	1.803 ± 0.10 <sup>a</sup>	0.542 ± 0.24 <sup>b</sup>
Cr	19.50 ± 0.49 <sup>a</sup>	16.44 ± 0.53 <sup>b</sup>
Sampling Event 3: Twelve weeks after fertilizer application / End of culture cycle		
Cd	1.864 ± 0.15 <sup>a</sup>	1.314 ± 0.21 <sup>a</sup>
Cr	19.67 ± 0.49 <sup>a</sup>	16.352 ± 0.36 <sup>b</sup>

In the compost applied treatments, the concentration of Cd in the root zone of the soil at the 12<sup>th</sup> week after fertilizer application (at the end of the culture cycle/ Sampling Event 3) showed a significant increase, while the concentration of Cr in the root zone of the soil did not show a significant increasing trend throughout the culture cycle. Organic substances in the compost can enhance formation of metal-humic complexes, which can increase solubility and bioavailability of Cd in the compost

applied soil (Hanc *et al* 2009; Chaab *et al.* 2016). This could be a reason for the increase in Cd concentration in the root zone of the soil in the compost applied pots. The concentrations of Cd and Cr in the root zone of the soil recorded, in this study, were lower than the maximum permissible limits for heavy metals in vegetable growing soils stipulated by the European Union (180 mg/kg for Cr and 3.0 mg/kg for Cd).

**Table 3:** Mean concentrations of Cd and Cr in the roots of *B. alba* collected from pots applied with urea, muriate of potash (MOP) and triple super phosphate (TSP) mixture and pots applied with compost.

Metal	Concentration (mg/kg)	
	Urea, MOP and TSP mixture	Compost
Sampling Event 1: Four weeks after fertilizer application		
Cd	2.12 ± 0.06 <sup>a</sup>	1.94 ± 0.34 <sup>a</sup>
Cr	13.9 ± 0.49 <sup>a</sup>	13.36 ± 0.62 <sup>a</sup>
Sampling Event 2: Eight weeks after fertilizer application		
Cd	2.30 ± 0.19 <sup>a</sup>	1.54 ± 0.21 <sup>b</sup>
Cr	20.07 ± 0.59 <sup>a</sup>	13.42 ± 0.31 <sup>b</sup>
Sampling Event 3: Twelve weeks after fertilizer application / End of culture cycle		
Cd	2.782 ± 0.19 <sup>a</sup>	1.714 ± 0.18 <sup>b</sup>
Cr	22.39 ± 0.66 <sup>a</sup>	16.215 ± 0.26 <sup>b</sup>

### Concentrations of cadmium and chromium in the roots of *B. alba* at the sampling events

Mean concentrations of Cd and Cr in the roots of *B. alba* at different sampling events are given in Table 3. The mean concentration of Cd in the roots of *B. alba* ranged from 1.54 to 2.78 mg/kg, and the mean concentration of Cr ranged from 13.36 to 22.39 mg/kg. The highest mean concentrations of Cd and Cr were found in the roots of *B. alba* collected from the pots treated with the Urea, MOP, TSP mixture at the end of the culture cycle (Table 3).

Results are presented as mean  $\pm$  SD. In each row at a particular sampling event, the mean values with different superscript letters are significantly different from each other (Student t- test,  $p < 0.05$ ;  $n = 40$ ). MOP: muriate of potash; TSP: triple super phosphate.

There was no significant difference in the concentrations of Cd and Cr in the roots of *B. alba* between the samples applied with urea, MOP, TSP and compost in the first sampling event (Student's t- test,  $p > 0.05$ , Table 2). However, in the second and third sampling events, the concentrations of Cd and Cr were significantly high in the roots of *B. alba* in the pots applied with urea, MOP and TSP compared to the pots applied with compost ( $p < 0.05$ , Table 3). Several studies have documented that, the mobility and bioavailability of Cd and Cr are influenced by the soil structure, availability of organic matter and soil pH. Furthermore, it has been reported that chemical fertilizers containing  $\text{NH}_4^+$  can reduce the pH of the soil within 8-10 weeks, increasing the mobility of Cd and Cr (Liao *et al.*, 2019; Senila and

Kovacs 2024). This may have resulted in increasing the bioavailability of Cd and Cr, in the present study, to be taken up by the roots of *B. alba*.

### Cadmium and chromium concentrations in the leaves of *B. alba* at the sampling events

Mean concentrations of Cd and Cr in the leaves of *B. alba* at different sampling events are given in Table 4. The mean concentration of Cd in leaves of *B. alba* ranged from 0.69 to 3.38 mg/kg while the mean Cr concentration ranged from 13.48 to 23.35 mg/kg. The mean concentration of Cr in the leaves of the *B. alba* was significantly higher than that of Cd in all sampling events in both treatments. Trends in the variation of Cd and Cr concentration in the leaves of *B. alba* were similar to that of the roots.

In the first sampling event, there was no significant difference in the concentrations of Cd and Cr in the leaves of *B. alba* harvested from the two treatments. However, in the subsequent sampling events, the concentrations of Cr and Cd in the leaves of *B. alba* harvested from the pots applied with the Urea-MOP-TSP mixture were significantly higher than those harvested from the pots applied with compost (Student t test,  $p < 0.05$ , Table 4). The recorded concentrations of Cr and Cd in leaves of *B. alba* harvested from both the treatments, exceeded the safe levels recommended by the WHO/FAO (2.3mg/kg for Cr and 0.2 mg/kg for Cd) (Tajik *et al.*, 2021).

Results are presented as Mean  $\pm$  SD. In each row at a particular sampling event, the mean values with different superscript letters are significantly different from each other (Student t- test,  $p < 0.05$ ;  $n = 40$ ).

**Table 4:** Mean concentrations of Cd and Cr in the leaves of *B. alba* collected from pots applied with (i) urea, muriate of potash (MOP) and triple super phosphate mixture (TSP) mixture, and (ii) Compost.

Metal	Concentration (mg/kg)	
	Urea, MOP and TSP mixture	Compost
Sampling Event 1: Four weeks after fertilizer application		
Cd	1.76 $\pm$ 0.20 <sup>a</sup>	0.91 $\pm$ 0.38 <sup>a</sup>
Cr	13.80 $\pm$ 0.53 <sup>a</sup>	13.48 $\pm$ 0.61 <sup>a</sup>
Sampling Event 2: Eight weeks after fertilizer application		
Cd	2.83 $\pm$ 0.14 <sup>a</sup>	0.69 $\pm$ 0.40 <sup>b</sup>
Cr	19.75 $\pm$ 0.50 <sup>a</sup>	18.08 $\pm$ 0.32 <sup>b</sup>
Sampling Event 3: Twelve weeks after fertilizer application / End of culture cycle		
Cd	3.38 $\pm$ 0.18 <sup>a</sup>	2.33 $\pm$ 0.092 <sup>b</sup>
Cr	23.35 $\pm$ 0.89 <sup>a</sup>	17.85 $\pm$ 0.50 <sup>b</sup>

### Cadmium and chromium concentrations in roots, leaves and the root zone soil of *B. alba* in the pots applied with Urea-MOP-TSP mixture and compost, over a culture cycle

There was a significant increase in the concentration of Cr in roots, leaves, and in the rootzone soil in the pots applied with Urea-MOP-TSP mixture in the successive sampling events towards the end of the culture cycle (ANOVA, Tukey's pairwise comparison,  $p < 0.00$ , Table 2, Table 3, Table 4).

The concentration of Cd in the roots of *B. alba* in the pots treated with compost was significantly higher than that in the leaves and root zone soil during the first and second sampling events. However, the concentration of Cd was significantly high in the leaves of *B. alba* harvested from the pots treated with compost at the end of the culture cycle (ANOVA, Tukey's pairwise comparison,  $p < 0.00$ , Figure 2). Similarly, an increasing trend and significantly high concentrations of Cr were recorded in the leaves of *B. alba* in the pots treated with compost and harvested during the second and third sampling events (ANOVA, Tukey's pairwise comparison,  $p < 0.00$ , Table 2, Table 3, Table 4). Therefore, the results of this study indicate that there is a possibility of the bioaccumulation of Cd and Cr in the leaves of *B. alba* towards the end of the culture cycle.

Similar results were reported by Noor *et al* (2023) who found high concentrations of Cd and Cr in the edible parts of spinach (*Spinacia oleracea*) in rural areas of Pakistan. Another study conducted using a pot experiment, with contaminated and non-contaminated soils, to assess the accumulation of heavy metals and major nutrients in leaves of spinach, revealed high levels of Cr (Zakir *et al.*, 2018).

#### Bioconcentration factor

The bioconcentration factors of *B. alba* harvested from pots applied with a Urea-MOP-TSP mixture and compost are given in Figure 1.

The bioconcentration factor of Cd for *B. alba* in pots applied with the Urea-MOP-TSP mixture ranged from 1.4 to 2.5 and for compost from 1.2 to 2.2 (Figure 1). The bioconcentration factor of Cr for *B. alba* in pots applied with the Urea-MOP-TSP mixture ranged from 0.7 to 1.7 and for compost from 0.75 to 1.5. (Figure 1). The mean bioconcentration factors for Cd and Cr in *B.*

*alba* from pots applied with the Urea-MOP-TSP mixture were not significantly different from those in the pots applied with compost (ANOVA,  $p > 0.05$ , Figure 1). The bioconcentration factor is a measure of the uptake, mobilization, and efficiency of heavy metal accumulation in plant tissues. A bio-concentration factor higher than 1 indicates a potential for hyperaccumulation (Raj *et al.*, 2020). In this study, it is evident from the results that *B. alba* is a potential hyperaccumulator for both Cd and Cr.

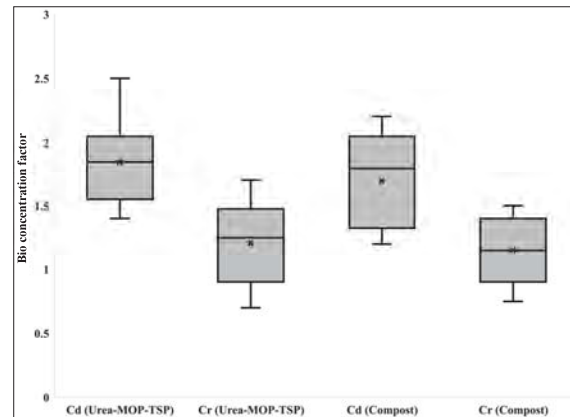


**Figure 1:** Bioconcentration factors for Cd and Cr of *B. alba* harvested at the end of the culture cycle from the pots applied with the Urea-MOP-TSP mixture and compost.

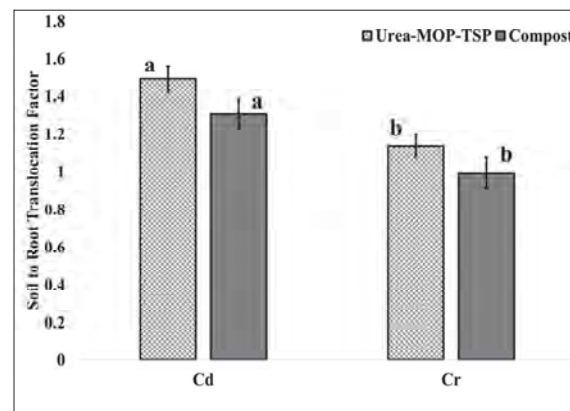


**Figure 2:** The soil to root translocation factors (TF<sub>s-r</sub>) for Cd and Cr of *B. alba* harvested from pots applied with the Urea-MOP-TSP mixture and compost at the end of the culture cycle.

### Translocation factor

The soil to root translocation factor ( $TF_{S-R}$ ) and root to leaf translocation factors ( $TF_{R-L}$ ) for Cd and Cr at the end of the culture cycle of *B. alba*, harvested from pots applied with the Urea-MOP-TSP mixture and compost are given in Figure 2 and Figure 3, respectively.

The  $TF_{S-R}$  of Cd ranged from 1.1 to 1.6 and for Cr it ranged from 0.8 to 1.1 (Figure 2). The  $TF_{R-L}$  for Cd ranged from 0.9 to 1.4 and for Cr from 0.9 to 1.3 (Figure 3).

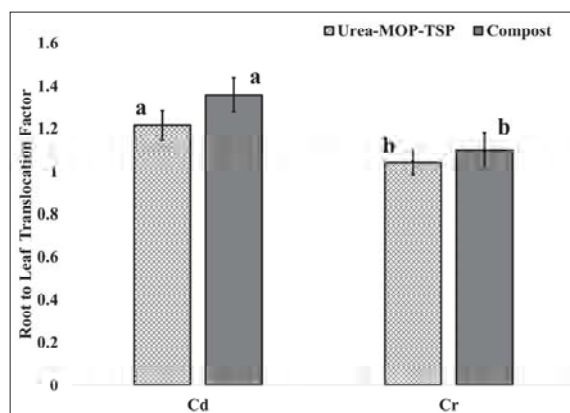


**Figure 3:** The root to soil translocation factors ( $TF_{R-S}$ ) for Cadmium and Chromium of *B. alba* harvested from pots applied with the Urea-MOP-TSP mixture and at the end of the culture cycle.

Mean  $TF_{S-R}$  and  $TF_{R-L}$  for Cd and Cr of *B. alba* in the pots applied with Urea-MOP-TSP mixture and compost were not significantly different from each other (ANOVA,  $p > 0.05$ , see Figure 2, Figure 3). The translocation factor is a measure of the movement of heavy metals from the soil to the roots and from roots to the leaves of a plant, and another factor that can be used to assess the hyperaccumulator ability of plants (Wijeyaratne & Kumari 2021). The  $TF_{R-L}$  for both Cd and Cr is higher than that of the  $TF_{S-R}$  in both the pots treated with Urea-MOP-TSP and compost (Figure 2, Figure 3). This is consistent with the conclusion of the BCF indicating that leaves of *B. alba* are hyperaccumulators of Cd and Cr irrespective of the use of chemical fertilizer or organic amendments.

It has been reported that Cr and Cd have a tendency to accumulate in the roots rather than in the shoots,

which decreases the bioaccumulation potential of these heavy metals in plants (Chaab *et al.* 2016). However, the results of this study do not agree with Chaab *et al.* (2016) since the bioconcentration factor, the soil to root translocation factor, and the root to leaf translocation factor for Cr and Cd in *B. alba* were greater than 1. This indicates a bioaccumulation potential for these heavy metals in the edible parts of *B. alba*. Furthermore, the bioconcentration factor, the soil to root translocation factor, and the root to leaf translocation factor for Cd in *B. alba* were higher than those of Cr indicating a higher bioaccumulating capacity for Cd in the edible parts of *B. alba* compared to Cr. The decreased bioaccumulation of Cr in the leaves of *B. alba* may be due to the ability of Cd to inhibit the translocation of Cr within the plant as seen in *Spinacea oleracea* L. (Çelik and Kunene 2021).

Additionally, studies on microbial interactions in the composting process have revealed that, inoculation of nitrogen retaining microbial agents into the compost helps to reduce the bioavailability of Cd and Cr (Guo *et al.*, 2022; Wang *et al.* 2023). Therefore, further studies should focus on the identification and propagation of such natural assemblages of nitrogen retaining microbial communities in the commercial cultivation of *B. alba* to reduce the risks associated with the hyperaccumulation of these heavy metals in the edible parts of *B. alba*.

### Assessing the health risks associated with consumption of *B. alba*

The daily metal intake values, health risk index and cancer index for adults and children based on concentrations of Cd and Cr in *B. alba* harvested from pots applied with urea, MOP, TSP and compost are given in Table 5.

The daily intake of Cr from *B. alba* by adults and children was significantly higher than that of Cd in both the urea, MOP, TSP mixture and compost treatments. However, the health risk index values for Cd in *B. alba* harvested from the Urea-MOP-TSP mixture treatment were significantly higher than that of the compost treated sites, for both adults and children, based on the recommended daily intake values by the FAO (Table 5). Further, the Cd based cancer risk index of *B. alba* harvested from the pots applied with Urea-MOP-TSP was significantly higher compared to that of the compost treatment for both adults and children. The Cr based cancer risk index for *B. alba* did not show significant variations among treatments for both adult and child populations. (Table 5).

**Table 5:** Daily metal intake (mg/day), health risk index and cancer risk index for adults and children based on the concentrations Cd and Cr in *B. alba*.

	Cd		Cr	
	Urea, MOP and TSP mixture	Compost	Urea, MOP and TSP mixture	Compost
Daily metal intake (Adult) (mg/day)	0.014 ± 0.0 <sup>a</sup>	0.007 ± 0.0 <sup>c</sup>	0.07 ± 0.0 <sup>b</sup>	0.07 ± 0.0 <sup>b</sup>
Daily metal intake (Children) (mg/day)	0.007 ± 0.0 <sup>a</sup>	0.0004 ± 0.0 <sup>c</sup>	0.004 ± 0.0 <sup>b</sup>	0.0004 ± 0.0 <sup>b</sup>
Health Risk Index (Adult)	1.4 ± 0.01 <sup>a</sup>	0.7 ± 0.03 <sup>c</sup>	0.05 ± 0.0 <sup>b</sup>	0.05 ± 0.0 <sup>b</sup>
Health Risk Index (Children)	0.7 ± 0.001 <sup>a</sup>	0.04 ± 0.001 <sup>c</sup>	0.003 ± 0.0 <sup>b</sup>	0.003 ± 0.0 <sup>b</sup>
Cancer Risk (Adult)	0.005 ± 0.001 <sup>a</sup>	0.00003 ± 0.0 <sup>c</sup>	0.0035 ± 0.0 <sup>b</sup>	0.0035 ± 0.0 <sup>b</sup>
Cancer risk (Children)	0.003 ± 0.001 <sup>a</sup>	0.00001 ± 0.0 <sup>c</sup>	0.002 ± 0.0 <sup>b</sup>	0.002 ± 0.0 <sup>b</sup>

Results are presented as Mean ± SD. The mean values with different superscript letters in each row are significantly different from each other (ANOVA, Tukey's pairwise comparison,  $p < 0.05$ ;  $n = 40$ ). MOP: muriate of potash; TSP: triple super phosphate.

Even though heavy metals bioaccumulate in the edible parts of green leafy vegetables, their toxic effects on consumers are controlled by the daily intake of metals. The maximum tolerable daily intake for Cd ranges between 0.02–0.07 mg/day, and for Cr between 0.035–0.2 mg/day (Kamunda *et al.* 2016; Shaheen *et al.* 2016). According to this study, the daily intake values of Cd and Cr from consuming *B. alba* by both adults and children did not exceed the maximum tolerable daily intake values. The health risk index is also important for assessing the health risks in dietary items. A health risk index greater than 1 indicates the possibility of significant health risks for consumers (Wijeyaratne & Kumari 2021). In this study, for Cd, the health risk index for adults and children by consuming *B. alba* cultivated using a mixture of Urea-MoP-TSP and compost was 1.4 and 0.7, respectively (Table 5). Therefore, there is a potential for Cd-associated health impairments in adults consuming *B. alba* cultivated using the mixture Urea-MoP-TSP.

Further, the cancer risk index for Cd and Cr for *B. alba* for both treatments exceeded the acceptable upper limit of  $1 \times 10^{-4}$  (Gebreyohannes & Gebrekidan 2018) for the risk of developing cancer due to long-term consumption.

Similar results were also recorded in studies conducted in Ethiopia (Gebreyohannes & Gebrekidan 2018) and Bangladesh (Sultana *et al.*, 2019) on the health risks associated with the consumption of vegetables.

## CONCLUSION

It is possible for *B. alba* leaves to hyperaccumulate Cd and Cr, irrespective of the type of fertilizer applied. The long term dietary intake of *B. alba* grown with chemical fertilizer is associated with a higher risk of health issues related to Cr and Cd. Therefore, reducing of chemical fertilizer use, adopting organic farming practices and introducing nitrogen-retaining microbial communities into compost are recommended to mitigate the health risks associated with the dietary intake of *B. alba*.

## Acknowledgements

The authors wish to acknowledge the Department of Zoology and Environmental Management, University of Kelaniya, Sri Lanka and the International Foundation for Science (IFS), Sweden.

Availability of data and materials: Data are available on request from the authors

Funding: The research project was funded by Grant I-3-E-6048-1 by the International Foundation for Science (IFS), Sweden.



## REFERENCES

- Addis, W., & Abebaw, A. (2017). Determination of heavy metal concentration in soils used for cultivation of *Allium Sativum* L. (Garlic) in East Gojjam Zone, Amhara Region, Ethiopia. *Cogent Chemistry*, 3(1), 1419422. <https://doi.org/https://doi.org/10.1080/23312009.2017.1419422>.
- Ahn, H. K., Richard, T. L., Glanville, T. D., Harmon, J. D., & Reynolds, D. L. (2004). Laboratory determination of compost modeling parameters. *ASAE Annual International Meeting*, 4913 - 4927. <https://doi.org/10.13031/2013.16772>. 16p
- Alam, M. G. M., Snow, E. T., & Tanaka, A. (2003). Arsenic and heavy metal contamination of vegetables Grown in Samta Village, Bangladesh. *Science of the Total Environment* 308 (1–3), 83-96. [https://doi.org/10.1016/s0048-9697\(02\)00651-4](https://doi.org/10.1016/s0048-9697(02)00651-4)
- Alengebawy, A., Abdelkhalek, S. T., Qureshi, S. R., & Wang, M. Q. (2021) Heavy metals and pesticides toxicity in agricultural soil and plants: Ecological risks and human health implications. *Toxics*, 259(3),42. Article: 33668829. <https://doi.org/10.3390/toxics9030042>
- AlKhader, F., & Asad, M. (2015). The Impact of phosphorus fertilizers on heavy metals content of soils and vegetables grown on selected farms in Jordan. *Agrotechnology* 05 (01), 1-5. <https://doi.org/10.4172/2168-9881.1000137>
- Amin, N. U., Hussain, A., Alamzeb, S., & Begum, S. (2013). Accumulation of heavy metals in edible parts of vegetables irrigated with waste water and their daily intake to adults and children, District Mardan, Pakistan. *Food Chemistry* 136(3-4), 1515-1523. <https://doi.org/10.1016/j.foodchem.2012.09.058>.
- APHA (1999). Standard methods for the examination of water & wastewater 21st Edition. American Public Health Association; American Water Works Association, Water Environment Federation.
- Bandara, J. M. R. S., Senevirathna, D. M. A. N., Dasanayake, D. M. R. S. B., Herath, V., Bandara, J. M. R. P., Abeysekara, T., & Rajapaksha, K. H. (2008). Chronic renal failure among farm families in cascade irrigation systems in Sri Lanka associated with elevated dietary Cadmium levels in rice and freshwater fish (Tilapia). *Environmental Geochemistry and Health*, 30(05), 465-78. <https://doi.org/10.1007/s10653-007-9129-6>
- Benson, B., Mills, A., & Wood, B. (2002). A review of the reference dose and reference concentration process. *Risk Assessment Forum*, U.S. Environmental Protection Agency, Washington, D.C.
- Bowman, J., & Hutka, G. M. (2002). Particle Size Analysis. In *Soil Physical Measurement and Interpretation for Land*. CSIRO Publishing: Victoria.
- Brouwer-Brolsma, E. M., Beate, B., Marion, E. C. B., Thomas, S., & Claudine, M. (2020). Food Intake biomarkers for green leafy vegetables, bulb vegetables, and stem vegetables: A review. *Genes and nutrition* 15(1), Article PMC7144047. <https://doi.org/10.1186/S12263-020-00667-Z>
- Çelik, H. & Kunene, S.S. (2021). Assessment of heavy metal amounts of spinach plants (*Spinach oleracea* L.) grown on Cd and chicken manure applied soil conditions. *Polish Journal of Environmental Studies*. 30(2), 1105-1115. <https://doi.org/10.15244/pjoes/125481>.
- Chaab, A., Moezzi, A.A., Sayyad, G.A., & Chorom, M. (2016). Effect of compost and humic acid in mobility and concentration of Cadmium and Chromium in soil and plant. *Global Journal of Environmental Science and Management* 2(4), 389-96. <https://doi.org/10.22034/gjesm.2016.02.04.008>.
- Chaturvedi, R., Favas, P. J. C., Pratas, J., Varun, M. & Paul, M.S. (2019) Metal(loid) induced toxicity and defense mechanisms in *Spinacia oleracea* L.: Ecological hazard and prospects for phytoremediation. *Ecotoxicology and Environmental Safety*, 183, Article 109570. <https://doi.org/10.1016/j.ecoenv.2019.109570>
- Department of Agriculture (2007). *Fertilizer recommendations for horticultural crops*. Department of Agriculture, Peradeniya, Sri Lanka
- Deshmukh, S.A., & Gaikwad, D.K. (2014). A review of the taxonomy, ethnobotany, phytochemistry and pharmacology of *Basella alba* (Basellaceae). *Journal of Applied Pharmaceutical Science*. 4(1), 153-65. <https://doi.org/10.7324/JAPS.2014.40125>
- Edelstein, M., & Ben-Hur, M. (2018). Heavy metals and metalloids: Sources, risks and strategies to reduce their accumulation in horticultural crops. *Scientia Horticulturae*. 234, 431-444. <https://doi.org/10.1016/j.scienta.2017.12.039>
- Gayathree, T. H. I., Karunarathne, S.I., Ranaweera, L.T., Jayarathne, H.S.M., Kannangara, S.K., Ranathunga, A. P.D.T., Weebadde, C., & Sooriyapathirana, S.S. (2020). Green-spinach, red-spinach, and tree-spinach (three-fold spinach' in Sri Lanka): An insight into phylogenetics and consumer preference. *Emirates Journal of Food and Agriculture*. 32(2), 82-91. <https://doi.org/10.9755/ejfa.2020.v32.i2.2065>
- Gebeyehu, H. R., & Bayissa, L. D. (2020). Levels of heavy metals in soil and vegetables and associated health risks in Mojo Area, Ethiopia. *PLoS ONE*. 15(1), 1-22. <https://doi.org/10.1371/journal.pone.0227883>.
- Gebreyohannes, F., & Gebrekidan, A. (2018). Health risk assessment of heavy metals via consumption of spinach vegetable grown in Elalla river. *Bulletin of the Chemical Society of Ethiopia* 32(1), 65–75. <https://doi.org/10.4314/bcse.v32i1.6>
- Grant, C. A., & Sheppard, S. C. (2008). Fertilizer impacts on Cadmium availability in agricultural soils and crops. *Human and Ecological Risk Assessment: An International Journal*. 14(2), 210-228. <https://doi.org/10.1080/10807030801934895>.
- Guo H., Liu H., & Wu S. (2022). Immobilization pathways

- of heavy metals in composting: Interactions of microbial community and functional gene under varying C/N ratios and bulking agents. *Journal of Hazardous Materials*. 426: 128103.  
<https://doi.org/10.1016/j.jhazmat.2021.128103>
- Hanc, A., Pavel, T., Jirina, S. & Habart, J. (2009). Changes in cadmium mobility during composting and after soil application. *Waste Management*, 29(8), 2282-2288.  
<https://doi.org/10.1016/J.WASMAN.2009.03.027>
- Jayasumana, C., Fonseka, S., Fernando, A., Jayalath, K., Amarasinghe, M., Siribaddana, S., Gunatilake, S., & Paranagama, P. (2015). Phosphate fertilizer is a main source of Arsenic in areas affected with chronic kidney disease of unknown etiology in Sri Lanka. *SpringerPlus*. 4(1), 1–8.  
<https://doi.org/10.1186/S40064-015-0868-Z>
- Kamunda, C., Mathuthu, M., & Madhuku, M. (2016). Health risk assessment of heavy metals in soils from Witwatersrand Gold Mining Basin, South Africa. *International Journal of Environmental Research and Public Health*, 13(7), 663.  
<https://doi.org/10.3390/IJERPH13070663>
- Kananke, T., Wansapala, J., & Gunaratne, A. (2014). Heavy metal contamination in green leafy vegetables collected from selected market sites of Piliyandala Area, Colombo District, Sri Lanka. *American Journal of Food Science and Technology*, 2(5), 139-44.  
<https://doi.org/10.12691/ajfst-2-5-1>
- Khan S., Robina F., Shagufta S., Khan M.A., & Sadique M. (2020). Health risk assessment of heavy metals for population via consumption of pulses and cereals. *International Journal of Biological Innovations*, 2(02), 241- 246.  
<https://doi.org/10.46505/ijbi.2020.2222>
- Liao, Z., Chen, Y., Ma, J., Islam, M.S., Weng, L., & Li Y. (2019). Cd, Cu, and Zn accumulations caused by long-term fertilization in greenhouse soils and their potential risk assessment. *International Journal of Environmental Research and Public Health*, 16(15), Article 2805.  
<https://doi.org/10.3390/ijerph16152805>
- Noor, A.E., Nisa, Z., Sultana, S., Al-Ghanim, K.A., Al-Misned F., Riaz, M.N., Ahmed, Z., & Mahboob S. (2023) Heavy metals toxicity in spinach (*Spinacia oleracea*) irrigated with sanitary wastewater in rural areas, *Journal of King Saud University - Science*, 35(1), Article 102382.  
<https://doi.org/10.1016/j.jksus.2022.102382>
- Pavliková, D., Zemanová, V., & Pavlík M. (2023). Health risk and quality assessment of vegetables cultivated on soils from a heavily polluted old mining area. *Toxics*, 11, Article 583.  
<https://doi.org/10.3390/toxics11070583>
- Raj, D., Kumar, A. & Maiti, S. K. (2020). Mercury remediation potential of *Brassica juncea* (L.) Czern. For clean-up of flyash contaminated sites. *Chemosphere* 248, Article 125857.  
<https://doi.org/10.1016/j.chemosphere.2020.125857>
- Rashmi, I., Roy, T., Kartika, K., Pal, R., Coumar, V., Kala, S., & Shinoji K.C. (2020). Organic and inorganic fertilizer contaminants in agriculture: Impact on soil and water resources. In *Contaminants in agriculture*. (eds: Naeem M. Ansari. A. & Gill S.), Springer, Cham, USA.  
[https://doi.org/10.1007/978-3-030-41552-5\\_1](https://doi.org/10.1007/978-3-030-41552-5_1)
- Rosliza, S., Ahmed, O.H., & Majid, N.M.A. (2009). Controlling ammonia volatilization by mixing urea with humic acid, fulvic acid, triple superphosphate and muriate of potash. *American Journal of Environmental Sciences*, 5(5), 605-609.  
<https://doi.org/10.3844/AJESSP.2009.605.609>
- Senila, M., & Kovacs, E. (2024). Use of diffusive gradients in thin-film technique to predict the mobility and transfer of nutrients and toxic elements from agricultural soil to crops - an overview of recent studies. *Environmental Science and Pollution Research*, 31,34817-34838.  
<https://doi.org/10.1007/s11356-024->
- Shaheen, N., Irfan, N.M, Khan, I.N., Islam, S., Islam, M.S. & Ahmed, M.K. (2016). Presence of heavy metals in fruits and vegetables: Health risk implications in Bangladesh. *Chemosphere*, 152, 431-438.  
<https://doi.org/10.1016/J.chemosphere.2016.02.060>
- Shakya, P. R., & Khwaounjoo, N. M. (2013). Heavy metal contamination in green leafy vegetables collected from different market sites of Kathmandu and their associated health risks. *Scientific World*, 11(11), 37-42.  
<https://doi.org/10.3126/sw.v11i11.8550>
- Shammi, M., Kashem, M.A., Rahman, M.M., Hossain, M.D., Rahman, R., & Uddin, M.K. (2016). Health risk assessment of textile effluent reuses as irrigation water in leafy vegetable *Basella alba*. *International Journal of Recycling of Organic Waste in Agriculture*, 525(2), 113-123.  
<https://doi.org/10.1007/S40093-016-0122-X>
- Sulaiman, F.R., Mustaffa, N.F.S., & Khazaai, S.N.M. (2016). Preliminary assessment of selected metals in agricultural soils in Jengka, Pahang, Malaysia. *Environmental Earth Sciences*, 75(3), 223.  
<https://doi.org/10.1007/s12665-015-4926-1>
- Sultana, M., Mondol, M.N., Mahir, A.A., Sultana, R., Elahi S.F., Afroze, N., & Chamon, A.S. (2019). Heavy metal concentration and health risk assessment in commonly sold vegetables in Dhaka City Market. *Bangladesh Journal of Scientific and Industrial Research*, 54(4), 357-366.  
<https://doi.org/10.3329/bjsir.v54i4.44570>
- Tajik, R., Alimoradian, A., Jamalain, M., Shamsi, M., Moradzadeh, R., Ansari, & Asl B. (2021) Lead and cadmium contaminations in fruits and vegetables, and arsenic in rice: a cross sectional study on risk assessment in Iran. *Iranian Journal of Toxicology*. 15(2),73-82.  
<https://dx.doi.org/10.32598/ijt.15.2.784.1>
- Upekshani, H. A. N., Dharmakeerthi, R S., Weerasinghe, P., & Dandeniya, W.S. (2018). Fertilizer usage and land productivity in intensively cultivated vegetable farming systems in Sri Lanka : An analysis based on a questionnaire survey. . *Tropical Agricultural Research*, 30(1), 44-55.  
<https://doi.org/10.4038/tar.v30i1.8277>
- US EPA, (2007a). Integrated Risk Information System (IRIS). United States EPA, USA.  
<http://www.epa.gov/iris>. Accessed on 14.06.2024.
- US EPA, (2007b). Guidance for evaluating the oral bioavailability of metals in soils for use in human health

- risk assessment. OSWER.
- Walpole, S. C., Prieto-Merino, D., Edwards, P., Cleland, J., Stevens, G., & Roberts I. (2012). The weight of nations: An estimation of adult human biomass. *BMC Public Health*, 12(1), 439.  
<https://doi.org/10.1186/1471-2458-12-439>
- Wang C., Jia Y., Li J., Li P., Wang Y., Yan F., Wu M., Fang W., Xu F., & Qiu Z. (2023). Influence of microbial augmentation on contaminated manure composting: metal immobilization, matter transformation, and bacterial response. *Journal of Hazardous Materials*, 441, Article 129762.  
<https://doi.org/10.1016/j.jhazmat.2022.129762>.
- WHO/FAO, (2007). Joint FAO/WHO Food Standards Program Codex.
- Wijeyaratne W. M. D. N., & Kumari E. A.C. S. ( 2021). Cadmium, chromium, and lead uptake associated health risk assessment of *alternanthera sessilis*: A commonly consumed green leafy vegetable. *Journal of Toxicology*, 17, 2021, Article: 9936254.  
<https://doi.org/10.1155/2021/9936254>.
- Yang, J.S.M., Zhou J., Song Y., & Li F. (2018). Heavy metal contamination in soils and vegetables and health risk assessment of inhabitants in Daye, China. *Journal of International Medical Research*, 46(8), 3374–3387.  
<https://doi.org/10.1177/0300060518758585>
- Zakir, H.M., Aysha, M.I.J., Mallick, S., Sharmin, S., Quadir, Q.F. & Hossain, M.A. (2018). Heavy metals and major nutrients accumulation pattern in spinach grown in farm and industrial contaminated soils and health risk assessment. *Archives of Agriculture and Environmental Science*, 3(1), 95-102.  
<https://doi.org/10.26832/24566632.2018.0301015>
- Zeng F., Wei W., Li M., Huang R., Yang F. & Duan Y. (2015). Heavy metal contamination in rice-producing soils of Hunan Province, China and potential health risks. *International Journal of Environmental Research and Public Health*, 12 (12), 15584.  
<https://doi.org/10.3390/IJERPH121215005>.



## RESEARCH ARTICLE

### Environmental Chemistry

# Effective removal of Pb(II) ions using Fe<sub>3</sub>O<sub>4</sub>/MgO adsorbent: A comprehensive study

V Gurunathanan<sup>1</sup>, KB Wijayaratne<sup>2</sup>, BS Dassanayake<sup>2</sup>, PG Mantilaka<sup>1</sup>, and CS Perera<sup>2\*</sup>

<sup>1</sup> Postgraduate Institute of Science, University of Peradeniya, Peradeniya, Sri Lanka.

<sup>2</sup> Department of Physics, Faculty of Science, University of Peradeniya, Peradeniya, Sri Lanka.

Submitted: 04 August 2023; Revised: 23 March 2024; Accepted: 19 April 2024

**Abstract:** The effective removal of heavy metal ions, particularly Pb(II), from contaminated water sources remains a pressing environmental concern. This study explores the potential of Fe<sub>3</sub>O<sub>4</sub>/MgO nanocomposite as an efficient adsorbent for selective Pb(II) removal. The Fe<sub>3</sub>O<sub>4</sub>/MgO nanocomposite was synthesized using a controlled sol-gel method and characterized using various techniques. X-ray diffraction (XRD) analysis confirmed the presence of cubic MgO and cubic Fe<sub>3</sub>O<sub>4</sub>. Pb(II) adsorption induced a crystallographic transformation, forming hexagonal Mg(OH)<sub>2</sub> crystals, indicating interaction with the adsorbent. Scanning electron microscope (SEM) analysis revealed pyramid-like and irregular crystal morphologies. Pyramid-like structures provided a larger surface area and active sites for effective Pb(II) interaction, while irregular crystal particles, representing magnetic Fe<sub>3</sub>O<sub>4</sub>, contributed to stability and dispersibility. Vibrating sample magnetometer (VSM) results confirmed superparamagnetic behaviour with a saturation magnetization of 32.02 emu g<sup>-1</sup>, indicating potential for magnetic separation and recovery in various wastewater treatment applications. Adsorption experiments utilized optimized conditions: an initial concentration of 600 mgL<sup>-1</sup>, adsorbent dosage of 0.25 gL<sup>-1</sup>, pH of 7, and 120 minutes of reaction time. The Fe<sub>3</sub>O<sub>4</sub>/MgO nanocomposite exhibited exceptional performance with a remarkable 99.98% removal efficiency and a high adsorption capacity of 2399.44 mg g<sup>-1</sup>. These impressive results underscore the outstanding adsorption potential of the nanocomposite. Adsorption kinetics followed the pseudo-second-order model (R<sup>2</sup> = 0.99), confirming suitability for Pb(II) removal. The Freundlich model indicated a heterogeneous surface with different adsorption sites. Overall, the Fe<sub>3</sub>O<sub>4</sub>/MgO nanocomposite exhibits potential

as a cost-effective, environmentally friendly adsorbent for removing Pb(II) ions, providing a promising solution for water purification and environmental remediation.

**Keywords:** Adsorption capacity, chemisorption, environmental remediation, heterogeneous surface, sol-gel method, superparamagnetic behaviour.

## INTRODUCTION

Lead (Pb) contamination in water sources poses a significant threat to human health and the environment due to its toxic nature and potential long-term effects. Exposure to Pb(II) ions can lead to various adverse health outcomes, particularly in children, including neurological damage, developmental disorders, and impaired cognitive functions (Lidsky & Schneider, 2003). Therefore, the development of efficient and sustainable methods for the removal of Pb(II) from contaminated water is of utmost importance. In recent years, nanomaterial-based adsorbents have shown great promise in the removal of heavy metals from aqueous solutions (Perera *et al.*, 2024). Among these nanomaterials, Fe<sub>3</sub>O<sub>4</sub>/MgO nanocomposite has emerged as highly effective adsorbents for Pb(II) removal. The combination of Fe<sub>3</sub>O<sub>4</sub> and MgO in a nanocomposite offers synergistic effects, leveraging the magnetic properties of Fe<sub>3</sub>O<sub>4</sub> and the excellent adsorption capacities and chemical stability of MgO. Fe<sub>3</sub>O<sub>4</sub>/MgO nanocomposite provides a versatile platform for the

\* Corresponding author (chanip@sci.pdn.ac.lk;  <https://orcid.org/0000-0001-8644-7396>)



This article is published under the Creative Commons CC-BY-ND License (<http://creativecommons.org/licenses/by-nd/4.0/>). This license permits use, distribution and reproduction, commercial and non-commercial, provided that the original work is properly cited and is not changed in anyway.

adsorption of Pb(II) ions through various mechanisms, including surface interactions, ion exchange, and complexation. The magnetic properties of  $\text{Fe}_3\text{O}_4$  facilitate easy separation and recyclability of the nanocomposite, minimizing secondary pollution and enabling repeated use (Sameera *et al.*, 2023). This makes  $\text{Fe}_3\text{O}_4/\text{MgO}$  nanocomposite highly suitable for practical applications in water treatment. Previous studies have demonstrated the effectiveness of  $\text{Fe}_3\text{O}_4/\text{MgO}$  nanocomposite in removing other heavy metals and dyes. For instance, Habiby *et al.* (2019) reported an adsorption capacity of  $2.5 \text{ mg g}^{-1}$  and a removal efficiency of 98.9% for phosphate, using chemical precipitation by synthesized  $\text{Fe}_3\text{O}_4/\text{MgO}$  nanocomposite. Similarly, Namvar-Mahboub *et al.* (2020) achieved removal efficiency of 98.2% and 95.5% for Pb(II), and Cd(II) using green synthesized  $\text{Fe}_3\text{O}_4/\text{MgO}$  nanocomposite, respectively. These findings underscore the potential of  $\text{Fe}_3\text{O}_4/\text{MgO}$  nanocomposite as efficient adsorbent for heavy metal removal. In another study by Nagarajah *et al.* (2017), MgO cores with silica-coated nano  $\text{Fe}_3\text{O}_4$  nanocomposite demonstrated exceptional performance in the removal of Pb(II) from aqueous solutions, compared with Cd(II) and Cu(II). The adsorption capacity of these nanocomposites for Pb(II) was found to be as high as  $238 \text{ mg g}^{-1}$ , highlighting their superior adsorption capability. These findings emphasize the significant potential of  $\text{Fe}_3\text{O}_4/\text{MgO}$  nanocomposite as efficient adsorbent for Pb(II) removal. However, there is a need for further investigation to explore the adsorption capacity, kinetics, and mechanisms of Pb(II) removal using  $\text{Fe}_3\text{O}_4/\text{MgO}$  nanocomposites. Understanding the influence of various parameters, such as pH, initial Pb(II) concentration, contact time, and temperature, on the adsorption process is crucial for optimizing the design of water treatment systems. We have modified the synthesis procedure based on the work conducted by Salem & Ahmed (2016), where they utilized this material for the removal of amaranth dye using adsorption studies. In our study, we have adapted this modified procedure to target the removal of Pb(II) ions, aiming to enhance the adsorption capacity compared to the existing literature. In this study, we aim to investigate the potential of  $\text{Fe}_3\text{O}_4/\text{MgO}$  nanocomposite as an efficient adsorbent for the removal of Pb(II) from aqueous solutions. The study evaluates the adsorption capacity, kinetics, and isotherms of Pb(II) adsorption onto  $\text{Fe}_3\text{O}_4/\text{MgO}$  nanocomposite. Additionally, the reported work will explore the effects of different experimental parameters on the adsorption process to optimize the removal efficiency. The insights gained from this research will contribute to the development of sustainable and effective strategies for Pb(II) removal from contaminated water sources.

## MATERIALS AND METHODS

### Materials

The chemicals used were iron (II) chloride tetrahydrate ( $\text{FeCl}_2 \cdot 4\text{H}_2\text{O}$ ), iron (III) chloride hexahydrate ( $\text{FeCl}_3 \cdot 6\text{H}_2\text{O}$ , Loba Chemie), magnesium chloride hexahydrate ( $\text{MgCl}_2 \cdot 6\text{H}_2\text{O}$ , Hopkin and Williams LTD.), cetyltrimethylammonium bromide (CTAB, Research Lab Fine Chem Industries), ammonia ( $\text{NH}_4 \cdot \text{OH}$ , Loba Chemie), ethanol ( $\text{C}_2\text{H}_5\text{OH}$ , VWR chemicals), silver nitrate ( $\text{AgNO}_3$ , Loba Chemie), and lead nitrate ( $\text{Pb}(\text{NO}_3)_2$ , Hemas( Drugs) Ltd.). All the substances utilized were of analytical grade. Deionized distilled water was employed in the preparation of all solutions.

### Synthesis of $\text{Fe}_3\text{O}_4/\text{MgO}$ nanocomposite

A modified synthesis procedure based on the work done by Salem & Ahmed (2016) was followed.  $\text{Fe}_3\text{O}_4/\text{MgO}$  nanocomposite was prepared using a controlled sol-gel method as described below. Initially, approximately 1 mL of cetyltrimethylammonium bromide (CTAB) solution, a cationic surfactant above its critical micelle concentration, was added to a 50 mL solution of 1 M  $\text{MgCl}_2$  with constant stirring for 1 h. Subsequently, a 1 M ammonia solution was added drop by drop to the  $\text{MgCl}_2$  solution until the clear solution turned into a white sol of  $\text{Mg}(\text{OH})_2$ . The sol was stirred for an additional 2 h and left undisturbed for two days to allow for the condensation of sol particles into solid gel nanoparticles. The gel particles were collected through filtration and thoroughly washed with distilled water multiple times to remove chloride ions. The effectiveness of the washing process was confirmed when the filtrate yielded a negative test result with silver nitrate solution. After washing, the final product was dried at  $90^\circ\text{C}$  overnight. The dried powders were then subjected to calcination in a high-temperature furnace at  $400^\circ\text{C}$  for 2 h to induce the crystallization of MgO nanoparticles. In parallel,  $\text{Fe}_3\text{O}_4$  nanoparticles were prepared by mixing an appropriate amount of ferrous chloride and ferric chloride solutions. Iron(II) chloride ( $\text{FeCl}_2$ , 1.9 g) and iron(III) chloride ( $\text{FeCl}_3$ , 3.2 g) were dissolved in 50 mL of deionized water at a molar ratio of 1:2 to prepare the  $\text{Fe}_3\text{O}_4$  precursor solution. The solution was stirred using a magnetic stirrer until the iron salts were completely dissolved. Ammonia solution was added to the mixture until a black precipitate was detected, indicating the formation of  $\text{Fe}_3\text{O}_4$ . The magnetic solution was subsequently separated using magnetic separation and washed with distilled water. The  $\text{Fe}_3\text{O}_4$

nanoparticles were then dried at 105 °C for 24 h. The synthesized Fe<sub>3</sub>O<sub>4</sub> nanoparticles and MgO nanoparticles were combined. The Fe<sub>3</sub>O<sub>4</sub>/MgO nanocomposite was prepared with 46.29 wt % Fe<sub>2</sub>O<sub>3</sub>, 53.71 wt % MgO and suspended in 50 mL of distilled water. Ultrasonication for 40 min was employed to promote the interaction between the two nanoparticle components, ensuring uniform dispersion and intimate contact. The Fe<sub>3</sub>O<sub>4</sub>/MgO nanocomposite was then separated from the suspension using magnetic separation and washed with deionized water to eliminate any residual impurities. Subsequently, the nanocomposites were dried at 90 °C for 24 h under controlled conditions to remove any remaining solvent and ensure their stability.

### Characterization of Fe<sub>3</sub>O<sub>4</sub>/MgO nanocomposite

Various characterization techniques were employed to test the Fe<sub>3</sub>O<sub>4</sub>/MgO nanocomposite and analyze the Pb(II) adsorbed Fe<sub>3</sub>O<sub>4</sub>/MgO nanocomposite. X-ray Diffraction (XRD, D8 ADVANCE ECO - Bruker, CuK $\alpha$   $\lambda$  = 0.154 nm, 2 $\theta$  range of 20–80°, step size of 0.02° and a step time of 1 s) analysis was used to identify the crystal structure and phase composition of the nanocomposite. scanning electron microscopy (SEM, Oxford/X-act, ZEISS, operated at 20 keV) was employed for the examination of the surface morphology and particle size distribution of the nanocomposite. Energy-dispersive X-ray spectroscopy (EDS, Oxford/X-act, ZEISS, operated at 20 keV) was used to determine the elemental composition of the nanocomposite. Fourier transform infrared spectroscopy (FTIR, Bruker VERTEX 80) analysis was used to identify the functional groups present in the nanocomposite while vibrating sample magnetometry (VSM, DXWD-60, and Xiamen Dexing Magnet Tech.Co.Ltd) was employed to investigate the magnetic properties of the nanocomposite. Atomic absorption spectroscopy (AAS, Shimadzu AA-7800) enabled the quantitative analysis of the concentration of Pb(II) ions in the solution before and after adsorption.

### Batch adsorption experiment

Initially, Fe<sub>3</sub>O<sub>4</sub>/MgO nanocomposite was synthesized using a controlled sol-gel method, as described previously. The nanocomposite was then washed with deionized water and dried to ensure their stability. The optimization of adsorbent dosage was carried out by adding different amounts of the nanocomposite (ranging from 0.05 g L<sup>-1</sup> to 0.4 g L<sup>-1</sup>) into separate solutions of 600 mg L<sup>-1</sup> concentration of Pb(II). The mixtures were agitated until adsorption equilibrium was reached, and the residual Pb(II) concentration was measured.

Similarly, the optimization of initial concentration involved preparing different concentrations of Pb(II) solutions (ranging from 400 to 1000 mg L<sup>-1</sup>) and adding 0.25 g L<sup>-1</sup> of the nanocomposite to each solution. The solutions were mixed to reach adsorption equilibrium, and the final Pb(II) concentrations were measured. The optimization of pH was accomplished by adjusting solutions of 600 mg L<sup>-1</sup> Pb(II) concentration to different pH levels (ranging from pH 4 to 10) using appropriate buffers. The 0.25 g L<sup>-1</sup> of nanocomposites were added, and the mixtures were agitated before measuring the final Pb(II) concentrations. The optimization of reaction time involved adding 0.25 g L<sup>-1</sup> of the nanocomposite to a solution of 600 mg L<sup>-1</sup> Pb(II) concentration and agitating the mixture for various time intervals ranging from 10 to 150 min. The residual Pb(II) concentrations were measured at each time interval.

To determine the equilibrium adsorption capacity and removal efficiency of Pb(II) ions using Fe<sub>3</sub>O<sub>4</sub>/MgO nanocomposite, batch adsorption experiments were conducted. An optimized mass of the nanocomposite was added to a Pb(II) ion solution of optimized initial concentration ( $C_0$ ) and volume ( $V$ ). The mixture was stirred continuously, and samples were taken at 10 min time intervals to measure the concentration of Pb(II) ions ( $C_t$ ) using atomic absorption spectroscopy. The adsorption capacity ( $q_t$ ) at each time interval was calculated using the formula  $q_t = ((C_0 - C_t) \times V)/m$ , where  $m$  is the mass of the adsorbent. The removal efficiency was calculated as  $\text{removal efficiency (\%)} = ((C_0 - C_t) \times 100)/C_0$ . The experiments continued until the system reached equilibrium, indicated by no significant change in  $C_t$ . In addition, various adsorption isotherm models, including Langmuir, Freundlich, and Temkin, were applied to the equilibrium data, while different kinetic models such as pseudo-first-order, pseudo-second-order, liquid film diffusion, and intraparticle diffusion were employed to analyze the kinetic data. Finally, the results obtained from the batch adsorption studies were analyzed to determine the optimum adsorbent dosage, initial concentration, pH, reaction time, and the adsorption isotherm and kinetic parameters associated with the removal of Pb(II) using Fe<sub>3</sub>O<sub>4</sub>/MgO nanocomposite.

## RESULTS AND DISCUSSION

### Scanning electron microscopy (SEM)

The morphology and microstructure of the Fe<sub>3</sub>O<sub>4</sub>/MgO nanocomposite were thoroughly investigated using SEM (Supplementary Figure S1a). The SEM images of the Fe<sub>3</sub>O<sub>4</sub>/MgO nanocomposite revealed distinct

morphological features. The  $\text{Fe}_3\text{O}_4$  nanoparticles exhibited an irregular crystal shape with varying sizes. Meanwhile, the pyramid-shaped MgO particles showed a unique morphology with sharp edges.

The combination of these two different morphologies created a highly interconnected and porous structure, potentially enhancing the material's adsorption capacity. The irregular crystal shape of  $\text{Fe}_3\text{O}_4$  nanoparticles contributed to a higher surface area and provided numerous active sites for Pb(II) adsorption. Additionally, the presence of pyramid-shaped MgO particles improved the overall structural stability of the nanocomposite, making it suitable for long-term usage in environmental applications. The SEM images of the  $\text{Fe}_3\text{O}_4/\text{MgO}$  nanocomposite after Pb(II) adsorption revealed notable agglomeration of Pb(II) ions on the surfaces of both the irregular crystal-shaped  $\text{Fe}_3\text{O}_4$  nanoparticles and the pyramid-shaped MgO particles (Supplementary Figure S1b). The irregular crystal-shaped  $\text{Fe}_3\text{O}_4$  nanoparticles exhibited a greater propensity for Pb(II) adsorption due to their increased surface area and numerous active sites. As a result, the surfaces of these nanoparticles displayed significant clusters of Pb(II) ions. Similarly, the pyramid-shaped MgO particles also demonstrated agglomeration of Pb(II) ions, suggesting their involvement in the adsorption process. The unique morphology of the pyramid-shaped particles, with their sharp edges and interconnected structure, facilitated the accumulation of Pb(II) ions on their surfaces. The agglomeration phenomenon observed on the irregular crystal and pyramid-shaped surfaces indicates the strong affinity of the  $\text{Fe}_3\text{O}_4/\text{MgO}$  nanocomposite for Pb(II) ions. The adsorption capacity of the nanocomposite was likely enhanced by the combined effect of the irregular crystal-shaped  $\text{Fe}_3\text{O}_4$  nanoparticles and the pyramid-shaped MgO particles, which provided ample binding sites and increased contact area for Pb(II) adsorption. These images provide visual evidence of the effective removal and accumulation of Pb(II) ions by  $\text{Fe}_3\text{O}_4/\text{MgO}$  nanocomposites. Moreover, the EDS analysis of the nanocomposite revealed the presence of Fe, O, and Mg elements with weight percentages of 28.97%, 25.55%, and 30.0%, respectively (Supplementary Figure S1c). This confirms the successful incorporation of these elements in the nanocomposite, supporting their potential in the efficient removal of Pb(II) ions from the water. EDS analysis performed after the adsorption of Pb(II) ions on the surface of  $\text{Fe}_3\text{O}_4/\text{MgO}$  nanocomposite confirmed the presence of Pb peaks, indicating successful binding of Pb(II) onto the adsorbent (Supplementary Figure S1d). The quantitative EDS data shown in Supplementary Table S1 reveals the incorporation of Pb(II) on the  $\text{Fe}_3\text{O}_4/\text{MgO}$  surface, further supporting the efficient removal of Pb(II) ions.

## X-ray diffraction (XRD)

The XRD analysis of the synthesized  $\text{Fe}_3\text{O}_4/\text{MgO}$  nanocomposite is presented in Supplementary Figure S2a. The observed peaks at  $2\theta = 30.22^\circ$ ,  $35.6^\circ$ ,  $53.98^\circ$ , and  $57.23^\circ$  indicate the presence of cubic  $\text{Fe}_3\text{O}_4$  with (220), (311), (422), and (511) planes, respectively (JCPDS 01-084-2782). Furthermore, the peaks at  $2\theta = 37.06^\circ$ ,  $43.06^\circ$ , and  $62.53^\circ$  suggest the presence of cubic MgO (periclase) with (111), (200), and (220) planes, respectively (JCPDS 01-075-1525). Additionally, peaks at  $2\theta = 33.33^\circ$ , and  $49.69^\circ$  indicate the presence of rhombohedral  $\text{Fe}_2\text{O}_3$  with (104), and (024) planes, respectively (JCPDS 01-072-6225). Hence, our analysis confirms that the synthesized final product consists of cubic structures of  $\text{Fe}_3\text{O}_4$  and periclase MgO. After adsorbing Pb(II) (Supplementary Figure S2b), a significant number of diffraction peaks were indexed to  $\text{Pb}_3(\text{CO}_3)_2(\text{OH})_2$ . Peaks observed at  $2\theta = 24.67^\circ$ ,  $41.28^\circ$ ,  $49.8^\circ$ , and  $56.99^\circ$  could be indexed to the presence of rhombohedral  $\text{Pb}_3(\text{CO}_3)_2(\text{OH})_2$  with (104), (211), (220), and (125) planes, respectively (JCPDS 01-073-4362). The peak observed at  $2\theta = 54.29^\circ$  indicates the presence of tetragonal PbO with a (211) plane (JCPDS 01-085-1292). Peaks observed at  $2\theta = 33.45^\circ$ ,  $35.8^\circ$ , and  $64.49^\circ$  indicate the presence of rhombohedral  $\text{Fe}_2\text{O}_3$  with (104), (110), and (300) planes, respectively (JCPDS 01-084-0311).

Peaks observed at  $2\theta = 38.28^\circ$ ,  $58.97^\circ$ , and  $62.41^\circ$  could be indexed to the presence of hexagonal  $\text{Mg}(\text{OH})_2$  with (011), (110), and (111) planes, respectively (JCPDS 01-086-0441). Peaks observed at  $2\theta = 30.38^\circ$ ,  $37.43^\circ$ , and  $43.49^\circ$  indicate the presence of cubic  $\text{Fe}_3\text{O}_4$  with (220), (222), and (400) planes, respectively (JCPDS 01-071-6339). It is well known that the MgO of  $\text{Fe}_3\text{O}_4/\text{MgO}$  nanocomposite could be hydrated by water to produce  $\text{Mg}(\text{OH})_2$ , which covers the surface. The produced  $\text{Mg}(\text{OH})_2$  can partially dissociate to release  $\text{OH}^-$ . Thus, Pb(II) easily assembles with  $\text{OH}^-$  and forms  $\text{Pb}(\text{OH})_2$ . Due to the lower stability of  $\text{Pb}(\text{OH})_2(\text{s})$ , it can react with  $\text{CO}_2$  dissolved in the solution to produce  $\text{Pb}_3(\text{CO}_3)_2(\text{OH})_2$  (Zhang *et al.*, 2014). The presence of these  $\text{Fe}_2\text{O}_3$  impurity peaks suggests the partial oxidation of  $\text{Fe}_3\text{O}_4$  in aqueous solution. The observed changes in crystal structure and phase provide confirmation of the adsorption process.

## Fourier-transform infrared spectroscopy (FTIR)

According to the FTIR analysis in Supplementary Figure S3 [curve (a)], results confirmed the presence of MgO and  $\text{Fe}_3\text{O}_4$  in the  $\text{Fe}_3\text{O}_4/\text{MgO}$  adsorbent composition, and evidence of Pb(II) adsorbed  $\text{Fe}_3\text{O}_4/\text{MgO}$  nanocomposite (Pb(II)- $\text{Fe}_3\text{O}_4/\text{MgO}$ ) [curve (b)] was obtained in the range of  $400 - 4000 \text{ cm}^{-1}$ . The presence of the strong, sharp



band at 1738 cm<sup>-1</sup> in the Fe<sub>3</sub>O<sub>4</sub>/MgO nanocomposite suggests the involvement of organic compounds with C=O stretching vibrations. The specific origin of these compounds could vary depending on the synthesis method, reaction conditions, and post-synthesis treatments applied to the nanocomposite. Exposure to air or oxygen during synthesis or storage can lead to the oxidation of organic compounds present in the system, resulting in the formation of carbonyl groups. This surface oxidation process can occur on both the Fe<sub>3</sub>O<sub>4</sub> nanoparticles and the MgO coating, leading to the presence of C=O stretching vibrations in the nanocomposite. The medium peak at approximately 1216 cm<sup>-1</sup> in the Fe<sub>3</sub>O<sub>4</sub>/MgO nanocomposite corresponds to C-N stretching vibrations. This may arise from the nitrogen atom present in the CTAB molecule, which contains a quaternary ammonium cation. Additionally, ammonia used in the synthesis process can provide nitrogen, facilitating the formation of C-N bonds with organic compounds present in the reaction mixture. The bands that appeared in the low wavenumber region are associated with characteristic peaks of metal-oxygen (M-O) bonds. The bands below 1000 cm<sup>-1</sup> are related to Mg-O absorption. This indicates the presence of MgO nanoparticles in calcined compounds. The frequency of heteropolar diatomic MgO stretching is confirmed by the peak at 874 cm<sup>-1</sup>. The bands at 442 cm<sup>-1</sup> and 536.7 cm<sup>-1</sup> are referred to as Fe<sub>3</sub>O<sub>4</sub>, and those bands are associated with the magnetic property on the adsorbent surface. The observed bands in this analysis appear at higher wavenumbers compared to the standard, indicating a shift caused by the alteration of electron density distribution on the surface of nanoparticles. This change in electron density results from the interaction between the nanoparticles and the surrounding environment, leading to the strengthening of chemical bonds within the nanocomposite structure. The Fe<sub>3</sub>O<sub>4</sub>/MgO nanocomposite also shows similar absorption peaks. A medium sharp peak appeared at 1365 cm<sup>-1</sup>, which is associated with the O-H bending vibration of hydroxyl groups. This vibration is attributed to the presence of residual hydroxyl groups from the hydroxide solution used during the synthesis process. This suggests the formation of a magnesium hydroxide (Mg(OH)<sub>2</sub>) layer with magnetite. This peak is weaker than curve (b) due to antisymmetric stretching in Mg(OH)<sub>2</sub> crystal structure. In addition, this fact also serves as an indication that the calcination process at 400 °C for 2 hours has resulted in the transformation of the structure compound from the hexagonal Mg(OH)<sub>2</sub> form to the cubic MgO form. After the Pb(II) adsorption, MgO reverted to Mg(OH)<sub>2</sub> due to the water present in the Pb(II) solution and the bands observed for the dried sample. Multiple broad peaks at 2970 cm<sup>-1</sup> reveal the asymmetric vibration of the C-H (-CH<sub>2</sub>) stretch arising

from the alkyl chains of CTAB. Curve (b) shows the FTIR spectra of Pb(II)-Fe<sub>3</sub>O<sub>4</sub>/MgO obtained in the range of 400–4000 cm<sup>-1</sup>. The new peaks that arose between 1092–874 cm<sup>-1</sup> indicate the presence of Pb–O. The weak band at 1092 cm<sup>-1</sup> corresponds to the stretching vibration of CO<sub>3</sub><sup>2-</sup> due to the formation of Pb<sub>3</sub>(CO<sub>3</sub>)<sub>2</sub>(OH)<sub>2</sub> on the surface of Fe<sub>3</sub>O<sub>4</sub>/MgO nanocomposite. The change in IR intensity between 1100 cm<sup>-1</sup> and 870 cm<sup>-1</sup> suggested Pb(II) adsorption, which occurred in the form of Fe-O-Mg-O-Pb(II), with bending modes at 1092 cm<sup>-1</sup> and 874 cm<sup>-1</sup>. New absorption peaks observed at 3692 cm<sup>-1</sup> correspond to O-H stretching vibration due to the PbO-adsorbed water moiety on the Fe<sub>3</sub>O<sub>4</sub>/MgO surface (Kawsihan *et al.*, 2023). Pb(II) can combine with OH<sup>-</sup> ions to form the insoluble hydroxide Pb(OH)<sub>2</sub>, which can further react with dissolved CO<sub>2</sub> to form Pb<sub>3</sub>(CO<sub>3</sub>)<sub>2</sub>(OH)<sub>2</sub>. The band at 2359 cm<sup>-1</sup> disappeared in curve (b), while it was present in curve (a), is ascribed to carbonate stretching and carbonate ions attached with Pb(II). After adsorption, bands at 1432 cm<sup>-1</sup> can be attributed to CO<sub>3</sub><sup>2-</sup> groups chemisorbed over the MgO surface. The peaks at 442 cm<sup>-1</sup> and 536.7 cm<sup>-1</sup> were shifted to 445 cm<sup>-1</sup> and 537.2 cm<sup>-1</sup> after Pb(II) adsorption, thereby, indicating that the MgO surface is covered by PbO and cation exchange between Mg(II) and Pb(II) may take place.

#### Vibrating sample magnetometry (VSM)

VSM analysis conducted on the Fe<sub>3</sub>O<sub>4</sub>/MgO nanocomposite revealed a magnetization saturation of 32.02 emu g<sup>-1</sup>, as shown in Supplementary Figure S4. This finding indicates that the nanocomposite exhibits superparamagnetic behaviour. The observed magnetization saturation is a crucial characteristic that highlights the potential of the Fe<sub>3</sub>O<sub>4</sub>/MgO nanocomposite for efficient magnetic separation and recovery in various wastewater treatment applications. The high saturation magnetization value signifies that the nanocomposites possess strong magnetic properties, enabling them to respond effectively to external magnetic fields. It allows for easy and rapid separation of the nanocomposite from the treated water using magnetic field-based separation techniques. This magnetic responsiveness facilitates the removal of the adsorbent from the water after the adsorption of Pb(II) ions, simplifying the purification process. Additionally, the high magnetization saturation value indicates that the Fe<sub>3</sub>O<sub>4</sub>/MgO nanocomposite can be easily regenerated and reused. Once separated from the water, the nanocomposite can be subjected to external magnetic fields to remove any remaining adsorbed Pb(II) ions. This capability of repeated use enhances the cost-effectiveness and sustainability of the nanocomposite as an adsorbent material. Moreover,

the magnetization saturation value provides valuable insights into the overall stability and dispersibility of the  $\text{Fe}_3\text{O}_4/\text{MgO}$  nanocomposite. It suggests that the magnetic  $\text{Fe}_3\text{O}_4$  component within the nanocomposite contributes significantly to their stability, allowing them to maintain their magnetic properties during the adsorption process. These attributes make the nanocomposite a promising candidate for wastewater treatment applications, offering enhanced performance and reusability in the removal of Pb(II) ions from contaminated water sources.

### Effect of adsorbent dose

Dosage optimization experiments were conducted using Pb(II) solutions prepared from  $\text{Pb}(\text{NO}_3)_2$  salt. The adsorption efficiency of Pb(II) ions onto  $\text{Fe}_3\text{O}_4/\text{MgO}$  nanocomposite increased with increasing adsorbent dosage up to a certain point and then reached a plateau. Figure 1a shows the variation in adsorption efficiency with different adsorbent dosages. The maximum adsorption efficiency was observed at  $0.25 \text{ g L}^{-1}$ , where a significant reduction in Pb(II) concentration was achieved. The adsorption capacity of the  $\text{Fe}_3\text{O}_4/\text{MgO}$  nanocomposite also followed a similar trend as the adsorption efficiency. Initially, the total adsorption increased with increasing dosage due to the availability of more adsorption sites. However, the adsorption capacity per unit mass ( $\text{mg g}^{-1}$ ) typically decreases with higher dosages because the additional adsorbent does not proportionally increase the amount of adsorbate. However, beyond  $0.25 \text{ g L}^{-1}$ , no significant changes in adsorption capacity were observed. The optimal adsorbent dosage of  $0.25 \text{ g L}^{-1}$  can be attributed to the balance between the available adsorption sites on the  $\text{Fe}_3\text{O}_4/\text{MgO}$  nanocomposite and the concentration of Pb(II) ions in the solution. At lower dosages, the number of active sites may be insufficient to accommodate all the Pb(II) ions, leading to incomplete adsorption. On the other hand, at higher dosages, excess adsorbent might result in aggregation or agglomeration, limiting the accessibility of active sites. This optimum dosage ensures the availability of sufficient active sites on the adsorbent while avoiding excessive aggregation.

### Effect of initial concentration

The initial concentration of Pb(II) ions varied within the range of  $400$  to  $1000 \text{ mg L}^{-1}$  while keeping other parameters constant. Figure 1b presents the variation in adsorption efficiency with different initial concentrations. The maximum removal efficiency was observed at an initial concentration of  $600 \text{ mg L}^{-1}$ , resulting in

a significant reduction in Pb(II) concentration. The adsorption capacity of the  $\text{Fe}_3\text{O}_4/\text{MgO}$  nanocomposites for Pb(II) ions also followed a similar trend as the adsorption efficiency. The adsorption capacity increased with the initial concentration up to  $600 \text{ mg L}^{-1}$  and then reached a plateau, suggesting saturation of the adsorption sites. The optimum initial concentration of  $600 \text{ mg L}^{-1}$  can be attributed to a balance between the availability of Pb(II) ions and the adsorption capacity of the  $\text{Fe}_3\text{O}_4/\text{MgO}$  nanocomposite. At lower initial concentrations, the limited number of metal ions may result in underutilization of the adsorbent's capacity. Conversely, at higher initial concentrations, the active sites on the adsorbent may become overwhelmed, leading to reduced adsorption efficiency.

### Effect of pH

The initial concentration of Pb(II) ions was kept constant, while the pH of the solution was adjusted within the range of 4 to 10 using HCl and NaOH. The removal efficiency of Pb(II) ions using  $\text{Fe}_3\text{O}_4/\text{MgO}$  nanocomposite was strongly influenced by the pH of the solution. Figure 1c illustrates the variation in adsorption efficiency with different pH values. The maximum removal efficiency was observed at pH 7, resulting in a significant reduction in Pb(II) concentration. The surface charge of both Pb(II) ions and the  $\text{Fe}_3\text{O}_4/\text{MgO}$  nanocomposite is crucial in adsorption. At low pH values ( $\text{pH} < 7$ ), the surface of the adsorbent is positively charged due to the protonation of surface hydroxyl groups. However, since Pb(II) ions are also positively charged, the adsorption in acidic conditions is less favourable due to electrostatic repulsion. As the pH increases and approaches neutral conditions, the adsorbent surface becomes less positively charged, reducing the repulsion between the adsorbent and Pb(II) ions, which enhances adsorption. At high pH values ( $\text{pH} > 7$ ), the surface of the adsorbent becomes negatively charged due to the deprotonation of surface hydroxyl groups. This negatively charged surface can interact favourably with the positively charged Pb(II) ions through electrostatic attraction. However, at very high pH values, the formation of  $\text{Pb}(\text{OH})_2$  precipitates can occur, which reduces the amount of Pb(II) ions available for adsorption. Therefore, the optimized pH of 7 can be attributed to a balance between surface charge interactions and the prevention of  $\text{Pb}(\text{OH})_2$  precipitation. The optimized pH of 7 can be attributed to the surface charge interaction between the Pb(II) ions and the adsorbent.

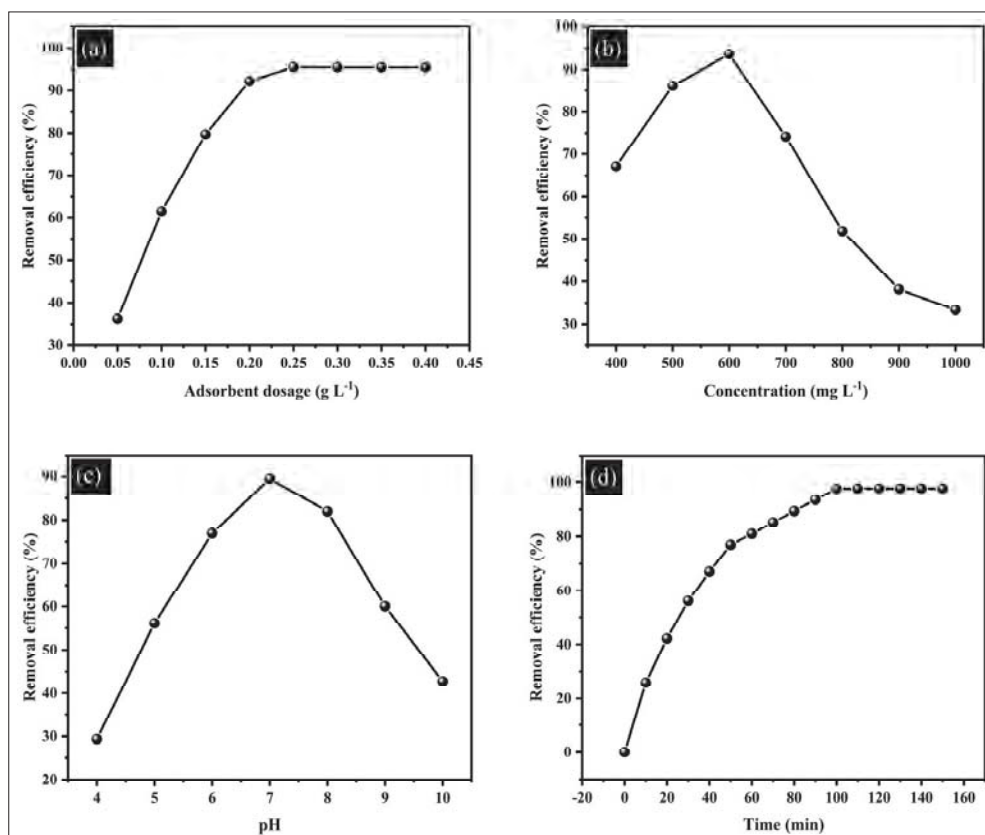


**Figure 1:** (a) The effect of the rate of adsorbent dose (b) The effect of initial concentration of lead (c) Effect of pH on the efficiency of removing lead (d) Effect of contact time on the efficiency of removing lead

At pH 7, the adsorbent surface is slightly negatively charged, which promotes the electrostatic attraction and adsorption of Pb(II) ions. Additionally, at this pH, the hydroxylation of Pb(II) ions is insignificant, preventing the formation of  $Pb(OH)_2$  precipitates, which could reduce the adsorption efficiency. Therefore, pH 7 provides the optimum conditions for maximizing the electrostatic attraction between the adsorbent surface and Pb(II) ions. This study demonstrated that the maximum removal efficiency was achieved at pH 7, which can be attributed to the surface charge interaction between Pb(II) ions and the adsorbent. The slightly negatively charged surface of the adsorbent at pH 7 facilitated the electrostatic attraction and enhanced the adsorption of Pb(II) ions. Additionally, chemical binding or complexation, with a significant covalent component, may also play a crucial role in the adsorption process.

#### Effect of reaction time

The initial concentration of Pb(II) ions was kept constant, and the contact time varied from 0 to 150 minutes. Figure 1d illustrates the variation in adsorption efficiency with different contact times. The adsorption efficiency increased rapidly within the first 50 minutes, followed by a slower increase until reaching equilibrium at 100 minutes. After 120 minutes, there was no significant change in efficiency, indicating the attainment of equilibrium. The initial rapid increase in adsorption efficiency within the first 50 minutes can be attributed to the availability of a large number of active sites on the adsorbent surface. During this stage, the concentration gradient between the solution and the adsorbent surface is high, leading to rapid diffusion of Pb(II) ions to the adsorbent surface and subsequent adsorption. The

adsorption process involves surface complexation, where Pb(II) ions form coordination bonds with active sites on the adsorbent surface. After the initial rapid increase, the adsorption efficiency gradually increases at a slower rate. This can be attributed to the reduction in the concentration gradient between the solution and the adsorbent surface as more Pb(II) ions are adsorbed. As the adsorption sites become occupied, the diffusion of Pb(II) ions to the remaining available sites becomes slower, resulting in a slower increase in adsorption efficiency. At 100 minutes, the adsorption efficiency starts to reach its maximum, indicating that the adsorption sites are nearly saturated. This study demonstrated that equilibrium was reached at 120 minutes, with an initial rapid increase in efficiency within the first 50 minutes. The adsorption kinetics and equilibrium dynamics suggest that the adsorption process involves surface complexation and diffusion of Pb(II) ions to the active sites on the adsorbent surface.

#### *Kinetics and isotherms of Pb (II) adsorption*

Equilibrium studies were conducted to investigate the adsorption behaviour of Pb(II) ions on Fe<sub>3</sub>O<sub>4</sub>/MgO nanocomposite (Figure 2a and 2b). The experiment was performed under optimized conditions, including a

pH of 7, adsorbent dosage of 0.25 g L<sup>-1</sup>, initial Pb(II) concentration of 600 mg L<sup>-1</sup>, and reaction time of 120 minutes. The equilibrium was achieved at 100 minutes, and further analysis was carried out at 120 minutes to ensure that equilibrium was reached. During the adsorption process, the concentration of Pb(II) ions gradually decreased with time. In the initial 50 minutes, a rapid reduction in concentration was observed, indicating a high adsorption rate. Subsequently, from 50 to 100 minutes, the concentration reduction slowed down, and the equilibrium state was reached. This behaviour suggests that the adsorption process involved both a rapid surface adsorption phase and a slower intra-particle diffusion phase. The experimental adsorption capacity and removal efficiency of Fe<sub>3</sub>O<sub>4</sub>/MgO nanocomposite for Pb(II) ions were determined to be approximately 2399 mg g<sup>-1</sup> and 99.98%, respectively. This high adsorption capacity indicates the strong affinity of Fe<sub>3</sub>O<sub>4</sub>/MgO nanocomposite towards Pb(II) ions and highlights their potential as efficient adsorbents for the removal of heavy metal pollutants from aqueous solutions. Comparison with previous literature findings related to the removal of Pb(II) ions using MgO nanoparticles revealed that the adsorption capacity of Fe<sub>3</sub>O<sub>4</sub>/MgO nanocomposite in this study is significantly higher (Supplementary Table S2).

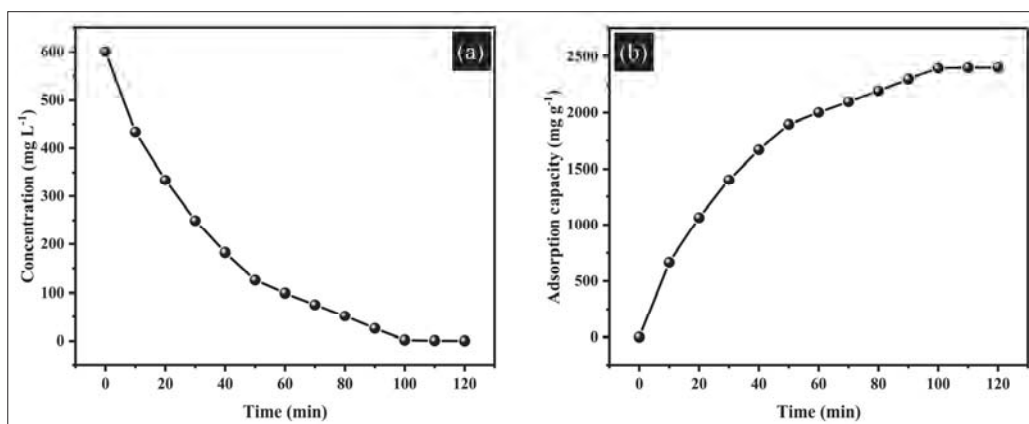


**Figure 2:** (a) Concentration variation with time (b) Adsorption capacity variation with time for Pb(II) adsorption

This enhancement can be attributed to the unique properties of the Fe<sub>3</sub>O<sub>4</sub>/MgO nanocomposite, such as their high surface area, well-defined morphology, and synergistic effects between Fe<sub>3</sub>O<sub>4</sub> and MgO nanoparticles. The obtained equilibrium at 120 minutes, the gradual decrease in concentration capacity with time, and the high experimental adsorption capacity of 2399.44

mg g<sup>-1</sup> highlight the effectiveness of the Fe<sub>3</sub>O<sub>4</sub>/MgO nanocomposite as adsorbents. The results consistently highlight the high adsorption capacity and efficiency of MgO nanoparticles in removing Pb(II) from aqueous solutions. The findings from these studies support and complement the superior adsorption performance of Fe<sub>3</sub>O<sub>4</sub>/MgO nanocomposites observed.

Adsorption kinetics of Pb(II) ions on  $Fe_3O_4/MgO$  nanocomposite was investigated using the pseudo-first-order, pseudo-second-order, Webber Morris model, and liquid film diffusion model (Figures 3a to 3d; Table 1). The pseudo-first-order model assumes that the adsorption rate is proportional to the difference between the equilibrium and adsorbate concentrations. The pseudo-second-order model considers the adsorption process as chemisorption involving the sharing or exchange

of electrons between the adsorbate and adsorbent. The kinetic rate constants and correlation coefficients ( $R^2$ ) were determined for both models. For the pseudo-first-order model, the calculated rate constant ( $k_1$ ) was found to be  $5.52 \times 10^{-2} \text{ min}^{-1}$ , and the correlation coefficient ( $R^2$ ) was 0.81. However, the experimental data did not fit well with the pseudo-first-order model, as indicated by the lower correlation coefficient.

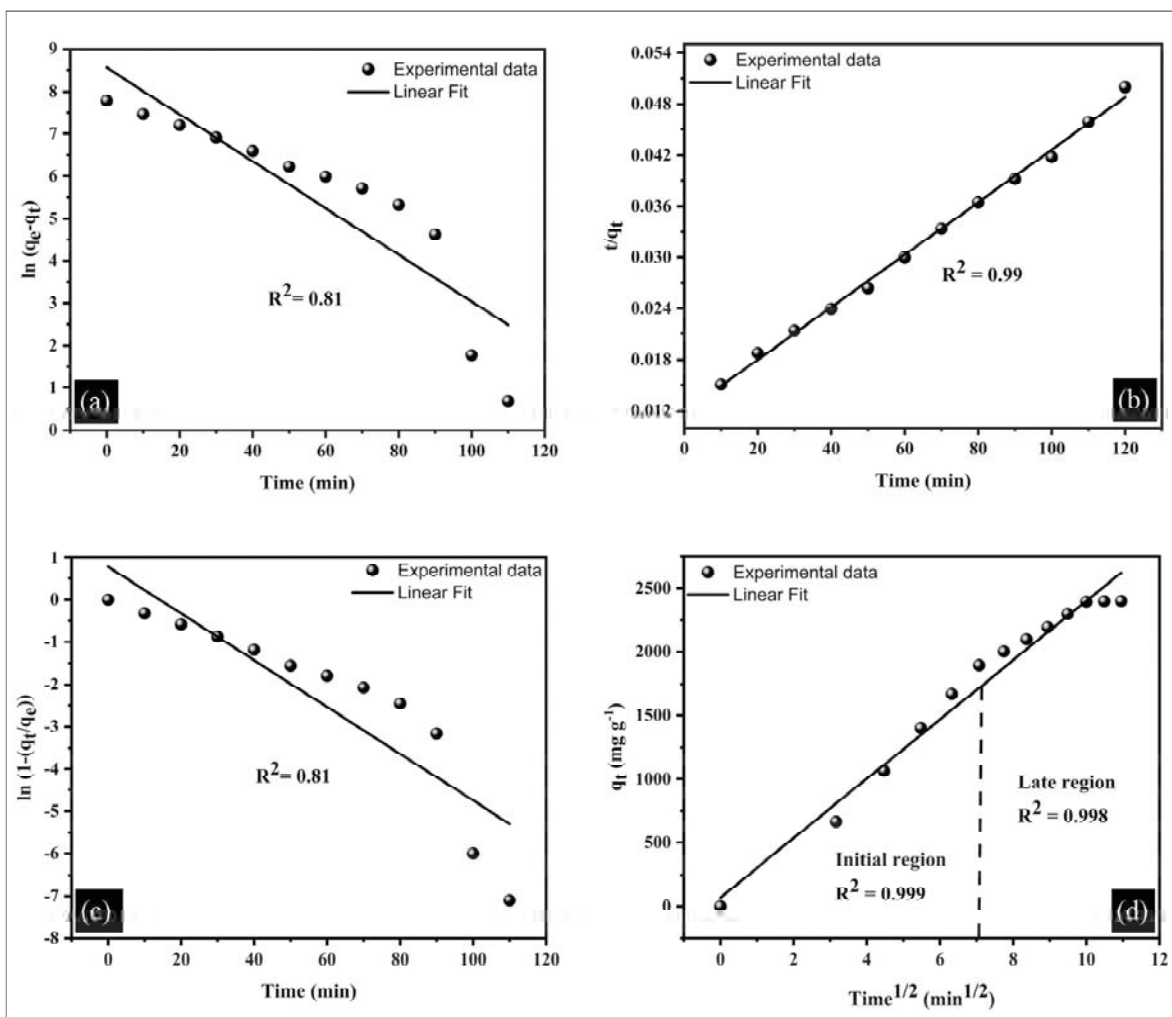


**Figure 3:** (a and b) Nonlinear pseudo-first-order and pseudo-second-order kinetic plots; (c and d) the liquid film diffusion model and intra-particle diffusion model plot of Pb(II) on  $Fe_3O_4/MgO$  nanocomposite

**Table 1:** Fitting parameters of pseudo first order, pseudo second order, liquid film diffusion model, and IPD (Intra-particle diffusion) rate constants and intercept values of Webber and Morris for Pb(II) adsorption

Kinetics model	Kinetic equation	Parameter	Value
Pseudo-first-order	$\ln(q_e - q_t) = \ln q_e - k_1 t$	$q_e$ (mg g <sup>-1</sup> )	5223.43
		$k_1$ ( $\times 10^{-2}$ min <sup>-1</sup> )	5.52
		R <sup>2</sup>	0.81
Pseudo-second-order	$\frac{t}{q_t} = \frac{1}{k_2 q_e^2} + \frac{1}{q_e} t$	$q_e$ (mg g <sup>-1</sup> )	3247.04
		$k_2$ ( $\times 10^{-6}$ g mg <sup>-1</sup> min <sup>-1</sup> )	7.19
		R <sup>2</sup>	0.997
Liquid film diffusion	$\ln\left(1 - \left(\frac{q_t}{q_e}\right)\right) = -k_{LF} \times t$	$k_{LF}$ ( $\times 10^{-2}$ min <sup>-1</sup> )	5.52
		R <sup>2</sup>	0.81
Intra-particle diffusion	$q_t = k_{diff} t^{1/2} + C$	Initial region	
		$k_{diff}$ (mg g <sup>-1</sup> min <sup>-0.5</sup> )	316.98
		C	-341.47
		R <sup>2</sup>	0.999
		Late region	
		$k_{diff}$ (mg g <sup>-1</sup> min <sup>-0.5</sup> )	174.45
		C	642.72
		R <sup>2</sup>	0.998

On the other hand, the pseudo-second-order model showed a better fit to the experimental data. The calculated rate constant ( $k_2$ ) was  $7.19 \times 10^{-6}$  g mg<sup>-1</sup> min<sup>-1</sup>, and the correlation coefficient ( $R^2$ ) was 0.997. The higher correlation coefficient suggests that the pseudo-second-order model more accurately describes the adsorption kinetics of Pb(II) ions on Fe<sub>3</sub>O<sub>4</sub>/MgO nanocomposite. Furthermore, the Webber Morris model was applied to evaluate the adsorption mechanism. The model consists of two regions: an initial region where the adsorption process is dominated by external film diffusion and a late region where intra-particle diffusion becomes the rate-controlling step. The initial region exhibited better efficiency ( $R^2 = 0.999$ ) with a higher adsorption rate constant ( $k_{diff} = 316.98$  mg g<sup>-1</sup> min<sup>-0.5</sup>) compared to the late region ( $k_{diff} = 174.45$  mg g<sup>-1</sup> min<sup>-0.5</sup>). This indicates that external film diffusion played a significant role in the early stages of the adsorption process. Additionally, the liquid film diffusion model was considered to understand the mass transfer mechanisms during adsorption. The model accounts for the resistance of mass transfer in the liquid film surrounding the adsorbent particles. The calculated film diffusion coefficient  $k_{LF}$  was found to be  $5.524 \times 10^{-2}$  min<sup>-1</sup>. This value indicates the effectiveness of the liquid film diffusion process in the overall adsorption mechanism. Comparing the results of the different kinetic models, it can be concluded that the pseudo-second-order model provided the best fit to the experimental data,

suggesting that the adsorption of Pb(II) ions on Fe<sub>3</sub>O<sub>4</sub>/MgO nanocomposite follows chemisorption kinetics. The Webber-Morris model indicated the importance of external film diffusion in the initial stages of adsorption. Furthermore, the liquid film diffusion model highlighted the role of mass transfer through the liquid film surrounding the adsorbent particles. These findings contribute to a better understanding of the adsorption kinetics and mechanisms involved in the removal of Pb(II) ions using Fe<sub>3</sub>O<sub>4</sub>/MgO nanocomposite.

The results of the isotherm models, namely Langmuir, Freundlich, and Temkin, are presented and discussed in this section (Figure 4a, 4b and 4c; Table 2). These models were used to analyze the adsorption behaviour of Pb(II) ions on Fe<sub>3</sub>O<sub>4</sub>/MgO nanocomposite. The Langmuir isotherm model assumes monolayer adsorption on a homogeneous surface with a limited number of adsorption sites. The Freundlich isotherm model describes the adsorption on heterogeneous surfaces with multilayer adsorption. The Temkin isotherm model assumes a uniform distribution of binding energies and accounts for the effects of adsorbate-adsorbent interactions. In our study, the experimental data were fitted to these isotherm models using regression analysis. The regression coefficients ( $R^2$ ) were used to evaluate the goodness of fit for each model.

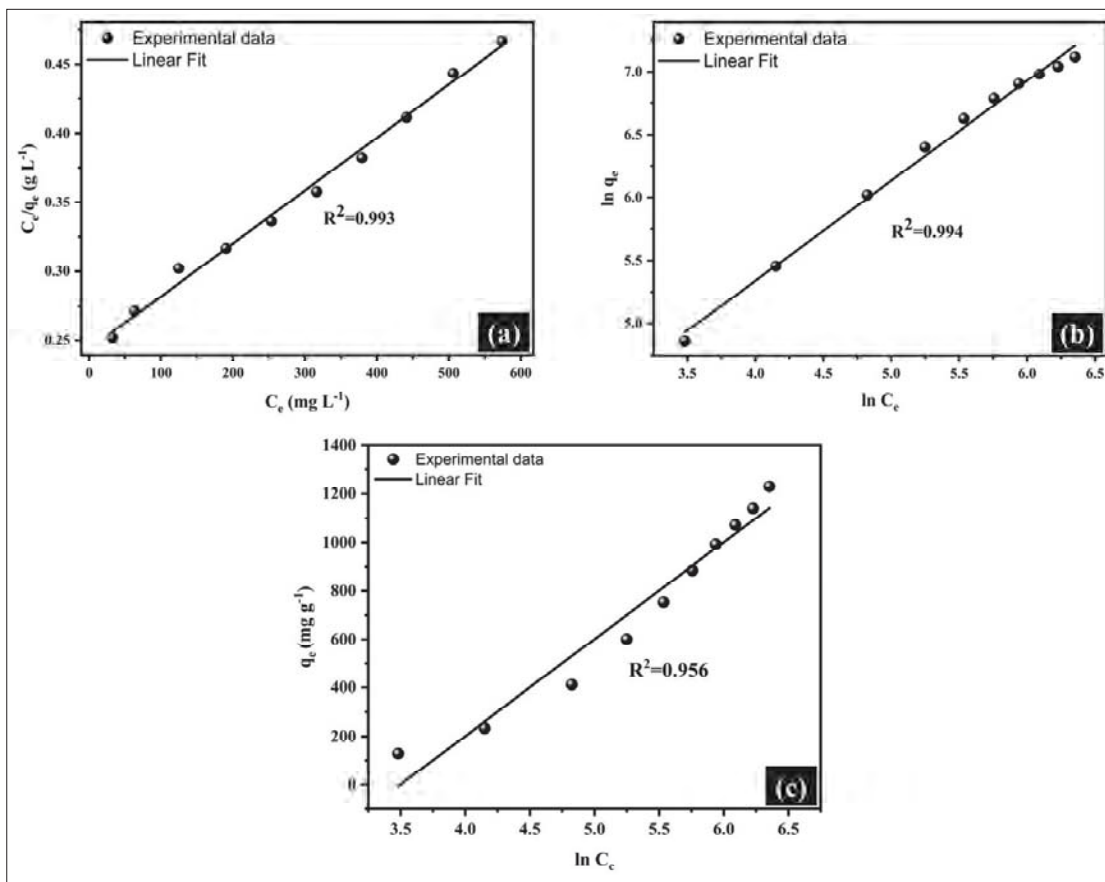


**Figure 4:** (a.) Langmuir model fit and (b.) Freundlich model fit (c.) Temkin model for adsorption of Pb(II) on Fe<sub>3</sub>O<sub>4</sub>/MgO nanocomposite

**Table 2:** Fitting parameters of Langmuir model, Freundlich model, and Temkin model for Pb(II) adsorption

Isotherm model	Equation	Parameter	Value
Langmuir	$\frac{C_e}{q_e} = \frac{1}{q_m k_L} + \frac{C_e}{q_m}$	$q_m$ (mg g <sup>-1</sup> )	2615.35
		$K_L$ (× 10 <sup>-3</sup> L mg <sup>-1</sup> )	1.57
		$R^2$	0.993
Freundlich	$\ln q_e = \ln k_f + \frac{1}{n} \ln C_e$	$n$	1.26
		$K_f$ (L mg <sup>-1</sup> )	8.75
		$R^2$	0.994
Temkin	$q_e = \frac{RT}{b} \ln k_T + \frac{RT}{b} \ln C_e$	$b$ (J mol <sup>-1</sup> )	6.2
		$K_T$ (L mg <sup>-1</sup> )	3.03×10 <sup>-2</sup>
		$R^2$	0.956

The results showed that the Freundlich model provided a slightly better regression coefficient ( $R^2 = 0.994$ ) compared to the Langmuir model ( $R^2 = 0.993$ ), while both models performed significantly better than the Temkin model ( $R^2 = 0.956$ ) for the removal of Pb(II) ions using  $\text{Fe}_3\text{O}_4/\text{MgO}$  nanocomposite. This indicates the adsorption process follows a multilayer adsorption mechanism on a heterogeneous surface. The Langmuir and Temkin models, although not providing as good a fit as the Freundlich model, still showed reasonable correlation coefficients. This suggests that there may be some monolayer adsorption and interactions between the adsorbate and adsorbent surface. Therefore, specific values of the Freundlich constant ( $k_f$ ) and exponent ( $n$ ) should be discussed. For instance, a high value of the constant ( $k_f = 8.75$ ) implies a higher adsorption capacity, while an exponent ( $n$ ) close to unity ( $n = 1.26$ ) suggests favourable adsorption intensity (Table 2). The higher adsorption capacity ( $k_f$ ) and favourable adsorption intensity ( $n$ ) indicate the effectiveness of the nanocomposite in removing Pb(II) ions from aqueous solutions. Overall, the results from the isotherm models, along with the specific parameter values (Table 2), confirm that the Freundlich model provides a better fit to the experimental data and highlights the significance of adsorption intensity in the removal of Pb(II) ions using  $\text{Fe}_3\text{O}_4/\text{MgO}$  nanocomposite. By fitting the experimental data to the Temkin isotherm equation, we can obtain the values of the Temkin constant ( $b = 6.2$ ) and the equilibrium binding constant ( $K_{\text{Temkin}} = 3.03 \times 10^{-2}$ ), which provide insights into the adsorption process. The obtained results showed that the Temkin model provided a relatively lower regression coefficient (0.956) compared to the Freundlich model. This suggests that the Temkin model may not be the most suitable model for describing the adsorption behaviour of Pb(II) ions on  $\text{Fe}_3\text{O}_4/\text{MgO}$  nanocomposite in our experimental conditions. However, it is important to note that the applicability of the Temkin model depends on various factors such as the nature of the adsorbate and adsorbent, as well as the experimental conditions. Therefore, further investigations and variations in experimental parameters may be required to better understand the suitability and limitations of the Temkin model for the adsorption of Pb(II) ions using  $\text{Fe}_3\text{O}_4/\text{MgO}$  nanocomposite.

In conclusion, while the Temkin model was utilized in our study, the obtained results indicated that the Freundlich model provided a better fit to the experimental data. This suggests that the Freundlich model may be more appropriate for describing the adsorption behaviour of Pb(II) ions on  $\text{Fe}_3\text{O}_4/\text{MgO}$  nanocomposite.

However, further research and analysis are needed to gain a comprehensive understanding of the adsorption mechanism and optimize the adsorption process for effective removal of Pb(II) ions. Overall, the results of the isotherm models indicate that the adsorption of Pb(II) ions on  $\text{Fe}_3\text{O}_4/\text{MgO}$  nanocomposite is influenced by both monolayer and multilayer adsorption mechanisms.

## CONCLUSION

The removal of Pb(II) ions using  $\text{Fe}_3\text{O}_4/\text{MgO}$  nanocomposite has been successfully investigated, and the following conclusions can be drawn from the experimental results. Firstly, the initial concentration of Pb(II) ions significantly influenced the adsorption capacity of the nanocomposite. Higher initial concentrations resulted in higher adsorption capacities, indicating that the adsorption process is concentration-dependent. Secondly, the adsorbent dosage played a crucial role in the adsorption efficiency. Increasing the dosage of  $\text{Fe}_3\text{O}_4/\text{MgO}$  nanocomposite led to an increase in the adsorption efficiency, reaching a maximum point where further increase in dosage did not significantly affect the adsorption efficiency. Thirdly, the pH of the solution had a notable impact on the adsorption process. The highest adsorption capacity was observed at an optimal pH value, suggesting the pH-dependent nature of the adsorption mechanism. The nanocomposite exhibited better adsorption performance at neutral pH ( $\text{pH} = 7$ ). Furthermore, the reaction time was found to be an essential parameter in achieving equilibrium adsorption. The adsorption process reached equilibrium within a specific time period, and prolonged contact time did not significantly affect the adsorption capacity. The experimental adsorbent capacity and removal efficiency were determined as  $2399.44 \text{ mg g}^{-1}$  and 99.98%, respectively. The Freundlich model provided a better fit, indicating multilayer adsorption on a heterogeneous surface. The pseudo-second-order model described the kinetics, suggesting chemisorption as the rate-controlling step. SEM-EDS, XRD, FTIR, and VSM techniques confirmed successful nanocomposite synthesis, revealing pyramid-like and irregular crystal morphology, crystalline cubic  $\text{Fe}_3\text{O}_4$  and MgO phases, chemical interactions, and superparamagnetic behaviour. These findings contribute to understanding Pb(II) ion adsorption using  $\text{Fe}_3\text{O}_4/\text{MgO}$  nanocomposite, highlighting their promising applications in environmental remediation. This study proved the enhancement of the removal efficiency and adsorption capacity for Pb(II) ions using sol-gel synthesized  $\text{Fe}_3\text{O}_4/\text{MgO}$  nanocomposite, compared with previously reported literature.



## Funding

This research was funded by the Science batch of 1976-1980 of the Faculty of Science, University of Peradeniya, Sri Lanka,

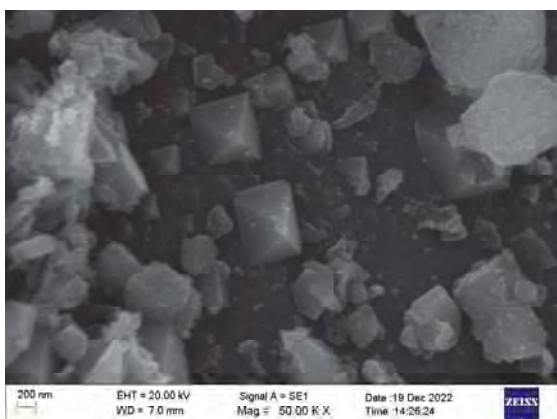
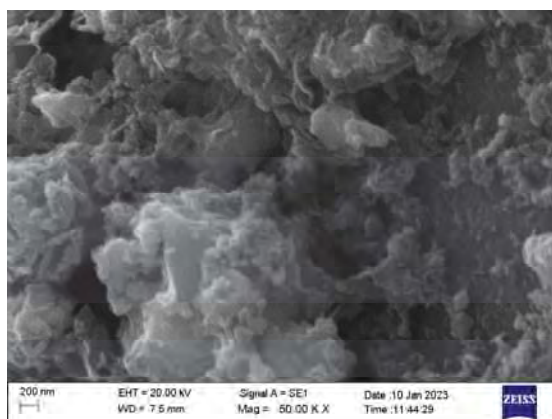
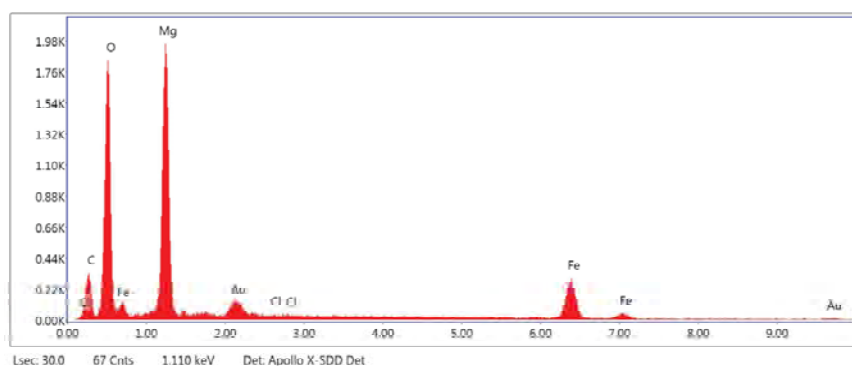
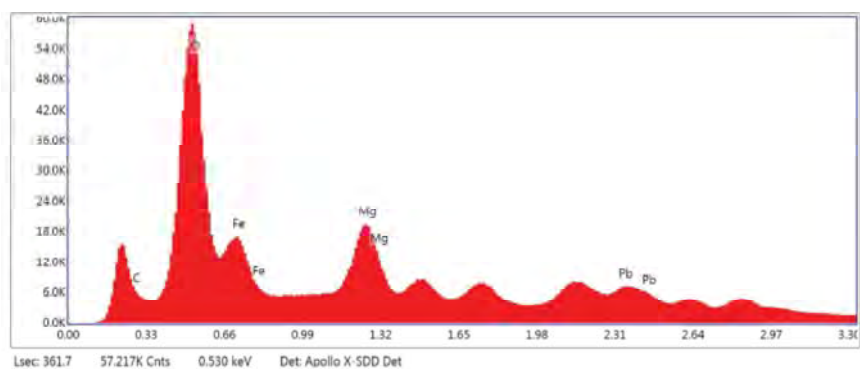
## Acknowledgment

This paper is dedicated to the memory of our co-author, Dr. Buddhika S. Dassanayake, who tragically passed away on December 25, 2023. Despite his untimely demise, Dr. Dassanayake's dedication and expertise left an indelible mark on the development of this work. His visionary leadership played a pivotal role in shaping the trajectory of this project. The collaborative spirit and collective effort that has shaped this manuscript are forever indebted to Dr. Dassanayake's significant role. His impact on this project, his academic legacy, and his enduring influence within the scientific community will be cherished and remembered with deep gratitude.

## REFERENCES

- Cabeza, A., & Aranda, M.A.G. (1996). Ab initio powder structure determination and thermal behavior of a new lead (II) phenylphosphonate, Pb (O<sub>3</sub>PC<sub>6</sub>H<sub>5</sub>). *Acta Crystallographica Section B: Structural Science, Crystal Engineering and Materials*, 52, 982-988.  
<https://doi.org/10.1107/S0108768196006829>
- Habiby, S.R., Esmacili, H., & Foroutan, R. (2019). Magnetically modified MgO nanoparticles as an efficient adsorbent for phosphate ions removal from wastewater. *Separation Science and Technology*, 55(11), 1-12.  
<https://doi.org/10.1080/01496395.2019.1617744>
- Lidsky, T.I., & Schneider, J.S. (2003). Lead neurotoxicity in children: Basic mechanisms and clinical correlates. *Brain*, 126(1), 5-19.  
<https://doi.org/10.1093/brain/awg014>
- Minju, N., Swaroop, K.V., Haribabu, K., Sivasubramanian, V., & Senthil, P. (2015). Removal of fluoride from aqueous media by magnesium oxide-coated nanoparticles. *Desalination and Water Treatment*, 53(11), 2911-2920.  
<https://doi.org/10.1080/19443994.2013.868837>
- Nagarajah, R., Wong, K. T., Lee, G., Chu, K. H., Yoon, Y., Kim, N. C., & Jang, M. (2017). Synthesis of a unique nanostructured magnesium oxide coated magnetite cluster composite and its application for the removal of selected heavy metals. *Separation and Purification Technology*, 174, 290-300.  
<https://doi.org/10.1016/j.seppur.2016.11.008>
- Namvar-Mahboub, M., Khodeir, E., Bahadori, M., & Mahdizadeh, S.M. (2020). Preparation of magnetic MgO/Fe<sub>3</sub>O<sub>4</sub> via the green method for competitive removal of Pb and Cd from aqueous solution. *Colloids and Surfaces*, 589, Article 124419.  
<https://doi.org/10.1016/j.colsurfa.2020.124419>
- Salem, A. M., & Ahmed, M. A. (2016). Selective adsorption of amaranth dye on Fe<sub>3</sub>O<sub>4</sub>/MgO nanoparticles. *Journal of Molecular Liquids*, 219, 780-788.  
<https://doi.org/10.1016/j.molliq.2016.03.084>
- Zhang, L., Zhu, W., Zhang, H., Bi, S., & Zhang, Q. (2014). Hydrothermal-thermal conversion synthesis of hierarchical porous MgO microrods as efficient adsorbents for lead (II) and chromium (VI) removal. *RSC Advances*, 4(58), 30542-30550.  
<https://doi.org/10.1039/C4RA03971H>
- Kawsihan, A., Dissanayake, D. M. S. N., Rathuwadu, N. P. W., Perera, H. C. S., Dayananda, K. E. D. Y. T., Koswattage, K. R., Mahadeva, R., Ganguly, A., Das, G., & Mantilaka, M. M. M. G. P. G. (2023). Synthesis of an eco-inspired anticorrosive composite for mild steel applications. *RSC Advances*, 13(41), 28852-28860.  
<https://doi.org/10.1039/D3RA02857G>
- Perera, H. C. S., Gurunathanan, V., Singh, A., Mantilaka, M. M. M. G. P. G., Das, G., & Arya, S. (2024). Magnesium oxide (MgO) nanoadsorbents in wastewater treatment: A comprehensive review. *Journal of Magnesium and Alloys*, 12(5), 1709-1773.  
<https://doi.org/10.1016/j.jma.2024.05.003>
- Sameera, S. A. L., Edirisinghe, N. P., Kannangara, Y. Y., Karunaratne, S., Koswattage, K. R., Perera, H. C. S., Das, G., Mantilaka, M. M. M. G. P. G., & Wijesinghe, W. P. S. L. (2023). Enhanced Wide Spectrum Photocatalytic Activity by in-Situ Magnetite-Graphite Nanoplatelets Heterostructure. *IEEE Access*, 11(June), 68912-68924.  
<https://doi.org/10.1109/ACCESS.2023.3290029>

## Supplementary data

Figure S1(a): SEM image of  $\text{Fe}_3\text{O}_4/\text{MgO}$  nanocompositesFigure S1(b): SEM image of Pb(II) adsorbed  $\text{Fe}_3\text{O}_4/\text{MgO}$  nanocompositesFigure S1(c): EDS analysis of  $\text{Fe}_3\text{O}_4/\text{MgO}$  nanocompositesFigure S1(d): EDS analysis of  $\text{Fe}_3\text{O}_4/\text{MgO}$  nanocomposites

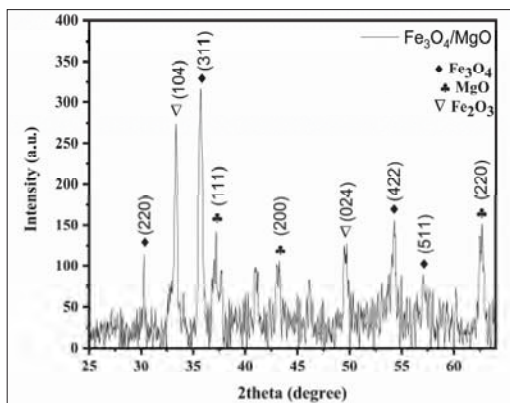


Figure S2(a): XRD analysis of Fe<sub>3</sub>O<sub>4</sub>/MgO nanocomposites

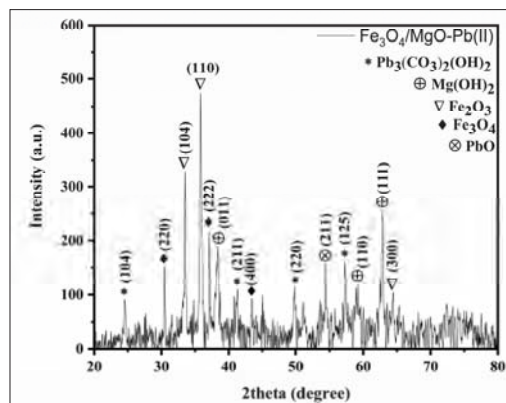


Figure S2(b): XRD analysis of Pb(II) adsorbed Fe<sub>3</sub>O<sub>4</sub>/MgO nanocomposites

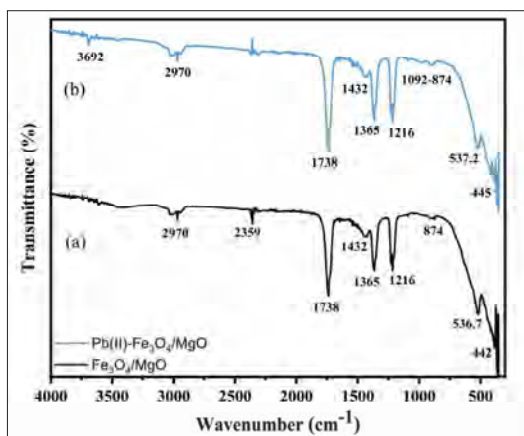


Figure S3: FTIR comparison between Fe<sub>3</sub>O<sub>4</sub>/MgO (Curve a) and Pb(II)-Fe<sub>3</sub>O<sub>4</sub>/MgO (Curve b)

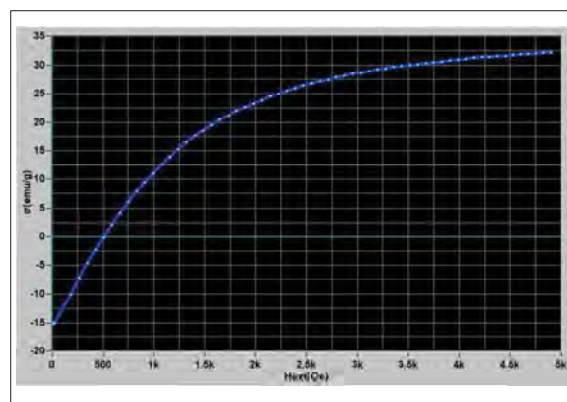


Figure S4: VSM data of Fe<sub>3</sub>O<sub>4</sub>/MgO nanocomposites (Hmax: 390 kA/m/4.896 kOe, Temperature: 272.3 K)

Table S1: Weight %, and Atomic % of Fe<sub>3</sub>O<sub>4</sub>/MgO nanocomposites, and Pb(II) adsorbed Fe<sub>3</sub>O<sub>4</sub>/MgO nanocomposites

Elements	Fe <sub>3</sub> O <sub>4</sub> /MgO nanocomposites		Pb(II)-Fe <sub>3</sub> O <sub>4</sub> /MgO nanocomposites	
	Weight%	Atomic%	Weight%	Atomic%
C K	12.23	22.72	10.53	22.30
O K	30.00	41.85	37.61	59.79
Fe L	28.97	11.58	7.06	3.22
MgK	25.55	23.46	9.95	10.41
PbM			34.84	4.28

**Table S2:** Comparison of loading capacities of MgO with Fe<sub>3</sub>O<sub>4</sub> for various adsorbate

Adsorbent	Pollutant	Adsorption capacity (mg g <sup>-1</sup> )	Reference
MgO/Fe <sub>3</sub> O <sub>4</sub>	Phosphate	2.95	(Habiby <i>et al.</i> , 2019)
Fe <sub>3</sub> O <sub>4</sub> /MgO	Amaranth dye	37.98	(Salem & Ahmed, 2016)
MgO cores with silica coated nano magnetite	Pb(II)	238	(Namvar-mahboub <i>et al.</i> , 2020)
	Cd(II)	85.1	
	Cu(II)	33.5	
MgO-Coated Fe <sub>3</sub> O <sub>4</sub>	F	10.96	(Minju <i>et al.</i> , 2015)
Fe <sub>3</sub> O <sub>4</sub> /MgO	Pb(II)	2399.44 (experimental)	This study

## RESEARCH ARTICLE

### Communication Engineering

# An efficient and improved algorithm for generating an equivalent planar architecture of the data vortex switch

A Soni and N Sharma

Electronics and Communication Engineering Department, Ujjain Engineering College, Ujjain, M.P., India.

Submitted: 28 September 2023; Revised: 28 August 2024; Accepted: 02 September 2024

**Abstract:** The data vortex (DV) switch was originally designed as an all optical interconnection network for high performance computing (HPC) applications. It was highly scalable with low latency and high throughput, compared to traditional switches used for optical packet switching (OPS) and HPC applications. The equivalent planar (chained MIN) model of the DV, proposed in previous literature, is a planar diagrammatic conversion of a 3-D model of the DV network. In this paper, we will focus on exploring a new, efficient and improved generalized algorithm that enables the arrangement of routing pathways to be implemented as an equivalent planar architecture (EPA, chained MIN) of a DV to find all possible routes between each source and target node pair. The original 3-D architecture of any size can be converted to a planar structure more simply by using the new generalized equivalent planar architecture (EPA) algorithm. To verify the proposed EPA algorithm, it was tested with different input traffic loads and network sizes while keeping the active angle 'A' constant. Network performance parameters, including injection rate (throughput) and latency (mean hops), obtained from simulation results are also provided to confirm the validity of the proposed EPA algorithm. This new algorithm is versatile, simpler and can be applied to networks of various sizes.

**Keywords:** Data vortex, equivalent planar architecture algorithm, high performance computing, optical buffering, optical interconnections, optical packet switching.

## INTRODUCTION

High-performance computing systems (HPCs) show that future higher generation supercomputers will require a large number of processors. The trend of increasing processor numbers to achieve better system performance highlights the importance of the high bandwidth (BW) interconnection system. A moderate system that causes multi-cycle delays on each inter-processor or processor to memory message can become a significant barrier in a parallel framework. To help mitigate this potential issue, lower latency optical fiber systems can replace electrical wire networks. Delay is additionally reduced by implementing dense wavelength division multiplexing (DWDM) (Glabowski *et al.*, 2020), which makes messages broad in the frequency domain (FD) and narrow in the time domain (TD). However, a significant obstacle to utilizing multistage optical DWDM systems is the lack of random access optical memory. This requires converting messages from an optical to electrical (O/E) structure within the system for storage purposes, and then converting them back from electrical to optical (E/O) structure later. This limits the switching speed while also increasing power consumption (Chen, 2019; Jokar *et al.*, 2020). To avoid this costly transformation at each

\* Corresponding author (amuujn@uecu.ac.in;  <https://orcid.org/0000-0003-3973-5955>)



This article is published under the Creative Commons CC-BY-ND License (<http://creativecommons.org/licenses/by-nd/4.0/>). This license permits use, distribution and reproduction, commercial and non-commercial, provided that the original work is properly cited and is not changed in anyway.

node of network conflict, buffering can be completely eliminated by using a deflection routing strategy. This creates a clear pathway for all-optical end to end communication throughout the system maintaining data flow and effectively bypassing any data drops or stops within the network. This eliminates message congestion within the network except for that experienced at the ingress nodes when a message is injected (Hawkins & Wills, 2006). Optical pathway interconnection systems utilizing dense wavelength division multiplexing can significantly improve supercomputer performance. A detailed study indicates that the lack of efficient optical buffering in optical packet switching (OPS) networks requires the exploration of new topologies and routing systems (Hawkins *et al.*, 2007).

As the number of nodes in the network increases, the need for internode communication grows exponentially. Hence, it is essential to design an efficient interconnection network (Halla *et al.*, 2021). Storing a large amount of data in data centres (DCs) and exchanging global data traffic require a large number of servers for large data centre networks (DCNs) to manage inter-server traffic. This has imposed the need for an ultra-high capacity interconnection network with fast switching speeds, at each switching node (Glick, 2017; Proietti *et al.*, 2018; Andreades *et al.*, 2019; Lallas, 2019).

The data vortex network is built on a multistage Banyan network architecture with a concentric cylinder structure and a distributed deflection routing control scheme to optimize packet switching and resolve contention. This innovative approach enhances the efficiency, scalability, and performance of the network (Duro *et al.*, 2021).

Likewise, as internet traffic continues to grow exponentially, data centres must scale their networks to handle higher volumes of data efficiently. This necessitates high-performance networks capable of rapid data transmission and processing (Sangeetha *et al.*, 2023). To meet the increasing demands for high-speed and long-distance communications, data centres are turning to fiber interconnections and optical switching technologies. Fiber optics provide the necessary bandwidth and scalability, while optical switches enable faster, more efficient data routing with reduced latency (Zhao *et al.*, 2023).

The increasing volume of traffic necessitates lower latency interconnection networks for future next-generation DCNs. This also calls for the investigation of new modified topologies to increase the transmission

capacities by increasing the bisection bandwidth of DCNs. It is also crucial that large traffic loads flow seamlessly from the optical layer (Soto, 2018; Minakhmetov, 2019; Minakhmetov *et al.*, 2020). The rapid expansion of cloud services has led to a significant increase in the number of servers within data centres. High server density generates substantial intra-data centre traffic, requiring network topologies that can efficiently manage and route this traffic while minimizing latency and bottlenecks (Castillo, 2022).

Fortunately, the data vortex switch was originally designed as an all optical interconnection network for HPC applications (Reed, 1999). It was highly scalable, with low latency and narrow latency distribution compared to traditional switches used for OPS HPC applications. Later, the Data Vortex switch was investigated in references (Yang *et al.*, 2001; Yang & Bergman, 2002a; Yang & Bergman, 2002b; Lu *et al.*, 2003; Papadimitriou *et al.*, 2003; Shacham *et al.*, 2005; Shacham & Bergman, 2007). For the first time, the equivalent chained planar (MIN) model, which is a planar diagrammatic conversion of a 3-D model DV network was presented (Sharma *et al.*, 2004; Sharma *et al.*, 2006; Sharma *et al.*, 2007a). This planar representation of DV from 3-D was very useful for studying fault tolerance, terminal reliability, network reliability of DV, and comparison with other MIN models, which were not considered previously (Sharma *et al.*, 2007a).

The augmented data vortex (ADV) network was proposed to enhance fault tolerance, terminal reliability, injection rate, latency and latency distribution of DV networks (Sharma *et al.*, 2007a; Sharma *et al.*, 2007b). Furthermore, the hardware planar layout of the Data Vortex was developed by Q. Yang as described in reference (Yang, 2012). A reverse DV architecture was proposed by Sangeetha *et al.*, (2013) and a bidirectional DV architecture (Sangeetha *et al.*, 2014). To ensure good quality of service (QoS) in OPS interconnection networks, a modular data vortex with hybrid switching was proposed in DV networks (Yang, 2014). The Data Vortex switch design is not only suitable for traditional HPCS, but also effective for asymmetrical access patterns and complex data analytics (Gioiosa *et al.*, 2016). It is also suitable for sporadic applications (Gioiosa *et al.*, 2017). After a detailed analysis it was observed that the DV not only has an inherent ability to overcome the limitations of earlier photonic technologies, but is also a versatile switch suitable for multiple applications using all optical packet switching.

For the simulations or analytics discussed in the literature above, the first step is to generate the interconnections of the 3-D DV switch. Additionally, Sharma (2007a), demonstrates that the equivalent planar prototype (EPA) architecture of 3-D DV is beneficial for fault tolerance and reliability analysis when compared to other MINs, QoS implementations etc.

In the above context, this paper aims to present an improved, generalized and efficient algorithm for generating the equivalent planar architecture (EPA) of the 3-D data vortex architecture. This will be achieved by utilizing the unique features of the C++ language to establish all potential interconnections between each source-target node pair. Earlier, an algorithm (Sharma *et al.*, 2004) was proposed to identify all possible routes in the data vortex switch, which also generated the EPA of a DV switch for the first time, albeit with limited versatility. This architecture has potential applications in various areas, such as survivability, congestion control and quality of service (QoS) applications. By utilizing the EPA, the creation of backup paths can be strategically planned, for use in the event of a network failure. The proposed algorithm can also assess fault tolerance by evaluating different links and node failures. Additionally, the performance of the planar architecture such as injection rate and latency is evaluated through numerical simulation written in C++.

The proposed EPA algorithm offers a significantly more adaptable configuration for various network levels, and research confirms that it provides routing performance comparable to the original structure. Due to the adaptability of the new planar design, future studies may investigate further improvements in routing resources and execution. The generalized algorithm facilitates smooth and fault free interconnections with high scalability.

## MATERIALS AND METHODS

### Original data vortex architecture

The original DV switch architecture was designed by Yang *et al.* (2001), supporting all optical OPS applications by using fewer switching and logic functions and avoiding the need for internal buffering in the network. In this 3-D design, the authors utilized two techniques to eliminate packet conflict and minimize the number of logic decisions required. These techniques, 'synchronous packet clocking' and 'distributed control signalling'

are useful to route data payload traffic easily in the optical network. A detailed explanation of the original architecture can be found in (Yang *et al.*, 2001; Yang & Bergman, 2002a; Yang & Bergman, 2002b; Lu *et al.*, 2003; Papadimitriou *et al.*, 2003; Shacham *et al.*, 2005; Shacham & Bergman, 2007).

In the design of the original DV, it was assumed that all packets were of similar size and had better timing alignment at the entry point from the input terminal. To manage synchronous slotted function, the routing pathways were properly designed. The routing nodes existed on a rich collection of concentric cylinders. The cylindrical design was defined by two dimensions: the height parameter 'H' corresponded to the number of nodes lying across the cylinder height and, the angle parameter 'A' should be an odd number less than 10. A lot of work has been done by researchers at Columbia University and Georgia Tech. and their simulation results show that the DV switch architecture achieves better performance when the angle parameter is a small odd number less than 10 (Dong *et al.*, 2008). The angle corresponds to the count of nodes across the circumference. 'H×A' represents the total count of nodes in each cylinder. The total count of cylinders can be calculated by 'C=1+log<sub>2</sub>H'. The total count of nodes in the entire architecture of the switch is 'C×H×A' with 'H×A' I/O ports.

Figure 1 shows a 3-D architecture for an A=3, H=4, C=3 DV switch fabric. Each square point represents a routing node. Each node (square point) is addressed by coordinates (a,c,h), where '0≤a<A', '0≤h<H' and '0≤c<C'. All the packets ingress at the c=0 cylinder level (outermost level) and exit at the c=log<sub>2</sub>H level (innermost level). Each packet adopts a self-routing scheme. At each cylinder level, the d<sub>i</sub> bit of the payload header (binary) is compared with the d<sub>i</sub> bit of node height. Here, 'i' is the current cylinder level. Suppose if a packet ingresses from c=0 (outermost) cylinder level then i is 0 (zero). At each level, packets are progressed in a synchronized way and in a parallel manner.

The mapping arrangement can be understood from the given example of an H=4 switch design (shown in Figure 1). The dashed-line pathways between adjacent cylinders maintain a consistent height as they are solely used to forward the packets. Conflict prevention, and therefore the required reduction in processing at the nodes, is achieved through independent control bits. Control messages are exchanged between nodes before a packet arrives at a given node to establish the correct routing option within the network.

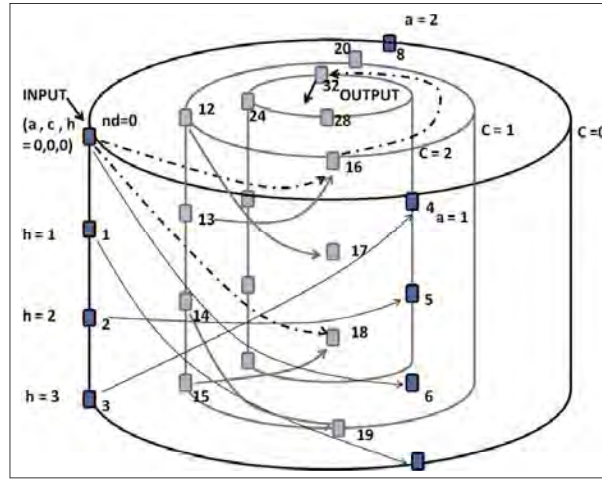


**Figure 1:** Interconnection arrangement of the original DV switch with adjacent cylinders for A=3, C=3, H=4 (Yang *et al.*, 2001)

**Equivalent planar architecture (EPA) of DV**

In the EPA architecture of DV, each three-dimensional cylinder level corresponds to the respective layer as shown in Figure 2 (Sharma *et al.*, 2007a). Thus, layer-0 represents the c=0 cylinder level (outermost cylinder) and layer M represents the cylinder level c=log<sub>2</sub>H (innermost cylinder). In each layer of the EPA, we have 2<sup>c</sup> subsections or rings. The total count of layers (L) should be equal to log<sub>2</sub>H+1 (equal to the total count of cylinders). In the EPA structure the I/O node count is also A×H. The total node count in a switch is A×C×H. The interconnection arrangement for each layer is the same, as given in Figure 1, for a distinct level of cylinders. The data packet enters from the input node of the outermost layer, i.e., layer 0, and exits from the output node from the innermost layer i.e., from layer log<sub>2</sub>H. The interconnection links between the layers cross in a binary tree fashion. In this type of arrangement, the next most significant bit (MSB) of the header address is fixed before the packet advances to the next adjacent layer. Interconnection links between layers forward packets to the correct destination.

Suppose we have an EPA design with A=3, H=4, and L=3 where a node is represented by (a,c,h). Every node has 2 input and 2 output connections. In the case of inputs, one input connects from the outer adjacent layer and another input connects from the current layer. In the case of outputs, one output goes to the adjacent inner layer and another output to the current layer.

The interconnection arrangement and self-routing scheme to forward the packets are the same as in the original DV. In the EPA, every node (a,c,h) and its 2 output connecting nodes are transformed into their equivalent representations in decimal form by the following expressions (Sharma *et al.*, 2004):

$$ndNode = H \times a + (A \times H) \times c + h \quad \dots(1)$$

To find out the node on the current layer, represented by ‘sndNode’, which is interconnected to ‘ndNode’, the interconnection pattern shown in Figure 1 is as follows:

$$sndNode = H \times nxa + (A \times H) \times c + nxh \quad \dots(2)$$

To find ‘nxa’, the expression is

$$nxa = (a + 1) \% A \quad \dots(3)$$

and ‘nxh’ can be found by the interconnection arrangement described in previous section.

To find the node on the next adjacent layer, ‘indNode’ is connected to ‘ndNode’ and the expression is

$$indNode = H \times nxa + (A \times H) \times (c + 1) + h \quad \dots(4)$$

Example: Suppose the node to be taken as (a=1, c=0, h=3), with A=3, H=4, L=3.

Then, nxa=2. nxh=0, given values are substituted in equation (1), (2) and (4)



$$\begin{aligned} \text{ndNode} &= 4 \times 1 + (3 \times 4) \times 0 + 3 = 7 \\ \text{sndNode} &= 4 \times 2 + (3 \times 4) \times 0 + 0 = 8 \\ \text{indNode} &= 4 \times 2 + (3 \times 4) \times (0 + 1) + 3 = 23 \end{aligned}$$

In a similar way, the remaining decimal values of interconnecting nodes can be found for the rest of the nodes.

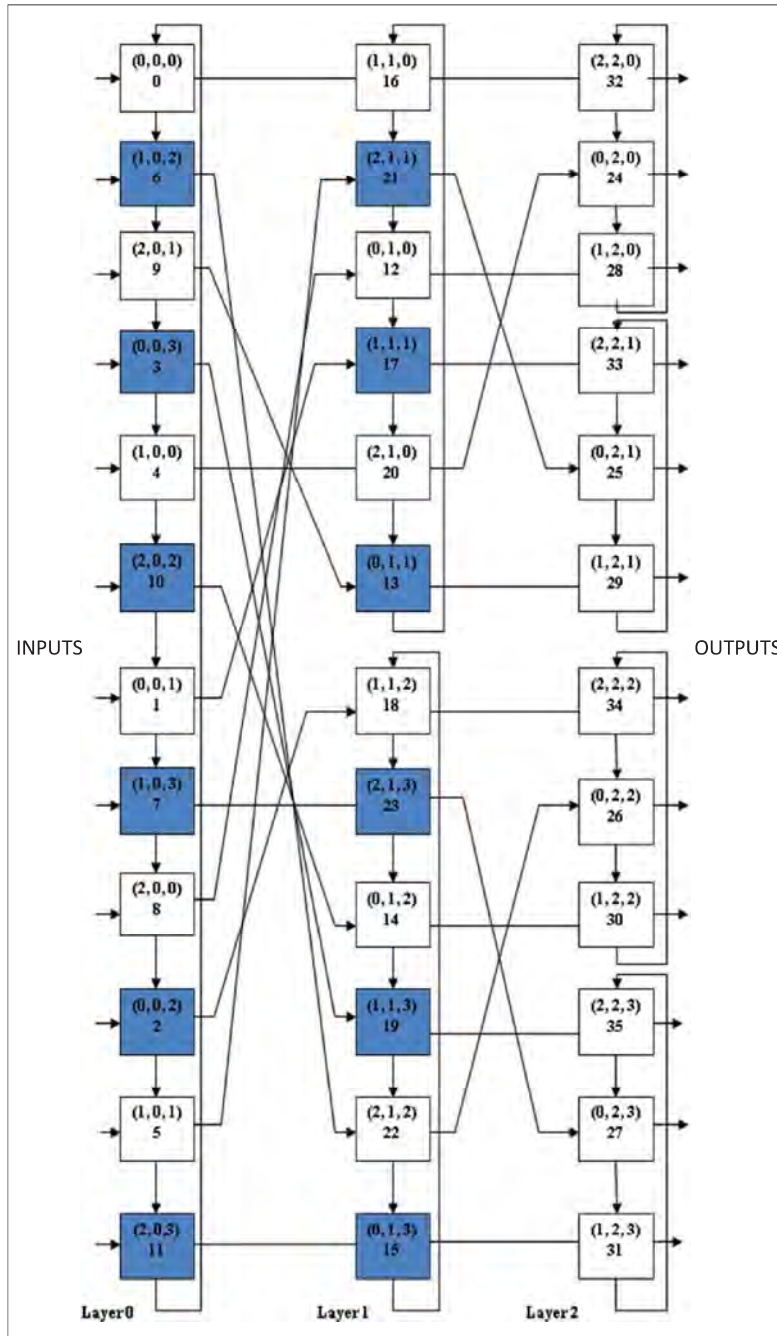


**Figure 2:** Equivalent planar architecture (EPA) for 3-D original DV architecture of size A=3, L=3, H=4 (Sharma *et al.*, 2007a)

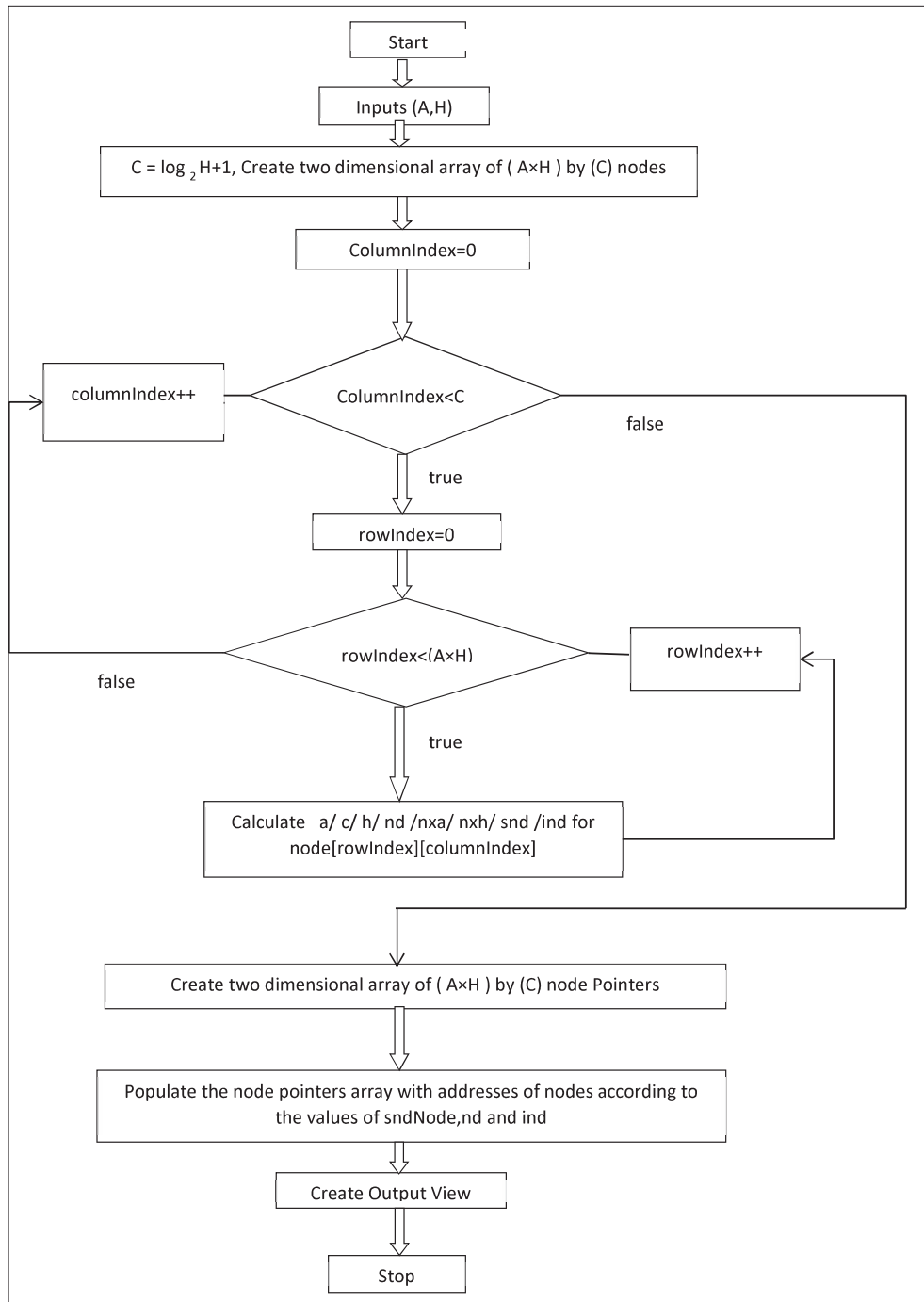


**Figure 3:** Flow chart of the proposed generalized equivalent planar architecture algorithm of DV (EPAA-DV)

**Flow chart and advantages of proposed EPA**

The flow chart of the algorithm is described in Figure 3. The steps of the EPAA-DV algorithm are given below:

- Step 1:** Initialize the angle A, and height H as inputs.
- Step 2:** Initialize the columnindex, let columnindex=0.
- Step 3:** If (columnindex<C), go to step 4, Else, go to step 9,
- Step 4:** Initialize rowindex, let rowindex=0,
- Step 5:** If (rowindex<(A×H)), go to step 6, Else, columnindex++ and go to step 3,
- Step 6:** Calculate a, c, h, ndNode, nxa, nxh, sndNode, indNode, for [rowindex] [columnindex],
- Step 7:** rowindex++ , Go to step 5 Else, columnindex++ and go to step 3,
- Step 8:** End,
- Step 9:** Create two dimensional array of (A×H) by C node pointer
- Step 10:** Populate the node pointer array with address of nodes according to the values of snd, nd, ind.
- Step 11 :** Create output view.
- Step 12 :** End.

1. The main advantage of a generalised EPA algorithm is that it can generate an equivalent planar architecture layout of 3-D, DV for any given size such as A and H.
2. The EPA algorithm simplifies the generation of interconnections of the original DV network in a fault-free and efficient manner, and hence it is easy to compare its topology with other similar types of MNs.
3. Here the 3-dimensional structure is converted into a planar architecture with multiple layers of routing levels making new construction and integration fast and easy with the help of this algorithm.
4. Since a new architecture is designed equivalent to the original DV network, the routing performance such as latency and throughput, is similar to that of the original DV network under similar system working conditions.
5. The proposed EPAA-DV algorithm is an improvement over the earlier algorithm as it is based on C++ language. An artificial simulation environment has been developed using threading, design of classes, file sharing, arrays and all other features of the C++

language. A programme in C++ language has been developed that automatically evaluates the nodes and represents all the nodes in a planar view with respect to each layer.

**Proposed equivalent planar architecture algorithm (EPAA) performance analysis**

The goal of our study is to explore the key performance parameters of an equivalent planar architecture of DV, generated using the new algorithm, which includes latency of switch and injection rate (IR). This will be done through numerical simulations based on an event simulator written in C++ environment. The statistics will be collected over 1000 clock cycles after the initial transient period. To transmit the data packets from source to target a uniform random traffic model will be used. In random traffic, the time slot of each packet injection is independent of other time slot injections. The amount of input traffic is identified by a parameter named the load parameter defined as the fraction of time a new packet injection is attempted. A load parameter of 0.5 indicates that a new packet injection is attempted at every other time slot. To simplify the investigation, only the height details of output ports are coded as the packet target address. All accessible angles accept the switched data packets at the output ports. The network performance of the equivalent planar architecture of DV will be investigated under different loads and for different switch sizes with the main performance evaluation parameters being latency and IR.

Table 1 shows different network arrangements of the Data Vortex switch for comparison. The following network arrangements labelled L, M, N and O are compared. Each network supports a different number of inputs and outputs. In network ‘M’ the number of switches used is between that of network ‘L’ and ‘N’. All of the network architectures use the same active angle A=5.

**Table 1:** Different network arrangements of the DV Switch

Network Name	‘A’	‘H’	Total Nodes
L	5	4	60
M	5	8	160
N	5	16	400
O	5	32	3160

**Latency**

The latency of a switching architecture is defined as the mean number of hops travelled by packets to reach the target.

Figure 4a shows the latency presented as a function of the switch size with A=5 for various loads. From the figure and Table 2, it is observed that the latency of the switch is low for small switch sizes and light loads, which is likely due to low traffic density. The planar DV showed almost a similar performance as reported by Reed (1999).

Due to the low traffic volume in a small switch, the likelihood of deflection is also reduced. In Figure 4a and Table 2, at full load 1.0, the switch requires 5 hops to reach its target for H=4, however, for H=32, it needs 15

hops. The reason is evident since with a small switch size there is less traffic congestion, and the probability of deflection is low. As the switch size increases the latency also increases but the behaviour of the planar switch remains consistent with the findings of Yang *et al.*, (2001).

**Injection rate**

The injection rate (IR) is defined as the ratio of successfully injected packets into the first layer of the switch over the total number of injection trials.

In Figure 4.1(b), the IR is plotted as a function of input loads for different switch heights with angle A=5. From the figure and Table 3, it can be observed that as the load increases the IR decreases, while for small loads the IR is good.

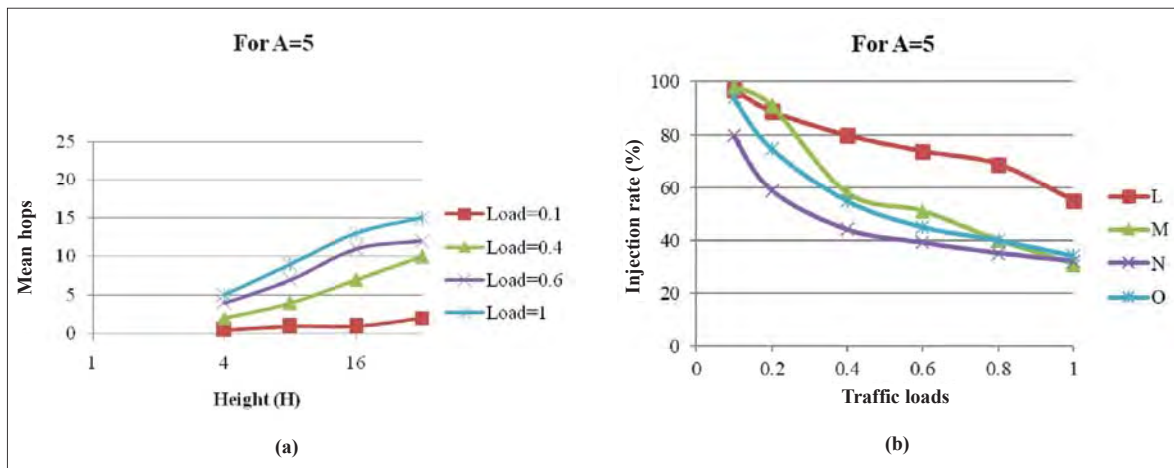


**Figure 4:** (a) Latency performance comparison for varying loads on different network arrangements of the DV  
 (b) Injection rate performance comparison for varying traffic loads on different network arrangements of DV

**Table 2:** Latency (mean hops) performance under varying input traffic loads for different arrangements of DV

Network arrangements	Traffic loads			
	0.1	0.4	0.6	1
latency				
Network L	0.5	2	4	5
Network M	1	4	7	9
Network N	1	7	11	13
Network O	2	10	12	15

**Table 3:** Injection rate (IR) performances for varying input traffic loads on different network arrangements of DV

Network arrangements	Traffic loads					
	0.1	0.2	0.4	0.6	0.8	1
injection rate (%)						
Network L	97	89	80	74	69	55
Network M	98	91	58	51	40	31
Network N	80	59	44	39	35	32
Network O	94	75	55	45	40	34

**RESULTS AND DISCUSSION**

The proposed EPA algorithm (see Figure 3) was utilized to identify all potential interconnections of the DV and validate the routes between any source-target pair. As mentioned earlier, the packet enters from the input node at layer 0 and exits from the output node at layer  $\log_2 H$ . As the packet moves from outer layers to the inner layer it updates the next most significant bit (MSB) of the header address before advancing to the next adjacent layer. It also maintains a consistent height during this process. However, if the destined inner layer interconnection link is blocked due to a header mismatch or the priority of another node, then the packet deflects within the current layer from ndNode (nd) to sndNode (snd). For example, in Figure 2, the Equivalent Planar Architecture is illustrated for a planar switch size of ‘A’=3 and ‘H’=4.

To confirm the routing of the DV, let’s consider a packet entering from the node address (2,0,1) or nd = 9 (from equation 1). The number of header bits count can be obtained using the formula  $\log_2 H$ . Here, with H=4 the frame has 2 bits header (binary). This indicates the destination address is 1, which was inserted into the packet upon injection at the input link of the input node at the 0<sup>th</sup> layer level. To verify the routing process only one packet was injected. In Figure 2, it is shown that the packet entered the inner layer 1 at node address (2,0,1) and by comparing the MSB of the packet’s header bit with the corresponding MSB of the node’s height it progresses into the next adjacent layer indNode (ind) =13 (from equation 4) or (0,1,1). Again the same step for header decoding is repeated and the packet enters the next adjacent layer, which is layer 1 at node (1,2,1). In this example, layer 2 is the last or innermost layer. It is assumed that if the packet’s header address matches the targeted node height of the last layer then the packet will exit successfully from that node if the output link is free. This can be seen in Figure 5, which shows the same routing path as explained above.

**Verification of routing of the planar DV by EPA Algorithm for planar switch size A=3 and H=4**

1.	nd=0	nd=16	nd=32
	a=0,c=0,h=0	a=1,c=1,h=0	a=2,c=2,h=0
	nxa=1	nxa=2	nxa=0
	nxb=2	nxb=1	nxb=0
	snd=6	snd=21	snd=24
	ind=16	ind=32	ind=36

2.	nd=6	nd=21	nd=24
	a=1,c=0,h=2	a=2,c=1,h=1	a=0,c=2,h=0
	nxa=2	nxa=0	nxa=1
	nxb=1	nxb=0	nxb=0
	snd=9	snd=12	snd=28
	ind=22	ind=25	ind=40
3.	nd=9	nd=12	nd=28
	a=2,c=0,h=1	a=0,c=1,h=0	a=1,c=2,h=0
	nxa=0	nxa=1	nxa=2
	nxb=3	nxb=1	nxb=0
	snd=3	snd=17	snd=32
	ind=13	ind=28	ind=44
4.	nd=3	nd=17	nd=33
	a=0,c=0,h=3	a=1,c=1,h=1	a=2,c=2,h=1
	nxa=1	nxa=2	nxa=0
	nxb=0	nxb=0	nxb=1
	snd=4	snd=20	snd=25
	ind=19	ind=33	ind=37
5.	nd=4	nd=20	nd=25
	a=1,c=0,h=0	a=2,c=1,h=0	a=0,c=2,h=1
	nxa=2	nxa=0	nxa=1
	nxb=2	nxb=1	nxb=1
	snd=10	snd=13	snd=29
	ind=20	ind=24	ind=41
6.	nd=10	nd=13	nd=29
	a=2,c=0,h=2	a=0,c=1,h=1	a=1,c=2,h=1
	nxa=0	nxa=1	nxa=2
	nxb=1	nxb=0	nxb=1
	snd=1	snd=16	snd=33
	ind=14	ind=29	ind=45
7.	nd=1	nd=18	nd=34
	a=0,c=0,h=1	a=1,c=1,h=2	a=2,c=2,h=2
	nxa=1	nxa=2	nxa=0
	nxb=3	nxb=3	nxb=2
	snd=7	snd=23	snd=26
	ind=17	ind=34	ind=38
8.	nd=7	nd=23	nd=26
	a=1,c=0,h=3	a=2,c=1,h=3	a=0,c=2,h=2
	nxa=2	nxa=0	nxa=1
	nxb=0	nxb=2	nxb=2
	snd=8	snd=14	snd=30
	ind=23	ind=27	ind=42
9.	nd=8	nd=14	nd=30
	a=2,c=0,h=0	a=0,c=1,h=2	a=1,c=2,h=2
	nxa=0	nxa=1	nxa=2
	nxb=2	nxb=3	nxb=2
	snd=2	snd=19	snd=34
	ind=12	ind=30	ind=46
10.	nd=2	nd=19	nd=35
	a=0,c=0,h=2	a=1,c=1,h=3	a=2,c=2,h=3
	nxa=1	nxa=2	nxa=0
	nxb=1	nxb=2	nxb=3
	snd=5	snd=22	snd=27
	ind=18	ind=35	ind=39

11.	nd=5 a=1,c=0,h=1	nd=22 a=2,c=1,h=2	nd=27 a=0,c=2,h=3
	nxa=2	nxa=0	nxa=1
	nxb=3	nxb=3	nxb=3
	snd=11 ind=21	snd=15 ind=26	snd=31 ind=43
12.	nd=11 a=2,c=0,h=3	nd=15 a=0,c=1,h=3	nd=31 a=1,c=2,h=3
	nxa=0	nxa=1	nxa=2
	nxb=0	nxb=2	nxb=3
	snd=0 ind=15	snd=18 ind=31	snd=35 ind=47

**Flow is as follows:**

Data Fed: 64321 in Node 9 on Layer 1 where c=0

The binary form of 64321 is 1111101101000001

Number of header bits 2

nd=9 a=2,c=0,h=1 nxa=0 nxb=3 snd=3 ind=13
nd=13 a=0,c=1,h=1 nxa=1 nxb=0 snd=16 ind=29
nd=29 a=1,c=2,h=1 nxa=2 nxb=1 snd=33 ind=45

Finally, 64321 reached its destination after 2 hops.

**Figure 5:** Verification of routing path using the EPA algorithm

**CONCLUSION**

In this paper an efficient and improved generalized equivalent planar architecture algorithm for data vortex has been developed. The main advantage of this algorithm is that it is able to identify all possible connections between every node-pair in the data vortex network and enable the design of circuits in equivalent planar model for any given size in simpler and more versatile way as compared to the methods used in earlier

literature. In addition, simulations were conducted to analyze the performance of the proposed EPA algorithm by including different network sizes with a wide dynamic range of varying input traffic loads to validate the results. Two performance parameters, latency of switching architecture and injection rate, were studied. Their behaviour was found to be similar which validated the routing behaviour to be similar to the original DV but easier to study in terms of fault tolerance. Based on these results, the proposed algorithm can be considered as a strong candidate for large scale systems, parallel computing and HPCS applications. The EPA algorithm is versatile and can easily adapt to the diverse needs of next generation HPCS and large Data Centre Networks application.

**REFERENCES**

Andreades, P., Clark, K., Watts, P.M., & Zervas, G. (2018). Experimental demonstration of an ultra-low latency control plane for optical packet switching in data centre networks. *Journal of Optical Switching and Networking*, 32(4), 51-60. <https://doi.org/10.1016/j.osn.2018.11.005>

Castillo, A. C. (2022). Various network topologies and an analysis comparative between fat tree and B cube for a data center network: An overview. *Proceedings of 2022 IEEE cloud Summit, VA, USA, 2022*, 1-8. <https://doi.org/10.1109/CloudSummit54781.2022.000007>

Chen, K. S. (2019). Multiple- code technique for multi-rate transmission in optical packet switching networks based on OCDMA tables. *Photonics*, 6(2),60. <https://doi.org/10.3390/photonics6020060>

Dong, L., Duo, Q., Fenz, Q., & Duo, w. (2008). A comparison study of the data vortex topologies with different angle parameter under asymmetric I/O mode. *International Conference on Computer Science Information Technology*, 453-457. <https://doi.org/10.1109/ICCSIT.2008.139>

Duro, J., Petit, S., Gonez, M.E., & Sahuquillo, J. (2021). Segment switching : A new switching strategy for optical HPC networks. *IEEE ACCESS*, 99(1-1).

Gioiosa, R., Yin, T. J., Tumeo, A., & Haglin, D. (2016). Exploring data vortex network architectures. *Proceedings of 24th Annual Symposium on High-Performance Interconnects HOTI*, 84–91. <https://doi.org/10.1109/HOTI.2016.025>

Gioiosa, R., Yin, T. J., Tumeo, A., Warfel, T., Haglin, D., & Betelu, S. (2017). Exploring data vortex systems for irregular applications. *2017 IEEE International Parallel and Distributed Processing Symposium IPDPS*, 409–418. <https://doi.org/10.1109/IPDPS.2017.121>

Glabowski, M., Ivanov, H., Leitgeb, E., Sobieraj, M., & Stasiak, M. (2020). Simulation studies of elastic optical networks based on 3-stage clos switching fabric. *Optical Switching and Networking*, 36 Article 100555. <https://doi.org/10.1016/j.osn.2020.100555>

- Glick, M. (2017). The role of integrated photonics in data centre networks. *Next Generation Optical Networks for Data Centre and Short-Reach Links IV*. University of Arizona. <https://doi.org/10.1117/12.2255794>
- Halla, M. N., Foersterb, K., Schmidb, S., & Durairajana, R. (2021). A survey of reconfigurable optical networks. *Journal of Optical Switching and Networking*, 41 Article 100621. <https://doi.org/10.1016/j.osn.2021.100621>
- Hawkins, C., & Wills, D. S. (2006). Impact of number of angles on the performance of the data vortex optical interconnection network. *Journal of Lightwave Technology*, 24(9), 3288–3294. <https://doi.org/10.1109/jlt.2006.879508>
- Hawkins, C., Small, B. A., Wills, D. S., & Bergman, K. (2007). The data vortex, an all-optical path multicomputer interconnection network. *IEEE Transaction on Parallel and Distributed Systems*, 18(3), 409–420. <https://doi.org/10.1109/TPDS.2007.48>
- Jokar, M.R., QIU, J., Chang, F.T., Goddard, L.L., Dallesasse, J.M., Fevg, M., & Li, Y. (2020). Baldur: A power-efficient and scalable network using all optical switches. Proceedings of *IEEE International Symposium on High Performance Computer Architecture (HPCA)*, CA, USA, 153-166. <https://doi.org/10.1109/HPCA47549.2020.00022>
- Lallas, Efthymios N. (2019). A Survey on key roles of optical switching and labeling technologies on big data traffic of data centers and HPC environments. *AIMS Electronic and Electrical Engineers*, 3(3), 233-256. <https://doi.org/10.39341/ElectrEng.2019.3.233>
- Lu W., Bergman, K., & Yang, Q. (2003). WDM routing with low cross-talk in the data vortex packet switching fabric. Proceedings of *Optical Fiber Communication Conference, Pap. FS4, Optical Society of America*, GA, USA, 795-797. <https://doi.org/10.1109/OFC.2003.316016>
- Minakhmetor, A. (2019). Cross-layer hybrid and optical packet switching. [Doctoral Dissertation, Institute Polytechnique de Paris]. <https://pastel.archives-ouvertes.fr/tel-02481270>
- Minakhmetor, A., Ware, C., & Iannone, L. (2020). Hybrid and optical packet switching supporting different service classes in data centre networks. *Journal of Photonic Network Communication*, 40, 293-302. <https://doi.org/10.1007/s11107-020-00894-9>
- Papadimitriou, G.I., Papazoglou, C., & Pomportsis, A.S. (2003). Optical switching: Switch fabrics, techniques, and architectures. *Journal of Lightwave Technology*, 21(2), 384–405. <https://doi.org/10.1109/JLT.2003.808766>
- Proietti, R., Xiao, X., Zhang, K., Liu, G., Lu, H., Fotouhi, P., Messing, J., & Yoo, S.J.B. (2018). Experimental demonstration of a 64 port wavelength routing thin-CLOS Systems for data centre switching architecture. *Journal of Optical Communications and Networking*, 10(7), B49. <https://doi.org/10.1364/JOCN.10.000B49>
- Reed C. S. (1999). *Multiple level minimum logic network*, US5996020A.
- Sangeetha, R.G., Chandra, V., & Chadha, D. (2013). Optical interconnection reverse data vortex network: Performance analysis. *Photonics Network Communication*, 25, 79–88. <https://doi.org/10.1007/s11107-013-0392-4>
- Sangeetha, R.G., Chandra, V., & Chadha, D. (2014). Bidirectional data vortex optical interconnection network: BER performance by hardware simulation and evaluation of terminal reliability. *Journal of Lightwave Technology*, 32(19), 3266–3276. <https://doi.org/10.1109/JLT.2014.2341735>
- Sangeetha, R. G., Chandran, H., Vijayan, N., Yadav, V., & Mishra, S. (2023). A machine learning assisted optical multistage interconnection network: Performance analysis & hardware demonstration. *ETRI Journal*, 45(1), 60-74. <https://doi.org/10.4218/etrij.2021-0182>
- Shacham, A., Small, B.A., Liboiron-Ladouceur, O., & Bergman, K. (2005). A fully implemented 12× 12 data vortex optical packet switching interconnection network. *Journal of Lightwave Technology*, 23(10), 3066-3075. <https://doi.org/10.1109/JLT.2005.856242>
- Shacham, A., & Bergman, K. (2007). On contention resolution in the data vortex optical interconnection network. *Journal of Optical Networking*, 6(6), 777-788. <https://doi.org/10.1364/JON.6.000777>
- Sharma, N., Chadha, D., & Chandra, V. (2004). Algorithm for finding all routes in data vortex switch. *Proceeding of the International Conference, Photonics, Cochin, India*. <https://www.researchgate.net/publication/228879753>
- Sharma, N., Chadha, D., & Chandra, V. (2006). Fault tolerance in multiplexed data vortex all-optical interconnection network. *National conference on communication, IIT Delhi*.
- Sharma, N., Chadha, D., & Chandra, V. (2007a). The augmented data vortex switch fabric: An all-optical packet switched interconnection network with enhanced fault tolerance. *Optical Switching and Networking*, 4, 92–105. <https://doi.org/10.1016/j.osn.2007.02.001>
- Sharma, N., Chadha, D., & Chandra, V. (2007b). Performance evaluation of the augmented data vortex switch fabric: An all-optical packet switched interconnection network. *Optical Switching and Networking*, 4, 213–224. <https://doi.org/10.1016/j.osn.2007.04.001>
- Soto, K. (2018). Realization and application of large scale fast optical circuit switch for data centre networking. *Journal of Lightwave Technology*, 36(7), 1411-1419. <https://doi.org/10.1109/JLT.2018.2801308>
- Yang, Q., Bergman, K., Hughes, G.D., & Johnson, F.G. (2001). WDM packet routing for high-capacity data networks. *Journal of Lightwave Technology*, 19, 1420–1426. <https://doi.org/10.1109/50.956129>
- Yang, Q., & Bergman, K. (2002a). Traffic control and WDM routing in the data vortex packet switch. *IEEE Photonics Technology Letter*, 14, 236–238. <https://doi.org/10.1109/68.980533>
- Yang, Q., & Bergman, K. (2002b). Performances of the data vortex switch architecture under nonuniform and bursty traffic. *Journal of Lightwave Technology*, 20, 1242–1247. <https://doi.org/10.1109/JLT.2002.800330>
- Yang, Q. (2012). Performance evaluation of a planar layout of

- data vortex optical interconnection network. *IARIA 2012, The international conference on fiber optic and photonics, Chennai, India*.
- Yang, Q. (2014). Hybrid switching in modular data vortex optical interconnection network. *Proceedings of 2014 16th International Conference Transparent Optical Networks, ICTON*. Graz, Austria, 1-4.
- <https://doi.org/10.1109/ICTON.2014.6876471>
- Zhao, Y. Xue, X., Ren, X., Li, W., Guo, Y., Yang, C., Dang, D., Zhang, S., Guo, B., & Huang, S. (2023). Optical switching data center networks : Understanding techniques and challenges. *Computer Networks and Communications Abstracts, 1(2)*, 272-291. <https://doi.org/10.37256/1220233159>.



RESEARCH ARTICLE

## Latin Squares

# Cycle structures with more than three nontrivial cycles of automorphisms of Latin squares

MJL Mendis\*

Department of Mathematics, Faculty of Science, University of Colombo, Colombo 03, Sri Lanka.

Submitted: 24 October 2023; Revised: 27 March 2024; Accepted: 23 July 2024

**Abstract:** A permutation  $\alpha \in S_n$  is said to be an automorphism of a Latin square if the Latin square is mapped to itself by permuting rows, columns and symbols by  $\alpha$ . Let  $\text{Aut}(n)$  be the set of all automorphisms of Latin squares of order  $n$ . Whether a permutation  $\alpha$  belongs to  $\text{Aut}(n)$  depends only on the cycle structure of  $\alpha$ . Stones *et al* characterised  $\alpha \in \text{Aut}(n)$  for which  $\alpha$  has at most three nontrivial cycles. In this research we prove some related results for automorphisms with four nontrivial cycles. Also we derived a necessary and sufficient condition for automorphisms opposite to said results when  $\alpha$  has finite number of nontrivial cycles such that each cycle is divisible by the next.

**Keywords:** Automorphism, autotopism, block diagram, cycle structure, Latin square.

## INTRODUCTION

A Latin square  $L$  of order  $n$  is an  $n \times n$  array containing  $n$  symbols from  $[n] = \{1, 2, \dots, n\}$  such that each element of  $[n]$  appears once in each row and each column of  $L$ . Rows and columns of  $L$  are indexed by elements of  $[n]$ . The element in the  $i^{\text{th}}$  row and  $j^{\text{th}}$  column is denoted by  $L(i, j)$ .

The set of  $n^2$  ordered triples,  $O(L) = \{(i, j, L(i, j)); i, j \in [n]\}$  is called the orthogonal array representation of  $L$ .

Let  $\theta = (\alpha, \beta, \gamma) \in S_n^3$ , where  $S_n$  is the symmetric group acting on  $[n]$ . A new Latin square  $\theta(L)$  is obtained by permuting rows, columns and symbols of  $L$  by  $\alpha, \beta, \gamma$  respectively. The elements  $\theta \in S_n^3$  are known as isotopisms and  $\theta(L)$  is said to be isotopic to  $L$ . If  $\theta(L) = L$ , then  $\theta$  is called an autotopism of  $L$ . If  $\theta = (\alpha, \alpha, \alpha)$ , then  $\alpha$  is said to be an automorphism.

Let  $\sigma = (\theta; \lambda) \in S_n \wr S_3$ , where  $\theta = (\alpha, \beta, \gamma)$ . A Latin square  $L^\sigma$  is obtained by permuting triples of  $O(\theta(L))$  by  $\lambda$ . For example, if  $(x, y, z)$  is a triple of  $L$  and  $\sigma = (\alpha, \beta, \gamma; (12))$  then  $\sigma(x, y, z) = (\beta(y), \alpha(x), \gamma(z))$ . The map  $\sigma$  is known as a paratopism of  $L$ . If  $L^\sigma = L$ , then  $\sigma$  is called an autoparatopism of  $L$ . Isotopism is one case of paratopism (i.e. when  $\lambda = id$ ). Let  $\text{Atp}(n)$ ,  $\text{Aut}(n)$  and  $\text{Par}(n)$  be the set of all autotopisms, automorphisms and autoparatopisms of Latin squares of order  $n$ , respectively.

Stones *et al.* (2012) characterised  $\alpha \in \text{Aut}(n)$  for which  $\alpha$  has at most three non-trivial cycles (i.e., cycles other than fixed points). A notable feature of this characterisation is that the length of the longest cycle of  $\alpha$  is always divisible by the length of every other cycle of  $\alpha$ . In this research we first prove a related result for automorphisms with four nontrivial cycles, before showing that no analogue holds for five nontrivial cycles.

\* jayama@maths.cmb.ac.lk;  <https://orcid.org/0000-0002-2308-6260>



Finally, we derive a sufficient condition for  $\alpha \in S_n$  to be an automorphism when the cycle structure of  $\alpha$  is  $d_1 \cdot d_2 \cdots d_{p-1} \cdot d_p^a$ , for some  $a \geq 1$ .

**METHODOLOGY**

**Cycle structures**

Every  $\alpha \in S_n$  decomposes into a product of disjoint cycles, where we consider fixed points to be cycles of length 1. We say  $\alpha$  has the cycle structure  $c_1^{\lambda_1} \cdot c_2^{\lambda_2} \cdots c_m^{\lambda_m}$  if there are  $\lambda_i$  cycles of length  $c_i$  in the unique cycle decomposition of  $\alpha$  and  $c_1 > c_2 > \cdots > c_m \geq 1$ . Hence  $n = \sum c_i \lambda_i$ . If  $\lambda_i = 1$ , we may write  $c_i$  instead of  $c_i^1$  in the cycle structure. If  $i$  is a point moved by a particular cycle  $C$  then we say that  $i$  is in  $C$  and write  $i \in C$ . We use  $o(C)$  to denote the length of a cycle  $C$  (in other words, the size of its orbit). We write  $o_\alpha(i) = c$  to denote that  $i$  is in some cycle  $C$  of the permutation  $\alpha$  for which  $o(C) = c$ .

A permutation in  $S_n$  is *canonical* if, (i) it is written as a product of disjoint cycles, including 1-cycles corresponding to fixed points; (ii) the cycles are ordered according to their length, starting with the longest cycles; (iii) each  $c$ -cycle is of the form  $(i, i + 1, \dots, i + c - 1)$ , with  $i$  being referred to as the leading symbol of the cycle, and (iv) if a cycle with leading symbol  $i$  is followed by a cycle with leading symbol  $j$ , then  $i < j$ . For each possible cycle structure there is precisely one canonical permutation with that cycle structure and there is a unique way to represent it as a product of disjoint cycles.

**Block diagrams**

Block diagrams are used to construct Latin squares with a prescribed autotopism. A block diagram of a Latin square  $L$  which admits an automorphism  $\alpha$  is described as follows.

Let  $\alpha_1, \alpha_2, \dots, \alpha_m$  be the nontrivial cycles of  $\alpha \in S_n$  with lengths  $d_1 \geq d_2 \geq \dots \geq d_m$  respectively. The Latin square  $L$  is divided into blocks  $M_{ij}$  for  $i, j \in [m]$  according to the cycle structure of  $\alpha$  such that  $i \in \alpha_i$  and  $j \in \alpha_j$ . If each symbol of  $\alpha_k$  appears  $f_k$  times in  $M_{ij}$  block then this is written as  $\alpha_k : f_k$  in this block.

In a block diagram the following two Latin square properties should be satisfied.

- (i)  $d_1 f_1(i, j) + d_2 f_2(i, j) + \dots + d_m f_m(i, j) = d_i d_j$  in every block  $M_{i,j}$ .
- (ii) For any  $i, k \in [m]$ ,  $\sum_{j \in [m]} f_k(i, j) = d_i$  and for any  $j, k \in [m]$ ,  $\sum_{i \in [m]} f_k(i, j) = d_j$ .

In addition to the above properties, the block diagram of a Latin square  $L$  with  $\alpha \in \text{Aut}(L)$  satisfies Lemma 3.1.

**Previous results**

The following lemma in Stones *et al.* (2012) gives a necessary condition for membership in  $\text{Atp}(n)$ .

**Lemma 3.1.** Let  $\theta = (\alpha, \beta, \gamma)$  be an autotopism of a Latin square  $L$ . If  $o_\alpha(i) = a$  and  $o_\beta(j) = b$ , then  $o_\gamma(L(i, j)) = c$ , where  $\text{lcm}(a, b) = \text{lcm}(b, c) = \text{lcm}(a, c) = \text{lcm}(a, b, c)$ .

**RESULTS AND DISCUSSION**

This theorem proves a necessary condition for  $\alpha \in S_n$  to be an automorphism when  $\alpha$  has four non-trivial cycles such that only longest cycle of  $\alpha$  is divisible by the length of every other cycles.

**Theorem 4.1.** Let  $d_1 d_2 d_3 d_4$  be the cycle structure of  $\alpha = \alpha_1 \alpha_2 \alpha_3 \alpha_4 \in S_n$  such that  $d_1 > d_2 > d_3 > d_4$  and  $d_4 \nmid d_3, d_4 \nmid d_2$  and  $d_3 \nmid d_2$ . If  $\alpha \in \text{Aut}(n)$  then

$$d_1 = \text{lcm}(d_2, d_3) = \text{lcm}(d_2, d_4) = \text{lcm}(d_3, d_4).$$

*Proof.* Suppose that  $d_2 \nmid d_1$ . Consider a cell  $(i, j)$  in the  $M_{12}$  block of a Latin square  $L$  for which  $\alpha \in \text{Aut}(L)$ . Then  $o_\alpha(i) = d_1$  and  $o_\alpha(j) = d_2$ . By Lemma 3.1,  $o_\alpha(L(i, j)) = c$ , where  $\text{lcm}(d_1, d_2) = \text{lcm}(c, d_1) = \text{lcm}(c, d_2)$ . Then,  $c \neq d_1$  since  $d_2 \nmid d_1$  and  $c \neq d_2$  since  $d_1 > d_2$ . Since  $\alpha_3$  or  $\alpha_4$  on its own cannot fill the  $M_{12}$  block, symbols from both these cycles must be used in this block. Therefore  $\text{lcm}(d_1, d_2) = \text{lcm}(d_1, d_3) = \text{lcm}(d_1, d_4) = \text{lcm}(d_2, d_3) = \text{lcm}(d_2, d_4)$ . If  $\text{lcm}(d_3, d_4)$  does not equal the lcm of the other pairs then there are no symbols available to fill the  $M_{34}$  block. Hence the lcm of all the different pairs are equal. Then the block diagram of  $L$  is as follows, where  $T_{bc}^a$  is the number of times each symbol in  $\alpha_a$  appears in the  $M_{bc}$  block.

	$\alpha_1$	$\alpha_2$	$\alpha_3$	$\alpha_4$
$\alpha_1$	$\alpha_1 : d_1$	$\alpha_3 : T_{12}^3$ $\alpha_4 : T_{12}^4$	$\alpha_2 : T_{13}^2$ $\alpha_4 : T_{13}^4$	$\alpha_2 : T_{14}^2$ $\alpha_3 : T_{14}^3$
$\alpha_2$	$\alpha_3 : T_{12}^3$ $\alpha_4 : T_{12}^4$	$\alpha_2 : d_2$	$\alpha_1 : T_{23}^1$ $\alpha_4 : T_{23}^4$	$\alpha_1 : T_{24}^1$ $\alpha_3 : T_{24}^3$
$\alpha_3$	$\alpha_2 : T_{13}^2$ $\alpha_4 : T_{13}^4$	$\alpha_1 : T_{23}^1$ $\alpha_4 : T_{23}^4$	$\alpha_3 : d_3$	$\alpha_1 : T_{34}^1$ $\alpha_2 : T_{34}^2$
$\alpha_4$	$\alpha_2 : T_{14}^2$ $\alpha_3 : T_{14}^3$	$\alpha_1 : T_{24}^1$ $\alpha_3 : T_{24}^3$	$\alpha_1 : T_{34}^1$ $\alpha_2 : T_{34}^2$	$\alpha_4 : d_4$

Considering the distribution of  $\alpha_3$  in the block diagram, we see that,  $T_{12}^3 + T_{14}^3 = d_1$ ,  $T_{21}^3 + T_{24}^3 = d_2$  and  $T_{14}^3 + T_{24}^3 = d_4$ . Hence  $T_{12}^3 + T_{21}^3 = d_1 + d_2 - d_4$ . A similar argument shows that  $T_{12}^4 + T_{21}^4 = d_1 + d_2 - d_3$ .

Counting symbols in  $M_{12} \cup M_{21}$ , we find that  $2d_1d_2 = d_3(T_{12}^3 + T_{21}^3) + d_4(T_{12}^4 + T_{21}^4) = d_3(d_1 + d_2 - d_4) + d_4(d_1 + d_2 - d_3)$  which implies that  $(d_1 - d_4)(d_2 - d_3) + (d_1 - d_3)(d_2 - d_4) = 0$ . This is a

contradiction since  $d_1 > d_2 > d_3 > d_4$ . Therefore  $d_2 \mid d_1$ .

Now consider the  $M_{23}$  block. Suppose  $o_\alpha(i) = c$  for some symbol  $i$  in the  $M_{23}$  block. Then by Lemma 3.1,  $\text{lcm}(d_2, d_3) = \text{lcm}(c, d_2) = \text{lcm}(c, d_3)$ . Then,  $c \neq d_3$  since  $d_2 > d_3$ , and  $c \neq d_2$  since  $d_3 \nmid d_2$ . Since  $\alpha_4$  cannot fill the  $M_{23}$  block on its own,  $T_{23}^1 > 0$ . Hence  $\text{lcm}(d_2, d_3) = \text{lcm}(d_1, d_3) = \text{lcm}(d_1, d_2) = d_1$ . Repeating this argument for  $M_{24}$  shows that  $\text{lcm}(d_2, d_4) = d_1$ . Now a similar argument for  $M_{34}$  shows that either  $T_{34}^1 > 0$  or  $T_{34}^2 > 0$ , and either will imply the result we need.

The argument used to prove Theorem 4.1 does not work when  $\alpha$  has five non-trivial cycles. We found the following block diagram satisfying Lemma 3.1 for  $\alpha = \alpha_1\alpha_2\alpha_3\alpha_4\alpha_5$  with lengths  $d_1 > d_2 > d_3 > d_4 > d_5$  such that none of  $d_2, d_3, d_4, d_5$  divide  $d_1$ :

	$\alpha_1$	$\alpha_2$	$\alpha_3$	$\alpha_4$	$\alpha_5$
$\alpha_1$	$\alpha_1 : 95381$	$\alpha_3 : 4451$ $\alpha_4 : 1776$ $\alpha_5 : 1844$	$\alpha_2 : 4304$ $\alpha_4 : 1370$ $\alpha_5 : 1163$	$\alpha_2 : 2274$ $\alpha_3 : 1591$ $\alpha_5 : 282$	$\alpha_2 : 1793$ $\alpha_3 : 1295$ $\alpha_4 : 201$
$\alpha_2$	$\alpha_3 : 4451$ $\alpha_4 : 1776$ $\alpha_5 : 1844$	$\alpha_2 : 60697$	$\alpha_1 : 4537$ $\alpha_4 : 63$ $\alpha_5 : 69$	$\alpha_1 : 2267$ $\alpha_3 : 192$ $\alpha_5 : 180$	$\alpha_1 : 1917$ $\alpha_3 : 26$ $\alpha_4 : 0$
$\alpha_3$	$\alpha_2 : 4304$ $\alpha_4 : 1370$ $\alpha_5 : 1163$	$\alpha_1 : 4537$ $\alpha_4 : 63$ $\alpha_5 : 69$	$\alpha_3 : 51359$	$\alpha_1 : 4304$ $\alpha_4 : 1370$ $\alpha_5 : 1163$	$\alpha_1 : 1171$ $\alpha_2 : 0$ $\alpha_4 : 600$
$\alpha_4$	$\alpha_2 : 2274$ $\alpha_3 : 1591$ $\alpha_5 : 282$	$\alpha_1 : 2267$ $\alpha_3 : 192$ $\alpha_5 : 180$	$\alpha_1 : 1679$ $\alpha_2 : 65$ $\alpha_5 : 539$	$\alpha_4 : 29029$	$\alpha_1 : 251$ $\alpha_2 : 300$ $\alpha_3 : 450$
$\alpha_5$	$\alpha_2 : 1793$ $\alpha_3 : 1295$ $\alpha_4 : 201$	$\alpha_1 : 1917$ $\alpha_3 : 26$ $\alpha_4 : 0$	$\alpha_1 : 1171$ $\alpha_2 : 0$ $\alpha_4 : 600$	$\alpha_1 : 251$ $\alpha_2 : 300$ $\alpha_3 : 450$	$\alpha_5 : 23023$

where

$$d_1 = o(\alpha_1) = 11 \times 13 \times 23 \times 29 = 95381,$$

$$d_2 = o(\alpha_2) = 7 \times 13 \times 23 \times 29 = 60697,$$

$$d_3 = o(\alpha_3) = 7 \times 11 \times 23 \times 29 = 51359,$$

$$d_4 = o(\alpha_4) = 7 \times 11 \times 13 \times 29 = 29029,$$

$$d_5 = o(\alpha_5) = 7 \times 11 \times 13 \times 23 = 23023.$$

It is not clear whether this block diagram is realised by any Latin square although we suspect that it is. In any case, McKay *et al.* (2015) have constructed a Latin square with an automorphism consisting of 5 non-trivial cycles, none of which has a length dividing the length of any other cycle. Hence it is clear that such things exist.

Next we look at the opposite scenario, where each cycle length is divisible by the next.

**Theorem 4.2.** Let  $d_1 \cdots d_{p-1} \cdot d_p^a$ , where  $a = m - p + 1$ , be the cycle structure of  $\alpha = \alpha_1\alpha_2 \cdots \alpha_m \in S_n$  such that  $d_i < d_{i-1}$  and  $d_i \mid d_{i-1}$  for  $2 \leq i \leq p$ , and  $d_1$  is odd. Then  $\alpha \in \text{Aut}(n)$  if and only if  $ad_p \leq d_{p-1}$ .

**Proof:** Suppose that  $\alpha \in \text{Aut}(L)$ . By [2, Thm 3.7],  $L$  has a subsquare induced by the cycles of  $\alpha$  of length  $d_p$ , inside a subsquare induced by the cycles of lengths  $d_{p-1}$  and  $d_p$ . It follows that  $ad_p \leq (ad_p + d_{p-1})/2$  and hence  $ad_p \leq d_{p-1}$ .

Now assume that  $ad_p \leq d_{p-1}$ . By induction on  $p$ , we will construct a Latin square  $L$  of order  $n$  having  $\alpha \in \text{Aut}(L)$ . The base case is provided by Stones (2012). In the general case Theorem 3.7 (Stones, 2012) shows that  $L$  has a subsquare induced by the cycles of  $\alpha$  other than  $\alpha_1$ .

This subsquare can be built, by the inductive hypothesis. So it suffices to give the following partial contour. Let  $e_q = \sum_{j=1}^q o(\alpha_j)$  for  $0 \leq q \leq m$ . In  $M_{11}$  we take,

$$C(i, d_1 + 1 - i) = \begin{cases} t_1, & \text{for } 1 \leq i \leq 2d_1 - n, \\ t_r, & \text{for } d_1 + e_{r-1} - n + 1 \leq i \leq d_1 + e_r - n, \\ \text{and } 2 \leq r \leq m, \end{cases}$$

In  $\bigcup_{r=2}^m M_{1,r}$  we take,  $C(d_1 + 1 - i, d_1 + i) = t_1$ , for  $1 \leq i \leq n - d_1$ . In  $\bigcup_{r=2}^m M_{r,1}$  we take  $C(n + 1 - i, i) = t_1$ , for  $1 \leq i \leq n - d_1$ .

For example, if  $d_1 \cdot d_2 \cdot d_3^3$  is the cycle structure of  $\alpha = \alpha_1\alpha_2\alpha_3\alpha_4\alpha_5$  then the block diagram is as follows.

	$\alpha_1$	$\alpha_2$	$\alpha_3$	$\alpha_4$	$\alpha_5$
$\alpha_1$	$\alpha_1 : d_1 - d_2 - 3d_3$ $\alpha_2 : d_2$ $\alpha_3 : d_3$ $\alpha_4 : d_3$ $\alpha_5 : d_3$	$\alpha_1 : d_2$	$\alpha_1 : d_3$	$\alpha_1 : d_3$	$\alpha_1 : d_3$
$\alpha_2$	$\alpha_2 : d_2$	$\alpha_2 : d_2 - 3d_3$ $\alpha_3 : d_3$ $\alpha_4 : d_3$ $\alpha_5 : d_3$	$\alpha_2 : d_3$	$\alpha_2 : d_3$	$\alpha_2 : d_3$
$\alpha_3$	$\alpha_1 : d_3$	$\alpha_2 : d_3$	$\alpha_3 : d_3$	$\alpha_4 : d_3$	$\alpha_5 : d_3$
$\alpha_4$	$\alpha_1 : d_3$	$\alpha_2 : d_3$	$\alpha_4 : d_3$	$\alpha_5 : d_3$	$\alpha_3 : d_3$
$\alpha_5$	$\alpha_1 : d_3$	$\alpha_2 : d_3$	$\alpha_5 : d_3$	$\alpha_3 : d_3$	$\alpha_4 : d_3$

**CONCLUSION**

Stones *et al.*, 2012 found automorphisms  $\alpha \in S_n$  when it has at most three non-trivial cycles. In this research, we proved a necessary condition for  $\alpha$  to be an automorphism when it consists of four non-trivial cycles having the property that only the length of largest cycle is divisible by the length of the other cycles. We were successful to make a block diagram to prove that the procedure used in the Theorem 4.2 cannot be continued for five non-trivial cycles.

Finally, we obtained a necessary and sufficient

condition for automorphisms opposite to above results when  $\alpha$  has finite number of non-trivial cycles such that each cycle is divisible by the next.

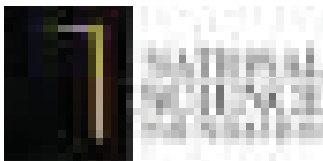
**REFERENCES**

McKay, B. D., Wanless, I. M., & Zhang, X. (2015). The order of automorphisms of quasigroups. *Journal of Combinatorial Designs*, 23, 275 - 288. <https://doi.org/10.1002/jcd.21389>

Stones, D. S., Vojt'echovsky', P., & Wanless, I. M. (2012). Cycle structure of autotopisms of quasigroups and Latin Squares. *Journal of Combinatorial Designs*, 20, 227 - 263. <https://doi.org/10.1002/jcd.20309>







# JOURNAL OF THE NATIONAL SCIENCE FOUNDATION OF SRI LANKA

## GUIDANCE TO CONTRIBUTORS

### GENERAL INFORMATION

#### Scope

The Journal of the National Science Foundation of Sri Lanka publishes the results of research in all aspects of Science and Technology. It is open for publication of Research Articles, Reviews, Research Communications and Correspondence.

#### IT related and other non-empirical articles

The JNSF is a journal primarily devoted to natural sciences. It also considers for publication significant and novel contributions from formal sciences. Authors of emerging sub-disciplines of Computing and related areas such as Machine Learning, Artificial Intelligence and Data Sciences are requested to carefully adhere to the following guidelines when submitting manuscripts for this journal.

- Clear formulation of outcome-oriented **Research Objective/s** for targeted knowledge (sub)domain/s or (sub)discipline/s.
- Selection and comprehensive summarization of **appropriate Research Method/s** adopted to achieve the stated Research Objective/s.
- Reporting a sound (**Empirical**) **Evaluation** of the research finding/s thereby arguing reliability, validity, and generalizability of research claim/s.

#### Categories of manuscripts

**Research Articles:** Research Articles are papers that present complete descriptions of original research. Research Articles should include an Abstract, Keywords, Introduction, Methodology, Results and Discussion, Conclusion and Recommendations where relevant. References should be prepared according to the “Guidelines for the preparation of manuscripts”. Maximum length of the article should be limited to 25 pages with a word count of 10,000 including references, figures and tables. Any articles above this limit will be returned.

**Reviews:** Reviews are critical presentations on selected topics of Science or Technology. They should be well focused and organized and avoid general “textbook” style. As reviews are intended to be critical presentations on selected topics, reviewers need to have had substantial leadership in research supported by a publication track record in the areas covered by the review. A person/s wishing to submit a Review Article should obtain prior approval from the Editorial Board by submitting a concise summary of the intended article, along with a list of the author’s publications in the related area ([jnsf@nsf.gov.lk](mailto:jnsf@nsf.gov.lk)). Maximum length of the article should be limited to 40 pages with a word count of 12,000 including references, figures and tables. Any articles above this limit will be returned.

**Research Communications:** Research Communications are intended to communicate important new findings in a specific area of limited scope that are worthy of rapid dissemination among the scientific community. Authors are required to provide a statement justifying the suitability of the submission for a Research Communication. The article should include an Abstract, Keywords, Introduction, Methodology, Results & Discussion, Conclusion and References. Maximum length of the article should be limited to 10 pages with a word count of 2,500 including references, figures and tables. Any articles above this limit will be returned.

**Correspondence:** Correspondence will be accepted regarding one or more articles in the preceding four issues of the Journal, as well as Letters to the Editor. Articles covering important scientific events or any other news of interest to scientists, reviews of books of scientific nature, articles presenting views on issues related to science and scientific activity will also be considered. Publication will be made at the discretion of the Editor-in-Chief. Maximum length of the article should be limited to 05 pages with a word count of 1,500 including references, figures and tables. Any articles above this limit will be returned.

### SUBMISSION OF MANUSCRIPT

Authors submitting articles to the JNSF should first create an account in the Sri Lanka Journals Online System (<https://jnsfsl.sljol.info/>). All manuscripts in MS Word format must be electronically submitted to the journal’s online platform at <https://jnsfsl.sljol.info/submit/start/>. Submissions *via* emails are not encouraged. Please make sure that no author information is mentioned in the article submitted. The names and details of affiliations of all authors and contact information of the corresponding author must be fed into the system during the online submission process. Authors (at least the corresponding author) are required to provide their personal, validated ORCID ID (by obtaining an ORCID ID from <https://orcid.org/>) when submitting the manuscript. No change to the authors or order of authors will be accepted after the submission. All those who have made significant contributions should be listed as co-authors. The corresponding author should ensure that all contributing co-authors are included in the author list and have approved the final version of the paper and have agreed to its submission for publication.

All submissions should be in English. If the manuscript conforms to the guidelines specified, the date received will be the date that the manuscript was submitted to the online system.

Submissions are accepted for processing on the understanding that they will be reviewed and that they have not been submitted for publication elsewhere (including publication as a full paper or extended abstract as a part of Conference Proceedings). The JNSF does not accept manuscripts that have already been submitted to pre-print servers.

#### Suggesting potential reviewers by authors

The authors may suggest up to three names of referees when submitting their manuscript, in the Cover Letter space provided at the bottom of the page in the first stage of online submission. Referees should not be from the institution where the work was carried out and should not have been co-authors in previous publications. The address, institutional affiliation and e-mail of the suggested referees should be supplied. Please note that the JNSF is not bound to select all or any of the suggested referees for sending the manuscript for reviewing

### Authorship

All authors designated as authors should be eligible for authorship. Those who have made a substantial contribution to the concept or design of the work; or acquisition, analysis or interpretation of data are recognized as Authors.

The corresponding author should be prompt and ensure adherence to timelines when responding to requests, queries and recommendation of reviewers conveyed by or on behalf of the Editor-in Chief and Editorial Board.

### Supplementary materials

Any experimental data necessary to evaluate the claims made in the paper but not included in the paper should be provided as supplementary materials. Supplementary materials will be sent to the reviewers and published online with the manuscript if accepted. The supplementary materials should conform to Journal guidelines and should be uploaded as separate files. Authors should number Supplementary Tables and Figures as, for example, 'Supplementary Table S1'. Refer to each piece of supplementary material at the appropriate point(s) in the main article. Supplementary Materials may include description of the materials and methods, controls, or tabulated data presented in Tables or Figures, and programming codes.

### Peer review

The manuscripts submitted to the JNSF will initially be screened by the Editorial Board and, if suitable, will be referred to at least two subject experts in the relevant field. The peer-review process of the JNSF is double-blind.

When revision of a manuscript has been requested, the revised manuscript should be submitted on or before the stated deadline. If the revised manuscript is not received on time, the manuscript will not be processed further. The authors' response to the comments of referees should be tabulated with the comment, response and the line number/s for reference. The decision of the Editorial Board shall be final.

Accepted papers are subject to editing. The date of acceptance will be the date when the Editorial Board has decided it to be acceptable for publication.

### Article publication fee

A total of US\$ 250 will be levied for each accepted manuscript for publication, except when the corresponding author is affiliated to a Sri Lankan Institute, in two stages as explained below.

- A processing fee of US\$ 20 will be levied for each manuscript at peer-review stage and the remaining US\$ 230 will be charged for accepted manuscripts at the time of publication.

Payments can be made online via NSF Payment Portal (<http://pg.nsf.gov.lk/>)

### Authors' declaration

When an article is accepted for publication, the authors are required to submit the Authors' Declaration signed by all the authors.

### Copyright

Articles in JNSF are published under the Creative Commons License CC-BY-ND. This license permits use, distribution and reproduction of articles for commercial and non-commercial purposes, provided that the original work is properly cited and is not changed in anyway. The copyright of the article is with the National Science Foundation of Sri Lanka. Therefore, authors are requested to check with institution's copyright and publication policy before submitting an article to the JNSF. Authors secure the right to reproduce any material that has already been published or copyrighted elsewhere. When an article is accepted for publication, the authors are required to submit the Transfer of Copyright document signed by all the authors.

### Post-publication corrections

The Editorial Board reserves the right to take action on publishing an erratum or corrigendum. If serious errors are identified in a published article, the Journal may consider a retraction or publishing a correction.

## STRUCTURE OF MANUSCRIPT

### Manuscript

The manuscript should be free of errors and prepared in single column, using double-spaced text of Times New Roman 12 font throughout with line numbers, leaving at least 2 cm margins on both sides, and liberal spacing at the top and bottom of each page. Pages should be numbered consecutively.

#### a. Style

The paper should be written clearly and concisely. The style of writing should conform to scholarly writing. Slang, jargon, unauthorized abbreviations, abbreviated phrasings should not be used. In general, the impersonal form should be used. Poor usage of language will result in rejection of the manuscript during initial screening.

#### b. Layout

Manuscripts other than review articles should be generally organized as follows: Title, Abstract, Keywords, Introduction, Methodology, Results and Discussion, Conclusions and Recommendations (where relevant), Acknowledgements and References. Pages should be arranged in the following order:

**Title page** should include the title of manuscript, and no author information should be mentioned in the title page. If a major part of the research has been published as an abstract in conference proceedings, it should be cited as a footnote on the title page. Authors must also indicate the **general and specific research area** of the manuscript in the title page. In order to highlight the significance of the manuscript, authors are required to provide the following highlights in brief. (1) Why was this study conducted? (2) What are the new findings? (3) Possible applications of the findings. Please limit your answers to 25-30 words for each.

**Title:** Should accurately and concisely reflect the contents of the article.

**Running title:** Should be a shortened title (limited to a maximum of 50 characters) that could be printed at the top of every other page of the Journal article.

**Abstract:** Should be between 200 - 250 words for full length articles and written as a single paragraph. It should not contain any references and should be able to stand on its own. It should outline objectives and methodology together with important results and conclusions. A Review Article should carry a summary of not more than 300 words.



**Keywords:** Include a maximum of six keywords, which may include the names of organisms (common or scientific), methods or other important words or phrases relevant to the study.

**Introduction:** This should state the reasons for performing the work with a brief review of related research studies in the context of the work described in the paper. Objectives of the study should be clearly stated.

**Materials and Methods:** This section should give the details of how you conducted your study. New methods may be described in detail with an indication of their limitations. Established methods can be mentioned with appropriate references. Sufficient details should be included to allow direct repetition of the work by others. Where human subjects are involved, they should be referred to by numbers or fictitious names. A paper reporting the results of investigations on human subjects or on animals must include a statement to the effect that the relevant national or other administrative and ethical guidelines have been adhered to, and a copy of the ethical clearance certificate should be submitted. Methods of statistical analyses used should be mentioned where relevant.

**Results and Discussion:** Results: the results should be concisely and logically presented. Repetition of the same results in figures, tables or text should be avoided.

Discussion: data essential for the conclusions emerging from the study should be discussed. Long, rambling discussions should be avoided. The discussion should deal with the interpretation of results. It should logically relate new findings to earlier ones. Unqualified statements and conclusions not completely supported by data should be avoided.

Molecular sequence data, such as gene or rDNA sequences, genome sequences, metagenomic sequences etc. must be deposited in a public molecular sequence repository, such as GenBank, that is part of the International Nucleotide Sequence Database Collaboration (INSDC). The accession numbers obtained must be cited in the text, Table or on Figures of phylogenetic trees of the manuscript.

**Conclusion:** The conclusion should be brief, highlight the outcomes of the study and should be aligned with the objectives of the study. It should not contain references.

**Conflict of interest statement:** All authors should include a statement on conflict of interest disclosing any financial or other substantive conflicts of interest that may be construed to influence the results or interpretation of their research. All sources of financial support for the project should be disclosed.

**Acknowledgement:** Should be brief and made for specific scientific, financial and technical assistance only. If a significant part of the research was performed in an institution other than in those indicated by the authors' affiliations given in the title page, this fact should be acknowledged. All those who have made substantial contribution to the research but do not qualify to be authors should be acknowledged.

#### References :

The JNSF uses APA ( 7<sup>th</sup> Edition) reference style from July 2024

All research work of other authors, when used or referred to or cited, should be correctly acknowledged in the text and in the References.

All the references in the text should be in the list and vice versa

Citing references in the text:

- References to the literature must be indicated in the text and tables as per the Author-Year System, by the author's last name and year, in parenthesis (i.e. Able, 1997) or (Able & Thompson, 1998).
- Citation to work by more than two authors should be abbreviated with the use of et al. (i.e. Able *et al.*, 1997).
- Multiple publications by the same first author in the same year should be coded by letters, (i.e. Thompson, 1991a, 1991b, 1992, 1993).
- Multiple citations of different authors should be made in chronological order and separated by a semicolon, (i.e. Zimmerman *et al.*, 1986; Able *et al.*, 1997).

Citing references in the List of references:

- The list of References should be arranged in alphabetical order based on the last name of the first author.
- In APA 7th ed., **up to 20 authors** should be included in a reference list entry. Write out the last name and first initial(s) for each contributor.

#### Example for 2–20 authors:

Wright, A., Komal, G., Siddharth, D., Boyd, G., Cayson, N., Beverley, K., Travers, K., Begum, A., Redmond, M., Mills, M., Cherry, D., Finley, B., Fox, M., Ferry, F., Almond, B., Howell, E., Gould, T., Berger, B., Bostock, T., & Fountain, A. (2020). Styling royalty. London Bridge Press.

- For references with more than 20 authors, after listing the 19th author replace any additional author names with an ellipsis ( ... ) followed by the final listed author's last name and first initial(s).

#### Example for 21+ authors:

Kalnay, E., Kanamitsu, M., Kistler, R., Collins, W., Deaven, D., Gandin, L., Iredell, M., Saha, S., White, G., Woolen, J., Zhu, Y., Chelliah, M., Ebisuzaki, W., Higgins, W., Janowiak, J., Mo, K.C., Ropelewski, C., Wang, J., Leetmaa, A., ... Joseph, D. (1996). The NCEP/NCAR 40-year reanalysis project. *Bulletin of the American Meteorological Society*, 77(3), 437-471. <http://doi.org/fg6rf9>

- All the initials of the author must be given after the last name and the year of publication should follow in parentheses.
- This should be followed by the full title of the referred publication.
- When journal articles are listed, the journal name should be given in full and in italics and followed by the volume number, issue number in parentheses and then the inclusive pages.
- Where there are several publications by the same author(s) and published in the same year they should be differentiated by adding a lower-case letter after the year.

#### Example

Clarke, P. N., & Fawcett, J. (2014a). Life as a mentor. *Nursing Science Quarterly*, 27(3), 213-215. <https://doi.org/10.1177/0894318414534492>

Clarke, P. N., & Fawcett, J. (2014b). Life as a nurse researcher. *Nursing Science Quarterly*, 27(1), 37-41. <https://doi.org/10.1177/0894318413509708>

- Digital object identifiers (DOIs) should be included for all references where available.

Details about this reference style can be obtained from below links

- <https://apastyle.apa.org/style-grammar-guidelines/references>
- <https://apastyle.apa.org/style-grammar-guidelines/references/examples>
- <https://libguides.jcu.edu.au/apa>

**Abbreviations and Symbols:** Unless common, these should be defined when first used, and not included in the abstract. The SI System of units should be used wherever possible. If measurements were made in units other than SI, the data should be reported in the same units followed by SI units in brackets, e.g. 5290 ft (1610 m).

**Formulae and Equations:** Equations should be typewritten and quadruple spaced. They should be started on the left margin and the number placed in parentheses to the right of the equation.

**Nomenclature:** Scientific names of plants and animals should be printed in italics. In the first citation, genus, species and authority must be given. e.g. *Borassus flabellifer* Linn. In latter citations, the generic name may be abbreviated, for example, *B. flabellifer* L.

**Tables and figures:** Tables and Figures should be clear and intelligible and kept to a minimum, and should not repeat data available elsewhere in the paper. Any reproduction of illustrations, tabulations, pictures etc. in the manuscript should be acknowledged.

**Tables:** Tables should be numbered consecutively with Arabic numerals and placed at the appropriate position in the manuscript. If a Table must be continued, a second sheet should be used and all the headings repeated. The number of columns or rows in each Table should be minimized. Each Table should have a title, which makes its general meaning clear, without reference to the text. All Table columns should have explanatory headings. Units of measurement, if any, should be indicated in parentheses in the heading of each column. Vertical lines should not be used and horizontal lines should be used only in the heading and at the bottom of the table. Footnotes to Tables should be placed directly below the Table and should be indicated by superscript lower case italic letters (<sup>a</sup>, <sup>b</sup>, <sup>c</sup>, etc.).

**Figures:** All illustrations are considered as figures, and each graph, drawing or photograph should be numbered consecutively with Arabic numerals and placed at the appropriate position in the manuscript. Any lettering to appear on the illustrations should be of a suitable size for reproduction and uniform lettering should be used in all the Figures of the manuscript. Scanned figures or photographs should be of high quality (**300 dpi**), to fit the proportions of the printed page (12 × 17 cm). Each figure should carry a legend so that the general meaning of the figure can be understood without reference to the text. Where magnifications are used, they should be stated.

#### Units of measurement

Length: km, m, mm, μm, nm

Area: ha, km<sup>2</sup>, m<sup>2</sup>

Capacity: kL, L, mL, μL

Volume: km<sup>3</sup>, m<sup>3</sup>, cm<sup>3</sup>

Mass: t, kg, g, mg, μg

Time: year(s), month(s), wk(s),

d(s), h, min, s

Concentration: M, mM, N, %,

g/L, mg/L, ppm

Temperature: °C, K

Gravity: x g

Molecular weight: mol wt

Others: Radio-isotopes: 32P

Radiation dose: Bq

Oxidation-reduction potential: rH

Hydrogen ion concentration: pH